LASER WELDING OF DISSIMILAR CARBON STEEL TO STAINLESS STEEL 316L

A thesis submitted to

Loughborough University

For the degree of

Doctor of Philosophy (PhD)

Mohammadreza Nekouie Esfahani

B131797

Supervisors:

Dr. Sundar Marimuthu

Prof. Jeremy Coupland

2015

The Wolfson School of Mechanical and Manufacturing Engineering

ABSTRACT

Laser welding of metals and alloys is extensively used in industry due to its advantages of controlled heating, narrow weld bead, low heat affected zone (HAZ) and its ability to weld a wide range of metals and dissimilar metals. Laser welding of dissimilar metals such as carbon steels and stainless steel is still a challenging task, particularly due to the formation of brittle phases in the weld, martensitic formation in the HAZ and solidification cracking in the fusion zone. These issues can significantly deteriorate the strength of the welded joint. The aim of this work is to investigate the fundamental phenomena that occur inside the dissimilar weld zone and their effect on weld quality. In order to establish the key process variables, an initial study concentrated on the effect of different laser process parameters on dissimilar weld quality. In the second part of the work, a comprehensive study was performed to understand and subsequently control the alloying composition in laser dissimilar welding of austenitic stainless steel and low carbon steel. A dissimilar weld that is predominantly austenitic and homogeneous was obtained by controlling the melt pool dynamics through specific point energy and beam alignment. The significance of dilution and alloying elements on joint strength was established. A coupled CFD and FEM numerical model was developed to assist in understanding the melt pool dynamics and transportation processes of alloying elements. The model has been validated by a series of laser welding experiments using various levels of specific point energy. The laser welding characteristics in terms of geometric dimensions, surface morphology, alloying concentration, and dilution, were compared, and it is concluded that the specific point energy and laser beam position are the key parameters that can be controlled to obtain a weld bead with characteristics most suitable for industrial applications. In the third part of the work, a comparative study was performed to understand the significance of cooling rate, and alloying composition on the microstructure and phase structure of the dissimilar weld zone. Results show that the HAZ within the high carbon steel has significantly higher hardness than the weld area, which severely undermines the weld quality. A new heat treatment strategy was proposed based on the results of the numerical simulation, and it is shown to control the brittle phase formation in HAZ of high carbon steel. A series of experiments was performed to verify the developed thermo-metallurgical FEA model and a good qualitative agreement of the predicted martensitic phase distribution is shown to exist. Although this work is presented in the context of dissimilar laser welding of mild steel to stainless steel, the concept is applicable to any dissimilar fusion welding process.

TABLE OF CONTENTS

LIST OF FIGURES

7

LIST OF TABLES

ACKNOWLEDGMENTS

DECLARATION

I hereby declare that no portion the work referred to in the thesis has been submitted in support of an application for another degree or qualification of this or any other university or other institute of learning.

LIST OF PUBLICATIONS

A list of publications taken from the thesis is given below. These are also included in full as appendices.

1. Esfahani, Reza, J. Coupland, and S. Marimuthu. "Microstructure and mechanical properties of a laser welded low carbon-stainless steel joint". *Journal of Materials Processing Technology* (2014).

2. Esfahani, MR Nekouie, J. Coupland, and S. Marimuthu. "Microstructural and mechanical characterisation of laser-welded high-carbon and stainless steel." *The International Journal of Advanced Manufacturing Technology* (2015): 1-8.

3. Esfahani, R., Marimuthu, S., and Coupland, J. "Numerical simulation and experimental investigation of laser dissimilar welding of carbon steel and austenitic stainless steel'', ". *Journal of Materials Processing Technology* under publication (2015)*.

4. Esfahani, MR Nekouie, J. Coupland, and S. Marimuthu. "Numerical simulation and experimental investigation of laser dissimilar welding of carbon steel and austenitic stainless steel." *Industrial Laser Applications Symposium 2015*. International Society for Optics and Photonics, 2015.

LIST OF ACRONYMS

LDW	Laser dissimilar welding
IMC	Intermetallic phases or compounds
YAG	Yttrium – aluminium garnet
CAD	Computer aided design
CAM	Computer aided manufacturing
CNC	Computer numerical control
CW	Continuous wave
EBW	Electron beam welding
EDX	Energy dispersive X-ray analysis
SEM	Scanning electron microscopy
HAZ	Heat affected zone
DOF	Depth of focus
DoE	Design of experiment
OM	Optical microscopy
FW	Friction welding
FSW	Friction stir welding
RSM	Response surface methodology
BPP	Beam parameter product
CO_2 laser	Carbon dioxide laser

Chapter 1 Introduction to Laser Dissimilar Welding

1.1 Metal welding process

The rapid exploitation of advanced materials over the last few decades can be attributed to the developments of novel joining techniques. Welding and other joining methods are extensively used in various engineering applications, and many modern products such as cars, transportation systems, and power plants could not be possible without it. The first phase in this technological revolution occurred when welding technology replaced fastening processes. This provided enhancement in efficiency, productivity, lightweight production and surface finishing of manufactured components. Modern welding technologies, such as laser welding, friction stir welding and electro-beam welding allow joining of advanced materials. Today laser technology is revolutionising manufacturing processes due to its ease and flexibility and of non-contact processing, amenability to materials with diverse shape/geometry, properties and chemistry, and high precision/productivity.

Over the last 50 years, the availability of lasers has opened up new opportunities in industrial applications replacing many conventional welding technologies. Laser processes provide higher beam power and quality, which consequently provide higher production rate, great focusability (as a result of delivering precise directed energy at the desired beam shape), lower heat input and distortion, improved welding surface finish, and lower residual stress in welding. The key strength of laser beam welding (LBW) is its ability to produce a weld without defects and with a narrow heat affected zone. LBW also has the potential to produce high weld quality with control of the thermal cycle and fluid flow in the fusion zone which makes it a favourable technique for dissimilar welding of austenitic/ferritic steels. It is also worth mentioning that as a result of complex nature of the process and contribution of multiple interconnection variables, purely experimental trials cannot provide an in depth understanding of the dissimilar welding process. This requires a robust methodology for predicting the results accompanied by numerical modelling techniques [1] and [2]. In general, the laser beam welding process is influenced by many parameters such as laser parameters (laser power, interaction/pulse time, gas flow rate, beam diameter, and beam alignment), thermo-mechanical properties

(thermal conductivity, coefficient of thermal expansion, etc.) and target dimensions of the workpiece (thickness, curvature, etc.).

Austenitic stainless steels and carbon steels are one of the most commonly used materials in heavy industries, especially in power generation, transportation, and petrochemical industry due their service performance, high weldability, and economical nature [3-5]. Most of the components (e.g. heat exchangers) work under different service conditions and therefore require appropriate materials. For instance components working under high temperature conditions are manufactured out of stainless steel (high oxidation resistance and creep strength) while carbon steel is used for parts working under low temperatures which make them more economical [3, 6, 7]. However there are many challenges during the welding of stainless steels to carbon steels, due to differences in thermo-physical properties and alloying composition, migration of carbon from higher carbon containing alloy to the steel with lower carbon content, residual stress, difficulties in performing post heat treatment, and metallurgical variations such as delta ferrite and sigma phases that must be carefully controlled. In addition such dissimilar joints are vulnerable to solidification cracks, uneven dilution, and phase transformation [6, 8-14]. Among these, the most critical challenges are related to martensitic phase transformation in the fusion zone and uneven dilution. The laser dissimilar welding process can be an efficient way of joining materials, however the above mentioned issues needs to be further understood.

1.2 Aims and objectives of the project

The aim of the work reported in this thesis is to investigate the basic underlying phenomena in laser dissimilar welding that influence the weld quality, through experimentation and numerical analysis. Stainless steel and carbon steel were used as the welding materials due to their wider use across range of sectors including power generation, chemical, petrochemical, and nuclear industries. Thus the following objectives were set:

- Investigate the key process variables that influence the dissimilar laser welding quality. This study will act as a foundation for further fundamental analysis.
- Investigate the significance of melt pool dynamics on microstructure, diffusion, hardness and weld strength of the dissimilar weld fusion zone.

- Develop a coupled CFD and FEM model to study the multiphase phenomena in dissimilar molten pool and to study the effect of melt pool dynamics on dissimilar weld fusion zone characteristic.

- Investigate the effect of cooling rate on the microstructure, and service performance of the dissimilar fusion zone.

- Develop a numerical model to simulate cooling rate and phase transformation in the weldment, and to study the influence of post-heat treatment on the mechanical properties of the dissimilar welded joint.

1.3   Thesis structure

This thesis presents a theoretical and experiment analysis on laser dissimilar welding of austenitic stainless steel to carbon steel. The thesis comprises of nine chapters which are described as follows.

Chapter 2 presents a fundamental review of lasers and laser welding theory. This is followed by a detailed literature review of the current state-of-the-art in welding science, including heat and mass transfer, melt pool dynamics, weld-track formation and solidification microstructure.

Chapter 3 discusses the experimental methodology and characterisation techniques used in this research. The statistical analysis technique employed with experimental results are also discussed.

Chapter 4 discusses the investigation carried out on CO_2 laser dissimilar welding of low carbon steel and stainless steel. The investigation was aimed at studying the effect of process parameters on weld quality and to establish the key process variables.

Chapter 5 investigates the effect of laser parameters on meltpool characteristics. The microstructure, diffusion, hardness and weld strength of the dissimilar weld fusion zone were studied. The influence of beam position on microstructural variations was also investigated.

Chapter 6 discusses a numerical model developed to assist in understanding the dissimilar melt pool dynamics and transportation of alloying elements. The volume of fluid technique was used to assess the dissimilar melt pool movement inside the fusion

zone. The effect of specific point energy on the weld geometry, surface morphology and mixing of the alloying elements was investigated.

Chapter 7 reports an investigation into the microstructure that arises from laser dissimilar welding of high carbon steel to austenitic stainless steel. The significance of high cooling rate and alloying composition on the microstructure and phase constitution of the dissimilar fusion zone was investigated. Typical issues that arise in welding higher carbon to stainless steel are also discussed.

Chapter 8 extends the experimental analysis described in chapter 7 and presents a sequentially coupled thermo-metallurgical finite element model, which was developed based on FLUENT code to predict cooling rate, thermal cycle and phase fraction of the heat affected zone of high carbon steel. The effect of various cooling rates on the martensitic phase transformation was also investigated. Strategies to achieve a weld that was predominantly homogenous with acceptable quality are discussed.

Chapter 9 gives a brief overview of the major conclusions and findings observed in this research as well as recommendations for future studies.

Chapter 2 Review of the Fundamental Theory of Laser Dissimilar Welding

2.1   Laser beam welding

This chapter presents a review of the current state-of-the-art in laser dissimilar welding (LDW). Laser fundamentals relevant to laser dissimilar welding including, lasing phenomena, laser systems and characteristics of laser beams are discussed. The basic fundamentals of laser dissimilar welding are discussed in detail and a detailed literature review on laser dissimilar welding is presented. This review includes mass and energy transfer, melt pool dynamics and weld bead formation during laser dissimilar welding. Melt pool solidification and microstructure with reference to the laser dissimilar welding were discussed. Features of laser dissimilar welding on the surface topology, geometry of the weld bead, alloying and microstructure, residual stress and distortion were also discussed.

Laser welding is a fusion welding technique used to join various materials through melting and solidification. Laser welding is predominantly used for joining components that needs high welding speeds, thin and small weld seams and low thermal distortion. According to Ribolla et al. [15], laser welding is one of the most robust technologies, which is widely used across various sectors including aerospace, automotive and nuclear industries.

A typical laser welding system is illustrated schematically in Figure 2-1. Laser welding process is achieved by melting the workpiece to form a weld pool/melt pool at the place of the joint followed by rapid re-solidification [16]. The melt pool on the surface is very dynamic and is protected from oxidation typically using a shielding gas (commonly argon or helium) from the nozzle. Depending on laser power density and speed, the laser welding process can either be of keyhole or conduction welding [17].

(a)   (b)
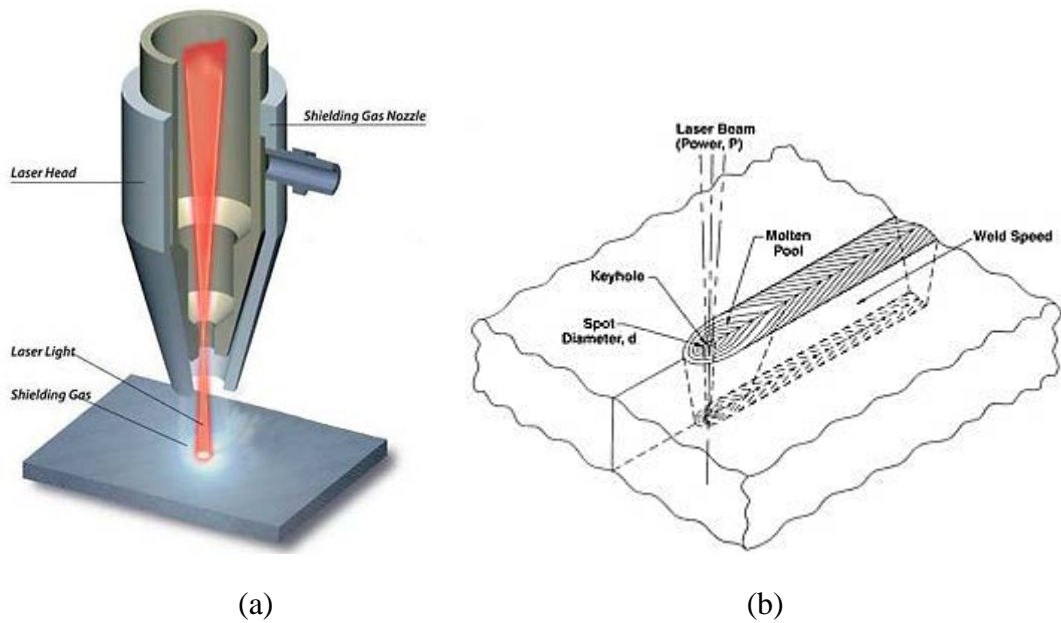
Figure 2-1 Schematic illustration of laser beam welding
(a) Laser welding setup (b) Close-up view of the laser welding process

2.1.1 Keyhole mode laser welding

Keyhole welding is mostly used for welding of high thickness materials [18] using high power density in the range of $1\times10^6 \text{W/cm}^2$ and $5\times10^7 \text{W/cm}^2$. High power density in keyhole welding leads to localized vaporization of the metals and formation of deep penetrating vapor/plasma cavity, called keyhole. The keyhole is surrounded by layers of molten materials. This layer is maintained at the equilibrium between vapor pressure (recoil pressure) and surface tension as the main driving force for keyhole formation [19]. Hydrodynamic pressure, recoil pressure and radiation pressure helps to keep the keyhole open and make it deep while hydrostatic pressure and surface tension force help to keep the keyhole close and restricts it from becoming deeper. However, as the magnitude of the recoil pressure and surface tension pressure is significantly higher comparison to the other pressures, only these two pressures were considered during numerical calculations [19]. Figure 2-2 illustrates the keyhole mode laser welding and cross section of laser welded sample in keyhole mode.

Welding direction (moving laser beam)

←

(a)   (b)
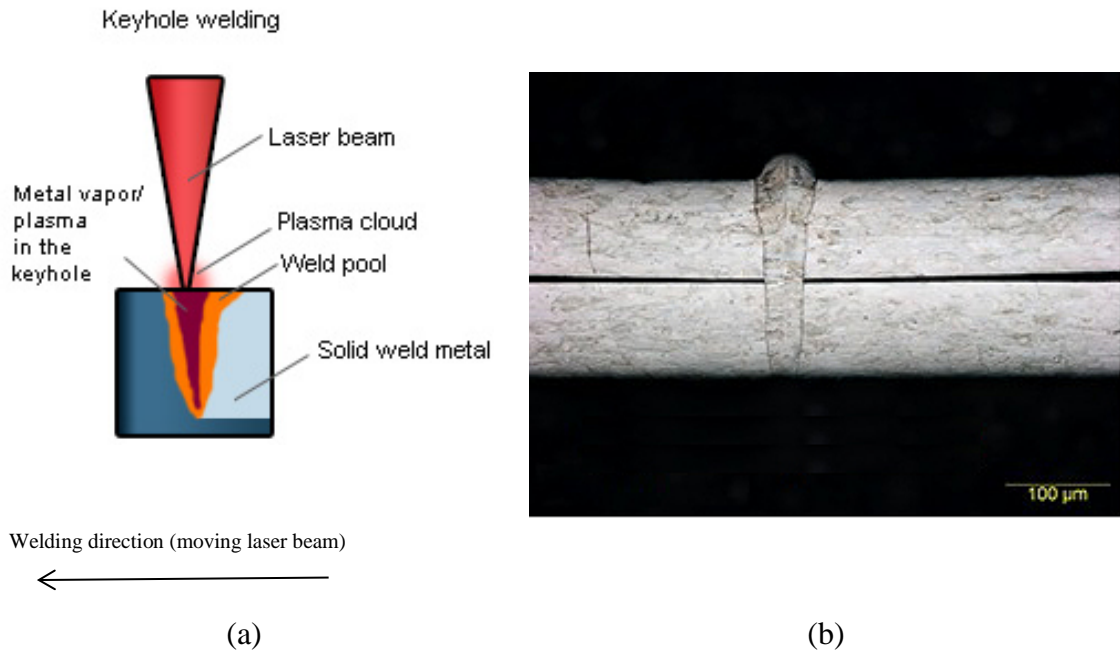
Figure 2-2 Keyhole laser welding (a) Schematic of keyhole mode welding and (b) Cross-section of laser welded sample in keyhole mode [17]

2.1.2 Conduction mode laser welding

In conduction mode, a low laser power density is applied to the weld joint, which heats up the surface of the material and melts it without any vaporization of base metals [18]. Conduction welding is mainly used for low thickness and low penetration welding with power density less than 10^6 W/cm^2 [19]. The laser material interaction happens only at the surface of the work piece and the heat is transferred into the substrate by conduction and convection of molten pool. In conduction welding, the width of the weld joint on the surface is generally larger (compared to keyhole welding). The keyhole mechanism often produces welding beads with high porosity due to collapse of the keyhole and gas entrapment occurring during the solidification of the weld pool. In contrast, conduction welding is a more stable and more linear compared to keyhole welding [20-22]. It has been recently shown that the magnesium and chromium within the austenitic stainless steel weld bead is lower in keyhole mode [23] than conduction mode welding [9]. Conduction welding also produces high quality smooth, rounded weld beads that do not require any extra grinding or finishing. Figure 2-3 illustrates conduction mode welding and cross section of conduction mode laser welded sample.
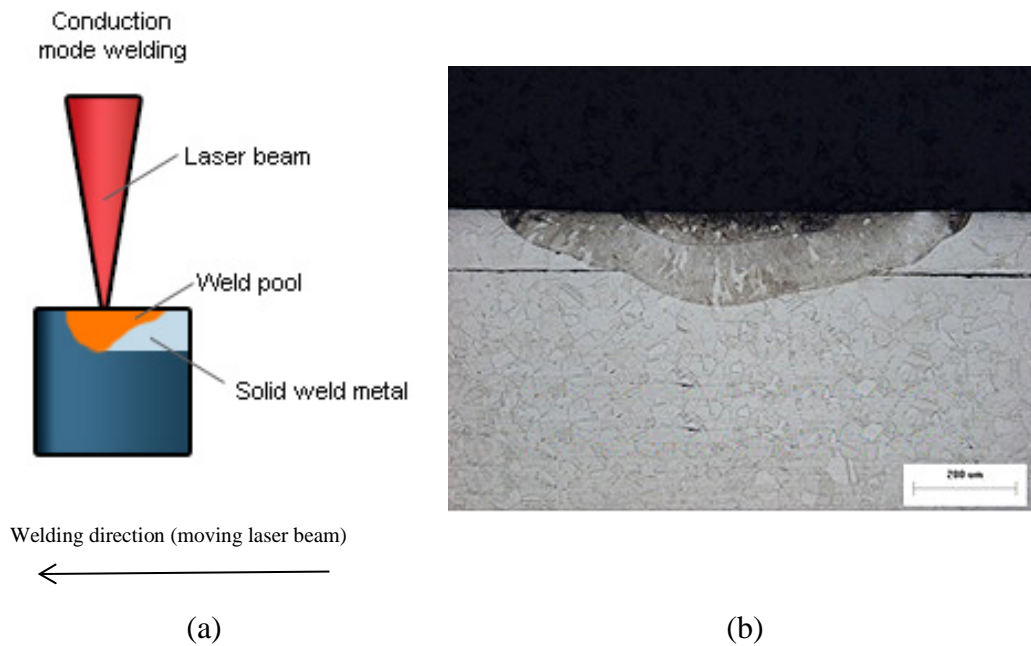
Figure 2-3 Conduction laser welding (a) Schematic of conduction mode welding and (b) Cross-section of laser welded sample in conduction mode [17]

2.1.3 Typical lasers for welding

During welding, a laser beam of sufficient intensity (or power density) is incident upon the work piece, and is moving at a constant velocity (scanning speed) to obtain a continuous weld. The laser beam intensity predominantly depends on the laser source and it significantly controls the laser welding process.

A range of laser sources, with various optical configurations were used for laser welding process. Despite recent developments in fibre laser systems, traditional lasers such as Nd:YAG and CO_2 lasers are still predominantly used in industrial welding systems. CO_2 lasers are reliable, robust and well-engineered industrial machines with output powers up to 50kW [24]. The configuration of a typical CO_2 laser is shown in Figure 2-4.
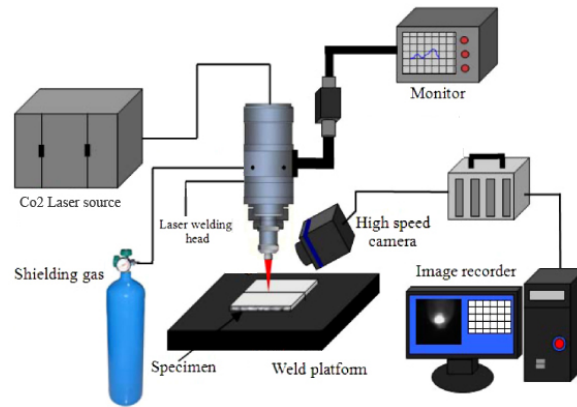
Figure 2-4 Configuration of a CO_2 laser beam welding [15]

Welding with high power CO_2 lasers (10.06μm wavelength) has been carried out for well over 30 years [24-26]. Locke et al. [27] investigated the laser welding of stainless steel 304 with depth of penetration up to 15mm and reported that the CO_2 laser welding can be a good replacement for electron beam welding. Zhu et al. [28] investigated the process characteristic and mechanisms involved in diode and CO_2 laser welding of AZ31 magnesium alloy. They reported that for 1mm thick AZ31, a power density of 8000W/cm^2 is desirable to obtain a full penetration at welding speed of 150mm/s employing CO_2 laser or 50mm/s employing diode laser. They also reported that the spot size of the diode laser is limited to conduction welding during defocusing, while good quality keyhole welding is produced by CO_2 lasers.

The trend in laser welding applications has been toward high power CO_2 welding with continuous laser beams of 5-10kW. Modern CO_2 lasers have beam qualities close to its diffraction limit [29]. The CO_2 laser system encapsulates N_2, He and CO_2 gas flow in an isolated system wherein majority of the gas is recycled via discharging process. This makes the CO_2 laser operate at relatively low operational costs [18, 24].

Many researchers have recently reported the advantages of fibre lasers compared to Nd:YAG and CO_2 lasers as a result of better beam quality and small beam diameter. The higher beam quality and smaller beam diameter of fibre lasers in comparison to CO_2 laser also facilitates higher penetration depth and lower residual stress/distortion [30]. However, in contrast to their findings, there are some reports which highlight the formation of humping, porosity and pearl-like shape in the weld root due to the small diameter of the keyhole, narrow melt pool and the high surface tension involved in fibre laser welding [29-31].

Prior to the introduction of fibre laser, Nd:YAG lasers were extensively used for keyhole laser welding. Nd:YAG lasers have higher processing efficiency compared to CO_2 lasers for similar power levels. Duly [24] showed higher weld penetration depth with Nd:YAG welding than CO_2 types for mild steel at the same power level. This is attributed to the shorter wavelength (1.06μm) of solid state lasers (Nd:YAG), which increases the absorption level. Also the shorter wavelength enables them to be less susceptible to plasma absorption, compared to CO_2 lasers. In terms of beam delivery, Nd:YAG lasers can propagate via fibres or lens systems, whereas CO_2 lasers propagate only via lens systems. Furthermore, Nd:YAG laser provide higher pulse energies and are smaller than a CO_2 lasers [32], [33] and [34]. However, Baardsen et al. [35] compared CO_2 and Nd:YAG lasers for welding of galvanized steels and showed that the CO_2 laser offers better reliability and higher welding speeds for the same power level.

Seng Ng [36] carried out an investigation of laser welding of high carbon steel using a pulsed 400W Nd: YAG laser, a 1.2 kW CW CO_2 laser and a 1.4 kW CW high power diode laser. He analysed and compared the weld quality of different laser systems and concluded that CO_2 lasers provide a better weld quality with lower hardness profiles, wider weld bead, higher tensile strength and greater weld volume formation.

Zhu et al. [28] discussed different welding mechanisms (conduction; keyhole) and studied Nd:YAG and CO_2 laser welding of magnesium alloys. Hiraga et al. [37] reviewed the weldability of 1.7 mm thickness wrought magnesium alloys (AZ31B-H24) using 2 kW CW CO_2 and Nd:YAG lasers and concluded that the CO_2 laser welded fusion zone is lower than that produced by Nd:YAG lasers [38], [39] and [37].

Baardsen et al. [35] performed high speed laser welding of galvanized steels using a CO_2 and YAG laser. He demonstrated that the CO2 laser offers better reliability and higher welding speeds comparison to Nd:YAG laser at similar laser power levels.

Lin Li [40] compared high-power diode lasers (HPDL) to Nd:YAG and CO_2 lasers and reported that a diode laser provide better surface finish, less heat-affected zone, better beam absorption as a result of its shorter wavelength and multiple beam integration during laser welding process.

Salminen et al. [30] made a comparison between CO_2 and fibre laser to analyse the weld penetration depth as a function of heat input (Figure 2-5) and showed that the fibre laser welding is 10–20 percent more efficient than the CO_2 laser welding.
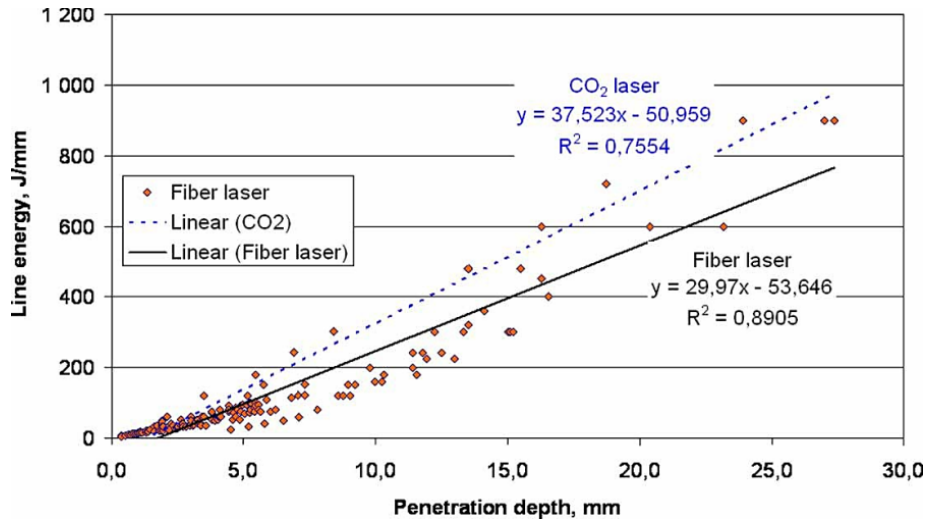
Figure 2-5 Comparison of heat input as a function of weld penetration depth for fibre and CO_2 laser [30]

2.2 Laser welding parameters

Laser welding is controlled by many parameters including laser power, welding speed, focus position and shielding gas [3]. In general, the weld geometry and penetration depth significantly depends on the energy per unit length which is delivered to the joint, which depends on the laser power and speed. Successful laser welding requires careful consideration of addition parameters such as the beam size, focus position, shielding gas type and flow rate and nozzle geometry. Typical parameters associated with CO_2 laser welding is shown in Table 2-1 [24].

Table 2-1 Typical processing parameters of CO_2 laser welding

No	Parameters
1	Laser power
2	Welding speed
3	Focal position
4	Power density
5	Shielding gas
6	Welding gap and alignment
7	Wavelength

Laser power

Laser beam power accompanied by welding speed is the two main important laser welding inputs which considerably influence the resulting weld. Extremely low laser power will result in a major weld defect such as lack of penetration and extremely high power will result in a drop through of the weld [41, 42].

Many researchers have highlighted the importance of laser power in welding process. Khana et al. [43] investigated laser welding of two different types of martensitic stainless steels (AISI 440FSe and AISI 416) employing a Nd:YAG continuous wave laser. Laser powers ranging from 800–1100 W, welding speeds ranging from 4.5–7.5 m/min and beam diameters ranging from 300-400 µm were used to study the influence of laser power, and welding speed and laser beam diameter on weld geometry and service performance. They discussed that laser power and welding speed play the most important role on shearing force and weld geometry of the weld as both affect weld resistance length and cooling rate.

Li et al. [44] used a continuous-wave Nd:YAG laser to weld overlap joints between H62 brass and 316L stainless steel. He investigated the influence of laser power and welding speed on microstructure, microhardness, element distribution and tensile shear strength of the dissimilar joint. They showed that above certain threshold of welding heat input (37.5 J/mm), laser power is the main factor which determines penetration-to-width ratio while below that threshold welding speed is the main parameters which affects the ratio and the weld geometry.

Kim [45] demonstrated that the absorptivity of the laser power is influenced by the wavelength of the laser beam and the optical properties of the workpiece material. Kim also showed that the key parameters of laser welding are the laser power, processing speed and beam diameter.

Welding speed

Welding speed has a significant influence on process productivity, weld pool flow pattern and fusion zone geometry. It also has inverse proportional effect on penetration depth and weld width (Figure 2-6). At low speeds the pool is large and wide, and may result in drop out. In this case the ferrostatic force is too large for the surface tension to keep the pool in place and so it drops out of the weld leaving a hole or depression. At higher speeds, the strong flow towards the center of the weld following the keyhole has no time to redistribute, and hence can solidify as an undercut at the sides of the weld [18]. Mai and Spowage [46] carried out an study on pulsed Nd:YAG laser welding of dissimilar metals for three combinations of metals (steel–kovar, copper–steel and copper–aluminium). They reported a strong correlation between welding speed and weld porosity. They concluded that increasing the welding speed result in reduction of weld porosity. This is due to the fact that high speed result in shallow molten pool thus favourable condition for pores to move to the weld surface, before melt solidification.
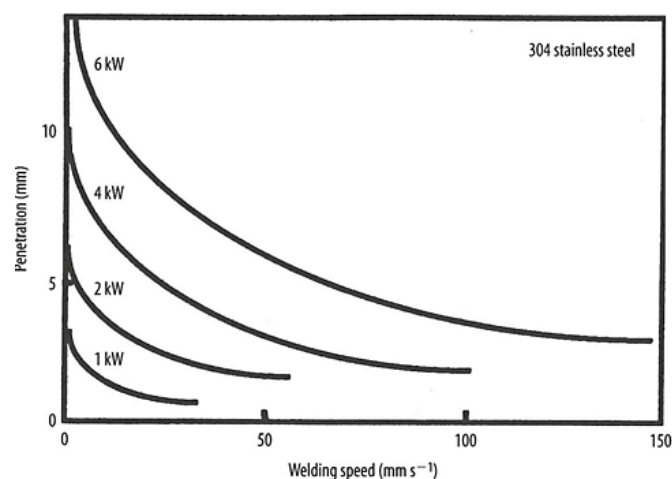
Figure 2-6 The relation between welding speed and penetration depth [47]

Focus position

The focal plane position can have a significant effect on welding quality. Normally the focal plane is tuned to achieve maximum penetration depth and best process tolerance. El-Batahgy [48], investigated the relationship between the defocusing distance and penetration depth of stainless steels. His research shows that, the maximum penetration depth was observed at a defocusing distance between 0 to -1mm (Figure 2-7). However, this needs to be confirmed for each material and laser configuration. Tsukomoto et al. [49] showed that the depth of penetration decreases rapidly at defocus values greater than 2mm above the surface. The decrease in depth of penetration is attributed to plasma shielding. Such phenomenon is relatively trivial when the beam is focused below the surface of the workpiece.
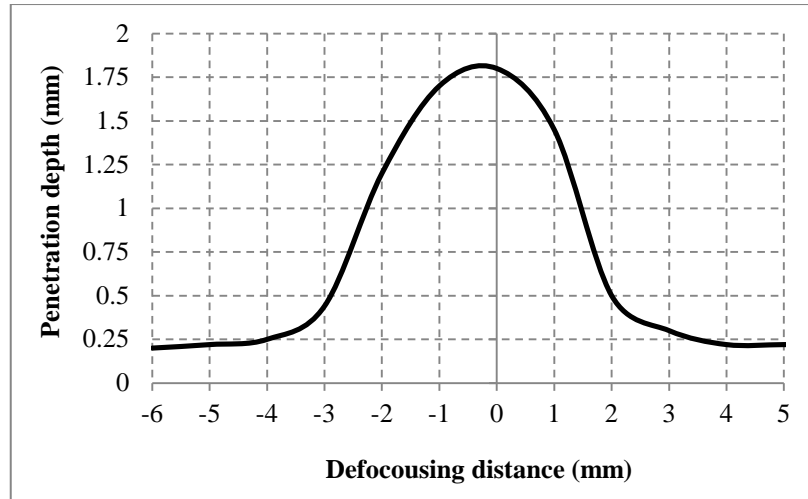
Figure 2-7 The effect of defocusing distance on penetration depth [48]

Power density

Laser power density significantly influences the type of welding i.e. conduction or keyhole laser welding. Power density has a direct effect on the weld geometry and fluid flow in the fusion zone [4, 5, 18, 50, 51]. The power density at the focal point is estimated from the incident laser power and the size of the beam over the surface. For a Gaussian distributed laser beam (TEM$_{00}$), the beam size is defined as the radial distance at which the intensity of the beam decreases to 13.5% of the peak intensity [52]. This is also the area that has approximately 87.5% of the total beam energy. The power density (intensity or irradiance), I, is given by

$$I = \frac{q}{\pi \omega^2}$$

E.q(5)

where q is the power of the laser beam (W) and ω is the beam radius (mm).

Torkamany et al. [4] carried out an investigation on dissimilar overlap welding between austhentic stainless steel and carbon steel. The influence of power density and consequent welding mode is studied on the microstructure and mechanical performance of dissimilar joint. It is showed that transition of the laser welding mode from conduction to keyhole welding as a result of power density variation have a significant impact on the dissimilar fusion zone geometry, dilution of carbon steel and consequent microstructure in the weld.

Kawahito et al. [31] studied the effect of laser power density on the formation of sound welds for austenitic stainless steel employing a high-power fibre laser with four different laser beams of 130, 200, 360 and 560μm spot diameters. Full penetration, without weld defects such as porosity, under filling or humping is obtained using spot diameters of 360 μm.

The relation between defects in welding with average power density, weld speed and pulse duration were investigated by Tzeng [53]. He discussed that that the increase in weld width with increasing pulse duration is enhanced by higher average power density as a result of stronger sideways heat flow during pulsed laser welding.

Cheng et al. [54] investigated the Influence of power density on defect/hole and centreline cracks of stainless steel weld. They showed that that the dimension of hole formation depends on the laser power density, and the hole disappears as the power density is below 3×10^5 W/cm^2.

Jouvard et al. [55] studied the Influence of power density on keyhole formation and weld depth during pulsed Nd:YAG laser welding. They reported that power density is the most critical parameter on formation of the keyhole and that the absorption of the beam increases significantly during the formation of the keyhole, and tends towards a limit value.

Mai and Spowage [46] performed dissimilar welding between steel–kovar, copper–steel and copper–aluminium using a pulsed Nd:YAG laser system. They reported the formation of intermetallic compound layers as undesirable compounds in the weldments. They also concluded that laser welding can minimise or avoid the formation of brittle intermetallic phases due to its locally restricted energy input and high power density.

Shielding gas

In laser welding the shielding gas is used to protect the weld pool from oxidation and porosity which can result in low weld quality. It also protects the beam delivery systems from metal vapor and any weld spatter. The shielding gas flow rate can also influence the melt pool stability. If it is too high, it will cool and blow away the molten metal rapidly, which result in very low welding quality. If the gas flow rate is too low, the molten pool losses its isolation from oxygen, which can oxidize the welding layer, and decrease the mechanical properties. Therefore, an optimal gas flow range should be used, that can protect both weld zone, and laser beam delivery system. It is also recommended to use Helium where high quality welds are required for materials like stainless steel, titanium, and zirconium. Argon is mostly used in the welds where oxidation is of greater concern at high temperature [18, 24].

Sattiya et al. [56] carried out an investigation on CO_2 laser–GMAW hybrid welding with different shielding gas mixtures (50%He + 50%Ar, 50%He + 45%Ar + 5%O_2, and 45%He + 45%Ar + 10%N_2) on 5 mm austenitic stainless steel sheet. It was reported that an addition of small amount of O_2 (5%) and N_2 (10%) to the 50%He + 45%Ar and 45%He + 45% Ar will change the shape of the fusion zone from shallow weld to a deep and narrow fusion zone. This was attributed to the suppression of plasma plume as a result of an increases in concentration of oxygen and nitrogen [56].

Keskitalo et al. [57] studied on laser welding of duplex stainless steel using a 4 kW disk laser, with argon and nitrogen as a shielding gas. They demonstrated that use of argon as shielding gas significantly reduces the austenitic microstructure level and toughness level in weld while nitrogen as shielding gas can enhance the weld toughness. Keskitalo concluded that, nitrogen as shielding gas can compensate for loss of the elements in weld which commonly occurs during laser dissimilar welding.

Westin and Serrander [58] studied CO_2 laser welding of duplex stainless steels and reported that use of nitrogen as shielding gas has a positive impact on austenite formation in the root side and corrosion resistance of the weld. Similar to other researchers, it was reported that using nitrogen can prevent nitrogen loss from the weld and hence enhances austenitic formation.

Welding gap and alignment

Alignment of the laser beam (with reference to the weld center) and welding gap between two workpiece can significantly influence the weld bead quality. In butt joints, the gap must be small enough that the beam cannot pass straight through the joint and it was reported that the gap should be smaller than half the beam diameter (<200µm) [59]. Sun [26] also demonstrated the importance of air gap size on controlling the alloying concentration of the filler wire and consequent microstructure in dissimilar laser welding between austenitic/ferritic dissimilar steel joints using nickel based filler wire. Torkamany et al.[60] carried out an investigation on dissimilar pulsed Nd:YAG laser welding of pure niobium to Ti–6Al–4V. They discussed that laser beam alignment relative to dissimilar joint interface has significantly important role on mixing and melting ratio of fusion zone and can significantly subsidise the formation of undesirable intermetallic compounds in the weldment.

Wavelength (λ)

Wavelength affects the absorption, resolution and focusability. Typically, shorter wavelength has higher resolution and focusability. Shorter wavelengths have higher photon energy and higher absorption in materials for both conduction and keyhole welding. Lasers with the shorter wavelength are more desirable for keyhole laser welding where higher penetration depth is required [18]. Figure 2-8 illustrates absorption of some metals as a function of laser radiation wavelength. Many researchers have been reported the importance of wavelength on weldability of various alloys. Sanders et al. [38] studied the weldability of magnesium alloys. He used Nd:YAG laser and CO_2 lasers and reported that the weldability of magnesium alloys is better with Nd:YAG compared to CO_2 lasers as a result of its shorter wavelength, which in turn decrease the keyhole threshold irradiance and form more stabilized molten pool.
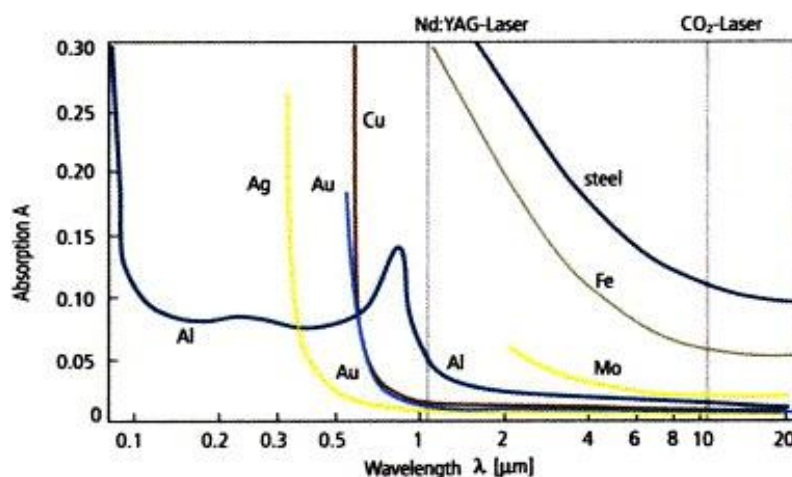
Figure 2-8 Absorption of a number of metals as a function of laser radiation wavelength of CO_2 and YAG laser [18]

The effect of laser wavelength and angle of incidence on the absorptivity of wavy molten steel surfaces during welding was investigated by Kaplan [61]. He showed that the CO_2 laser has a fairly steady, high, flat-domain-absorptivity on steels molten pool from low to moderate angles-of-incidence. In addition, it is concluded that strong surface waviness of molten pool during welding enhances the absorptivity and the overall absorptance for laser wavelengths between 532 and 1070nm.

2.3   Dissimilar laser welding of metals and alloys

Dissimilar welding can be produced using various techniques, including laser beam welding, arc welding, electron beam welding, friction stir welding, etc. Tungsten inert gas (TIG) is a most well-known conventional welding technique, used for joining dissimilar materials. TIG welding uses an electric arc between a non-consumable electrode (tungsten), and workpiece to generate sufficient heat to melt the workpiece. An inert gas is used with the TIG welding to shield and cool the welding torch, welding zone, and heat affected zone [62]. A simple configuration of the TIG welding process is shown in Figure 2-10 [63].
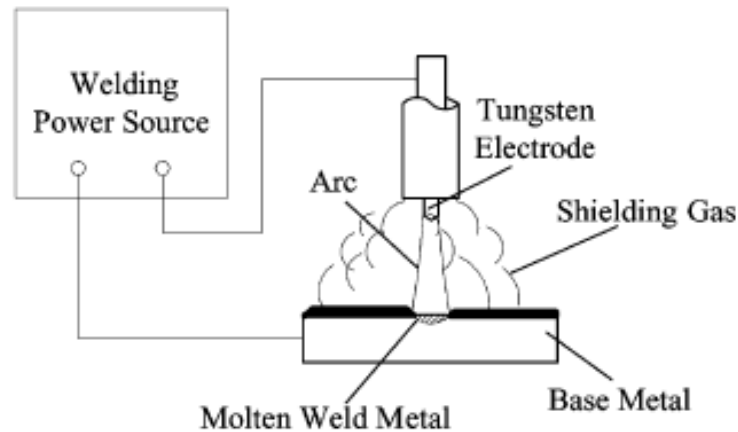
Figure 2-9 Configuration for TIG welding [63]

Electron beam welding is normally used to produce high quality dissimilar welding of thick materials in high value manufacturing industries. Electron beam welding is a non-conventional welding process, in which the workpiece is bombarded with a high density electrons at vacuum environment [63]. During the electron/substrate interaction, kinetic energy of the electron converts into heat energy, which is used to melts the workpiece. Recently some non-vacuum EBW [64] were introduced, but still they are at the early stage of industrial implementation.

Like every process in industry, conventional arc welding has some advantages including economic, capability to weld a wide range of materials, etc. [65]. However, large heat affected zones (HAZ) and fusion zones (FZ), high thermal residual stress and distortion, inhomogeneous microstructures and properties, evaporative loss of alloying elements and low productivity of arc-welded joints have made laser welding a preferred choice for dissimilar welding [66]. Laser welding is preferred compared to arc welding, due to its low and precise heat input, narrow FZ and HAZ, high adaptability to automation, low residual stress and thermal distortion, and high productivity [5], [67], [68], [26], [15] and [63]. Sun and Ion [26] compared laser, plasma and TIG welding of austenitic/ferritic joints and showed that the width of heat affected zone in laser welded joints are approximately one-quarter and one-sixth of those in plasma and TIG welds, respectively. Sun et al. [26] studied dissimilar laser welded of copper and AISI 304 stainless steel and showed weld bead of superior mechanical properties compare to MIG welding.

Along with fusion welding, there are other types of joining technologies (low temperature techniques) which operate below melting temperature of base metals such as friction stir welding. Friction stir welding, developed by TWI in 1991 is a solid state welding process which produces high quality weld in difficult-to-weld materials, without melting the substrate material, and is becoming the process of choice for joining dissimilar materials [63]. The process is achieved by using cylindrical tool which is forced on to the workpiece or parts that have already pushed together with a shoulder fixture [63]. The tool will start to rotate and drive the separate line of the parts. As the solid tool is moving along the separation line, the heat derived by friction between the tool and the parts will soften and yield without changing the phase, (i.e. from solid to melting). The mentioned heat flow allows deformed material to relocate from the leading edge of the tool to the following edge. As a result, the material will be welded by close contact of the tool shoulder and its probe during the rotation. A schematic of the friction stir welding process is shown in Figure 2-10.
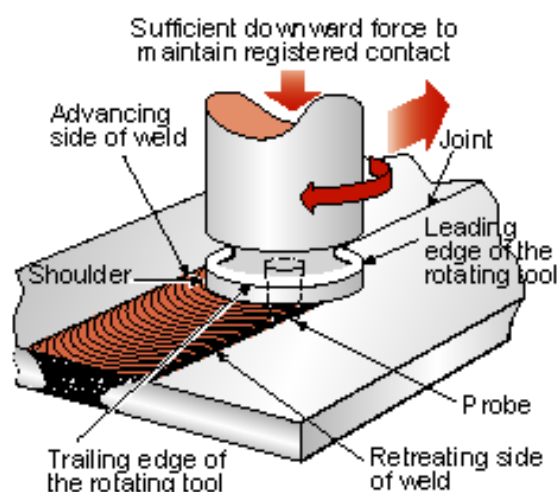
Figure 2-10 Configuration for friction stir welding [63]

Arivazhagan et al. [69] studied the microstructure and mechanical properties of stainless steel and low alloy steel using gas tungsten arc welding (GTAW), electron beam welding (EBW) and friction welding (FSW). They reported that the joint made by EBW has the highest tensile strength (681 MPa) compare to joints made by GTAW (635 MPa) and FSW (494 MPa). In addition, the ductility of the EBW and GTA weldment (32% and 25% respectively) were showed to be higher than friction weldments (19%). Impact test were also performed and it is concluded that GTAW technology produces joints with higher impact strength compare to EBW and FSW. Torkmany et al. [4] reported higher

service performance of dissimilar joints (carbon steel and stainless steel) welded by high energy density technologies such as laser beam welding and electron beam welding compared to conventional welding technologies.

The microstructure and mechanical properties of stainless steel welded by TIG welding, laser welding and laser-TIG hybrid welding was studied by Yan et al. [70]. X-ray diffraction and optical microscopy are used to study the phase fraction and microstructure of the welded joint and tensile test were carried out to study the service performance of the joint. They reported that the laser welded joints had highest tensile strength and smallest dendrite size in all joints, while the TIG welded joints had lowest tensile strength, and biggest dendrite size. They also discussed higher production rate and superior mechanical properties as the advantages of laser and hybrid welding for joining austenitic stainless steel.

Sun [71] showed that distortion and residual stresses are significantly lower in laser welding compare to plasma and TIG dissimilar welding of austenitic stainless steel and carbon steel. He discussed that this is due to highly focused nature of the laser beam welding. Kohyama et al. [63, 72, 73] discussed that the high thickness joints made by electron beam welding have lower workpiece distortion and residual stress, higher depth to width ratio and extremely narrow heat affected zone (HAZ) compare to other welding technologies. Yunlian et al. [74] carried out an investigation on mechanical properties of titanium joints. They employed laser, electron beam, and TIG welding as welding technologies, and reported laser welded joints have the narrowest weld-seam, the least deformation and the finest grains among the other welding technologies as result of faster welding speed capability of laser beam welding compare to other welding technologies.

Haferkamp et al. [67] carried out an investigation on the fatigue performance of welded magnesium alloy components. They employed laser and electron beam as welding technologies, and reported that the laser welded joints can stand higher level of load magnitude compare to electron beam welded joints for a given number of cycles to failure. This reported to be as a result of lower notch sensitivity of laser-welded joints. Miles et al. [75] studied the formability of welded dual phase 590 (DP 590) steel sheets employing friction stir welding and laser welding. A series of mechanical tests, including transverse tension and plane strain formability testing are carried out. The hardness of the

weld bead was higher with laser, compared to FSW, due to the higher cooling rate with laser welding. It was also reported that FSW joints are 20% more formable than the laser welded sheets during plane strain formability tests. Sun and Duley [24, 76] discussed that friction stir welding can significantly reduce the problems associated with fusion welding due to their solid state nature; however the service conditions may make particular processes inappropriate.

The possibility of using CO_2 laser-GMAW hybrid welding process was studied for the stainless steel and influence of the shielding gas was overseen as the potent factor in the weld quality [77]. The microstructure of the mild steel after the hybrid welding process showed coarse columnar dendrites and fine acicular dendrites in the heat affected zone (HAZ) and fine equiaxed dendrites and columnar dendrites in the weld zone. Laser zone showed the finer grain size and higher microhardness in the fusion zone and narrower heat affected zone in comparison to the arc weld region. Yan and Lee [78] studied the laser spot welding with the resistance spot welds (RSW) and demonstrated the weld strength of laser spot welds is greater than that of resistance spot welds. They also showed that laser spot welding can be advantageous in terms of decreasing stress distribution and welding costs in automotive industry as a result of high speed, precision and low heat distortion.

Compared to conventional arc welding, laser welding produces significantly narrower heat affected zone and fusion zone geometry (Figure 2-11). Laser welding also produces high aspect ratio welding with less distortion and residual stress in comparison with other welding methods such as conventional arc welding [15]. Laser beam welding is predominantly carried out in ambient atmosphere (with some shielding gas), eliminating the need to control the atmospheric pressure (compare to EBW) [47]. Also, Laser welding is fully compatible with robots to work in harsh environments (like nuclear reactors) where humans cannot operate. In addition, compared to diffusion based joining techniques such as friction stir welding, laser material processing has significantly higher productivity and flexibility for joints that have complex geometries and require non-contact welding. Despite of aforementioned advantages, laser welding is also associated with some limitations and drawbacks. Having a very high cooling rate, laser welded joints of carbon steel are often suffered from formation of martensitic phases and hot cracks in the weldments [36, 79]. Keyhole instability and formation of porosity as a result of

39

keyhole collapse during welding is another major drawback of laser welding. As a result of health and safety risks posed by using laser for welding this process requires researchers to undergo extensive training before they can operate it. Finally, since laser material processing is an advanced technology, it requires high amount of investments and maintenance costs compare to conventional welding technologies [24]. Table 2-2 details the comparison of laser welding to other welding technologies.

(a)   (b)
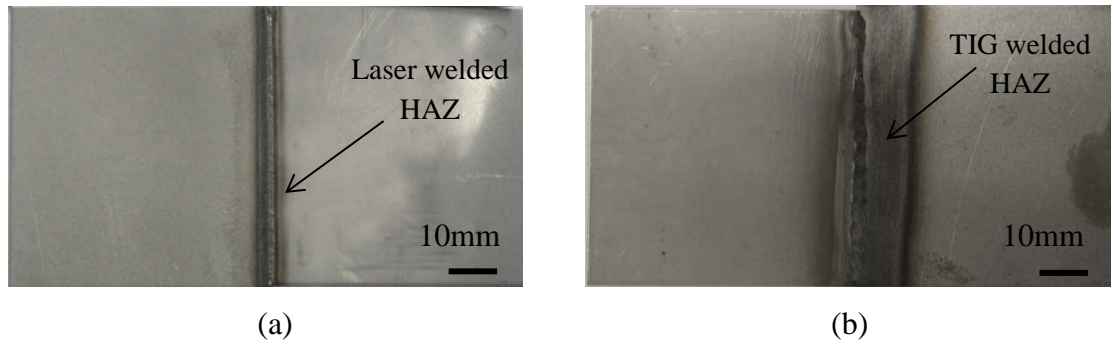
Figure 2-11 Weld bead shape and HAZ geometry of (a) laser welded joint (power 500(W), speed 15(mm/s), argon gas pressure 1.5 (bar)) and (b) TIG welded joint (DC current 25 Ampere, non-flow rod, thoriated tungsten electrodes)

Table 2-2 Comparison of laser welding technology to other welding technologies [18, 24, 80]

No	Parameter	LBW	EBW	TIG	RW	GTA	GMA
1	High production rate	+	+		+		
2	Low heat input				+		
3	High aspect ratio	+	+				
4	Joining efficiency				+		
5	Small heat affected zone	+	+				
6	High processing speed	+	+				+
7	Weld bead appearance	+		+			
8	Atmospheric pressure welding	+		+			
9	Weld reflective materials	-	+	+	+	+	+
10	Weld heat sensitive materials	+	+	-	-		
11	Weld magnetic materials	+	-	+	+		
12	Combine with filler		-	+	-	+	+
13	Automate process	+	-	+	+	+	
14	Operation cost	-	-		+	+	+
15	Capital cost	-	-		+	+	+
16	Narrow HAZ	+	+	-			
17	Environment, noise, fume	+	+	-	-		
18	Fixturing	+	-	-	-	-	-
19	Reliability	+	-	+	+	+	+

'+' = advantageous; '-' = disadvantageous; 'LB'= laser beam; 'EB'= electronic beam; 'RW'= resistance welding; 'GTA'= gas tungsten are 'GMA'= gas metal arc

As seen from the literature, welding of dissimilar metals is often involved with many challenges arising out of problems associated with metallurgical incompatibility, e.g. the formation of brittle intermetallic compounds, the segregation of high and low melting phases due to chemical mismatch, asymmetric weld pool shape, and possibly residual stresses from the thermo-physical mismatch (Figure 2-12) [81]. Another important issue that needs to be addressed in dissimilar welding is the mutual solubility and the need for a homogenous dissimilar joint with minimal variation of mechanical properties within the weld bead and between the weld and heat affected zone. These issues are not yet fully addressed but highlighted in laser dissimilar welding research [4, 5, 24, 51, 76, 82, 83].
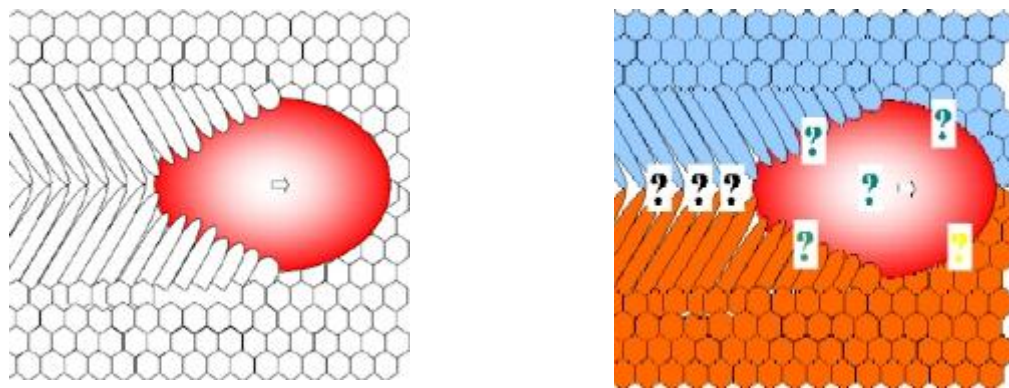
Figure 2-12 Welding of (a) Similar metals/alloys (b) Dissimilar metals/alloys [84]

2.4 Melt pool dynamics in laser welding

Melt pool convection plays a major role on final geometry, surface topology and microstructure in laser dissimilar welding. In addition, many of the weld defects such as porosity, undercuts, lack of penetration, inhomogeneous alloys and chemical composition is strongly related to the melt pool convection [62].

Convection in molten pool can be due to natural convection and marangoni forces. Natural convection (buoyancy) results from the change in density of the molten fluid as temperature changes. Surface tension induced convection, also known as thermocapillary flow or Marangoni flow, is caused by surface temperature gradients resulting in shear stress and induced fluid motion. The resulting flows from these forces are named as gravity-induced buoyancy convection and Marangoni convection. Marangoni driven convection forces is predominantly higher than natural convection/gravity and tend to dictate the direction of fluid flow, and the alloying composition of the fusion zone [85-87].

41

The extent of the Marangoni convection can be defined by Marangoni number, M_a, which is a dimensionless number and is proportional to the thermal coefficient of surface tension divided by viscosity and thermal diffusivity as in equation 12:

$$M_a = -\frac{\partial \gamma}{\partial T}\frac{1}{\eta \alpha}.L.\Delta T \qquad\qquad E.q(12)$$

where η is dynamic viscosity [Ns/m], α is thermal diffusivity [m²/s], $\partial \gamma/\partial T$ is temperature coefficient of surface tension, L is radius of fusion zone [m] and ΔT is the temperature gradient between center and edge of the melt pool.

Many researchers have attempted to investigate the predominant role of Marangoni convection in laser welding using numerical modelling techniques. He, X et al, 2003, used a numerical analysis to calculate the weld pool geometry, weld thermal cycles and various solidification parameters of stainless steel. They also performed dimensional analysis to understand the importance of heat transfer by conduction and convection and the roles of various driving forces (e.g. effect of Marangoni and buoyancy on weld pool convection). The analysis indicated that the main driving force for liquid flow in fusion zone is the surface tension. The buoyancy force has much less effect on the fluid flow in comparison to surface tension. Also, it was mentioned that cooling rate, temperature gradient and the subsequent solidification rate in the laser welding melt pool is significantly higher, compare to other welding technologies [88].

Kou and Sun [89] established a steady-state two-dimensional model to simulate weld pool fluid flow and its effect on weld penetration in stationary arc welding. The enthalpy method was used for the heat transfer equations, and the viscosity method was incorporated in the fluid flow equations. The thermal cycle and fluid flow velocities were obtained from the coupled model. Buoyancy, electromagnetic and surface tension forces were considered as the main driving forces in the model. It was showed that surface tension dominated the melt pool flow.

Srinivasan and Basu [90], studied the surface tension flow during laser melting and showed that the effect of buoyancy force is negligible compared to the Marangoni force. Recently, Pang [91] developed a three dimensional CFD based model, incorporating coupled heat transfer, fluid flow and keyhole geometry. Pang [91] demonstrates the significance of welding speed and surface tension co-efficient on change in surface topology. Marangoni flow (caused by surface tension gradient) and thermal buoyancy

significantly affects the solidifying process, and make a molten pool wider and shallower. It is also demonstrated that Marangoni convection enhances the heat transfer in molten pool [92, 93]. Zhao et al. [94] studied the influence of heat transfer, mass transfer and liquid metal flow during stationary laser welding for different concentrations of oxygen in the surrounding environment. He found that the oxygen concentration affects not only the flow motion, but also the laser absorption coefficient, which increases with increasing environmental oxygen concentration. Also he showed that the evolution of dissolved oxygen in the weld pool (as a function of temperature) can have a profound influence on the fluid flow and hence on energy transport. The surface tension depends predominantly on the temperature gradient along the molten pool surface. The temperature dependency of surface tension is one of the thermo-physical properties of the materials and is defined as:

$$\frac{\partial \sigma}{\partial x} = \frac{\partial T}{\partial x}\frac{\partial \sigma}{\partial T} \qquad\qquad E.q(13)$$

where, σ is surface tension, $\frac{\partial T}{\partial x}$ is temperature gradient along the molten pool surface, and $\frac{\partial \sigma}{\partial T}$ is temperature coefficient of surface tension.

Generally lower surface tension is noticed at the center of the molten pool (where melt pool temperature is high) for materials with negative temperature coefficient of surface tension. This is due to the low temperature gradient at the center of the molten pool. On the other hand, the surface tension increases along the periphery of the molten pool, due to the increase in temperature gradient (temperature decreases). As a result of the increased surface tension, the liquid is pulled toward the outer edge of molten pool creating concave liquid surface at the middle and humping of liquid metal at the periphery of the molten pool [95, 96].

Voelkel and Mazumder [97] reported such depression at the middle of melt pool (illustrated in Figure 2-13). Using numerical analysis, the variation of Marangoni convection forces is investigated by Lie et al. [98]. He reported the formation of shallow and wide weld as a result of an outward flow (from molten pool center to weld periphery) which has driven by a negative surface tension temperature coefficient. Such observation is also reported by Zacharia et al. [95].
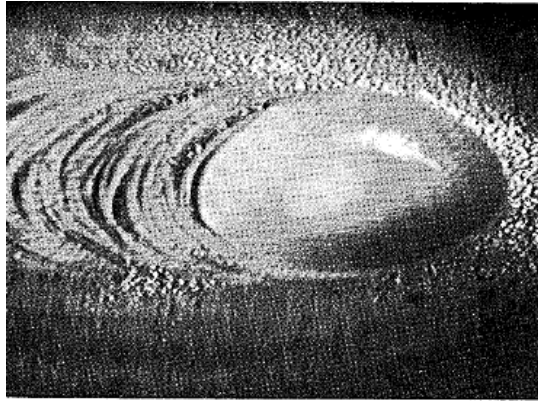
Figure 2-13 Concave molten pool of steel formed using a CO_2 laser [97]

The outward behavior of molten stainless steel flow as a result of negative surface tension coefficient is illustrated in Figure 2-14. However, positive surface tension coefficient causes an inward flow from pool periphery toward the pool center which consequently results in narrower and deeper weld pool (Figure 2-15).
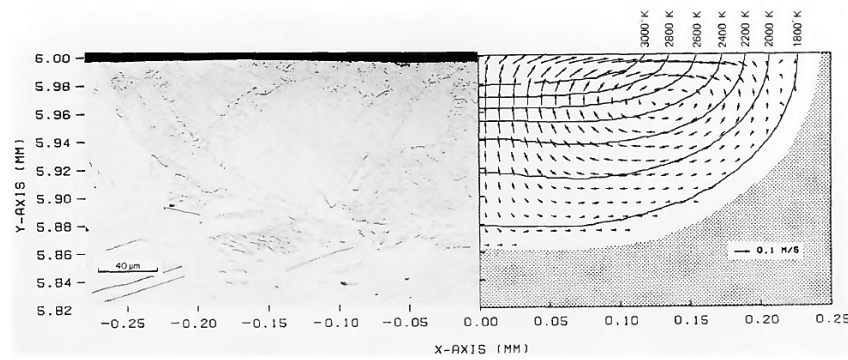
Figure 2-14 Comparison of the calculated and experimentally observed laser welded fusion zone of stainless steel with outward flow as a result of negative surface tension temperature coefficient [95]
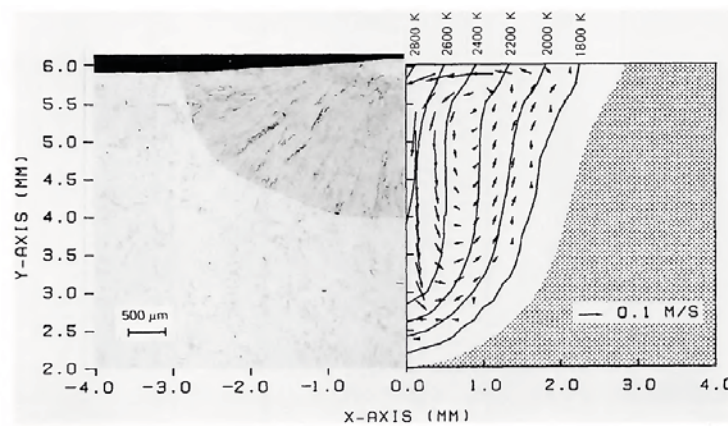
Figure 2-15 Comparison of the calculated and experimentally observed laser welded fusion zone of steel with inward flow as a result of positive surface tension temperature coefficient [95]

Thermocapillary forces, not only affect the flow direction in melt pool, but also have noticeable impact on the welding defects such as porosity. Rai and debroy [99] developed a technique for weld bead geometry design by combining 3D modeling, generic algorithm optimisation and small number of experiments. They found that heat transfer in the upper part of the melt pool is dominated by convection due to vigorous circulation of molten material driven by Marangoni effect.

Regardless of the fluid flow direction, it is well discussed in the literature that the Marangoni convection force significantly controls the fluid convection in welding process. Hence an in depth analysis of dissimilar welding melt pool dynamics has been performed as detailed in the numerical analysis chapters.

2.5 Features of laser beam welding

2.5.1 Alloying and microstructure in laser welding

As stated in the previous section, one of the main challenges with dissimilar welding is the differences in material properties e.g. thermo-physical properties leading to large stresses and the formation of intermetallic brittle phases that readily occur within the weld for certain alloys. Intermetallic phases or compounds (IMC) are solid-state compounds that have two or more metals with different crystallographic microstructure compared to the parent metals [100]. The intermetallic compounds inside the weld bead can undermine the service performance and reliability of fabricated components.

The use of laser welding for dissimilar materials has the potential to restrict the formation of intermetallic phases [83], due to its localized energy input, and more controllable welding process. Control of the welding process including, diffusion process and melt pool dynamics is expected to help overcome some of the typical defects in dissimilar welding including the formation of intermetallic compounds and weld bead inhomogeneity.

Over the past decades, several numerical [88, 101-110] and experimental investigations [26, 46, 83, 101, 111] of laser dissimilar welding have been reported by various researchers. One of the major studies was carried out by Torkamany et al. [83] who investigated laser welding of low carbon steel sheet (0.8mm thickness) with aluminium

alloy (2mm thickness) with steel on overlap configuration. The effect of laser peak power and pulse duration on weld defects, percentage of intermetallic components and weld quality were investigated. They showed Fe_xAl_y intermetallic phases occur if the formation threshold had been reached. Optimised process parameters were suggested. The microstructure formations phase, percentage of intermetallic compounds, and chemical composition were analysed using SEM and energy dispersive X-ray (EDX). Higher percentages of intermetallic components (PIC) are shown as a result of higher peak power and consequently higher dilution of aluminium (Figure 2-16). They also reported the formation of cracks in the dissimilar weld as a result of different thermal expansion coefficients of IMC which result in stress crack generation and propagation (Figure 2-17). This was also observed by Theron et al. [112] who reported extremely hard phases in the fusion zones as a result of intermetallic compounds, fine microstructure (due to high cooling rate in laser welding) and super saturated solid solutions. In fact, they found that the hardness of dissimilar welds increases as the content of Al in Al-SS in weld zone increases.
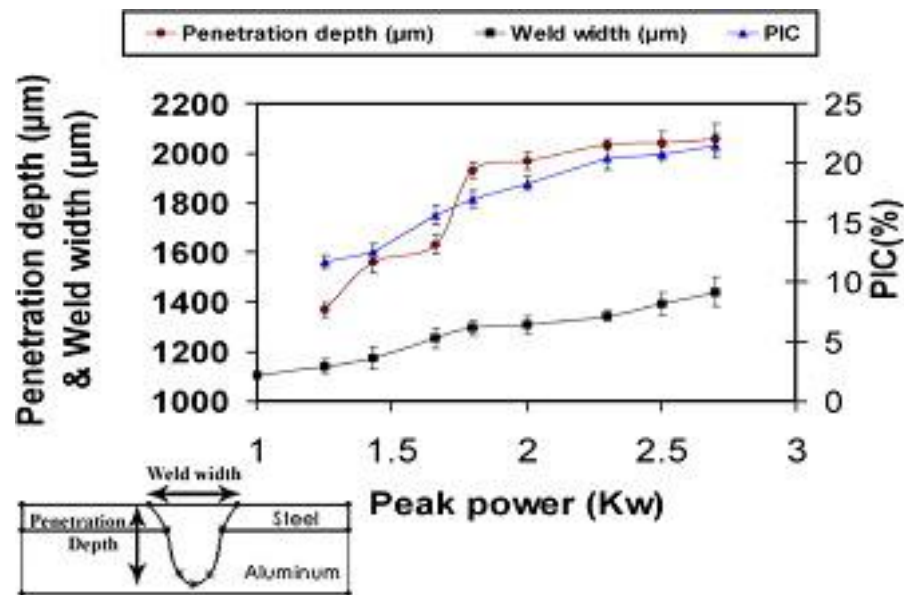
Figure 2-16 Variation of penetration depth, weld width and PIC as a function of peak power [83]
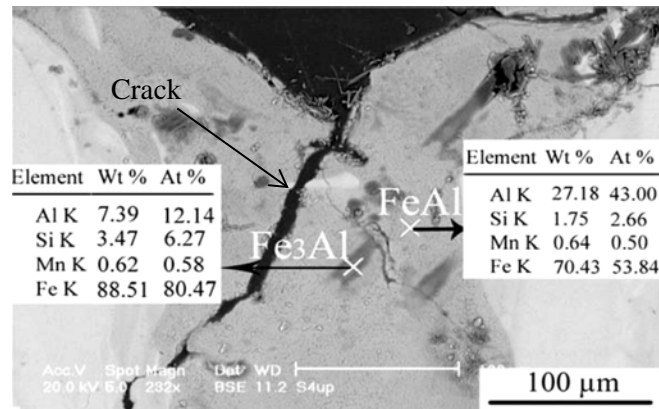
Figure 2-17 SEM microscopy and EDX result around a crack with corresponding chemical composition [83]

Borrisutthekul et al. [113] studied the issues of IMC layers in laser welding of magnesium and aluminium. They showed that the occurrence IMC layers can result in tensile-shear failures at interface of magnesium and aluminium laser welded joint. They claimed that, welding of aluminium and magnesium is more difficult due to the immense difference in melting temperature and consequently formation of IMC in the weld bead. Also, they noted that penetration depth has significant relation with the IMC layer (Al_3Mg_2, $Al_{12}Mg_{17}$) thickness. They developed a numerical model to study and control the amount of IMC in the weldment. Using the numerical model, they proposed a new weld configuration "edge-line welding lap joint" (illustrated in Figure 2-18) and processing parameters to address the IMC thickness. They subsequently managed to suppress the formation of intermetallic compound by controlling the penetration depth of Al in Mg and magnesium vaporization. Figures 2-19 (a) and (b) show their results presenting the relationship between penetration depth, thickness of intermetallic layer and processing speed for edge-line welding of lap joins. As can be seen from the Figure 2-19, increasing in welding speed decrease the penetration depth and the thickness of IMC.
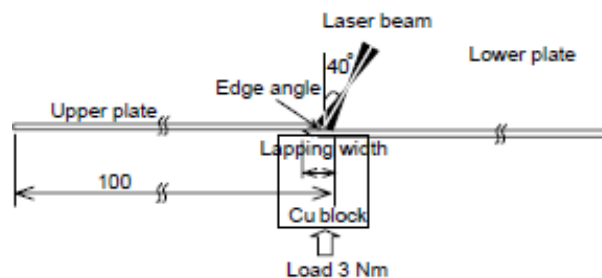
Figure 2-18 Configuration of edge-line welding [113]
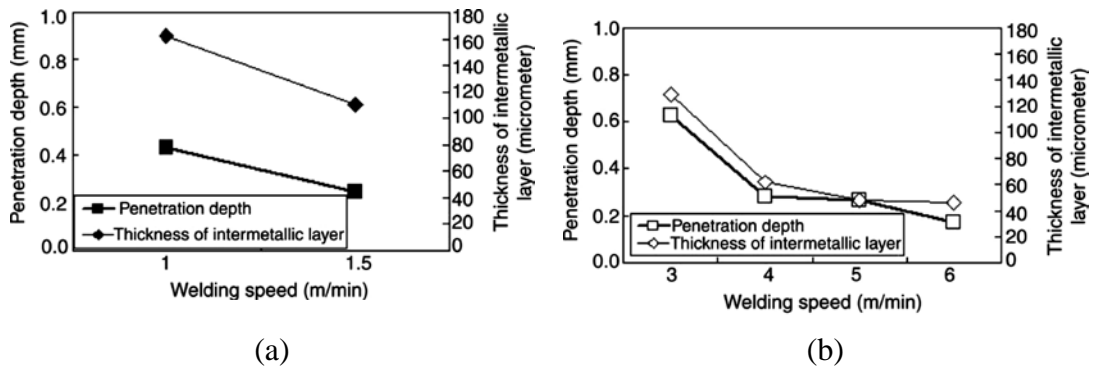
Figure 2-19 Effect of welding speed on penetration depth and thickness (a) AZ31B (b) A5052-O [113]

A new welding technique called laser roll welding is developed by Ozaki and Kutsuna [114] who reported that the IMC thickness in dissimilar welding of zinc coated steel and aluminium can be minimised using the method (Figure 2-20) along with proper selection of welding speed. They employed a roller (which is mounted with a calibrated compression spring) to apply pre-determined roll pressure on the laser welded seam [114]. The welding configuration was of lap joint type. The laser beam provides enough heat for conduction at the weld line and roller helps in to fuse the weld line. Figure 2-20 (a) and (b) shows the schematic of the laser roll welding setup. They also studied the influence of processing speed in detail and concluded that optimal welding speed can significantly decrease the thickness of IMC.
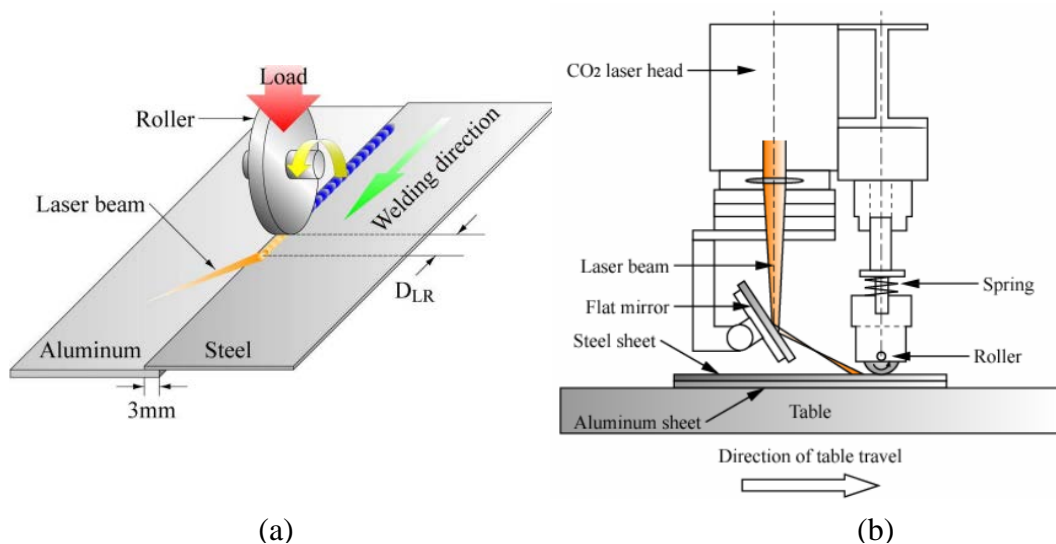
Figure 2-20 Laser roll welding (a) Schematic of laser roll welding; (b) Side view of laser roll welding [114]

Microstructural evolution and solidification cracking susceptibility of dissimilar metal welds between austenitic stainless steel (Type 310) and nickel-based alloy (Inconel 657) were investigated employing a combination of electron microscopy analysis and Varestraint testing techniques [115]. The importance of filler metal alloying composition on weld microstructure is also studied. It is reported that small amount of secondary phase (NbC) can enhance crack resistivity of the weld while wide solidification temperature range and high concentration of secondary phases can deteriorate weld crack resistivity. Inconel type A is shown as the best filler material to avoid cracks and having best weldability for such dissimilar joints. Li and Fontana [116] investigated the relationships between the redistribution of elements and the as-welded microstructure in the dissimilar fusion zone of AISI304L and AISI12L13. They developed a technique to avoid solidification cracking and micro-fissuring in the fusion zone.

Chen et al. [117] investigated lap welding of Zn-coated steel and Al alloy, which is predominantly used in automotive industries. They showed that the formation of IMC phases (FeAl$_2$, Fe$_2$Al$_5$ and FeAl$_3$) is due to the rapid heating and cooling cycles observed in laser welding process. Also, the formation of IMC results in micro-cracks at the weld interfacial layer (Figure 2-21). They further studied the effects of shielding gas (argon and nitrogen) on the IMC formations and mechanical properties of the joint and found that the thermal conductivity and density of shielding gas significantly control the welding quality. They concluded that higher thermal conductivity shielding gas such as nitrogen increases the cooling rate and decreases the weld penetration depth (Figure 2-22). As a result, the degree of heat flow and activity of diffusion in melt pool reduces the amount of IMC decreases, and consequently higher shear strength in joints was obtained (Figure 2-23).
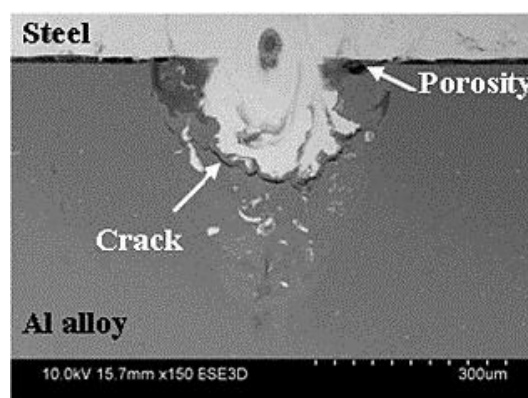
Figure 2-21 Formation of IMC and weld defects in Steel-Al joint [117]

49
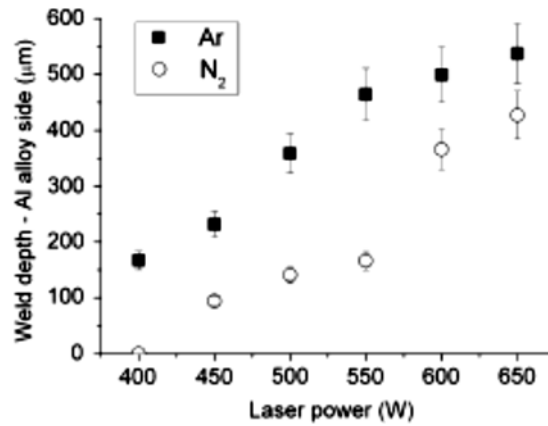
Figure 2-22 Relationship between the weld penetration depth and the shielding gas [117]
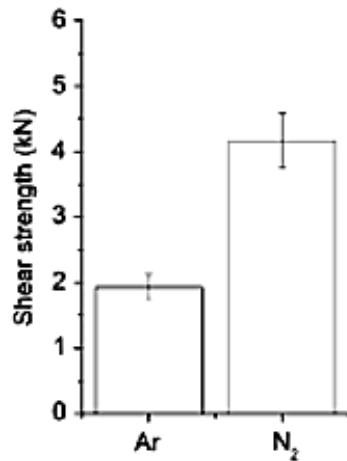
Figure 2-23 Shear strength of single pass welds (600 W, 100 mm/s, f.p.p. of 0 mm) with different shielding gases [117]

The transport phenomena in laser dissimilar welding of Cu to Ni were numerically studied by some researchers with the emphasis on mixing. Chakraborty [102] extended Phanikumar's work [106] and developed a 3D model to study conduction mode laser dissimilar welding of Cu–Ni applying finite volume based method and later discussed the significance of turbulence. Melt pool convention and shape of the fusion zone subjected to Marangoni forces in different directions in dissimilar welding of aluminium and steel was investigated by Chung and Wei [103, 107].

Mukhrejee et al. [1] attempted to numerically simulate the transport phenomena that take place during laser dissimilar welding of Fe–Al metallic coupled with Tantalum (Ta) sheet as a diffusion barrier using the finite volume formulation. They concluded that the formation of Fe–Al intermetallic compounds can be significantly restricted by using a refractory metal like Ta as a diffusion barrier and that the interest in laser dissimilar welding lies, due to its narrow fusion zone which can result in minimal intermetallic phases, compared with other welding techniques.

Hu [104] developed a model to predict heat and mass transfer in laser welding of stainless steel to Ni, and concluded that mass transfer is highest during the initial stage of weld pool formation and thereafter decreases with time. It was also observed that the distribution of the element Fe in the fusion zone became uniform after 90ms (0.090s). This is also reported by Paventhan, Lakshminarayanan [118] who studied the fatigue behavior of a friction welded carbon steel–stainless steel dissimilar joint and concluded that the formation of an intermetallic phase is a result of alloying element diffusion at the weld interface.

One of the most key researches of laser dissimilar welding has done with Torkamany et al. [4] who studied the effect of laser welding (overlap configuration) mode on microstructure and mechanical performance of low carbon-austenitic stainless steel. They discussed that the dissimilar weld microstructure is dependent on the size of fusion zone and dilution percentage of low carbon steel which itself is highly dependent on the transition of laser welding mode from conduction to keyhole. Figure 2-24 shows weld size in low carbon and stainless steel sides as a function of the laser mean power. As can be seen, a sharp increase is occurred in weld size of carbon steel from 210W to 240W which is due to keyhole formation at the mean power of approximately 210 W. In addition they have reported that the dissimilar weld metal is consisting of triplex (austenite, ferrite and martensite) and fully martensitic microstructure. It is worth mentioning that their evaluation of the microstructure is based on only dilution and ignores the cooling rate involved in the laser welding.
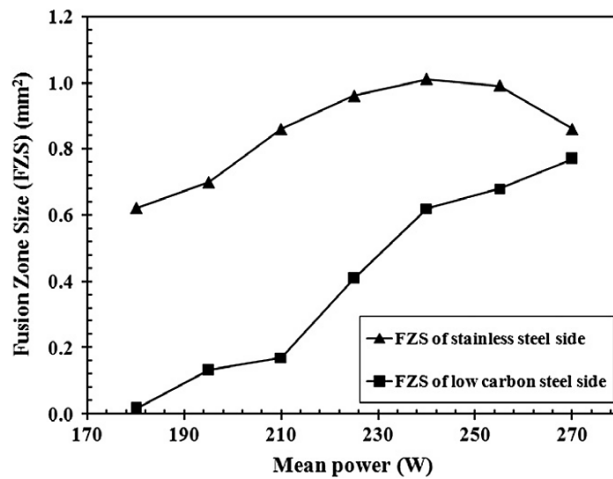
Figure 2-24 low carbon and stainless steel fusion zone size as a function of the laser mean power

Anawa and Olabi [119] have also reported complex austenitic–ferritic structure in the fusion zone of a dissimilar laser weld between AISI 316 and AISI 1008 steels, however their microhardness measurements (approximately 460 Hv) contrarily confirmed the formation of martensitic microstructures in the dissimilar weld metal.

Sadeghian et al. [120] reported an experimental investigation to understand and subsequently control the amount of detrimental ferrite phases in GTAW welding of super duplex stainless steel and high strength low alloy steel. An energy dispersive spectrometer and scanning electron microscopy were used to analyse the ferrite percentage, and detrimental phases as a result of changing GTAW welding heat input. The investigation revealed that an increase in heat input result in a decrease in weld's ferrite percentage, and detrimental phases. It is also discussed that due to low heat input, the HAZ microstructure of high strength low alloy steel will transform to bainite and ferrite phases while in a case of high heat input, the HAZ microstructure transforms to perlite and ferrite phases.

A research of Alexandru Pascu et al. [121] explains microstructural variation during laser dissimilar welding. Steel alloys such as AISI 304 and AISI 1010 when joined by continuous wave YAG laser and the microstructures are observed at transverse sections of weld. A narrower HAZ and well mixed weld is reported beyond certain spot diameter and energy density. It is shown that the weld microstructure is consisting of austenite, ferrite and martensite with acicular ferrite at the dendrite boundaries. It is discussed that the formation of the martensite microstructure in the welding zone is attributed by high

52

process cooling rate which result in hardening of the weld metal and HAZ of carbon steel (Figure 2-25). In addition, low homogeneity and Cr carbide precipitation in microstructures is also observed at the grain boundaries in the HAZ of AISI 304. The tensile testing of the dissimilar weld was performed and it is discussed that despite of lower plasticity of weld, the failure of the joint during tensile test occurs on the carbon steel parent metal.
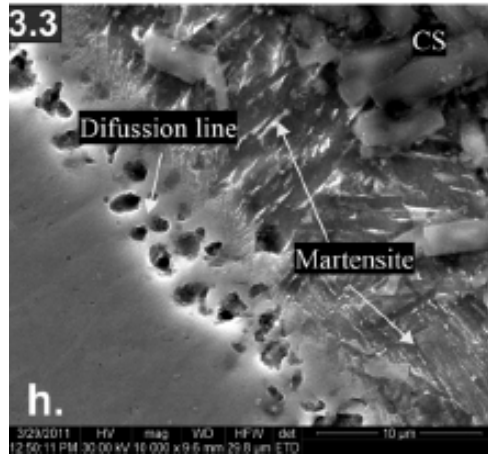
Figure 2-25 Martensitic transformation in HAZ of carbon steel in laser dissimilar welding of carbon steel to stainless steel

The formation of martensitic microstructure in dissimilar weld between carbon steel and stainless steel is also highlighted by Sun and Moisio [82] who investigated the laser beam welding of austenitic/ferritic dissimilar joints using a nickel based filler wire. They reported that dilution from low alloyed steel substantially influenced the final microstructure.

The importance of dilution of low alloy steels in dissimilar weld is also reported by Marashi et al. [122] who studied the failure behaviour of dissimilar resistance spot welds (RSW) of low carbon steel and austenitic stainless steel was studied by. Marashi investigated the relationship between the failure behaviour of the RSWs and fusion zone characteristics. He concluded that the distribution of alloying elements significantly influences the corrosion resistance and mechanical properties of the welded joint. He also demonstrated that the failure mode of RSW welded joint can be effectively controlled by influencing the fusion zone dilution (ratio of the two base metals).

Bahrami [123] developed a numerical model to study transport phenomena in spot GTAW of low-carbon steel to duplex stainless steel. The distribution of alloying elements across the fusion zone was obtained using EDS analysis, and based on that, the dilution of each steels is determined. His results demonstrated relatively uniform mixing of alloys across the fusion zone as a result of very high velocity inside the fusion zone.

2.5.2 Weld bead geometry

Weld bead geometry plays an important role in the mechanical properties of the weld joint. For most of the welds, it is often recommended to have appropriate fusion layer width and thickness in order to avoid wasting of energy, edge burn-off, undercut, sagging of the weld pool and deep weld end craters [124]. In addition, the weld pool shape significantly influences the grain structure and dendrite growth process [125, 126]. Unlike similar welding, laser dissimilar weld bead shape is asymmetric and the process is highly non-linear [4, 122, 127]. Therefore, having a clear understanding of the laser welding parameters that controls the weld bead geometry, is a necessity [128]. Experimental analysis in laser welding has been received noticeable attentions during the past years and they are broadly reported in literature [6, 113, 129, 130].

Recently studies using statistical tools to analyse the interaction effects between two or more laser welding parameters have been reported. Benyounis et al. [131] investigated the effect of CO_2 laser welding process parameters on weld width, depth of penetration and heat affected zone width of carbon steel. Their experimental plan was based on a Box-Behnken design of experimental methods. They analysed the effect of laser power, welding speed, and focusing position on weld geometry. They concluded that, laser power and focusing position significantly affects the penetration depth, while welding speed and focusing position significantly affects the weld width and heat affected zone width is influenced predominantly by welding speed.

Anawa et al. [101, 119, 132, 133] used Taguchi methods and response surface methodology to study the effect of the process parameters (inert gas pressure, processing speed, laser power, beam incidence angle, and focal position) against weld width, depth and area. He optimised the laser welding process of dissimilar materials (e.g., stainless steel and carbon steel). Many investigations on laser welding parameter optimisation were carried by various researchers [8, 119, 127, 134, 135]. The main findings are, laser

welding speed is the most influential parameter with the reverse effect on weld bead geometry (bead dimensions, the middle width and the area), increased gas pressure can lead to welding geometry defects, laser power has a direct impact on all investigated weld geometries and laser focal position has less impact on weld pool geometry (although it can increase the weld area and weld width when it is position above the surface (F> 0)).

Some researchers [3, 4, 24, 136] have discussed the weld bead geometry in terms of weld width to depth ratio. Their general conclusion is that the increase in laser power or decrease in welding speed results in a higher penetration depth. They also justified their conclusion based on the fact that increasing the laser power has a direct impact on the laser power density and decreasing welding speed has inverse impact on energy input. As a result high power density or high energy input can change the laser welding mode form conduction welding to predominantly keyhole welding which in turn causes a higher penetration depth. The penetration depth and weld width also depend on the surface composition and surface tension.

Formation of keyhole results in rapid change in the weld geometrical features (cylindrical weld bead shape) within a certain range of energy input (more than 20 kJ/m). This is reported to be attributed to the creation of upper keyhole plasma plume that acts as a point heat source above weld plane. This generated plasma plume acts in the keyhole and forms 'chalice' shaped weld bead profile when energy input is more than 20 kJ/m [137].

The dependency of weld depth and width to temperature coefficient of surface tension is aforementioned earlier in this chapter however; some other researches have explained the weld bead geometry in terms of the concentration of surface active elements in the weld metal. A research of Heiple et al. [138] explains that when a surface active agent is present in the weld metal in a small but significant amount, $d\sigma/dT$ can be altered from negative to positive, thus reversing Marangoni convection and making the weld pool much deeper. S, O, Se, and Te are the surface-active agents in steel and stainless steel. Figure 2-26 illustrates the surface tension data of two different heats of the stainless steel 316, one with approximately 160 ppm more sulfur content than the other.
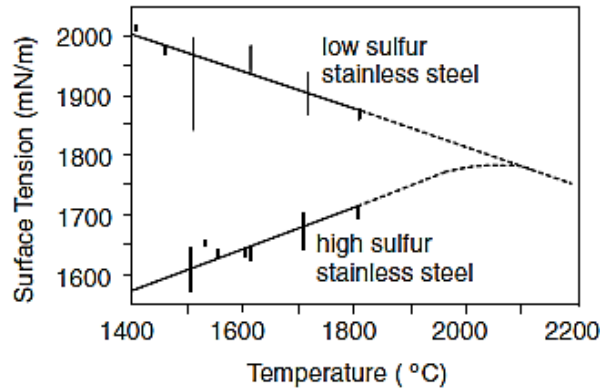
Figure 2-26 Surface tension variation of stainless steel (316) with surface active elements and temperature

Figure 2-27 presents two stainless steel (304) plates which are welded using YAG laser at 3000W and 3.39mm/s. The plate with the wider and shallower weld contains about 40ppm sulphur while the one with deeper and narrower weld bead profile contains about 140ppm of sulphur.

(a)   (b)
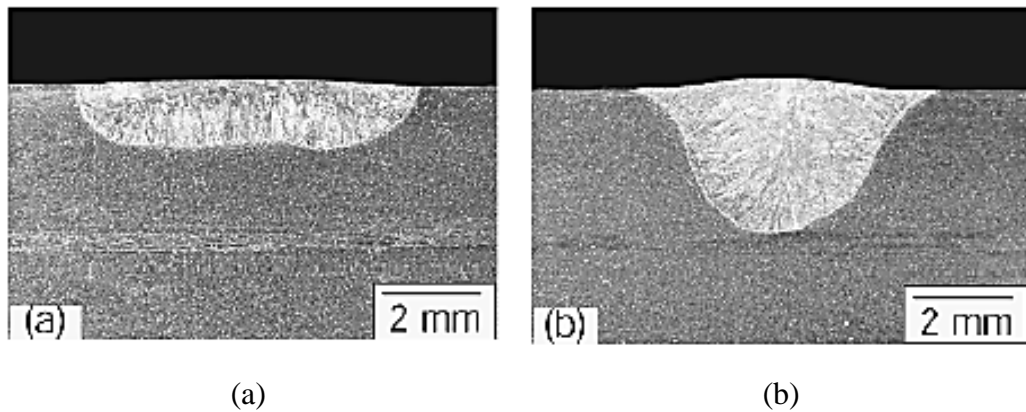
Figure 2-27 Variation of stainless steel (304) weld geometry with surface active elements
(a) 40ppm sulphur content and (b) 140ppm sulphur content

This is also confirmed by Zacharia et al. [139] who explained the effect of the surface active elements on the fluid flow magnitude, direction and bead geometry of stainless steel. He showed that the weld penetration and aspect ratio (depth to width ratio) are not only based on the level of surface active elements in the parent metals, but rather by a combination of temperature distribution and the percentage of the surface active elements in the fusion zone. He also reported that increased sulphur content in the alloy leads to higher weld to depth ratio and deeper penetration regardless of the welding technology. For most of steel with low oxygen and sulphur content, the surface tension effects decrease by increasing the temperature, which results in a negative surface tension temperature coefficient ($d\gamma/dT$) [94, 139-141].

Such experimental findings are validated by Chung and Wei [103, 107] who developed a model to investigate the melt pool convention and shape subjected to marangoni forces in different directions in dissimilar welding of aluminium to steel. They showed that the depth and width of the molten pool governed by variation of the signs and magnitudes of the surface-tension coefficients.

Several numerical investigations of dissimilar weld geometry have been reported by various researchers. Ranjbarnodeh [110], developed three dimensional model using finite element analysis (FEA) to predict the temperature distribution and weld geometry in dissimilar arc welding of ferritic stainless steel to carbon steel, and concluded that in the absence of melt pool convection, the temperature distribution in weld bead is asymmetrical with maximum temperature shifted toward low carbon steel. However, the size of the weld HAZ were reported to be wider toward ferritic stainless steel than carbon steel (Figure 2-28).
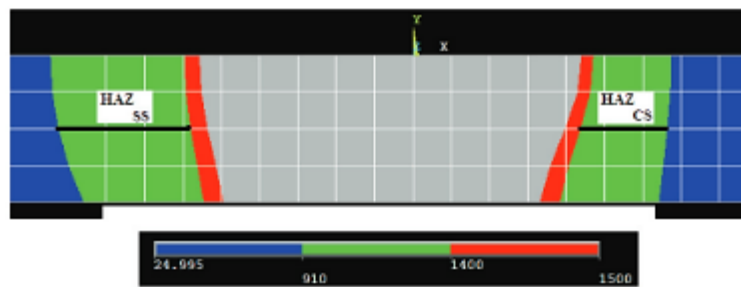
Figure 2-28 Predicted HAZ regions in the stainless steel and the carbon steel sides according to calculated temperature distribution (°C)

Xue et al. [142] developed a 3D finite volume simulation model for laser welding of a Cu–Al lap joint to investigate the weld geometry, alloying element distribution and transition layer thickness. Validation of the simulation results as well as the weld pool characteristics were obtained by SEM and EDX analysis of the laser welded joint. They found a bowl shape fusion zone between Cu and Al as a result of different thermo-physical properties of Cu and Al. Their numerical results show reasonable agreements with experimental analysis (Figure 2-29).
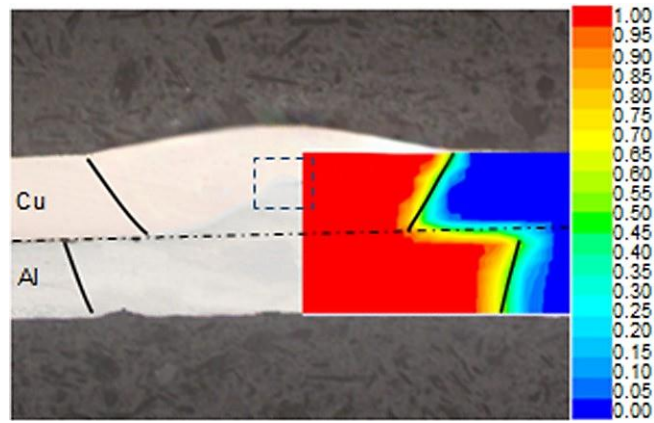
Figure 2-29 Comparison of weld pool shape between simulated and experimental results with Cu on top (the colour bar on the right indicates the fraction of molten material) [142]

Yang et al. [92], developed numerical modelling to investigate the characteristics of melt pool convection on weld bead shape in laser processing of AISI 304 stainless steel. He concluded that Marangoni convection due to a negative surface tension coefficient enhances the heat transfer in molten pool and result in wider and shallower weld bead.

As it is conspicuous from the literature, most of the researchers have considered laser welding speed and laser power as the main factors which defines the weld geometry, however a recent investigation by Suder et al. [136] presented the characterisation of the laser welding process by three laser material interaction parameters which are power density, interaction time and specific point energy. They showed that the depth of penetration (weld depth) is mainly dependent on the power density and specific point energy while the weld width is mainly controlled by process speed. Figure 2-30 illustrates the effect of interaction time on weld with at constant power density and specific point energy.

(a)   (b)
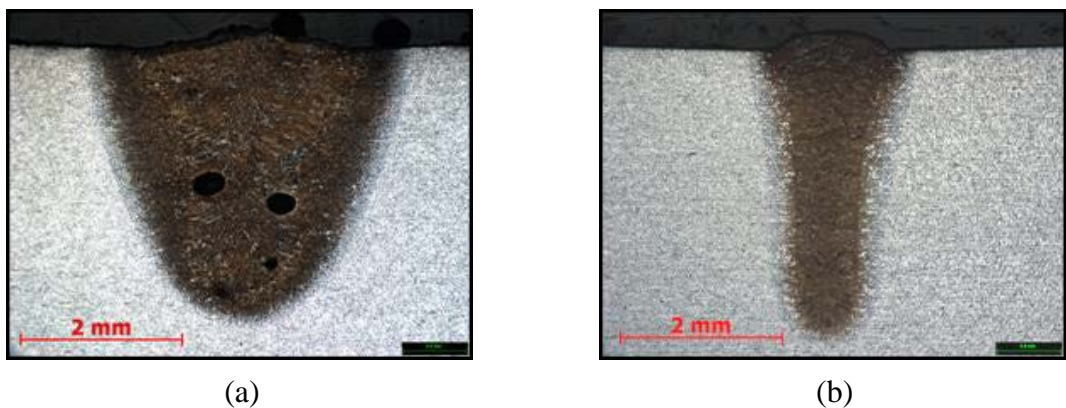
Figure 2-30 Macrographs at constant power density of 1.6MWcm^{-2} and specific point energy of 60J (a) Interaction time of 38ms, (b) Interaction time of 8ms [29]

2.5.3 Surface topology

Similar to weld bead geometry, surface morphology of the weld significantly influences the quality of the welded joint. Controlling the weld shape is essential since the mechanical strength of the welded joint is influenced not only by the cooling rate and chemical composition, but also by surface morphology of the weld.

The geometry and surface topology of the fusion zone is influenced by many factors including the surface active elements and fluid flow dynamics [139]. The fluid flow dynamics inside the melt pool and the subsequent solidification of weld dependents significantly on the thermal cycle. The thermal cycle is again influenced by the process parameters (e.g. power density, interaction time and subsequent energy input) and surface active elements.

It was reported that the temperature and element concentration leads to a substantial variation of surface tension which initiates Marangoni stresses at the free surface [68, 88, 104, 143, 144]. These stresses must be balanced by shear stresses owing to the liquid metal viscosity. The gradient of the shear stress from the area of low to high surface tension initiates the main flows in the fusion zone. Hence, the Marangoni driven flow have significant impact on the final bead surface morphology [85-87]. The influence of the surface tension temperature coefficient ($d\sigma/dT$), on weld geometry was investigated by Bäuerle [145]. As illustrated in Figure 2-31, hump was formed for $d\sigma/dT > 0$ (due to inward flow of molten pool), and depression was formed for $d\sigma/dT < 0$ (due to outward flow of molten pool).

(a)   (b)
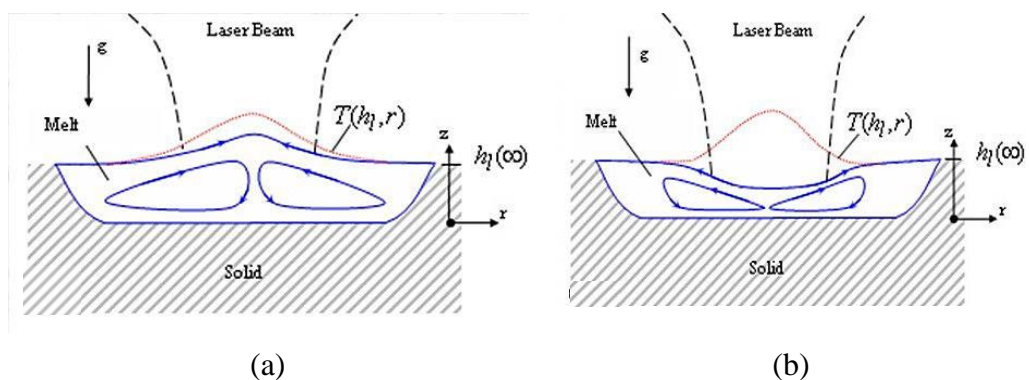
Figure 2-31 Midpoint cross section parallel to the laser beam pass of the laser melted surface showing (a) Humping and (b) Depression [145]

A number of previous studies have investigated the underlying mechanism of weld surface topography during weld solidification. Anthony and Cline [146] showed a depression of the liquid surface beneath the beam and ridging of the liquid surface as a result of temperature gradients and consequent surface-tension gradients between laser-beam irradiation zone and the intersection line of the solid-liquid interface. They also produced a weld with less surface topography variation (surface rippling), by increasing the welding speed. They concluded that the increase in speed reduce the time for the free surface to deform and create ripples. Figure 2-32 (a), (b) and (c) illustrate the formation of depression and rippling at initiation of laser beam sweep, during the welding, and when the beam is off.
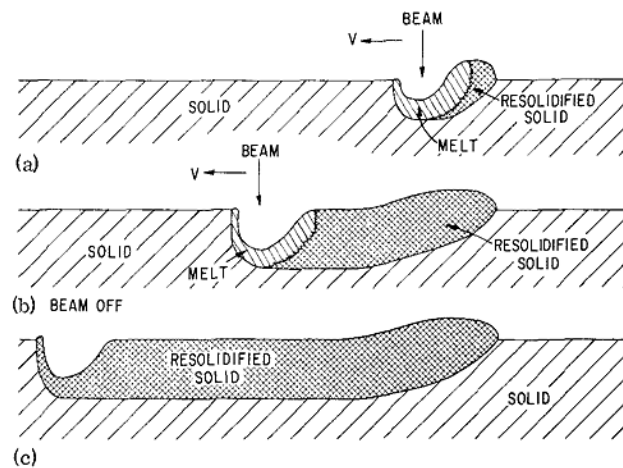
Figure 2-32 Midpoint cross section parallel to the laser beam pass of the laser melted surface showing depression and rippling (a) Immediately after initiation of laser beam sweep (b) In steady state (c) At the end of the laser beam sweep [146]

The effect of surface tension as a function of molten pool temperature and sulphur content on molten pool fluid flow, mixing, and weld penetration have been systematically investigated by Wang and Tsai [147]. They showed that surface tension can be a main driving force that controls the surface topography, and that the weld penetration depth enhances as a result of higher sulphur content and consequent downward flow. This is of significant importance for materials with high sulphur content. Kotecki et al. [148], carried out an experimental investigation and explained the ripples formation on surface of GTA spot welds based on molten pool oscillations during solidification.

Marimuthu et al. [68] developed a sequentially coupled thermo-structural multiphase analysis to predict the effect of laser parameters on the change in surface topology of the weld bead and its subsequent effect on structural properties. They showed that the laser welding parameters strongly affect the weld bead shape, which eventually affects the weld quality, and a net shaped weld bead demonstrates better performance in terms of stress distribution than other weld bead shapes. Figure 2-33 illustrates the weld bead profile and temperature contour as a result of different welding speed.

| (a) | (b) | (c) |
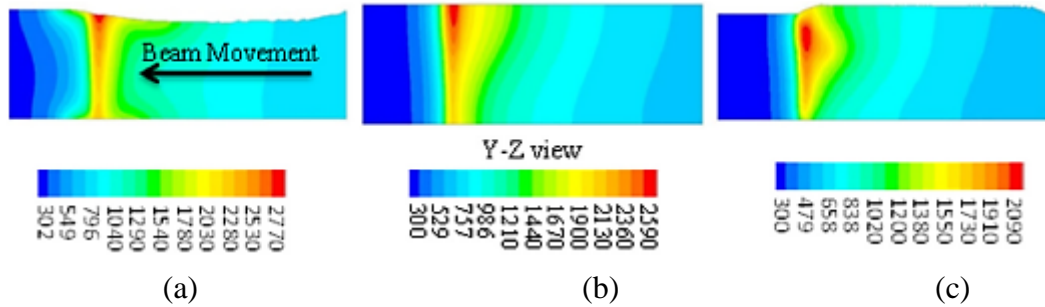
Figure 2-33 Weld bead profiles and temperature contour (K) with for 600W laser power and speed: (a) 75 mm/s, (b) 100 mm/s, (c) 125 mm/s

Ma et al. [149], established a transient, two-dimensional, coupled heat transfer, and fluid mechanics model for pulsed laser polishing of titanium alloy Ti6Al4V. The model predicted the temperature and velocity fields as well as the evolution of surface profile on a free deformable surface. The effect of laser pulse duration on the melt pool flow model was also studied in the coupled model. It was found that the surface topography of the molten pool is dominated by differentiation between capillary and thermocapillary regime during different process pulse duration. A very good agreement is observed between their numerical and experimental validation.

Baumgart et al. [150], Chen et al. [151] and Willis and Xu [152] experimentally studied the deformation of the free surface during pulsed laser-materials interaction. They revealed several kinds of surface shape by varying the laser pulse energy.

Effects of processing parameters on surface quality for the pulsed laser welding of zinc-coated steel are experimentally investigated by Tzeng [153]. The influence of average peak power density (APPD), the average output power, the processing speed, pulse energy and the pulse duration on weld surface topology are measured. They showed desired top surface quality of laser lap welds by controlling the processing parameters. It is also found that welding speed, laser power, the pulse duration are most determinable factors that form surface topology.

2.5.4 Residual stress and service performance

Residual stresses are self-balancing internal stresses that develop during a similar or dissimilar welding process [154]. Residual stress will be induced at every stage (during or after) of the welding process. Fusion welding samples can have higher tensile stresses in the welded region balanced by lower compressive residual stresses elsewhere in the component. If not addressed properly, residual stresses and distortion can pose a serious threat to the welded joint. This is of particular importance in dissimilar laser welding due to the notable differences in material properties of the two materials, including coefficient of thermal expansion [8]. An understanding of residual stress generation and service performance are important to achieve high quality dissimilar welded of joint.

The fatigue behaviour of resistance spot welds and laser spot welds of dissimilar materials, including dual phase and deep drawing steel is compared by Daneshpour et al. [155]. They suggested that the fatigue strength of laser spot welds is higher than resistive welds due to the laser's higher penetration depth and narrower heat affected zone. In an another study carried out by Daneshpour et al. [156], dissimilar and similar laser spot welds was investigated. They joined dual phase high strength steel with deep drawn steel, using two joining processes (resistance and laser spot welding), and examined their monotonic performance under tensile shear loading. They concluded that the dissimilar laser spot weld's strength is governed by the strength of the weaker material and investigating the mechanical performance of dissimilar spot welds is of paramount importance. The sensivity of the joint strength to the weaker material is also confirmed by Alenius et al. [157] who studied weldability of various dissimilar metal joints between austenitic stainless steel and non-stainless steels. They concluded that the strength of the dissimilar joint in the tensile-shear test is dictated by strength and thickness of non-stainless steels.

Laser welding of carbon steel and stainless steel was investigated by Anawa EM [8], who reported that the tensile strength of the dissimilar joint can be controlled by laser power and welding speed. The failure behaviour and stress distribution of dissimilar RSWs of low carbon steel and high strength steel was studied by Pouranvari et al. [158]. They investigated the relationship between the failure behaviour of the RSWs and fusion zone characteristics and concluded that the failure mode and stress distribution is predominantly controlled by weld nugget size.

A number of finite element models [136, 159-164] have been also developed to predict thermal cycle and residual stresses in similar and dissimilar stainless-carbon steel butt-welded joints. A comprehensive FEA model was developed by Deng et al. [165] to compute residual stresses in a dissimilar metal pipe joint with considering cladding, buttering, post weld heat treatment and multi-pass welding using a united fashion technique. The influences of cladding, buttering and post weld heat treatment on the final residual stresses are also determined after welding process is finished; however he failed to consider the solid-phase transformation.

Yagi [108] developed a FEA model of welding of P92 steel pipe and IN625, but concentrated on predicting the residual stress and distortion. Katsareas [109] developed a FEA model to predict thermal and residual stress distributions in a dissimilar joint between A508 and AISI 304L. They used the "element birth and death" technique to model the filler metal added during the welding process. Element birth and death involves deactivating (death) all the filler elements at the start (the elements are still in the model but have zero stiffness, and hence to effect) and activating them during the simulation to simulate metal addition.

In general, a material with higher yield stress can tolerate higher residual stresses particularly when the material experiences significantly high thermal gradients [159-161, 166]. A numerical and experimental investigation was carried out by Akbari and Sattarifar [161] to study the thermo-mechanical behaviour and residual stresses in dissimilar arc butt-welded stainless steel and carbon steel. They suggested that the maximum residual stress in the weld area tend to be in the stainless steel part due to the higher yield strength of stainless steel TP304 compared to carbon steel A106-B, and this causes an unbalanced distribution of residual stresses. It is also reported that the heat

input significantly affects the compressive stress.

A thermo-mechanical FEA model was utilized by Ranjbarnodeh et al. [160] to investigate the effects of processing parameters, welding sequence and workpiece length on the residual stresses distribution of dissimilar TIG welds of low carbon and ferritic stainless steels. Their numerical results are validated using X-ray diffraction and good agreement is observed. Figure 2-34 shows the comparison of their simulation and experiments. It was found the maximum residual stresses occurred in the carbon steel part (approximately 250 MPa for carbon steel and 180 MPa for stainless steel). It is also reported that the maximum tensile residual stresses decreases with the increase in the workpiece length while the weld distortion increases. In addition, lower magnitude tensile residual stresses are observed by increasing the welding current. Furthermore he observed that a symmetric welding sequence can result in low magnitudes of residual stress.

(a)   (b)
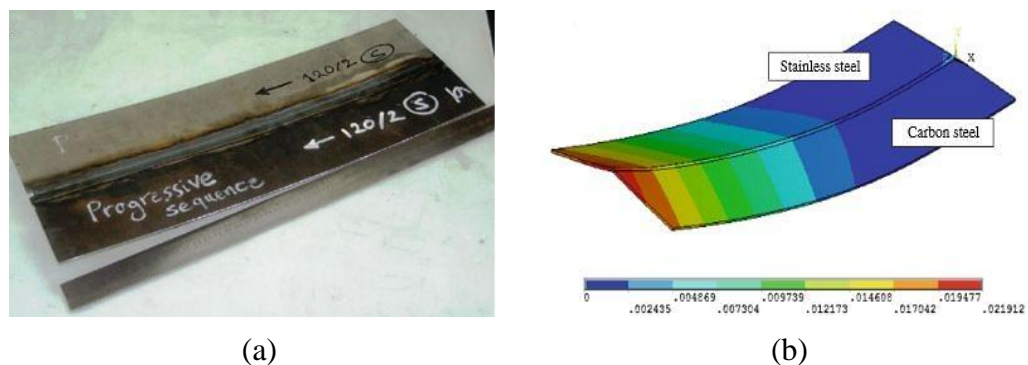
Figure 2-34 Residual thermal distortion in dissimilar weld [160] (a) Experimental result, (b) Numerical result

Some researchers also discuss the effect of thermo-physical properties of the welded steels as the main reason for residual stress distribution in dissimilar welding [159, 162, 167]. Lee and chang [162] estimated the residual stress distribution in dissimilar welding of carbon and austenitic stainless steels using the finite element (FE) method. They found higher magnitude residual stress at the base metal near the weld area in the stainless steel compared to the carbon steel side. Furthermore, it was proposed that the higher thermal expansion coefficient and strain hardening rate of stainless steel result in higher tensile longitudinal stresses balanced by the higher transition rate toward compressive stress. The effect of cooling rate on the mechanical properties of carbon and stainless steel butt weld was investigated by Lee et al [166]. Using a FE simulation they found that the

residual stress is higher inside the stainless steel weld metal due to its lower thermal conductivity and larger coefficient of thermal expansion compare to carbon steel. Dawes [25] found that stainless steel is prone to unequal expansion and distortion during dissimilar welding due to its higher thermal expansion (50%) compared to other common materials like low carbon steel.

Although many scholars have focused on the fusion zone mechanical properties, there are many reports that have shown the microstructural transformation in HAZ as one of most serious issues in dissimilar welding. Hajiania et al. [168] studied the microstructure and mechanical properties of TIG welded dissimilar joint (stainless steel/ low alloy steel) and found that, in most cases, the weld failures occurs at HAZ of low alloy steel. This is due to the carbon migration from the low alloy steel HAZ toward the fusion zone, which resulted in formation of relatively soft ferrite region between the stronger weld metal and base metal. Arivazhagan [69] and Chen [169] studied the dissimilar welds of low alloy steel to austenitic stainless steel, and showed that fracture happened in the HAZ of low alloy steel, which is similar to previous observations.

Through experimentation and a finite element (FE) simulation, a deep analysis was performed by Zeng et al. [170] on the final microstructure, microhardness and residual stress of specimens undergo laser surface treatment for different laser powers. Solid phase transformations from austenite to ferrite, pearlite, bainite and martensite were considered in their model for both HAZ and laser treated surface. Figure 2-35 illustrate their obtained temperature profile and corresponding microstructural variation in the depth direction. They discussed that as a result of material contraction during cooling, formation of martensite and other solid-state phase transformations, thermal damages and residual stresses are generated around the laser path in the form of tensile stresses along with few compressive stresses.
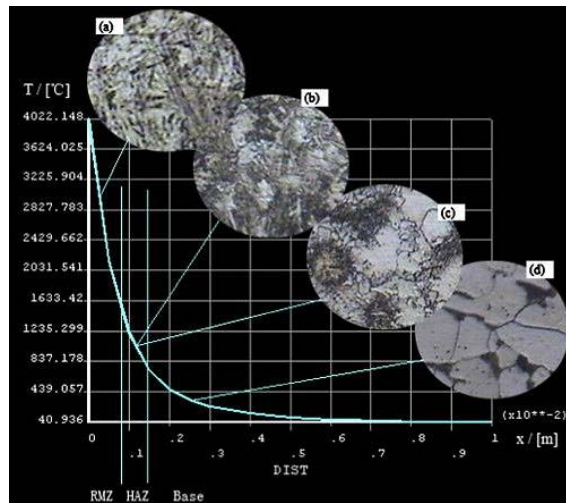
Figure 2-35 Temperature profile and the corresponding metallographic structure

Kong et al. [171] employed a thermal-microstructure model, as a combination of the finite element method with the Monte Carlo model (FE–MC), to investigate the heat transfer, martensitic transformation and grain evolution processes in the heat-treated zone of dual phase steel (DP980). He concluded that the increase in scanning speed controls the grain size and martensite decomposition in the HAZ.

The importance of microstructural transformation and its effect on mechanical properties in the HAZ of steel is studied by Nady et al. [172]. In this investigation, a sequentially coupled thermal, metallurgical, mechanical 2-D finite element model is developed (based on ABAQUS code). The simulation results revealed that the final residual stress in substrate steel depends on the HAZ and its microstructural variation.

Elmer et al. [173] used a combination of numerical models, phase kinetics calculator and SRXRD phase mapping to measure the thermal cycle in the weld and calculated the kinetics of the ferrite to austenite phase transformation in HAZ of an AISI 1005 C-Mn steel during SAW welding. Employing the data from the numerical model and phase mapping, they developed a new CHT diagram form the steel which consequently predicted the phase percentages of austenite and ferrite over a relatively wide range of HAZ and weld heating rates.

A sequentially coupled three-dimensional (3-D) thermal, metallurgical and mechanical FE model of high carbon steel multipass butt weld were employed by Lee et al. [174] considering solid-state phase transformations. The longitudinal, transverse and through-

thickness residual stresses were analysed using FEA simulation. It was demonstrated that a volumetric increase during austenite to martensite phase transition reduced longitudinal tensile residual stresses in the fusion and the HAZ (Figure 2-36). The volumetric increase during the austenite to martensite phase transformation is reported to be the main reason for the significant reduction of the longitudinal tensile residual stresses in fusion zone and the HAZ. It is also highlighted that the influence of such solid-state phase transformation cannot be ignored in modelling of residual stresses during welding of particularly high carbon.
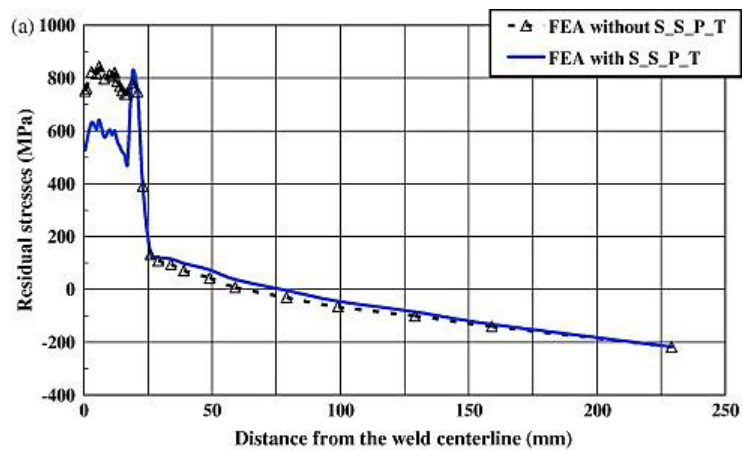
Figure 2-36 FE analysis results with and without solid-state phase transformation (S_S_P_T) longitudinal residual stresses

Both weld and HAZ are risk zones since local mechanical properties are significantly altered with a higher risk of exposure to microstructural transformation, impurities, and residual stresses. Post weld heat treatment (PWHT) is generally privileged to restore some of the properties of weld and HAZ which are at these risk zones. This is including the relief of residual stress, prevention of stress concentration, and release of residual hydrogen in the HAZ [175-177]. Dewan et al. [178] carried out an investigation to explain the effect of post-weld heat treatment and electrolytic plasma process (EPP) on improvement of microstructures, residual stresses and tensile strength during TIG welding of AISI 4140 steel. Significant increase (About 88%) in toughness values of weld and HAZ was achieved by PWHT at 650 °C compared to as-welded samples. It is shown that such improvement is attributed to the decomposition of martensite, grain refinement, homogenised microstructure between weld and HAZ, and removal of tensile residual stresses during PWHT.

67

Another strategy is to develop a welding or tempering technique with a setup capable of manipulating the microstructure at risk zones simultaneously. Chen et al. [179] employed arc-ultrasonic technique, an ultrasonic power source coupled to the TIG power source to modulate the welding arc, to study the influence of various arc-ultrasonic parameters on weld and HAZ microstructures, hardness and tensile strengths of steel. They showed that the arc-ultrasonic technique improves mechanical performance of the weld metal and HAZ by refining the microstructure and providing even distribution of carbides in weld and HAZ.

In another study Baghjari et al. [180], carried out two PWHT strategy on a Nd:YAG laser welded joint of martensitic stainless steel (AISI 420) to achieve the discontinuity-free weld. They found that the HAZ hardness is significantly higher than weld as a result of over precipitation and increasing amount of $M_{23}C_6$ carbide precipitations (Figure 2-37a). To reduce the hardness, and increase the integrity, and toughness of the weld and HAZ, two types of post-weld heat treatments (PWHTs) were carried out. In type 1, samples tempered for 2h. In type 2, samples were held in austenitizing temperature (1010 °C) for 0.5h and then tempered for 2h. Considering achieving high strength and toughness joint, optimum tempering temperature for the steel were found at 595 and 537 °C. Figure 2-37b illustrates the hardness profile of the same joint (sample No.3) as figure 2-37a after developed tempering approach.

(a)   (b)
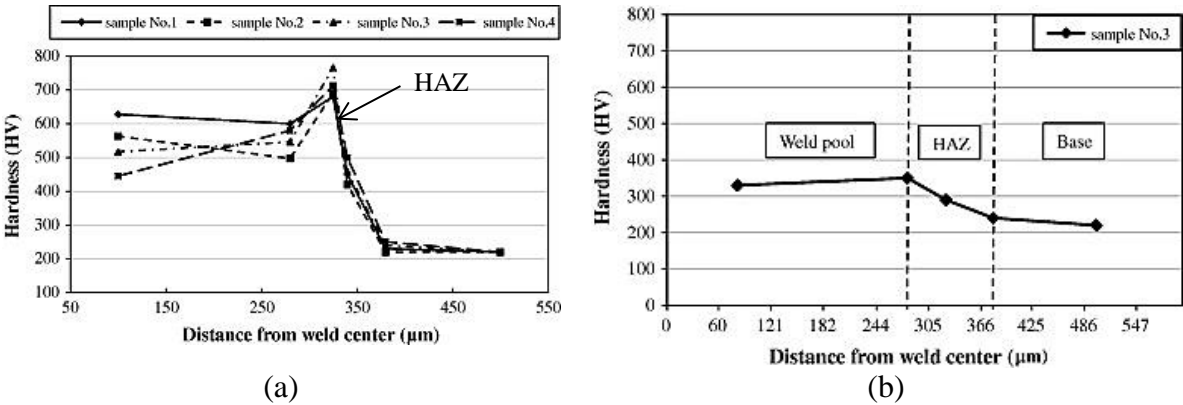
Figure 2-37 Microhardness profiles of the weld and HAZ (a) without PWHT and (b) with PWHT (tempered at 600 °C for 2h)

2.6   Summary

This chapter summarized the primary aspects of laser dissimilar welding and concluded that it is a promising technique for joining metals and alloys across range of sectors. The interdependent phenomena involved in the laser dissimilar welding and their effects on the final performance of the dissimilar joint were detailed in this chapter. Despite the fact that there has been an extensive research in this field for the last thirty years, there are still challenges. Undesired microstructure and the formation of inhomogeneous fusion zone are the main issues still associated with the dissimilar laser welding. Many researchers have investigated dissimilar laser welding; however until now the significance of thermo-physical conditions in the dissimilar laser welded melt pool (of carbon steel and stainless steel) have not been investigated in detail. In particular, the mechanisms to control the melt pool dynamics and dilution, so as to achieve a full penetration, a homogenous fusion zone and a predominantly austenitic microstructure require further study.

Chapter 3 Materials, Methodology and Equipment

3.1   Introduction

This chapter gives a brief introduction to the material and experimental equipment used in this research. The laser used in the experimental setup, configuration of the welding nozzle and the shielding gas that were used during the experiments are summarised. The statistical method used to interpret the experimental data is also discussed.

3.2   Materials

The dimension of the work piece materials used for dissimilar welding is detailed in table 3-1. The dimensions of the materials were selected so as to achieve quasi-steady state during welding and to have sufficient materials for mechanical and metallurgical analysis. Chemical composition of the carbon steels and austenitic steel are presented in table 3-2 in terms of weight percentage [36, 181-183].

Table 3-1 Materials used in experiments

Name of steel	Thickness (mm)	Length (mm)	Width (mm)
Stainless steel 316L	1	50	50
Low carbon steel 10130	1	50	50
High carbon steel AISI O1	1	50	50

Table 3-2 Chemical composition of the ferrous materials (wt %)

Element	C	Si	Tu	Va	Mn	P	S	Si	Cr	Ni	Mo	Nb	Fe
SS	0.03	-	-	-	2	0.01	0.03	1	18.02	10.15	2-3	0.09	Bal.
LCS	0.12	0.011	-	-	0.6	0.045	0.045	0.011	0.008	0.035	0.003	0.001	Bal.
HCS	0.95	0.4	0.5	0.15	1.2	0.045	0.045	0.011	0.55	0.035	0.003	0.001	Bal.

Stainless steel's resistance to corrosion and low maintenance make it a preferable material for numerous applications. The alloy is milled into different shapes such as coils, sheets, bars, wire, and tubing to be used in furnace parts, valve and pump trim, jet engine parts, exhaust manifolds, automotive and aerospace structural alloy [184]. Laser welding processes are widely used for joining stainless steel (SS) type 316L due to their ability to reduce carbide precipitation and produce a highly corrosion resistive weld. Currently, laser welded SS parts are extensive used in the aerospace, biomedical and chemical industries [5, 184]. Low carbon steel is one of the most common materials used in many industries from power plants to body panels. Its low cost, high malleability and weldability make it as one the highly used steels in various industry sectors. Recently various industries such as petrochemical and modern railways are starting to use high carbon steel due to its high wear resistance and high strength [36, 185]. Both high carbon and low carbon steels were used in this investigation. High carbon steel were used specifically to investigate the importance of cooling rate and study the welding issues that occurs outside the fusion zone.

Both types of steels (stainless steel and carbon steel) have distinct crystallographic structures which characterise their properties. Austenitic stainless steels have a face-centered cubic structure (γ phase) (Figure 3.1a), at room and at high temperature which has one atom at each corner of the cube and one in the middle of each face. This grain structure forms when a sufficient quantity of nickel is added to the alloy (8-10% in a standard 18% chromium alloy) [184, 186]. Carbon steel has body centred cubic (bcc) crystalline structure (α phase) (Figure 3.1b) at room temperature which transforms to face centred cubic (fcc) crystalline structure (γ phase) above the austenite phase transformation temperature of Ac_3 [187, 188]. The Ac_3 temperature of steel is a function of carbon and other alloying element contents and can be calculated from phase transformation temperature formulas which are discussed in later chapters.

<center>(a)   (b)</center>
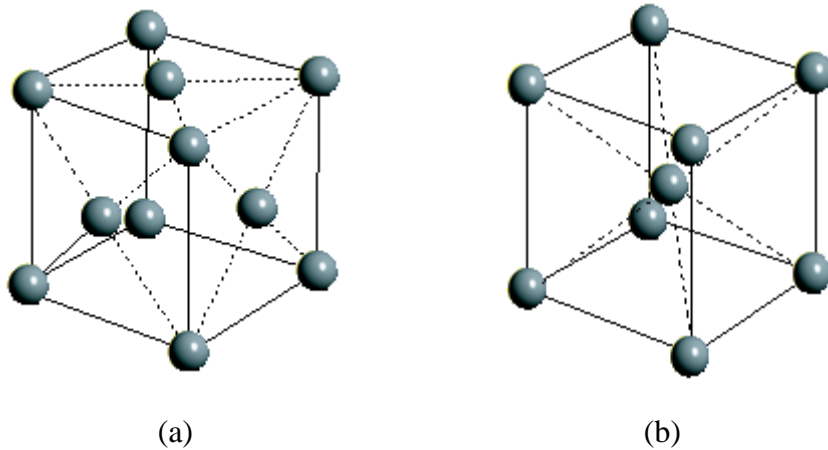
Figure 3-1 Crystallographic structures of (a) Face-centred cubic structure (fcc), and (b) Body-centred cubic structure (bcc)

Because of high weldability, low cost, wear and corrosion resistance, carbon and stainless steel are considered as the most suitable steels for dissimilar welding of various components in industries such as pressure vessels, boilers, and heat exchangers (e.g. reheaters and superheaters) in power plant, railway and gas industry [4, 69, 119, 122, 168]. In particular, austenitic stainless steel is commonly used for parts performing at relatively high temperatures and carbon or ferritic steel is used for those parts working under lower temperatures and higher pressures. Table 3-3 and 3-4 show thermo-physical and mechanical properties of these metals.

Table 3-3 Temperature dependent thermal properties of the substrate [189-192]

Temp. (K)	Stainless steel			Carbon steel		Low carbon steel	High carbon steel
	Specific heat (J/kgK)	Density (kg/m^3)	Conductivity (W/mK)	Specific heat (J/kgK)	Density (kg/m^3)	Conductivity (W/mK)	Conductivity (W/mK)
273	462	7900	14.6	444	7872	51.9	45.9
373	496	7880	15.1	472	7845	44.8	44.8
473	512	7830	16.1	503	7816	43.4	43.4
573	525	7790	17.9	537	7740	41.4	41.4
673	540	7750	18.0	579	7733	38.9	38.9
873	577	7660	20.8	692	7669	33.6	33.6
1073	604	7560	23.9	837	7578	28.7	28.7
1473	676	7370	32.2	860	7440	28.6	28.6
1573	692	7320	33.7	863	7380	29.5	29.5
1673	696	7320	76.8	863	7324	29.5	29.5
1773	700	7320	120	863	7268	29.5	29.5

Table 3-4 Physical properties of the parent metals [119]

Physical properties	Stainless steel	Low carbon steel	High carbon steel
Melting temperature [^{o}C]	1510	1420	1400
Ultimate tensile strength [MPa]	560	440	1690
Yield strength [MPa]	290	240	1500
Vickers hardness [HV]	150	120	560

3.3 Experimental setup

A butt joint configuration was used through-out the experimentation. All the samples were polished by abrasive paper so as to clean the sample edges from any external impurity and dirt, which may affect the weld quality. A custom fixture was designed in order to hold the samples during experimentation. The plate's edges were clamped together in a way that ensures full contact between the samples alongside the welding line during the process. Figure 3-2 shows the set up configuration of the welded samples.
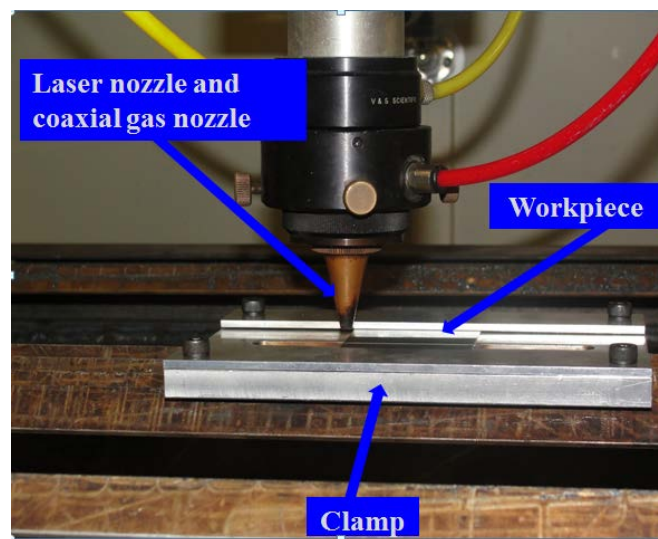
Figure 3-2 Laser and workpiece configuration

In all of the experiments the distance between the laser nozzle and the workpiece (stand-off distance) was kept constant at 5mm. An AEROTECH based CNC table was used to provide a precise controlled motion in X and Y direction. A touch probe was used to ensure flatness of the fixture.

A CW COHERENT S48 CO_2 laser (Figure 3-3) was used as the laser source. It has a maximum power of around 1.2kW at near infrared wavelength of 10.6µm. The energy distribution of the CO_2 laser was predominantly Gaussian. CO_2 lasers are extensively used in various applications like cutting, welding, cladding and surface treatment of a variety of different materials including plastics, woods, alloys and metals. It can operate as continuous wave or as modulated pulsed modes with pulse lengths of 0.01ms-CW. However the pulsed peak power is limited to 1.2kW. The raw beam from the laser is approximately 15mm with the minimum focused spot size 0.5mm. The focusing lens diameter is 127mm with focal length of 63.3mm. The focusing position can be coaxially adjusted using a large rotating telescope (view window range -10 to +10mm). The laser head is stationary and an X-Y table is controlled by a PC based CNC controller. The laser head and operating controller are illustrated in Figure 3-4 (a) and (b) respectively. The beam is delivered through a bending mirror to the V & S scientific laser welding head which houses gas nozzle and focusing lens.

Figure 3-3 1.2kW Carbon dioxide (CO_2) coherent S48 laser systems

<div align="center">

(a)   (b)

</div>

Figure 3-4 Photographic image of (a) Nozzle fibre laser welding head and (b) CO_2 laser operating controller

3.4 Characterization of weld quality

As discussed in chapter 2, laser welding has the advantages of focused energy input and consequently, controlled heat input which eventually help to achieve high quality weld. The laser have a very small spot size and relatively high traveling speeds, hence the laser welded samples experience extremely high cooling rates. These cooling rates generate a very small localised heat affected zone, thus minimising distortion. Complete penetration and reasonable weld width are also recognized as the primary requirement of a laser welding joint. Having a narrower heat affected zone is more desirable. This is because of the fact that wider heat affected zone will cause the parent metal to undergo wider microstructural variation, metallurgic effects and phase transformation which can affects the mechanical properties of the welded joint [125, 193].

Another important factor to be considered during characterization of the weld joint is the strength of the weld. Typically the weld joints should be stronger than the parent metals in terms of tensile and impact strength [193, 194]. Surface morphology of the weld is another important parameters that controls the weld quality [193, 194]. In other words, controlling the weld bead shape is essential since the mechanical strength of the weld joint is influenced not only by the cooling rate and chemical composition in the weld metal, but also by surface morphology of the weld.

In this study, weld bead geometry, microstructure and service performance were considered as the key quality indicators [195]. A schematic view of the typical quality measurements for the weld geometry is illustrated in Figure 3-5. As can be noted from the figure, the weld width was measured as the average of weld width length in the top of the weld metal. This weld width length is measured by using an optical microscope in transverse sectioned weld specimens.

Heat affected zone (HAZ) width was measured from the weld metal interface toward the parent metals (Figure 3-6). HAZ width is the region that undergoes grain growth and phase transformation due to the heat from melt pool, but not enough to melt and change its phase from solid to liquid. In order to avoid systematic errors, each experiment was repeated three times and their averages are recorded.
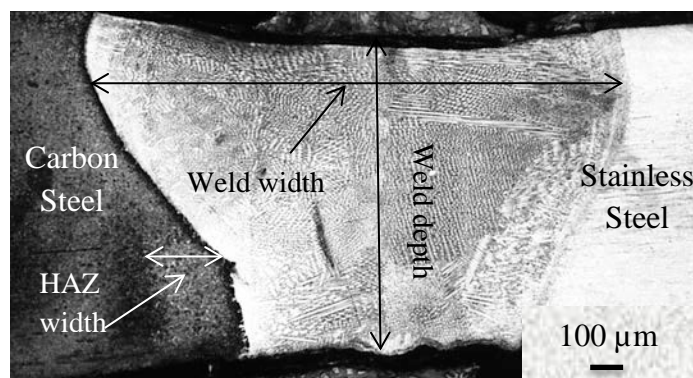
Figure 3-5 Schematic view of typical quality measurements applied in the study
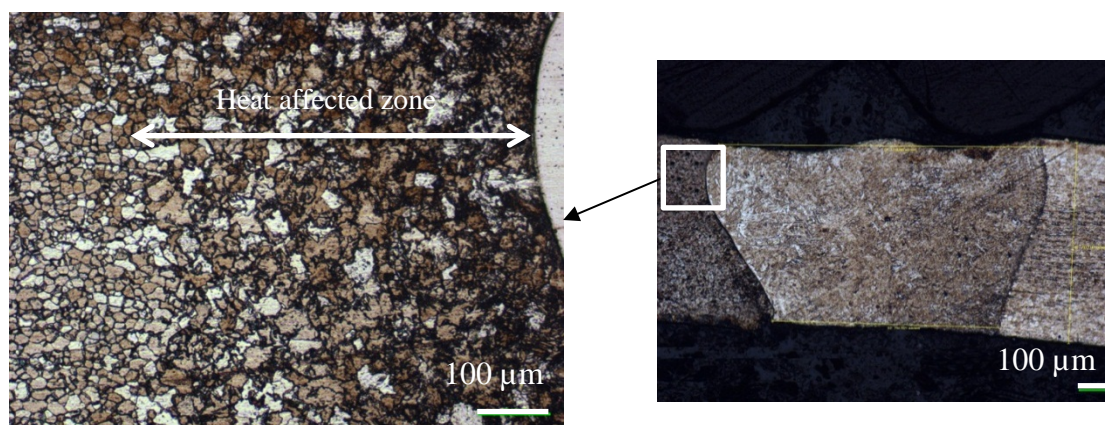
Figure 3-6 Schematic view of heat affected zone

For metallography analysis, all the laser welded specimens were sectioned in traverse planes at the middle of the welded region, where the thermal cycle have reached quasi-steady state condition. The sectioned specimens were hot mounted in a resin (Polyfast) using Struers Labo Press 3. The cross-sectioned samples were ground using abrasive papers (from grit 120 to 1200) on a Struers-127 polishing machine, and then polished with diamond suspensions of 6μm, 3μm and 1μm grain size using the same machines. The welded samples were then prepared for metallographic analysis as per ASTM E3-11 standards [196]. Metallographic samples were etched using three etchants. The carbon steel side of the weldment was etched using Nital 5% regent, stainless steel side was etched using Kalling's No.2 (5g $CuCl_2$, 100ml HCl, 100ml ethanol), and the fusion zone was etched using a mixture of Ferric Chloride, Hydrochloric acid and Nitric acid. In order to avoid the effect of each etchant on other regions the samples were polished after applying each enchant (for the particular steel side and fusion zone).

3.4.1   Optical microscopy and scanning electron microscopy

Optical microscopic imaging is commonly used as an effective technique for quantitative evaluation of weld geometry [119], microstructure, and heat affected zone which are the dominant thermal dependent parameters that controls the dissimilar weld quality [197]. Only carbon steel HAZ width was considered in the study as, significantly higher HAZ width was noticed in the carbon side compared to the stainless steel side, and the non-transformable HAZ microstructure in stainless steel makes it less important to study compared to HAZ in carbon steel [122]. The optical microscopic imaging was carried out using Nikon optical microscope with PC interface via a 5 mega pixel CCD camera into image pro software. Figure 3-7 illustrates the optical microscopy setup.

Figure 3-7 Optical microscopy used in this study

A conductive polyfast mount material was used to produce scanning electron microscope (SEM) samples. The polyfast mounted sample enables the SEM equipped with an EBSD as shown in Figure 3-8 to analyse the weld metal. SEM is particularly useful in understanding the main microstructure, phase transformation, and grain boundary studies inside the weld metal. An energy dispersive X-ray (EDX) analysis was used to investigate the chemical composition of the weld metal and the interfaces obtained after dissimilar laser welding of stainless steel and low carbon steel. The SEM system used was a LEO 1530VP scanning electron microscope with secondary electron (SE) and back scattered electron (BSE) detectors. The analysis was performed along the cross section at an acceleration voltage of 25V and the current electron beam of 30pA. The results were studied using SEM Quant ZAF EDS analysis software. The EDS was equipped with an Oxford Instruments X-Max 80mm2 detectors which in this case, the electron beam and current was set 20kV and 9.09nA respectively. In order to quantify the dilution rate and the size of the weld pool, point counting and line-scan intensity profiles were performed across the weld at 0.5mm from the top surface. The elements analysed within the weld pool includes chromium, nickel, manganese, silicon, molybdenum, niobium and iron. The concentrations of these elements were normalized to 100 wt%.

Figure 3-8 Scanning electron microscopy used in this study

To quantify the ferrite content of weld metals, there are generally two common methods which are most used by researchers: the point count procedure and a magnetic method using a Fisher ferrite scope [198]. The benefit of the point counting method is that it can be employed for all types of microstructures. However, it is difficult to apply in situ and is relatively expensive. In this investigation Fischer (Figure 3-9) ferrite scope was used.

Figure 3-9 Determination of the ferrite content in the weld seam area using the FERITSCOPE

3.4.2 Micro-hardness and tensile testing

Vickers micro-hardness testing Figure 3-10 was performed to quantify the relationship between the microstructures and mechanical properties of the weld. The micro-hardness tests were undertaken on the polished mounted weld cross section. The Vickers hardness test method consists of indenting the test material with a diamond indenter, in the form of a right pyramid with a square base and an angle of 136 degrees between opposite faces as shown in figure 3-9. The materials are exposed to load value of 1 to

100 kgf, and loading time between 10-15 seconds. The Vickers hardness number was then estimated from the dimension of the impression.
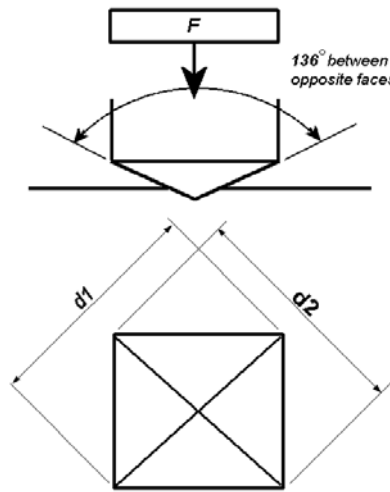
Figure 3-10 Vickers hardness test [199]

The two diagonals indentation impression is measured in millimetres, and their mean value is recorded. The diagonal lengths of indentations were measured under the magnification of 10X. The Vickers hardness number can be then calculated using the following relation:

$$HV \text{ (Vickers hardness)} = \frac{2W \sin\frac{136^{\circ}}{2}}{d^2} = \frac{1.854W}{d^2} \text{ (Aproximately)} \qquad \text{E.q(1)}$$

Where W is the applied force in kilogram and d is the mean value of diagonal (in mm), and 136 is the plane angle of indenter. The hardness was measured on the weld cross section at the centre line of the thickness (across the weld metal with offset value of 200µm from the centre line toward both low carbon and stainless steel side) applying 50g, $HV_{0.05}$, load on the micro-hardness tester.

Notched tensile strength (NTS) samples [200] were prepared from the laser welded samples to study the mechanical properties of the weld bead. The dimension of notched tensile test sample is illustrated in Figure 3-11. The dimensions were selected based on ASTM E8M-04 guidelines. As weld zone has higher tensile strength in comparison to the parent metals, a NTS test is expected to give more information on the fusion zone compared to traditional tensile test experiments [3, 130]. The samples were tested in the plane perpendicular to the direction of welding line at room

temperature of 20ºC. Instron Universal Electromechanical testing machine was used with a gauge length of 25mm and crosshead speed of 5mm/min, and sampling rate of 10 points per second. Load-Displacement graph was plotted and the maximum load and stress was estimated from the curve. In order to avoid systematic errors, three samples were tested for each experimental condition, and the average values were used.
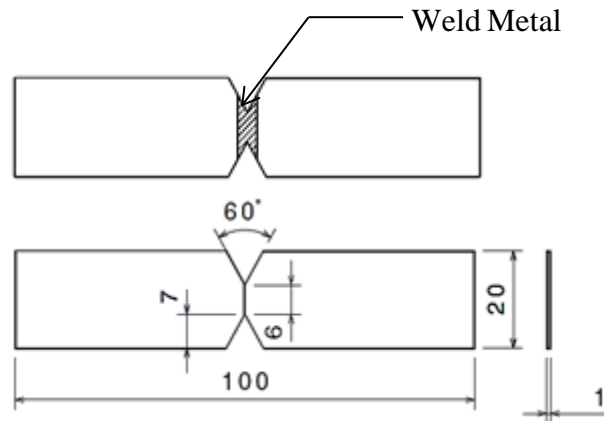
Figure 3-11 Notched tensile test sample with dimension

In this research, a two colours pyrometry with the temperature ranging 772K-2272K was used to measure the substrate temperatures during the laser dissimilar welding. Pyrometry is a non-contact temperature measurement technique based on the working principle; every material above the absolute temperature emits radiations which are dependent on the temperature of that particular material. The radiated energy is interpreted to calculate the temperature of the material being measured. Two colours pyrometer measures the radiations using two different wavelengths, the ratios of the signal and finally calculate the temperature. The emissivity is eradicated during calculations; hence the calculation of temperature becomes independent of emissivity.

3.5   Design of experiments (DoE)

Dissimilar laser welding is a complex process involving multiple input parameters. In most experimental investigations the weld quality is assessed based on its response to variation of one process parameter at a time [136]. This requires a large number of experimental runs and therefore can be expensive with respects to both the process and the material requirements. Also, studying the interaction effect between two process

parameters is a challenging task with this approach.

Statistical analysis as a scientific approach has been diversely used in experimental research studies not only to minimise the experimental runs but also to optimise the quality criteria [3, 128, 132]. Statistical analysis allows all main effects as well as their interactions to be analysed using minimum number of experimental runs. The statistical design of experiments can be tailored based on the ideal number of experiments (i.e. sample size), the suitable order of experimental runs (depending on the experimental system and its limitations) and confirming whether or not blocking or other randomisation restrictions are involved. This is therefore effective both in terms of the material usage and the study time, mainly, for laser welding of dissimilar metals which is primarily a multi-parameter process [134, 201]. Prior to actual experimentation, beads on plate welding were performed to estimate the appropriate ranges for the laser parameters. These ranges were then used in the statistical analysis. The experiments were thereafter implemented according to the statistical design. The experimental results were measured and recorded as responses. This was then followed by analysis of variance (ANOVA). This method reduces the window of process parameters which was then employed for detailed analyses on the given system. A summary of the experimental procedure is given in Figure 3-12.
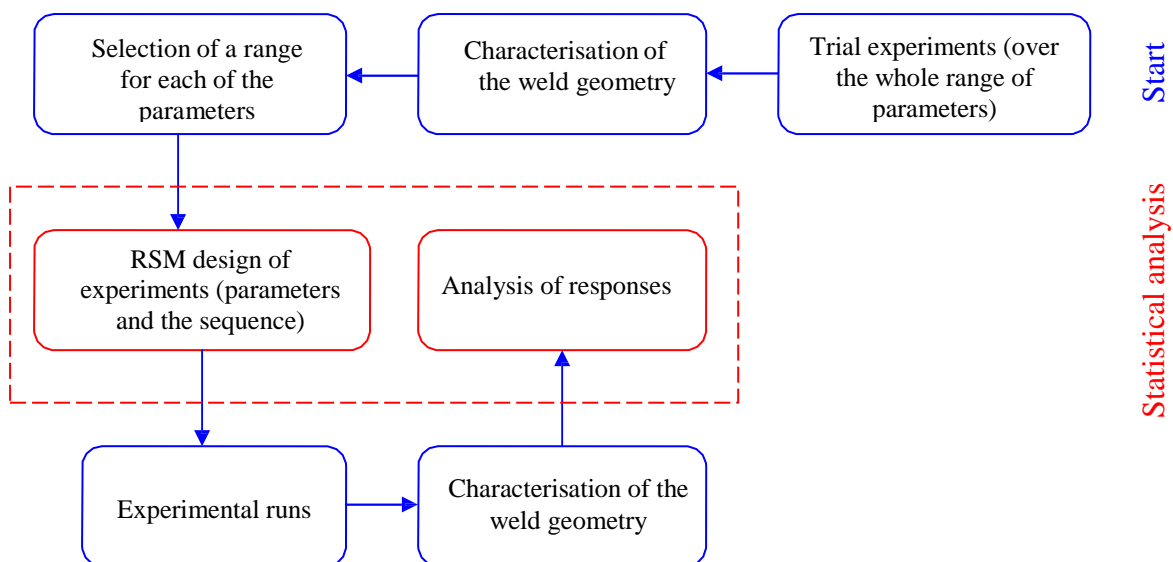
Figure 3-12 Sequential procedure of experimental investigations

82

Response surface methodology (RSM)

In general, the various statistical design methods which can be employed based on the application are as follows:

- Mixture design: employed for analysing the sensitivity of responses when the process factors are complementary to each other and combine to a fixed total.
- Factorial design: employed mainly for studying the important factors, however, the method is also able to model and refine the process.
- Crossed design: employed for investigating the effect of both mixture components and the process factors on the responses.
- Response surface method (RSM).

The response surface method (RSM) designs are predominantly beneficial in associating the quality criteria in response to process parameters while it is envisioned to meet a set of requirements for several responses at the same time. Since one of the main purpose of this study is to optimise different quality criteria (including minimised heat affected zone, thermal stresses, and maximised weld width), RSM can be effectively employed. In this investigation, central composite design (CCD) was employed. CCD is based on three groups of design points namely centre, factorial and axial design points. These points are highlighted in Figure 3-13 which typically illustrate the CCD for n=3 factors (n is the number of independent variables or factors).
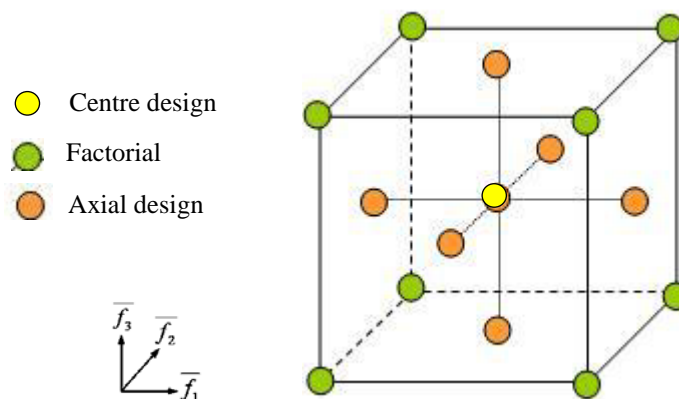
Figure 3-13 Central composite design points for three factors (i.e. f_1, f_2, f_3)

Centre design points:

The centre points are the midpoints of all factor ranges, therefore, the coded level for all of the factors is set to 0 (i.e. α'=0). The centre points are usually repeated 4 to 6 times to achieve a reasonable estimation of experimental error (pure error).

Factorial design points:

These groups of design points are including all the possible combinations of the +1 and −1 levels of the factors. Therefore, the number of the factorial design points can be obtained from:

$$k = 2^n \qquad\qquad E.q(2)$$

where k is the number of points in the factorial part of the design and n is the number of process factors in the analysis. For the three factors (i.e. f_1, f_2, f_3) these points would be:

$$(f_1, f_2, f_3)$$
$$\in \{(+1,+1,+1),(+1,+1,-1),(+1,-1,-1),(-1,-1,-1),(-1,-1,+1),(-1,+1,+1),$$
$$(+1,-1,+1),(-1,+1,-1)\} \qquad E.q(3)$$

Axial design points:

Axial design points specify the midpoint (i.e. α'=0) for all of the factors except one of them which +α' or -α' is considered. The number of axial design points is therefore twice the number of independent factors (i.e. 2 n). Hence, for a three-factor analysis, the axial design points are:

$$(f_1, f_2, f_3)$$
$$\in \{(+\alpha',0,0),(-\alpha',0,0),(0,0,-\alpha'),(0,0,+\alpha'),(0,+\alpha',0),(0,-\alpha',0)\} \qquad E.q(4)$$

The value of α' in the design is obtained by rotatability and orthogonality. Rotatability is used for maintaining the variation of the predicted response constant in the model and at a given distance from the centre of the design. In contrast to rotatability, orthogonality ensures that the variables can be calculated independently, where there would then be no correlation between the experimental levels of the independent variables. The central composite design may be made rotatable by suitable selection of axial spacing so that:

$$\alpha' = (k)^{0.25} \qquad\qquad E.q(5)$$

After employing the design and running the experiments, the responses would be measured and studied by regression techniques. The model for the given response (η_r) is of second order, represented as [134] :

$$\eta_r = \beta_0 + \sum_{j=1}^{k} \beta_j \chi_j + \sum_{j=1}^{k} \beta_{jj} \chi^2{}_j + \sum_{i<j} \sum \beta_{ij} \chi_i \chi_j \qquad \text{E.q(6)}$$

Where η_r is the predicted response, β_0 is the response at the centre of experiment, β_j is the ith linear coefficient of main effects, β_{jj} is the coefficient of quadratic effects and β_{ij} is linear by linear interaction effects [202]. The β regression coefficients provided in the equation are estimated by applying the least squares method and then finalized by a stepwise regression technique [202].

In the next step, the fitted surface is employed to conduct the response surface analysis. In all scenarios, modelling was initiated with a second order model as this includes the interaction, and also quadratic terms of independent variables. Applying this method, any non-linearity or curvature in the response would be included. In a case of non-suitable non-linearity in the model, it will be reduced to first order.

The responses were developed depend on the response surface method and multiple regression analysis. The effects of the independent variables were analysed using mathematical modelling and the significance of the parameters were investigated by analysis of variance (ANOVA).

3.6   Summary

In this chapter an experimental setup for evaluating the dissimilar laser welded joint between carbon steel and stainless steel technique has been introduced; the setup includes facilities and developed systems designed to improve the welding performance. This chapter also introduced statistical techniques as an efficient method to minimise the number of experiments and investigate the interrelation between the laser processing parameters and dissimilar weld's geometry.

Chapter 4 Weld Bead Geometry and Surface Topology in Laser Dissimilar Welding

4.1   Introduction

This chapter discuss the influences of key process variables on dissimilar weld bead characteristic (i.e. weld bead width, surface topology and HAZ width). Statistical techniques were used to investigate the effect of parameters on CW CO_2 laser welding of carbon steel and stainless steel. The results of this chapter will act as a guide for subsequent fundamental study on dissimilar laser welding including, temperature and fluid flow dynamics analysis, and investigation on microstructural transformation.

In laser welding process the parts to be joined are locally melted by an intense laser beam, followed by a solidification process as the beam moves away. The mechanical strength and microstructure of such joints strongly dependents on many factors including size/shape of the weld bead, weld bead topology and size of the nearby heat affected zone (HAZ). One of the main advantages of laser welding is its relatively narrow and smooth weld bead geometry. Weld bead geometry is a critical quality factor that can significantly influence the final mechanical properties (e.g. tensile and fatigue properties) and microstructures. To keep track of the weld bead geometry and other properties, it is necessary to have a thorough understanding of the key laser welding parameters and its effects on the laser weld quality.

Recently, there is an increased need across range of industries for joining of dissimilar materials. Being a highly controlled process, laser welding has an excellent potential in producing high quality dissimilar joints. The two main requirements for successful dissimilar welding are both the metals should melt to form a metallurgical joint, and that the joint should meet the mechanical property criteria imposed by service conditions. The difference in properties (like melting temperature and thermal diffusivity) that usually exists in dissimilar welding makes it very difficult to fulfil even the first criterion by conventional welding processes with low energy density

[62]. In welding of dissimilar metals, high energy-density beams like lasers offer several advantages including ease of melting of metals even with different melting points, narrow fusion and heat affected zones.

This chapter studies the effect of key process variables on dissimilar weld bead characteristic (i.e. weld bead width, surface topology and HAZ width). The process parameters have direct impact on the thermal cycle of the fusion zone, resulting microstructure, and consequent mechanical properties. Statistical techniques were used to analyse the influence of interaction parameters for CW CO_2 laser welding of carbon steel and stainless steel. The prediction of the optimal combinations of the welding parameters is performed with an objective of minimizing the HAZ width, with optimal penetration and weld width. The key process variables and its range obtained from this chapter will act as a foundation for further in-depth analysis on dissimilar welding including, weld pool convection, weld pool diffusion and microstructure phase transformation.

4.2   Previous work

Experimental analysis in laser welding had received noticeable attentions during the past decades and they are broadly reported in literature [8, 88, 122, 128]. Many studies on welding had used statistical techniques to analyse the interaction effects between two or more parameters (e.g. inert gas pressure, processing speed, laser power, beam incidence angle, and focal position) and find the key process variables. Unlike welding of similar materials, laser dissimilar welding is a highly nonlinear process and the interaction effects of parameters significantly affects the final characteristics of weld [8, 131, 134, 135]. Based on experimental analysis, many researchers found that laser power and welding speed are the key process variables that significantly control the weld bead geometries. They [128, 135, 137] also concluded that; welding speed is the most influential parameter with the reverse effect on weld pool geometry (bead dimensions, width and the area); higher inert gas pressure can creates welding geometry defects; laser power has a direct impact on all investigated weld bead characteristic; laser focal position has less impact on weld pool geometry although it can increase the weld area and weld width [9]. Some researcher discussed the weld geometry based on weld width to depth ratio [83, 203]. Their studies revealed that, increasing the laser

power or decreasing the welding speed lead to higher penetration depth. They justified their conclusion base on the fact that increasing the laser power has a direct impact on the laser power density and decreasing welding speed has inverse impact on energy input. As a result, high power density or high energy input can change the laser welding mode form conduction welding to predominantly keyhole welding, which in turn causes higher penetration depth. The penetration depth also depends on the surface element composition and surface tension (which will be discussed in following chapters). As noted from literature, most of the researchers have considered laser welding speed and laser power as the main factors which defines the weld geometry, however a recent investigation [136] claimed that the depth of penetration depends predominantly on the power density and specific point energy while the weld width depends mainly on welding speed. Benyounis et al. [204] have used statistical approach RSM to study the effect of laser welding parameters (laser power, welding speed and focal point position) based on four responses (heat input, penetration, bead width and width of HAZ) in CO_2 laser butt-welding of medium carbon steel plates of 5mm thick. They found that the heat input plays an imported rule in the weld-bead parameters; welding speed has a negative effect while laser power has a positive effect on all the responses.

The importance of weld bead geometry on mechanical behaviour of dissimilar laser welded joints (low carbon steel to austenitic stainless steel) is investigated broadly in literatures. Torkamany et al. [4] found that in lap welding of the dissimilar welds (stainless steel on top and mild steel on bottom), increasing the laser power can result in an increase in the load bearing capability. This is mainly attributed to the increase in fusion zone size of low carbon steel sheet.

The surface topology of the weld is another key factor which has significant effects on the performances of the welded joined [105, 205]. The commonly accepted good weld bead geometry is to have a section of the weld bead slightly above the parent material surface; though in some cases these are machined flat to the surface after the welding [105]. For some applications, a flat weld bead surface may be desirable for precision assemblies, removal of surface stress raisers, application of surface coatings, lowering the resistance to fluid flows (for pipes and vessels), better corrosion protections and

cosmetic effects etc. Li et al. [105] introduced a new concept in laser welding i.e. net shape welding, whereby the weld bead is flat to the parent material surface (for both the face and the root) within the welding process.

Fluid flow dynamics of molten pool during melting and solidification significantly controls the weld surface topology and geometry. The fluid flow dynamics inside the melt pool and the subsequent solidification of weld dependents significantly on the thermal cycle. The thermal cycle is again influenced by the process parameters (e.g. power density, interaction time and subsequent energy input) and surface active elements [88, 144, 206] .

Many researchers carried out experimental and numerical analysis to study fluid flow and consequent surface topology [68, 85, 207, 208]. The weld bead geometry on the top and bottom surfaces of laser net shape welded joint is investigated by Li et al. [105]. They reported that the shape of melt pool is determined by the welding speed and oxygen content and that the weld bead shape can be depressed, bulged or flattened after solidification base on the level welding speed.

4.3   Experimental procedure

A high power CO_2 (10.6µm wavelength) laser system was used for this investigation. The maximum power output of the system is 1.2kW and the focal point beam diameter was maintained at 0.5mm. The samples used in the analysis were cold rolled low carbon steel (BS EN 10130) and austenitic stainless steel (AISI 316L) sheets. The samples are positioned in a butt shape on a fixture and clamped firmly. A coaxial nozzle assembly with an exit diameter of 4mm was used to direct the beam. The nozzle to workpiece stand-off distance was maintained constant at 2mm. The size of each workpiece was 50mm by 50mm with 1mm thicknesses, and is mounted on an X-Y axis CNC table (Figure 4-1). In order to provide enough time for CNC table to accelerate and stabilized, welding were started 20mm way from the fixture edge. The welded samples were sectioned and then analysed using optical microscope. The measurement of the weld and HAZ width is obtained on cross section from the top of weld boundary on the carbon steel side as per the methodology explained in chapter 3. (See chapter 3 for the details of the optical analysis procedure). Shielding of the

molten pool from oxidization is achieved by using pure argon gas (99%). The gas pressure and mass flow rate were kept constant at 1.5bar and 2.5l/min respectively. Prior to the welding, the sample was cleaned using acetone to avoid any contamination.

Figure 4-1 Experimental setup used for laser welding

The experiments in this chapter are divided in to two parts, the first part concentrates on the effect of laser power, welding speed, specific point energy and beam position on weld width, heat affected zone (HAZ) width. In the second part, statistical analysis was performed to find the most important parameters which influences each respond (weld width and HAZ width) and also the interaction of the process parameters on the weld geometry.

4.3.1   Design of experiment

A statistical analysis employing response surface methodology (RSM) was developed to further optimise the process. A three steps approach was employed to obtain more realistic results. The first step is to choose the appropriate experimental range for experimentation. This was accomplished by performing a set of bead-on laser welding experiments to find the working range of each parameter. The second step is to develop a polynomial model which fits to the obtained experimental data through regression analysis, and the third step, is to define the value of factors satisfying the optimum conditions (the criteria for optimum condition is explained in chapter 3). In this study, central composite design (CCD) with five levels was used. The total obtained number of experiments was 30 and is obtained through the following equation [209]:

$$Total\ run = 2^k + 2k + n_0 \qquad\qquad E.q(1)$$

where k is the number of independent factors.

The first term on the Eq. (1) (2^k) refers to the factorial runs, the second term (2k) refers to the number of axial runs and the third term (n_0) represents the number of replicated runs. Initial trials (bead-on-plate welding) were used to assess the range of feasible welding parameters, with the objective of obtaining full penetration. The parameters and their levels used for laser welding experimentation are shown in Table 4-1.

Table 4-1 Process parameters with design levels

Variable	Notation	Unit	-2	-1	0	1	+2
Laser power	P	[W]	300	500	650	700	800
Welding speed	S	[mm/s]	5	10	15	20	25
Beam position	B	[mm]	-0.4	-0.2	0	0.2	0.4
Gas pressure	G	[bar]	0.5	1	1.5	2	2.5

To predict the curvature of responses, the behaviour of weld geometry were described by an empirical second-order polynomial. The typical form of such a polynomial is:

$$\eta_r = \beta_0 + \sum_{j=1}^{k}\beta_j\chi_j + \sum_{j=1}^{k}\beta_{jj}\chi^2_{\ j} + \sum\sum_{i<j}\beta_{ij}\chi_i\chi_j \qquad\qquad E.q(2)$$

Where η_r is the predicted response, β_0 is a constant, β_j is the ith linear coefficient, β_{jj} is the ith quadratic coefficient, β_{ij} is the ith interaction coefficient, χ_j is the independent variable, and k is number of factors. In addition, the coefficients of the model are predicted through regression. Details of the parameter estimations for such a model are reported elsewhere [209, 210].

4.4   Results and discussion

To evaluate the effect of laser parameters (variables) on the dissimilar weld bead characteristic, experiments were performed based on the design matrix of CCD with six central point replications. The design points and experimental results for weld geometry are shown in Table 4-2.

Table 4-2 Central composite design experiment matrix and experimental results for this study

Run	Laser power (W)	Welding speed (mm/s)	Beam position (mm)	Gas pressure (bar)	HAZ width (mm)	Weld width (mm)
1	500	15	0	1.5	0.302	1.009
2	400	20	0.2	1	0.226	1.008
3	300	15	0	1.5	0.15	0.76
4	400	20	-0.2	2	0.217	1.02
5	600	10	-0.2	2	0.52	1.58
6	600	10	+0.2	1	0.471	1.22
7	400	10	+0.2	1	0.5	1.44
8	500	15	0	2.5	0.236	0.996
9	700	15	0	1.5	0.41	1.11
10	500	15	0	1.5	0.34	1.1
11	500	15	0	1.5	0.308	1.005
12	600	20	+0.2	2	0.253	0.6
13	500	15	0	1.5	0.309	1.003
14	400	20	-0.2	1	0.26	1.1
15	500	25	0	1.5	0.189	0.753
16	600	10	+0.2	2	0.284	1.194
17	400	10	+0.2	2	0.346	1.37
18	400	20	0.2	2	0.209	0.84
19	500	15	0	0.5	0.335	1.15
20	600	20	-0.2	1	0.278	1.01
21	500	15	+0.4	1.5	0.266	1.1
22	500	15	0	1.5	0.305	1.03
23	600	10	-0.2	1	0.53	2
24	400	10	-0.2	2	0.347	1.3
25	500	5	0	1.5	0.68	1.76
26	600	20	+0.2	1	0.261	0.816
27	400	10	-0.2	1	0.364	1.32
28	500	15	-0.4	1.5	0.29	1.22
29	600	20	-0.2	2	0.26	0.971
30	500	15	0	1.5	0.31	0.996

4.4.1   Effect of laser power on the weld bead characteristic

As explained in Chapter 2, laser power is an important factor in characterising the weld bead shape. The welding mode and consequent weld bead shape has direct relation to laser power [18].

Figures 4-2 shows the effect of laser power on the weld width. Figure 4-3 illustrates the corresponding optical microscopic image at three power levels of 300W, 500W and 800W. As can be observed, increase in laser power result in increased weld bead width. However, the rate of increase was prominent at the earlier stage and gradual at higher power levels. This was caused by reduced heat transfer between the melt pool and surrounding metal at higher power levels. Increase in laser power result in increased temperature difference between workpiece surface and the bulk of metal, which results in more heat transferred via conduction and convection to the parent metal. This causes bigger melt pool, which subsequently defines the weld width and area. The heat transfer continues to rise with increased laser power until the power reaches a threshold where the temperature difference between the molten region and surrounding mushy zone becomes small. The small difference in temperature will cause less heat transfer via conduction; hence increasing the laser power at that high level doesn't significantly change the weld bead characteristics [18, 25, 131, 211].
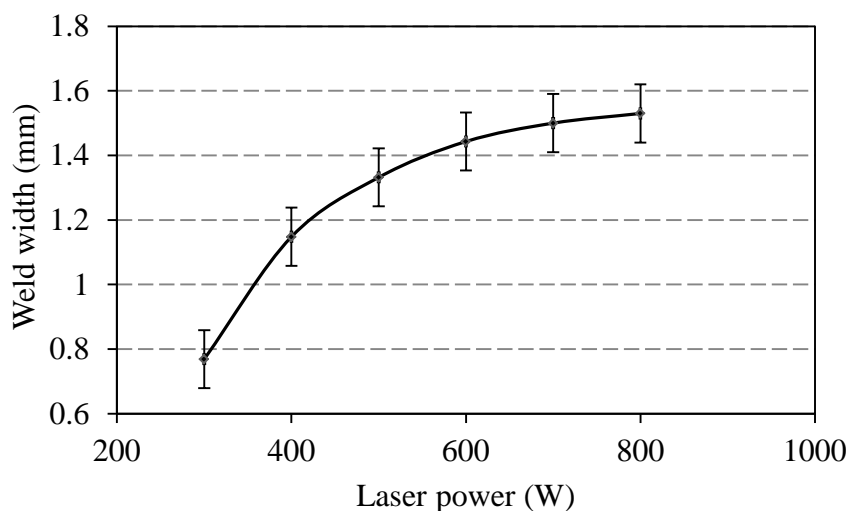
Figure 4-2 Effect of laser power on weld bead characteristic (focal position 0, gas pressure 1.5bar, gas flow rate 1.5lit/min)

(a)   (b)   (c)
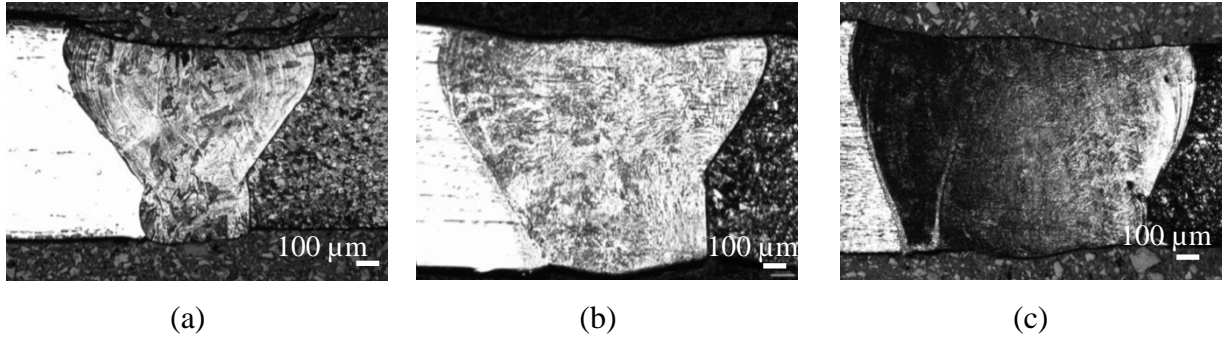
Figure 4-3 Effect of laser power on weld width and weld area (a) Power 300W (b) Power 500W and (c) Power 800W (welding speed 15mm/s, focal position 0mm, gas pressure 1.5bar, gas flow rate 1.5lit/min)

Figure 4-4 show the effect of laser power on HAZ width and Figure 4-5 illustrates the corresponding optical microscopic image for laser powers of 300W, 500W and 800W respectively. HAZ is the region that undergoes grain growth and grain refinement. Due to the non-transformable nature of stainless steel, significantly narrower HAZ width was noticed in stainless steel compare to low carbon steel. Hence, all the HAZ reported in this chapter corresponds to low carbon steel. As can be seen from the figure, increase in laser power result in more heat to be conducted from molten pool to the parent metal and consequently wider HAZ.
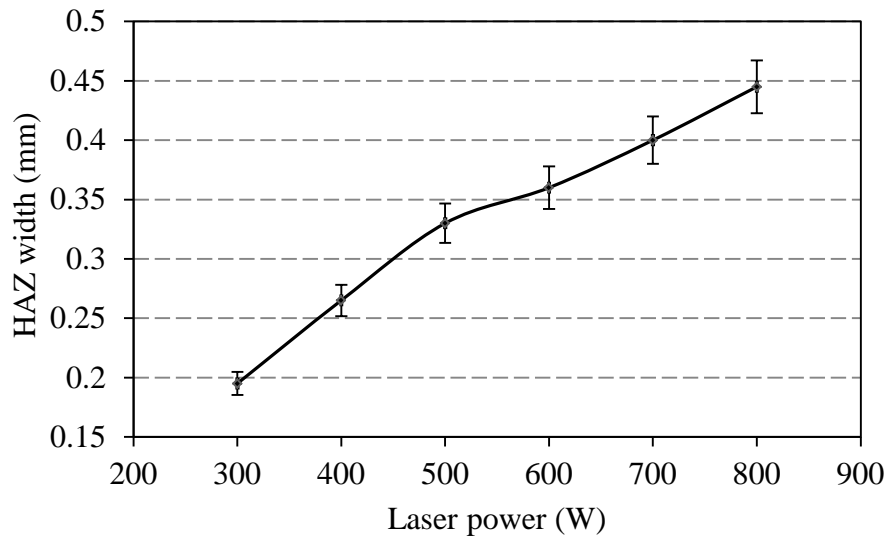
Figure 4-4 Effect of laser power on HAZ width

(a)   (b)   (c)
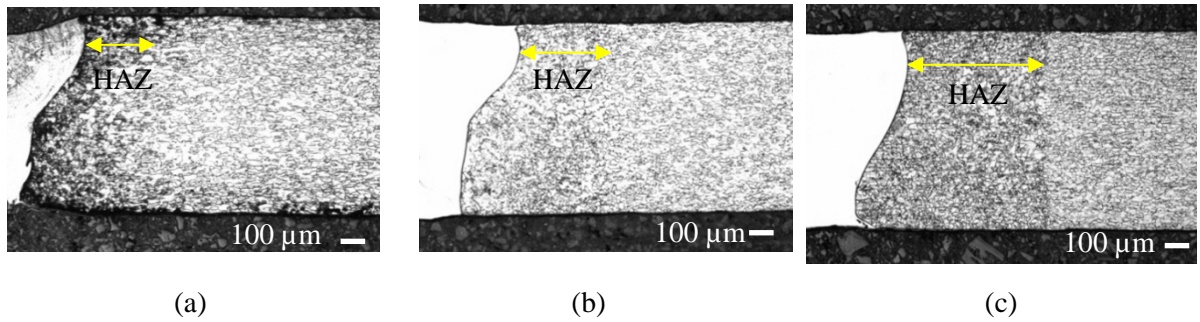
Figure 4-5 Effect of laser power on HAZ width (a) power 300W (b) power 500W and (c) 800W (welding speed 15mm/s, focal position 0mm, gas pressure 1.5bar, gas flow rate 1.5lit/min)

4.4.2   Effect of speed on the weld bead characteristic

Welding speed is another major process parameter that significantly influences the laser welded joint. Many researcher have addressed the welding speed influence on the fluid flow dynamics within the molten pool and consequent weld bead geometry [18]. In the case of dissimilar welding of carbon to stainless steel, the research on the effect of this factor is limited.

The laser input energy at the workpiece surface changes with welding speed. Figures 4-6 shows the effect of welding speed and resulting interaction time on the weld width. The interaction time is calculated based on the ratio of beam diameter (0.5mm) to welding speed. Figure 4-7 illustrates the optical microscopic image for various welding speed (10mm/s, 17mm/s, and 35mm/s).

The size of the weld width decreases over the range of 5–20mm/s of welding speed and beyond 20mm/s speed it is observed that the fluctuation in the dimensions of weld width lies within a significantly smaller range. This was caused by lower convective heat transfer between the melt pool and surrounding metal at higher speed levels. The results indicate that at high welding speed, the process condition is close to the threshold of creating the fusion zone. As welding speed decreases the weld width increases. This is possibly due to increase in heat input per unit length. The high temperature gradient (as a result of high heat input) enhances the convective fluid flow which causes a predominating outward flow that transports the heat from the centre to the weld periphery and cause a significantly wider weld width [95]. Note that the rate

of increase in weld width is prominent at lower welding speed (higher interaction time) which might be attributed to the higher fluid flow and heat convection at higher interaction time.
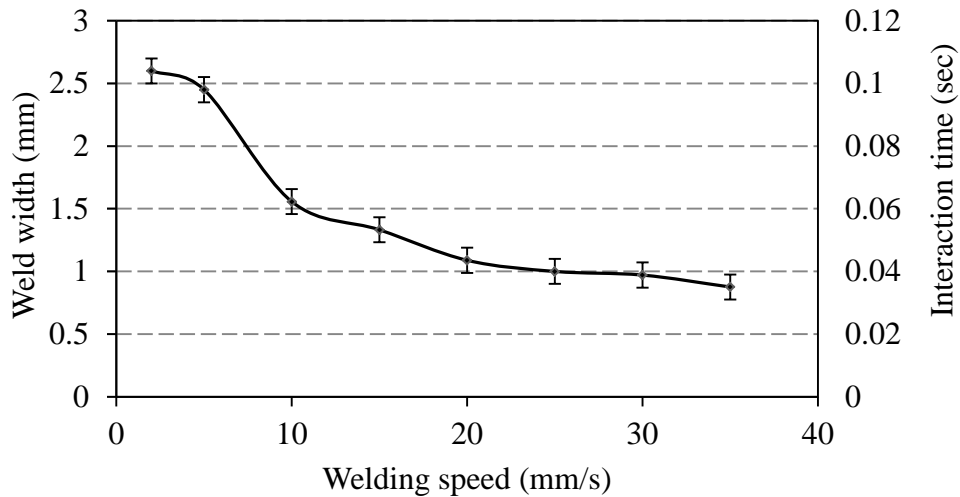
Figure 4-6 Effect of interaction time as a consequence of changing welding speed on weld bead characteristic

(a)   (b)   (c)
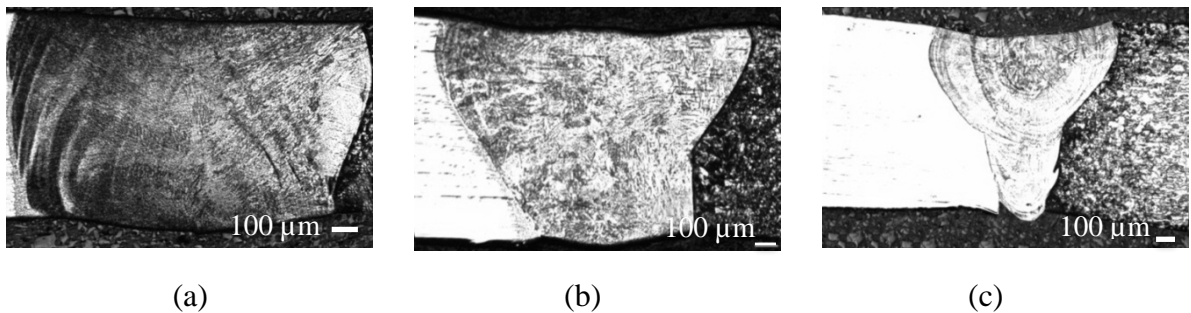
Figure 4-7 Effect of welding speed on weld width (a) 10mm/s (b) 17mm/s and (c) 35mm/s (welding power 500W, focal position 0mm, gas pressure 1.5bar, gas flow rate 1.5lit/min)

Figures 4-8 shows the effect of welding speed on the HAZ width and Figure 4-9 illustrates the optical microscopic image for various welding speeds (5mm/s, 10mm/s, and 17mm/s). As can be seen from the figure, the width of the heat affected zone decreases with increase in welding speed. That is attributed to shorter interaction time between laser and HAZ as a result of higher welding speed. As a result of higher welding speed, the time that HAZ region experiences peak temperature will decrease and the rate of the change of grain size (grain growth) decreases. On the other hand at

lower welding speed, the HAZ will be exposed at high temperature (above austenitiing temperature 800°C) for a longer period of time which in turn causes grain growth in the heat affected region [212].
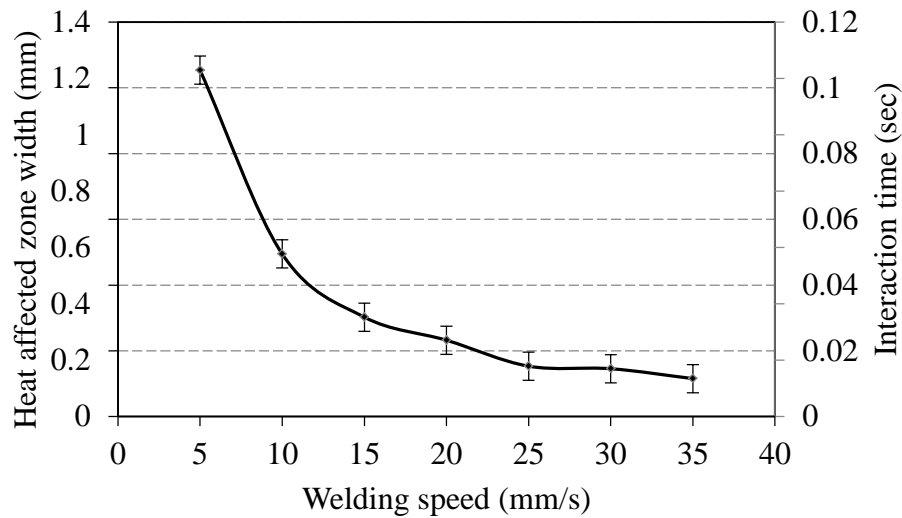
Figure 4-8 Effect of speed on HAZ width

(a)   (b)   (c)
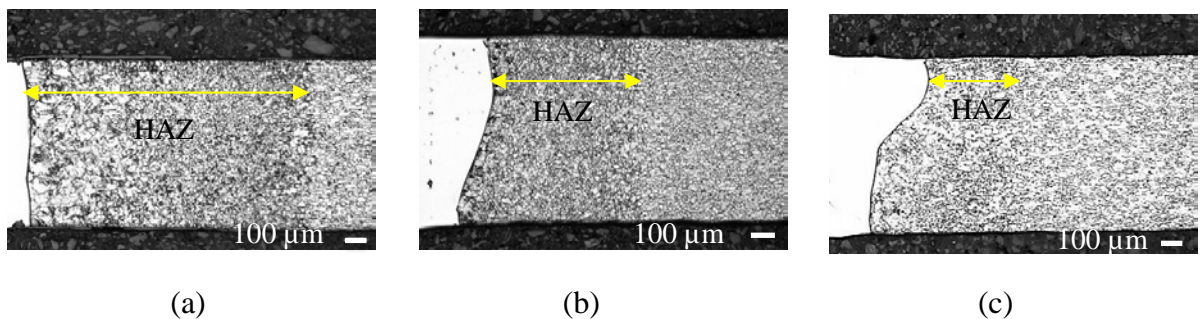
Figure 4-9 Effect of welding speed on HAZ width (a) 5mm/s (b) 10mm/s and (c) 17mm/s (laser power 500W, focal position 0mm, gas pressure 1.5bar, gas flow rate 1.5lit/min)

4.4.3   Effect of specific point energy on the weld bead characteristic

Considering laser welding as an impulsive process characterised by the interaction time, the amount of energy delivered to the irradiation zone can be defined in terms of specific point energy [136]. Specific point energy significantly affects thermocapillary forces in the melt pool and subsequent weld bead morphology by changing the main driving force for fluid flow [5, 136]. Specific point energy is defined as the integral of laser beam intensity and interaction time over the diameter of the laser spot given by:

$$E_S = \iint I(x,y).t_i dxdy \qquad\qquad\qquad\qquad E.q(3)$$

where $I(x,y)$ is energy intensity distribution along x and y, t_i is the interaction time (s) (proportional to spot diameter divided by welding speed) [213]. Assuming uniform power density and interaction time, the specific point energy can be written as:

$$E_S = P.t_i \qquad\qquad\qquad\qquad\qquad\qquad E.q(4)$$

where P is laser power (W). Specific point energy is expected to have effects similar to laser power and interaction time.

Figure 4-10 illustrates the optical microscopic image of the weld bead morphologies for the specific point energies of 10J, 17J and 50J (two extreme level of energy and one with moderate level). As it can be seen form the figure the weld bead morphology noticeably changes with specific point energy. This is mainly attributed to the influence of specific point energy on melt pool fluid dynamics.

| (a) | (b) | (c) |
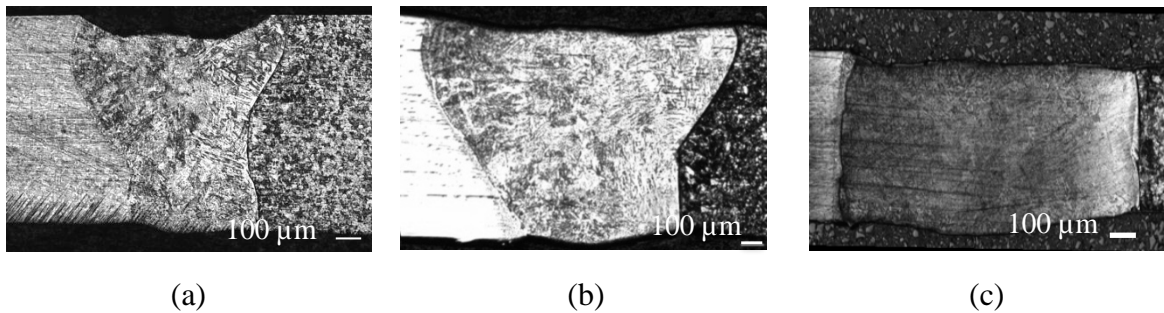
Figure 4-10 Effect of specific point energy on weld beam morphology (a) 10J (b) 17J (c) 50J

Figure 4-10(a) shows the weld bead geometry for low specific point energy of 10J. Note that there is a depression on the top surface of the weld. That might be due to substantial difference between high fluid flow velocity at the surface and low fluid flow velocity in bulk's molten pool, result in an accumulation of the liquid metal at solidification front (liquid- solid interface) [95, 141, 214, 215]. Figure 4-10(c) shows the weld bead surface shape at high specific point energy (50J). The shape of the weld is almost flat with no significant depression or bulged shape after solidification. Such a flat shape might be attributed to the low gradient of the fluid flow velocties across the weld from the center to the weld periphery. Having high specific point energy leads to a bigger molten pool which provides longer time for high molten velocity to stabilize

hence the gradient of the fluid flow velocities is expected to be lower for high specific point energy compared to low energy, resulting in more flat shape weld.

Specific point energy of 17J seems optimal in terms of weld bead geometry, HAZ width and surface topology. Figure 4-10b shows the most common surface topology among the welded samples with optimum processing parameters. As noted from Figure 4-10(b), the surface is not flat; it has a wavy shape with small hump at the middle of the weld bead. The small hump can be attributed to the low pressure zone created by the interference of two fluid flows with clockwise and counter clockwise direction [139]. The formation and explanation of weld bead shape depends on many other parameters and it cannot be explained based on pure experimental analysis. Hence in the following chapters, a numerical model will be used to perform an in depth study on the effect of welding parameters on weld bead morphology.

4.4.4   Effect of beam position on the weld bead characteristic

Beam power of 500W, scanning speed of 15mm/s and argon pressure of 1.5bar were employed to investigate the influence of beam position on the weld geometry. The proposed parameters provide sufficient fusion zone and penetration to the parent metals. The concept of beam position with regards to the weld seam of the two butt plates is given in Figure 4-11.
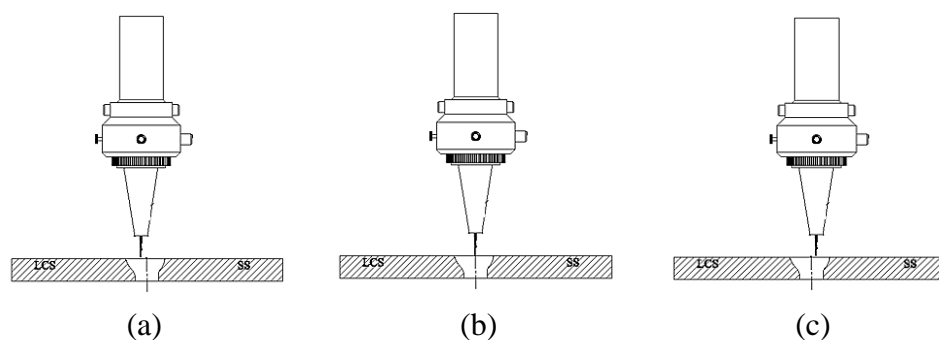
Figure 4-11 Concept of beam position with regards to weld centreline (a) beam position toward carbon steel (b) beam position at the centre and (c) beam position toward stainless steel

The beam position with reference to the middle of the joint is expected to have significant effect on the weld bead characteristic in laser dissimilar welding. Since the shape of the fusion zone is asymmetrical (due to the different in thermal conductivity and absorptivity of the dissimilar materials), shifting the beam toward either side can provide the chance to compensate any undesirable weld geometry [4, 122, 127].

Figures 4-12 illustrates the effect of beam position on the weld width. Positive sign means the beam is positioned toward low carbon steel while negative sign indicates that beam is positioned toward stainless steel.
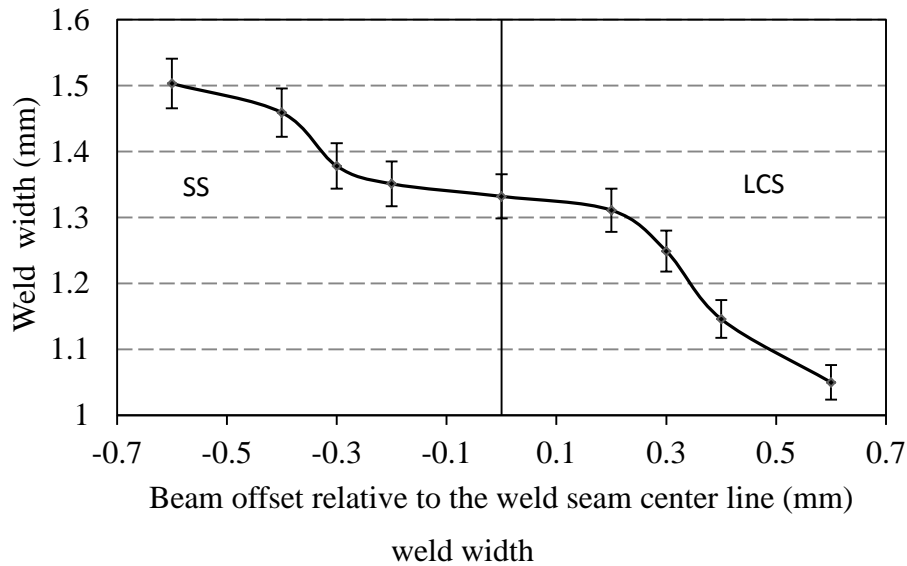
weld width

Figure 4-12 Effect of beam offset on weld bead characteristic

As seen from the figure, moving the beam towards stainless steel, result in increased weld width. This is attributed to significantly low thermal conductivity of stainless steel compared to low carbon steel which causes a larger fusion zone and wider weld bead. The low thermal conductivity of stainless steel results in more heat to be accumulated in the molten pool, causing a larger weld width [191]. Figure 4-13 shows the corresponding optical microscopic image on the effect of beam offset position (-0.3mm, 0 and 0.3mm).

(a)   (b)   (c)
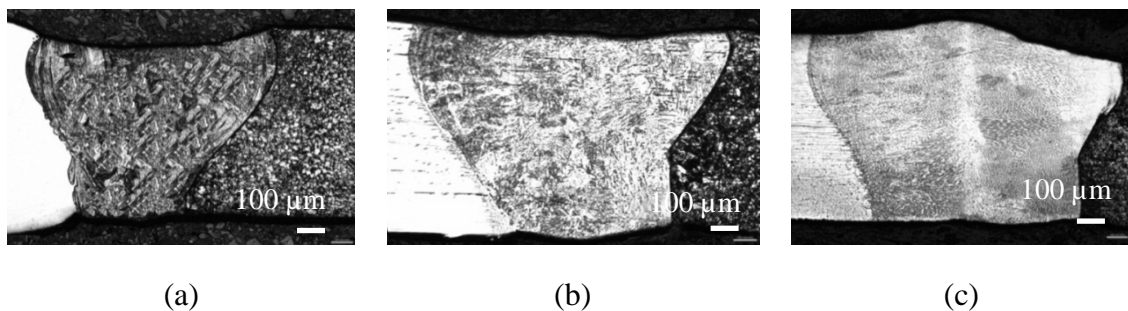
Figure 4-13 Effect of beam positioning on weld width and weld area (a) +0.3mm toward carbon steel (b) 0mm at the centre of weld seam and (c) -0.3mm toward stainless steel (welding speed 15mm/s, laser power 500W, focal position 0mm, gas pressure 1.5bar, gas flow rate 1.5lit/min)

The HAZ width is also affected by shifting of laser beam toward either side of the weld seam. Figure 4-14 shows the influence of the beam position on the size of HAZ in stainless steel and low carbon steel. As it can be seen from the figure, the rate of increasing the HAZ size by offsetting the beam is significantly lower in stainless steel compared to low carbon steel. That is mainly due to solution-annealed condition of the as received stainless steel which restricts the grain growth in stainless steel compare to low carbon steel [122, 216]. It can also be noticed that positioning the beam toward stainless steel leads to narrower HAZ width in low carbon steel which is due to less conducted heat toward carbon steel. Figure 4-15 illustrates the corresponding image for the variation of HAZ width with respect to beam position using three offset position +0.3mm, 0, and -0.3mm.
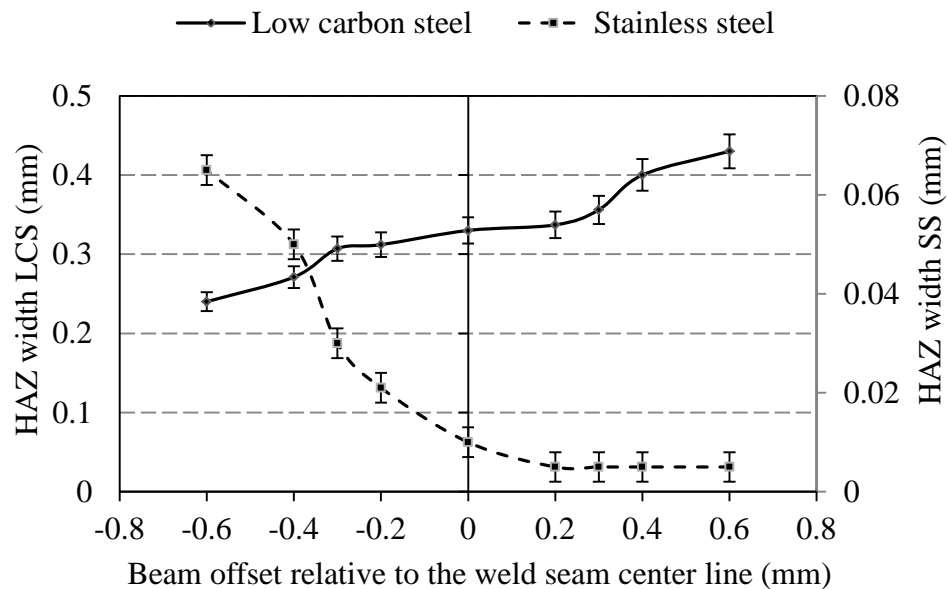
Figure 4-14 Effect of beam offset on HAZ width of the low carbon steel side

(a)   (b)   (c)
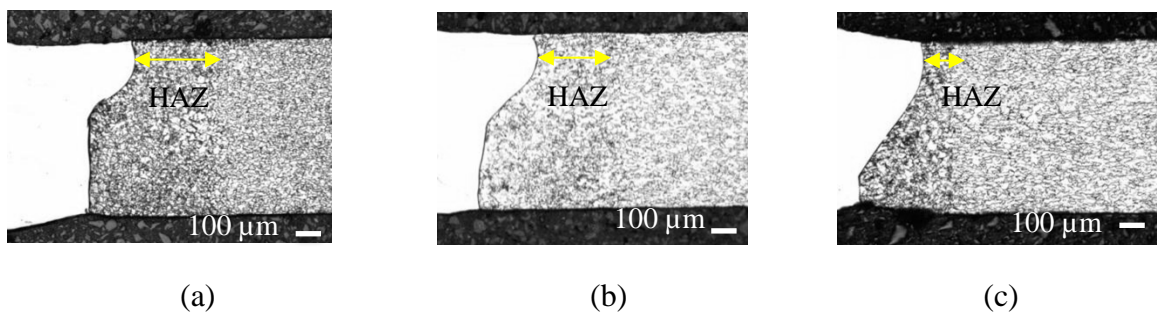
Figure 4-15 Effect of beam offset on HAZ width (a) +0.3mm toward mild steel (b) 0mm at the centre and (c) -0.3mm toward stainless steel (laser power 500W, laser power 500W,focal position 0mm, gas pressure 1.5bar, gas flow rate 1.5lit/min)

101

4.4.5 Statistical analysis of results

The test for significance of the regression models, the test for significance on individual model coefficients and the lack-of-fit test were performed using the Design-Expert statistical package. By selecting the step-wise regression method, which eliminates the insignificant model terms automatically, the resulting ANOVA Tables 4-3 and 4-4 summaries the analysis of variance of each response and shows the significant model terms. The same table also demonstrates the other adequacy measures R^2, adjusted R^2 and predicted R^2. The entire adequacy measures are close to 1, which is in reasonable agreement and indicates adequate models. The adequate precision compares the range of the predicted value at the design points to the average prediction error. In all cases the value of adequate precision are dramatically greater than 4. The adequate precision ratio above 4 indicates adequate model discrimination [217]. It is worth mentioning that the F value in ANOVA table is determined by term mean square divided by residual mean square. Prob>F: Probability of seeing the observed F value if the null hypothesis is true (there is no factor effect). Values of Prob> F lower than 0.05 shows that individual terms in the model have a significant effect on the response [119].

Table 4-3 shows the ANOVA table for weld width. The result shows that welding speed (WS) is the most influencing parameter, followed by the laser power (LP). It is also noted that the interaction of welding speed and laser power (LP×WS) or laser power and beam position (BP) are also the significant model terms. The final regression model for the weld width is:

Weld width $=1.04+0.029LP-0.25WS+0.086BP+0.056GP-0.071LP\times WS+0.10WS\times BP+0.068\ WS^2+0.044BP^2$

Table 4-3 ANOVA table for weld width with reduced quadratic model

Source	Sum of squares	df	Mean square	F value	p-value (Prob > F)
Model	2.23	8	0.28	21.47	< 0.0001
LP	0.18	1	0.18	13.54	0.0087
WS	1.54	1	1.54	118.47	< 0.0001
BP	0.02	1	0.02	1.54	0.2279
GP	0.076	1	0.076	5.83	0.051

102

LP×WS	0.081	1	0.081	6.21	0.0212
WS×BP	0.17	1	0.17	13.1	0.0016
WS^2	0.13	1	0.13	10.12	0.0045
BP^2	0.055	1	0.055	4.21	0.0529
Residual	0.27	21	0.013		
Lack of Fit	0.048	6	0.0008	0.330	0.891
Pure Error	7.62E-03	5	1.53E-03		
Cor Total	2.5	29			
R^2 = 0.8910, Adjusted R^2 =0.851, Predicted R^2 =0.7228, Adequate Precision=19.331					

The interaction effect of laser power and welding speed on weld width at constant gas pressure, focal position, beam spot size and gas flow rate is shown in Figure 4-16. It is clear from the result that reduction of welding speed and increases in laser power leads to a wider weld width. The decrease in welding speed and increase in laser power results in more energy per unit length transferred to the materials which in turn leads to a wider and bigger molten pool size [133].
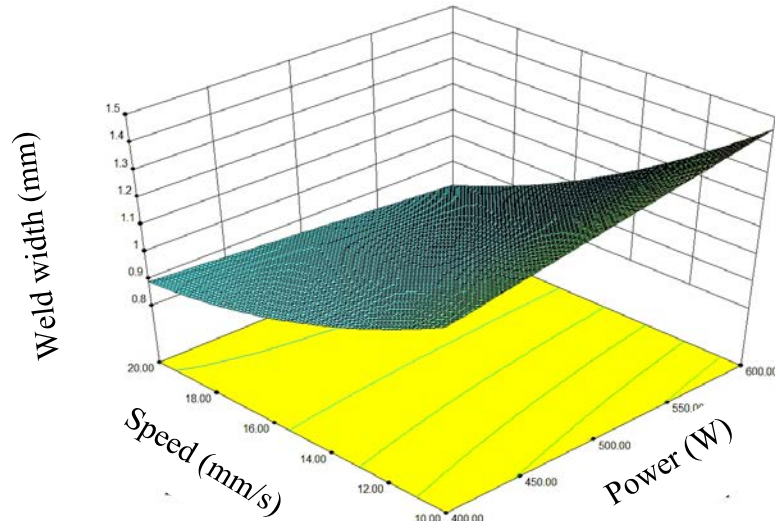
Figure 4-16 Variation of welding width responses in terms of laser power and welding speed (focal position 0mm, gas pressure 1.5bar, beam position at centre)

The welding speed and laser power also have a significant effect on the HAZ width. As can be seen from the ANOVA table, (table 4-4), welding speed and laser power were the two significant factors. Figure 4-17 shows the effect of welding speed (WS) and laser power (LP) on HAZ width with a constant gas pressure (1.5bar), focal (0mm) beam position (BP) (at centre). Increase in power and decrease in welding speed result in increase of melt pool temperature and subsequently higher HAZ width. Moreover the interaction effect of the laser power (LP) and beam position (BP) also has significant influence on the HAZ width. Hence, regarding to the analysis, and process parameters, the final regression model for the HAZ width is:

HAZ width $=0.91844+3.00480\text{E-}004 \times \text{LP} - 0.035484 \times \text{WS} - 0.36069 \times \text{BP} - 0.040461 \times \text{GP} + 8.06797\text{E-}004 \times \text{LP} \times \text{BP} + 7.17565\text{E-}004 \times \text{WS}^2$

Table 4-4 ANOVA table for HAZ width with reduced quadratic model

Source	Sum of squares	df	Mean square	F value	p-value Prob > F
Model	0.16355	6	0.027258385	22.88111988	< 0.0001
LP	0.021669	1	0.021669199	18.18946851	0.0030
WS	0.116873	1	0.116873384	98.1053701	< 0.0001
BP	0.001751	1	0.001750867	1.469705604	0.2377
GP	0.009823	1	0.009822758	8.245378261	0.0086
LP×BP	0.004166	1	0.004165902	3.496923956	0.0743
WS^2	0.009268	1	0.009268199	7.779872848	0.0104
Residual	0.0274	23	0.001191305		
Lack of Fit	0.012852	8	0.002491763	0.990	0.5436
Pure Error	0.000548	5	0.000109656		
Cor Total	0.19095	29			
R^2 = 0.8565, Adjusted R^2 =0.8191, Predicted R^2 =0.7285, Adequate Precision=19.256					
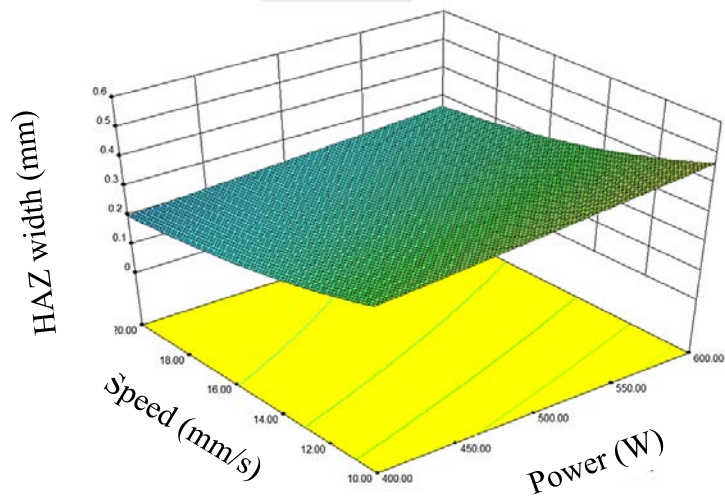
Figure 4-17 Variation of HAZ width response in terms of laser power and welding speed (focal position 0mm, gas pressure 1.5bar, beam position at centre)

It can be also noted from ANOVA table 4-4 that positioning of the laser beam has significant influence on final geometry of the weld. The variation of weld width and HAZ width against welding speed and beam position at constant gas pressure, focal position, beam spot size and gas flow rate is shown in Figure 4-18 (a and b).
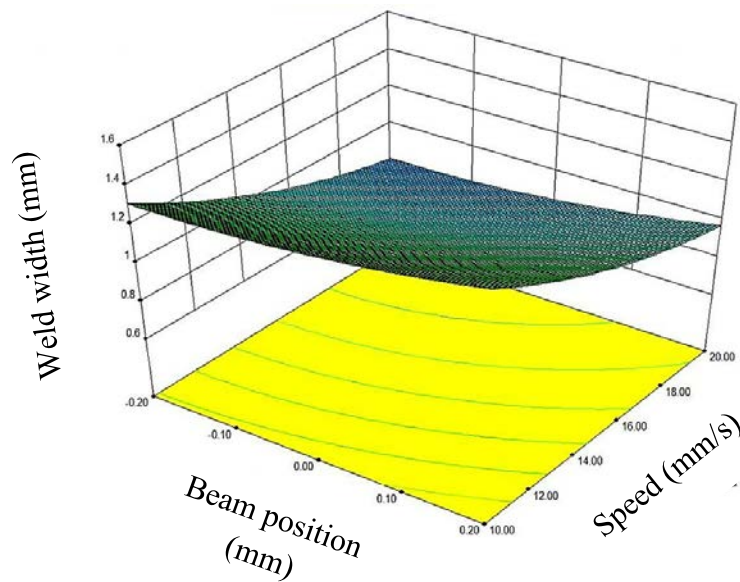
(a)
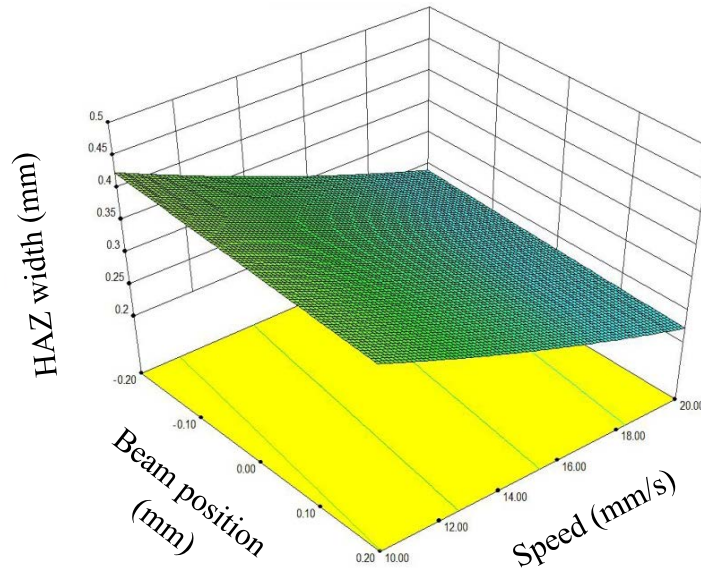
(b)

Figure 4-18 Interaction effect of speed and beam position in weld bead characteristic (a) on welding width (b) on HAZ width (focal position 0mm, gas pressure 1.5bar)

As noticed from the results, decrease of welding speed and positioning the beam toward stainless steel cause a wider weld width. This is attributed to the higher energy per unit length (due to decrease in welding speed) which is transferred to the material and form a wider weld bead. Also positioning of beam toward stainless steel leads to high energy over less conductive material (SS) which in turn leads to wider and bigger molten pool [160].

4.5   Summary

This study presents quantitative analysis of the parameters which affect laser material interaction (i.e. weld bead width, surface topology and HAZ width). The most influential parameters on welding characterisation are determined, and the following conclusions have been drawn:

1. Welding speed and laser power were found to be the most important factors in laser dissimilar welding. Decrease in welding speed and increase in laser power lead to higher weld width and HAZ width; however the relationship between the mentioned parameters and weld geometry is not linear.

2. Specific point energy has a major effect on surface morphology of the weld bead.

A significant increase in specific point energy results in a flat weld bead surface while very low energy leads to weld bead with concavity shape and ripple at solidification boundary.

3. Beam offset has a major effect on the weld and HAZ width. A shift in beam offset from -0.6mm to 0.6mm with a constant laser power, beam position, and gas pressure results in a decrease of weld width from 1.5mm to 1.05mm and an increase of HAZ width in low carbon steel side from 0.24mm to 0.44mm.

4. Regression models of the effect of welding speed, laser power and beam position on the quality characteristic have been developed. The model predicts the results to reasonable agreement. Based on these models a good understanding of physics of the laser material interaction, in terms of the quality of the weld and the significant parameters that affect the weld quality can be obtained. It is noted however, that this doesn't consider the fusion zone microstructure or alloying distribution.

Chapter 5 Diffusion Phenomena and its Effects in Dissimilar Laser Welding

5.1   Introduction

This chapter reports on an experimental investigation carried out to understand and subsequently control the alloying composition in laser welding of austenitic stainless steel (SS) and low carbon steel (LCS). An X-ray energy dispersive spectrometer was used to analyse the alloying composition, while the microscopy and tensile test was used to study the microstructural characters and mechanical performance of the welded joint respectively. The importance of specific point energy and laser beam alignment on melt pool convection and dilution was investigated, so as to obtaining a weld bead with characteristics most suitable for industrial applications. Strategies to control the composition leading to dramatic changes in hardness, microstructure and mechanical properties of the dissimilar laser welded joint are discussed.

Joining of dissimilar materials like low-carbon steel and stainless steel has excellent potential in various industrial applications due to its ability to produce tailor-engineered properties at reasonable cost. The demand for such joints in industry is continually expanding; for example, boilers & heat exchangers [111] (due to higher operating temperature of superheaters and hot steam pipes, it is required to use dissimilar joints to control the manufacturing cost and increase the service performance), power plants [111] (high pressure pipes uses dissimilar ferritic-austenitic joints), hydraulic valves (manufactured from nonmagnetic stainless steel and mild steel tubular parts [218]). Recently, the potential of dissimilar metals has drawn wide attention from automotive industries for manufacturing of light weight car bodies [4]. Despite the wide spread advantages, laser dissimilar welding of stainless steel and low carbon steel is challenging due to the immense differences in thermo-mechanical properties of the materials (e.g. thermal expansion, thermal conductivity, latent heat of fusion). This can lead to uneven alloying composition in the fusion zone, brittle microstructure in the weldbead and subsequent deterioration of the mechanical performance of the joint.

In this present investigation, the effect of laser specific point energy (which is a function of laser power; speed and beam size) on dilution, alloying element concentration, hardness, between two metals, and weld microstructure variation in fusion zone is discussed. The dissimilar weld failure mechanism was analysed and the effect of dilution and alloying element (which depends on the laser specific point energy) on joint strength was studied for dissimilar laser welding and discussed for the first time.

5.2   Previous work

In dissimilar laser welding, the joint performance is significantly influenced by the composition and microstructure of the weld bead. The most common issues with the dissimilar LCS-SS laser weld joint includes, phase transition in the fusion zone (FZ) (from austenitic to martensitic phases) [9, 82, 130, 219, 220], uneven distribution of alloying elements across the weld [9], crack formation & distortion due to difference in thermal expansion coefficient [82, 122], low toughness and ductility in the joint due to the uneven of phase transformation [130, 219, 221] and low corrosion resistance due to variation of alloying elements across the weld [12].

The above mentioned problems can result in significant deterioration in ductility of the weld and its service performance. Therefore a robust methodology is needed to predict and control the phase transition in dissimilar laser welding. Many researchers have in the past attempted to address the issues with dissimilar laser welding. Recent researchers also have highlighted the paramount importance of alloying elements concentration and dilution on the microstructure and mechanical performance of low carbon-austenitic stainless steel [4, 122, 158]. Sun and Moisio [82] studied the influence of laser welding parameters including air gap (the distance between two butt welded plates) and laser beam alignment on austenitic/ferritic dissimilar joints. They also discussed the reliability of controlling alloying elements and the consequent microstructure across the fusion zone via optimizing air gap. Sun demonstrated that the air gap size can significantly influence the delivered heat input to the substrate. They finally concluded that the dilution from low alloyed steel substantially influenced the final microstructure.

As discussed in literature (chapter 2), the laser dissimilar welding was extensively studied by various researchers and most of the earlier studies on laser dissimilar welding, concentrated on optimising and analysing of the laser welding parameters [116, 127, 191, 218, 222]. Until now, however the significance of thermo-physical conditions in the dissimilar laser welded melt pool (of carbon steel and stainless steel) has not been fully investigated. In particular, the mechanisms to control the melt pool dynamics and dilution, so as to achieve a full penetration, a homogenous fusion zone and a predominantly austenitic microstructure. It's paramount to understand the basic mechanisms in laser dissimilar welding including, diffusion of alloying elements across the fusion zone, variation of cooling rate and consequent microstructures, and the laser welding parameters that influences the fusion zone. It is worth mentioning that the experimental results and analysis needs to be coupled with a fundamental analysis (of diffusion; cooling rate; melt pool convection) to have a wider picture of the underlying mechanism inside the melt pool. These fundamental mechanisms will provide valuable information's, which will help to increase the control over the welding process and overcome the existing challenges. Despite of broad investigations on the similar and dissimilar laser welding of these steels, there are limited studies in literature which addresses the significance of the basic fundamentals.

5.3   Experimental procedure

The base materials used in this chapter were low carbon (BS EN 10130) and austenitic stainless steel (AISI 316L). The chemical compositions and thermal conductivity of the low carbon steel and the stainless steel are given in chapter 3. The yield strength and ultimate tensile strength of LCS sheet were 270 and 410MPa, respectively. The corresponding values for SS sheets were 330 and 600MPa, respectively [223].

Laser welding was performed using a continuous wave CO_2 laser with a maximum laser power of 1.2KW. Argon gas was used for protecting the melt pool form oxidization. Trial experiments were used to find the feasible operating range for joining low carbon and austenitic stainless steel. The beam diameter was set to 0.5mm on the workpiece surface and the laser stand-off distance was set to 5mm above the workpiece. The laser power, interaction time, beam position and consequent input energy were varied in the subsequent investigation. As discussed in chapter 3, a butt

joint configuration (Figure 5-1) was used for joining the dissimilar metals, the size of each metal plate were 50mm x 50mm with 1mm thicknesses.
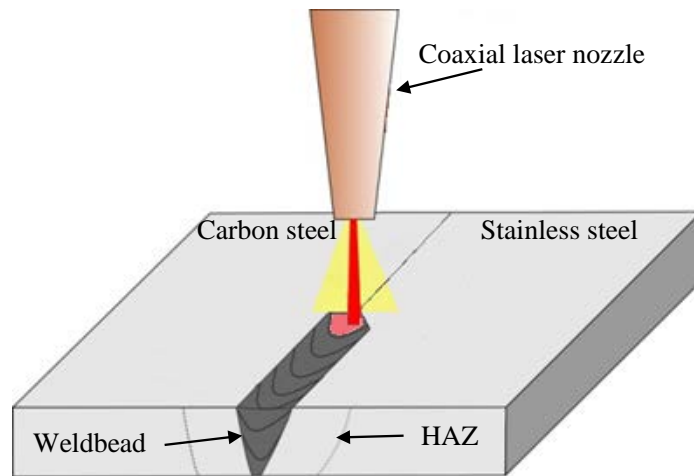
Figure 5-1 Schematic diagram of a laser dissimilar welding process

The amount of energy that is delivered to the workpiece plays major role [136] in thermal cycle, fluid dynamics and consequent microstructure of fusion zone. Besides laser power density and heat input, specific point energy is one of the effective parameters on the melt pool fluid flow regime and microstructure [136]. Specific point energy can be defined in terms of the specific point energy (SP) which is defined by the relation:

$$Specific\ Point\ Energy = \frac{P \times D}{V}$$
E. q (1)

where P is the laser power, D is the laser beam diameter and V is the welding speed. In addition, since welding speed has a substantial effect on the weld bead characteristic [105], the energy applied to the dissimilar fusion zone was altered based on the welding speed. Initial trials were used to assess the range of feasible welding parameters, with the objective of obtaining full penetration. The process parameters used for experimentation are given in table 5-1.

Table 5-1 Laser dissimilar welding parameters use in present investigation

Experiment No.	Laser power (W)	Welding speed (mm/s)	Focal position (mm)	Specific point energy (J)	Gas pressure (bar)	Beam offset (mm)
1	500	30	0	8.3	1.5	0
2	500	25	0	10	1.5	0
3	500	20	0	12.5	1.5	0
4	500	15	0	17	1.5	0
5	500	10	0	25	1.5	0
6	500	5	0	50	1.5	0
7	500	15	0	17	1.5	0.6
8	500	15	0	17	1.5	0.4
9	500	15	0	17	1.5	0.2
10	500	15	0	17	1.5	0
11	500	15	0	17	1.5	-0.2
12	500	15	0	17	1.5	-0.4
13	500	15	0	17	1.5	-0.6

Separate experiments were also performed to understand the significance of beam positioning on the melt pool. The beam position was shifted toward each side by up to 0.6mm. A special fixture was designed and fabricated to position the metal plates in a flat position during welding process.

For analysing the weld microstructure, standard metallographic samples were prepared according to ASTM E3-11 standards [196] and as of mentioned in chapter 3. The etchants were applied sequentially to the weld region and after re-polishing of the weldment to avoid any interference of etchants on revealing the microstructure of each region in the dissimilar joint. A typical laser welded sample is shown in Figure 5-2.
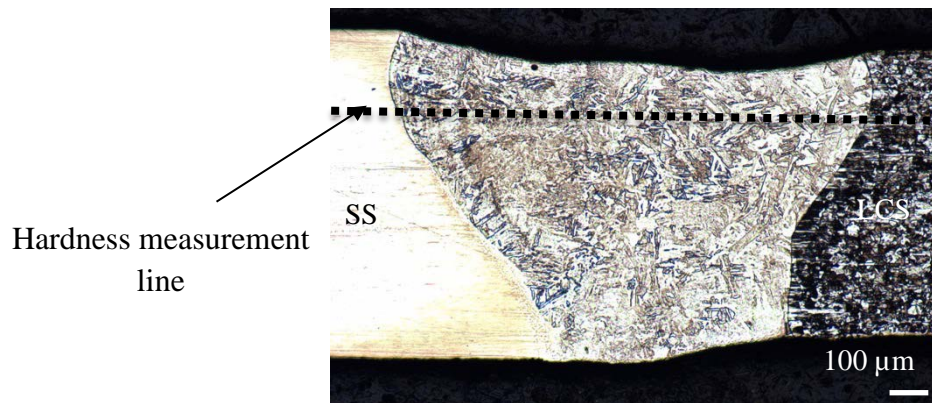
Figure 5-2 Typical weld bead cross section

As shown in Figure 5-2, hardness was measured on the weld cross section (across the weld metal with offset value of 200µm from the centre line toward both low carbon and stainless steel side) applying 50g load on Buehler KV400 micro-hardness tester. The microstructure of the dissimilar joint was investigated using optical microscopy. In addition and as discussed in chapter 3, compositional variation and alloying element diffusion across the dissimilar weldment were analysed using a scanning electron microscope (SEM) equipped with an energy dispersive spectrometer (EDS). Notched tensile strength (NTS) samples [200] were prepared from the laser welded samples and according to chapter 3 to study the mechanical properties of the weld bead.

In general, during welding of low carbon steel to stainless steel, efforts must be taken to control the formation of martensite microstructure within the fusion zone. The martensitic transformation is a diffusionless solid-state shear deformation. In steels, martensite is made from austenite containing carbon atoms and, as a result of the diffusionless nature of its formation, it preferably receives the carbon atoms of the parent austenite. The carbon atoms are trapped in octahedral interstitial sites between iron atoms, creating a body centred tetragonal (bct) structure, and are in super saturation relative to the body centred cubic (bcc) ferrite [163, 165, 224].

As mentioned before, significant martensite formation can result in loss of ductility and can lead to hydrogen-related weld defects [216]. In fact, it is more desirable to have a weld bead rich in austenitic structure. Austenitic weld bead has the advantages of better resistance to hot cracking, higher toughness and work hardening rate, better capability to work hardened, higher ductility, and higher weldability [82]. In addition, dissimilar

113

weld metal must meet the desire mechanical property of the service environment. The mechanical properties of the weld zone should be equal or stronger than the weaker part of the two parent metals.

5.4   Results and discussion

5.4.1   Microstructure and composition in dissimilar laser welding

The mechanical and service performance of the dissimilar joint depends strongly on the weld bead microstructure. The fusion zone microstructure predominantly depends on the solidification behaviour and subsequent solid phase transformation, which are controlled by cooling rate, and weld composition. Moreover the chemical composition in the fusion zone of dissimilar joints mostly depends on the melting ratio and dilution of the two materials to be joined which in turn dependents on the laser process parameters. Figure 5-3 shows a typical weld bead shape and microstructure observed in dissimilar laser welding of low carbon to stainless steel (power = 500W, welding speed = 15mm/s).

Figure 5-3 (a) and (b) illustrates the base material microstructure of stainless and low carbon steel, which is predominantly of equiaxed austenitic (γ) grain and medium sized ferritic (*F*) grain respectively. Figure 5-3 (c) shows the shape of the weld bead and Figure 5-3 (d) illustrates the nucleation of fine equiaxed grain at the fusion zone-parent metal interface. The fusion zone is predominantly of columnar dendrites, which has nucleated at the fusion boundary, and grown towards the centre of the molten pool (opposite to the direction of heat flow). The existence of dendritic structure is predominantly due to the high cooling rate observed in the laser welded melt pool [4].
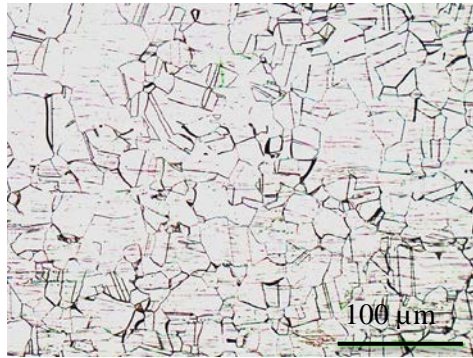
(a) Microstructure of stainless steel consists of austenite grains
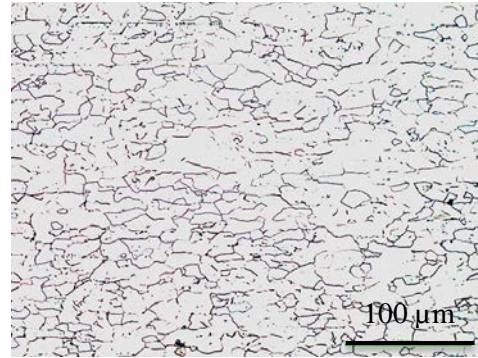
(b) Microstructure of the low carbon steel consists of ferrite
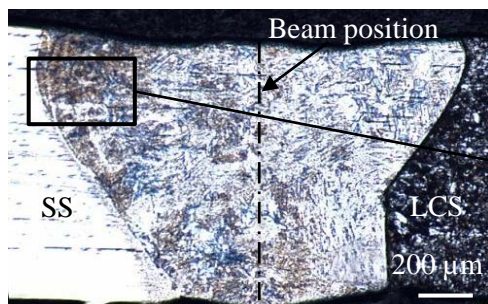
(c) Dissimilar weld bead cross section and microstructure

(d) Magnified image showing growth of columnar dendrites perpendicular to the weld boundary
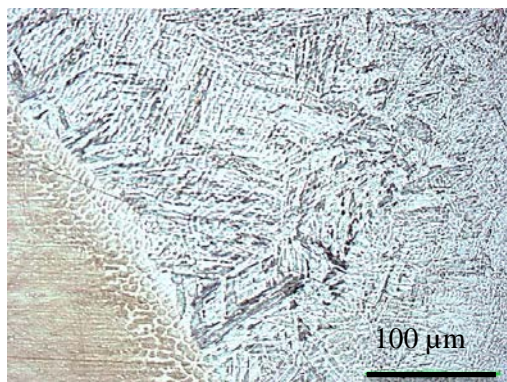
(e) Microscopic structure of HAZ in stainless steel
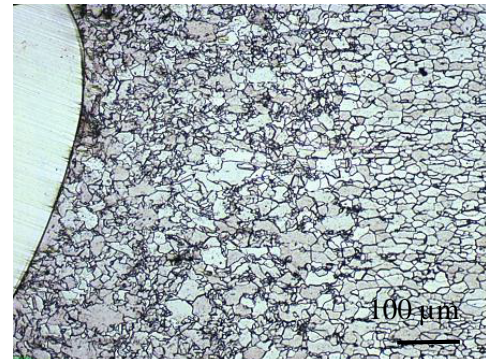
(f) Microscopic structure and grain coarsened HAZ in low carbon steel

Figure 5-3 Typical weld bead shape and microstructure observed in dissimilar welding of low carbon to stainless steel (power = 500W, welding speed = 15mm/s)

As can be noted from Figure 5-3 (c), despite positioning the beam at the centre of the weld seam, the shape of the fusion zone is asymmetrical. Figure 5-3 (e) and (f) show the HAZ in both stainless steel and low carbon steel. As observed, the grain growth and recrystallization occurs in the HAZ of low carbon steel and stainless steel. Within the experimental range considered, the HAZ width is significantly narrower in the stainless steel compared to the low carbon steel due to its low thermal conductivity

(HAZ maximum 70μm for stainless steel and 400μm for low carbon steel respectively). In addition, no phase transformation was observed in the HAZ of stainless steel since the austenitic stainless steel is not transformable [4]. At the specific point energy of 17J (Figure 5-3(c)), the fusion zone has formed such that the stainless steel has melted preferentially to the low carbon steel. This is attributed to the low thermal conductivity of stainless steel (compared to low carbon steel), which results in rapid heating and fast melting at the start of the melt pool formation (before low carbon steel reaches the melting temperature) [122]. This was confirmed by solving the one-dimensional heat equation. The time required to increase the workpiece temperature t_{ref} to melting temperature is given by [106]:

$$t_{ref} = \rho C K \left(\frac{T_m - T_a}{q}\right)^2 \qquad\qquad E.q(2)$$

where ρ, K, C, T_m, T_a and q are material density, thermal conductivity, specific heat, melting temperature, ambient temperature, and laser heat flux respectively. Using materials properties at room temperature, Eq. (2) shows that stainless steel will reach its melting temperature 2.8 times faster than low carbon steel and accordingly can contribute more to the initial melt pool formation. As shown in the Figure 5-4, however, the conductivity of the stainless steel significantly changes at around 1550°C which can result in a non-linear variation of the alloy concentration and melt ratio in the weld bead.
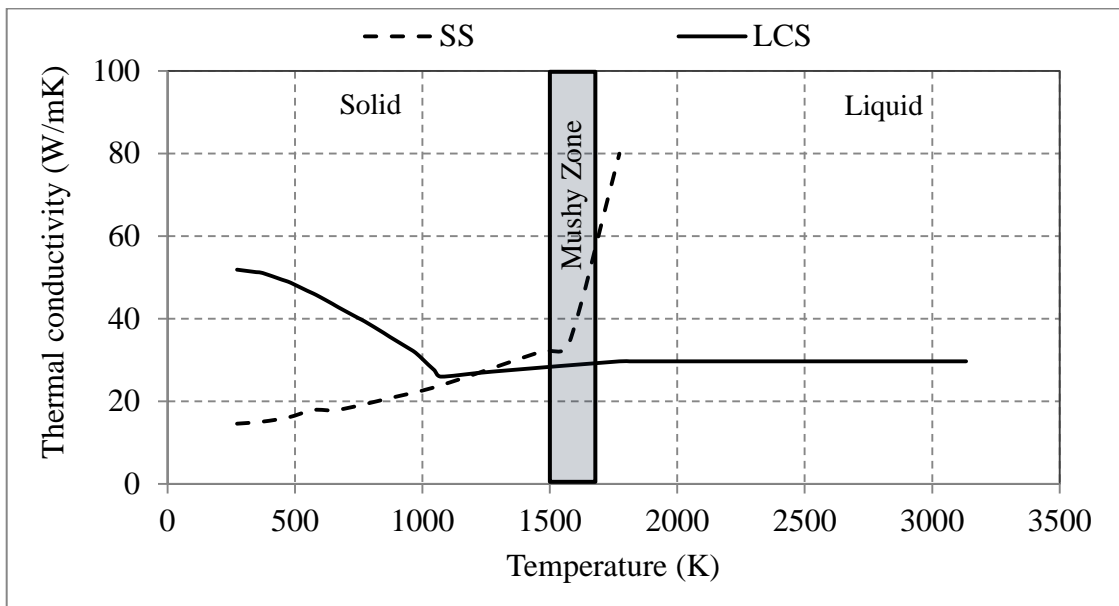
Figure 5-4 Thermal conductivity of stainless steel and low carbon steel [110]

5.4.2 Effect of laser welding parameters on dilution and alloying elements transformation

Figure 5-5 (a) and (b) shows the chemical compositional profile of the weld bead obtained from EDS analyses. As can be seen from the figure, the concentration of alloying elements (chromium (Cr) and nickel (Ni)) decreases in the weldment with increase in specific point energy. This can be explained on basis of dilution of the weld bead. Dilution is defined as the percentage contribution of low carbon steel in the weld fusion zone such that dilution of 30% means that the weld metal contains 30% low carbon steel and 70% stainless steel. Dilutions (D) of the weld bead was determined based on the alloying elements of the weld (obtained by the EDS analysis) and is given by [225]:

$$D = \frac{C_{fz} - C_{fm}}{C_s - C_{fm}}$$ E. q (3)

where C_{fz}, C_{fm}, and C_s are the chemical compositions of weld, stainless steel and low carbon steel, respectively.

(a) (b)
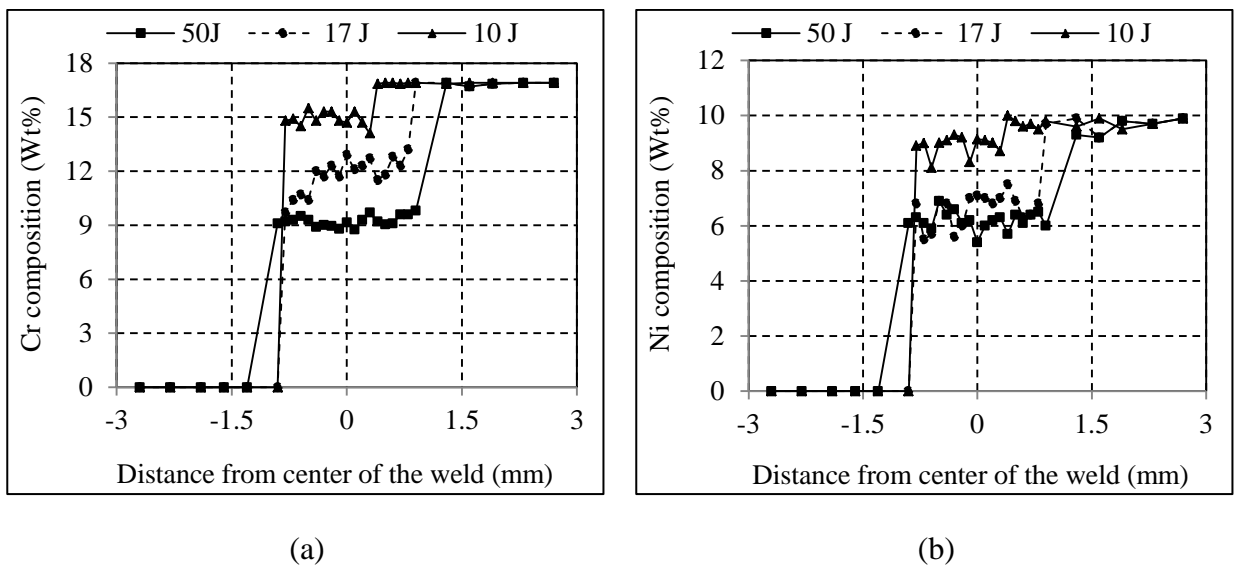
Figure 5-5 Composition of the main alloying element along the weld bead (a) Cr composition, (b) Ni composition

The carbon content of the dissimilar weld was estimated based on the average dilution of the dissimilar weld. The effect of specific point energy on the dilution and consequent alloying elements is given in Figure 5-6 and Table 5-2 respectively. The average chromium and nickel equivalents given in Table 5-2 was calculated on basis of Schaeffler Equivalents given by [82]:

Chromium equivalent (Cr_{eq})   = $\%Cr + \%Mo + 1.5\%Si + 0.5\%Nb$ E. q (4)

Nickel equivalent (Ni_{eq})   = $\%Ni + 30\ \%C + 0.5\%Mn$ E. q (5)

As can be observed from Figure 5-6, dilution of low carbon steel in the weld bead increases with an increase in specific point energy. As the dilution of low carbon steel increases, due to higher energies, the concentration of Cr_{eq} and Ni_{eq} as the main alloying element decreases (Table 5-2) while the concentration of carbon increases (carbon comes mostly from LCS). At higher temperature, as a result of higher specific point energy, the low carbon steel's thermal conductivity decreases while the thermal conductivity of stainless steel increases (Figure 5-4). This results in a greater temperature increase in the low carbon steel and consequently, more dilution of low carbon steel (which has a lower chromium-nickel weight percentage) in the fusion zone. Accordingly, the concentration of alloying elements which can stabilize austenite or ferrite phases decrease in the fusion zone and the weld metal is preferentially transformed to the martensitic phase. The dilution of low carbon steel and its impact on the final microstructure was also analysed in terms of melt pool fluid dynamics which is discussed later in the CFD simulation of fusion zone (Chapter 6).
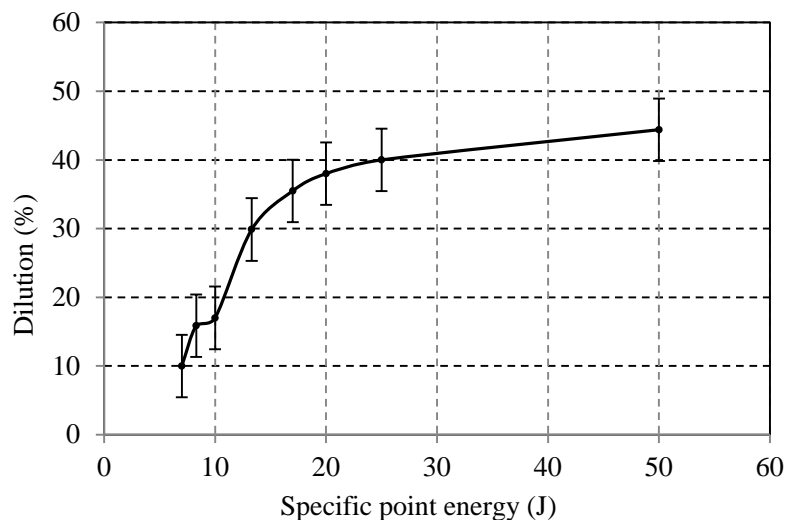
Figure 5-6 Effect of specific point energy on dilution (contribution of LCS to the fusion zone)

118

Table 5-2 Average chromium and nickel equivalents calculated based on Schaeffler equivalents (gas pressure = 1.5bar, beam diameter = 0.5mm)

Specific point energy (J)	Cr_{eq} (%)	Ni_{eq} (%)
8.3	18.1	12.78
10	17.8	11.39
12.5	15.0	9.8
17	14.7	9.6
25	12.5	9.05
50	11.6	8.04

5.4.3   Effect of laser welding parameters on microstructure

The weld bead composition and corresponding microstructure were predicted based as the alloy content (Table 5-2) and Schaeffler diagram (Figure 5-7), and presented in Table 5-3 [4, 82, 218, 226]. The Schaeffler diagram is based on the concept that the alloying elements within the weld zone can be divided into ferrite stabilisers and austenite stabilisers. This means that the elements (e.g. Cr, and Ni) can promote the formation of either ferrite or austenite in the structure. The microhardness value of the fusion zone obtained by experiment (Table 5-3) is in line with the predicted microstructures. There was a significant increase in the hardness values for the specific point energy equal to or higher than 12.5J which corresponds to the formation of martensite phase and is attributed to a higher dilution of low carbon steel. A specific point energy more than 17J results in a complete martensitic phase transformation within the weld bead which is not ideal for applications that requires high toughness and good fatigue performance. This is attributed to the fact that with increase in specific point energy result in more melting of low carbon steel (which has lower chromium-nickel weight percentage) and subsequently more martensite in the fusion zone. Therefore, increasing the dilution of carbon steel leads to a decrease of essential alloying elements for formation of austenitic weld and hence martensitic microstructure are formed in the weld metal.
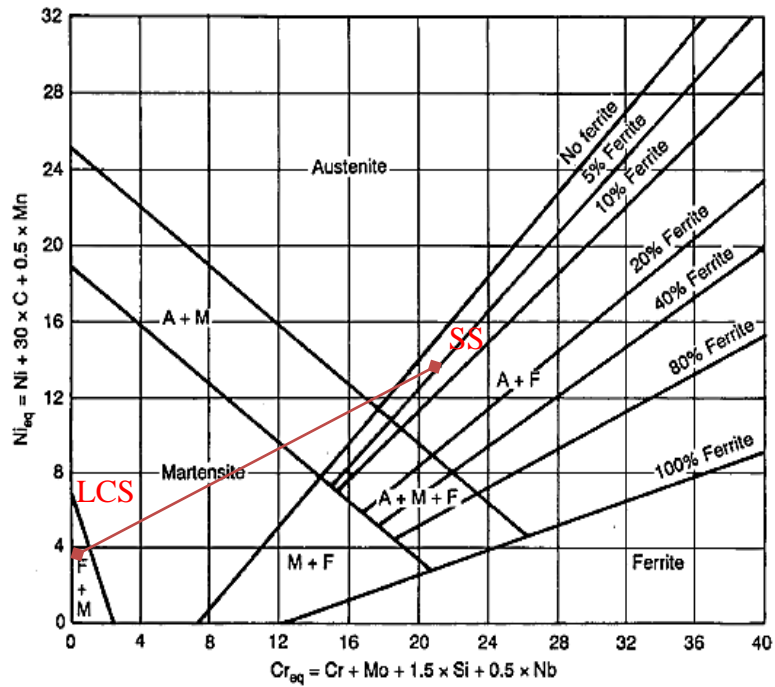
Figure 5-7 Schaeffler diagram predicting the microstructure in the fusion zone [82]

Table 5-3 Effect of specific point energy on weld microstructure

Specific point energy (J)	Microstructure predicted from Schaeffler diagram	Average fusion zone hardness ($HV_{0.05}$)
8.3	A	210
10	A	220
12.5	A + M	310
17	A + M	315
25	M	378
50	M	370
A: Austenite, M: Martensite		
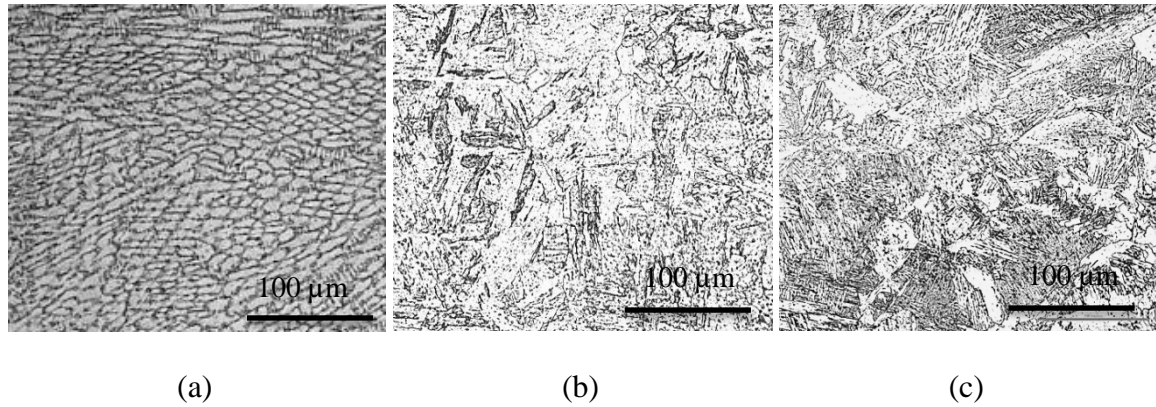
Figure 5-8 Microstructure of the fusion zone (a) Austenitic microstructure for specific point energy of 10J; (b) Martensitic-austenitic microstructure for specific point energy of 17J; (c) Martensitic microstructure for the specific point energy of 50J

The optical microscopy image shown in Figure 5-8 supports the microstructure predicted by the Schaeffler diagram and the microhardness test. Predominantly austenitic microstructure (specific point energy of 10J), duplex microstructure (martensitic-austenitic, specific point energy of 17J) and fully martensitic microstructures (specific point energy of 50J) were observed in the weld bead for various specific point energies, and are shown in Figure 5-8(a), (b) and (c), respectively. Examination of the weld microstructure in this report indicates considerable agreement with those reported by previous experimental investigations. Torkamany et al. [4] investigation on the microstructure of low carbon and stainless steel (using hardness test, optical analysis and Schaeffler diagram) showed that the weld metal is made of either martensite or a combination of austenite, martensite and ferrite. Sun et al. [82] conclusion on dissimilar laser weld joining AISI 347 and 13CrMo44 steels revealed that the weld metals microstructure contained austenite and martensite. Anawa and Olabi [3] investigation on the fusion zone of a weld between AISI 316 and AISI 1008 steels predicted a complex austenitic–ferritic structure although their high hardness test value in the weld (around 450HV) was indicating more martensitic phase than a complex austenitic–ferritic structure.

5.4.4   Effect of laser welding parameters on microhardness

Figure 5-9 depicts the hardness distribution from the centre of the joint (along the thickness) for low, medium and high value of specific point energy (10J, 17J, and 50J). Microhardness values of the weld bead can be a good indicator of the homogeneity of

the weld bead. An inhomogeneous weld can lead to stress concentrations, corrosion and subsequent crack formation [69]. As can be seen in the figure, despite convection fluid flow within the melt pool, there is significant hardness variation across the weld for low specific point energy and vice versa. This suggests that the weld bead is inhomogeneous for specific point energies less than 10J. This is attributed to the difference in surface tension temperature coefficient of the materials in the molten pool and less convective fluid flow resulting in inhomogeneous alloying and consequent hardness variation across the weld. The maximum hardness values were observed at the fusion zone, where the average hardness reaches up to 2.5 times that of the parent metals (low carbon and stainless steel hardness values were about 110 and 150 $HV_{0.05}$ respectively). The high hardness value (for specific point energy more than 12.5J) is due to the formation of the martensitic phase which is attributed to the higher dilution rate of LCS and cooling rate involved in laser welding. High cooling rate increase the presence of supersaturated solid solution (martensite) and varies the distribution of alloying elements. Under rapid solidification, and high cooling rate, there is not enough time for solute (e.g. carbon) to diffuse or precipitate into the steel crystal lattice. Therefore, the solute solubility increases significantly in solvent which consequently prevents marked segregation and cause supersaturated solid solution and then a new microstructure. The solid solution create a tension within the solvent crystal structure which stops the dislocation movements (plastic deformation) during tensile or compressive forces and increases the hardness of the fusion zone [227].
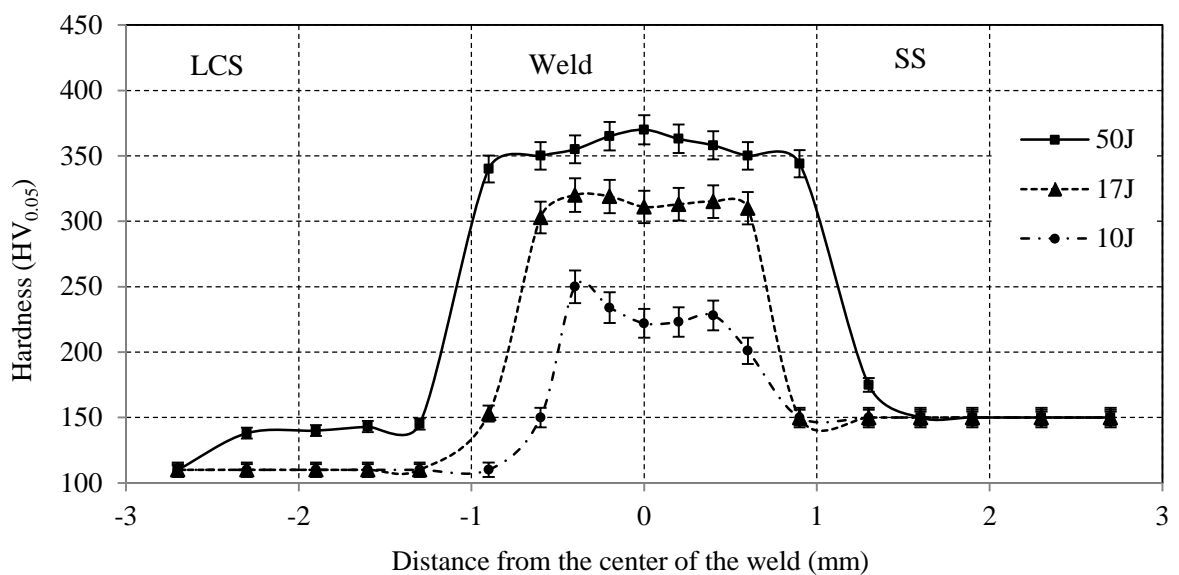
Figure 5-9 Hardness profile versus distance from the centre of the weld

5.4.5 Effect of laser welding parameters on mechanical properties

A notched tensile test was performed on the samples to study the influence of microstructure and the strength of the weld [5, 128]. As can be seen from Figure 5-10, an increase in specific point energy results in an increased on weld bead peak strength and load capacity. As discussed before, this is attributed to the fact that increasing specific point energy leads to formation of the martensitic phase which have higher load bearing capacity. Though martensite has high hardness and consequent high fracture load onset, its impact toughness value is significantly less than the austenitic phase [219]. Within the parameters considered, the optimum specific point energy is approximately 17J, meeting the primary requirement of a weld joint with complete penetration, homogenous alloying concentration (in the weld bead) and predominantly austenitic microstructure, and higher strength than parent metals. Moreover, specific point energy of 17J is preferred to 12.5J due to its higher failure peak strength and load (Figure 5-10) while maintaining predominantly austenitic microstructure (Figure 5-10). Figure 5-11 shows the photographic views of the notched tensile test results for specific point energy of 17J. As expected with NTS, all the samples failed at the weld zone.
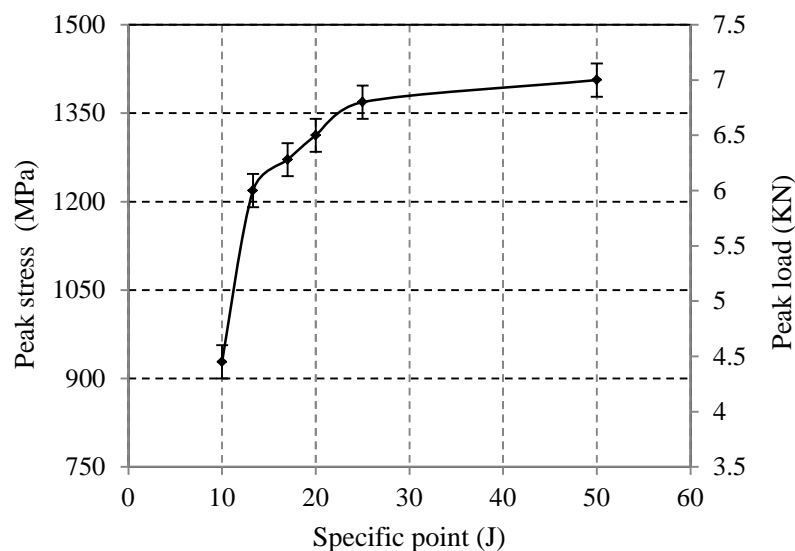
Figure 5-10 Effect of specific point energy on the weld load bearing capacity of the low carbon and stainless steel laser welded joint
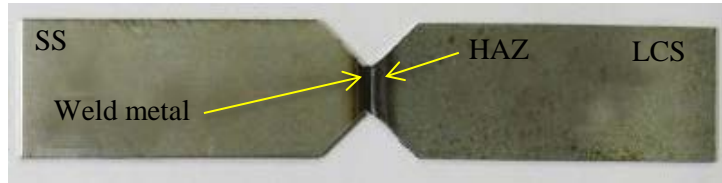
Figure 5-11 Influence of specific point energy on peak load strength of the weld joint at specific point of 17J

5.4.6   Effect of beam alignment on the alloying composition

The service performance of the joint depends on the concentration of the alloying elements and the final microstructure which is controlled by the specific point energy. However, control of microstructure by specific point energy has a clear threshold (for specific energy of 17J, the Cr_{eq}% is ~14.7 (Cr Wt% is ~12) with a mixture of austenitic and martensitic phases) and subsequently requires careful control of other parameters that influence the fusion zone alloying concentration. With the optimal specific point energy (17J), the beam alignment with reference to the dissimilar joint position was shifted by up to ±0.4mm in increments of 0.2mm, to further influence the fraction of the alloying elements. Figure 5-12 illustrates the beam alignment configuration. Positive offset means that the beam is positioned toward low carbon steel. Table 5-4 shows the beam offset and its corresponding weld bead characteristic. As seen from the table 5-4, the beam position significantly influences the weld metal composition and the microstructure across the weld. With a beam offset of more than 0.2mm (towards stainless steel), martensitic phase transition in the weld bead can be avoided. Figure 5-13 illustrates the EDS mapping and variation of the chromium element across the weld metal with three different beam positions (+0.4, 0, -0.4) for a specific point energy of 17J. A beam offset above ± 0.4mm fails to provide sufficient melting along the low carbon-stainless steel interface.

124

Laser Beam-Centred
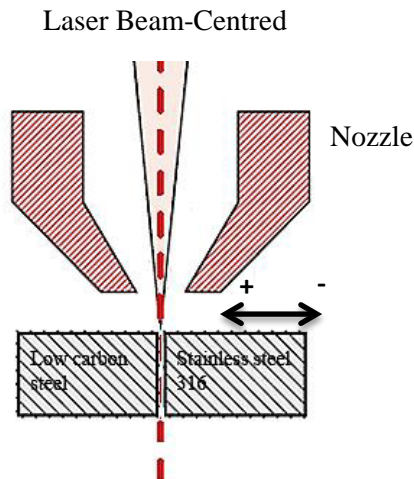
Figure 5-12 Beam position and alignment toward stainless steel (-) or low carbon steel (+)

Table 5-4 Effect of beam alignment on the composition of main alloying elements

Specific point energy (J)	Beam offset (mm)	Cr_{eq} (wt%)	Ni_{eq} (wt%)	Microstructure
17	0.4	2.85	5.1	M
17	0.2	11.5	6.5	M
17	0	14.7	9.6	A + M
17	-0.2	17.4	11.4	A
17	-0.4	18	12.6	A
A: Austenite, M: Martensite				

As shown in Figure 5-14, beam offset toward stainless steel yields a higher percentage of weld bead alloy concentration. When the beam is positioned toward the stainless steel, more of stainless steel is melted and transferred toward the weld interface. In such a case, the low carbon steel is melted not only through heat transfer via laser beam, but through the heat conduction from the molten stainless steel. Shifting the laser beam position is therefore vital to control the alloying concentration of the weld bead without losing the weld bead strength. However the beam position and its distance from the weld centre must be carefully selected since positioning the beam on the stainless steel too far away from weld seam will lead to lack of fusion and weak weld strength.
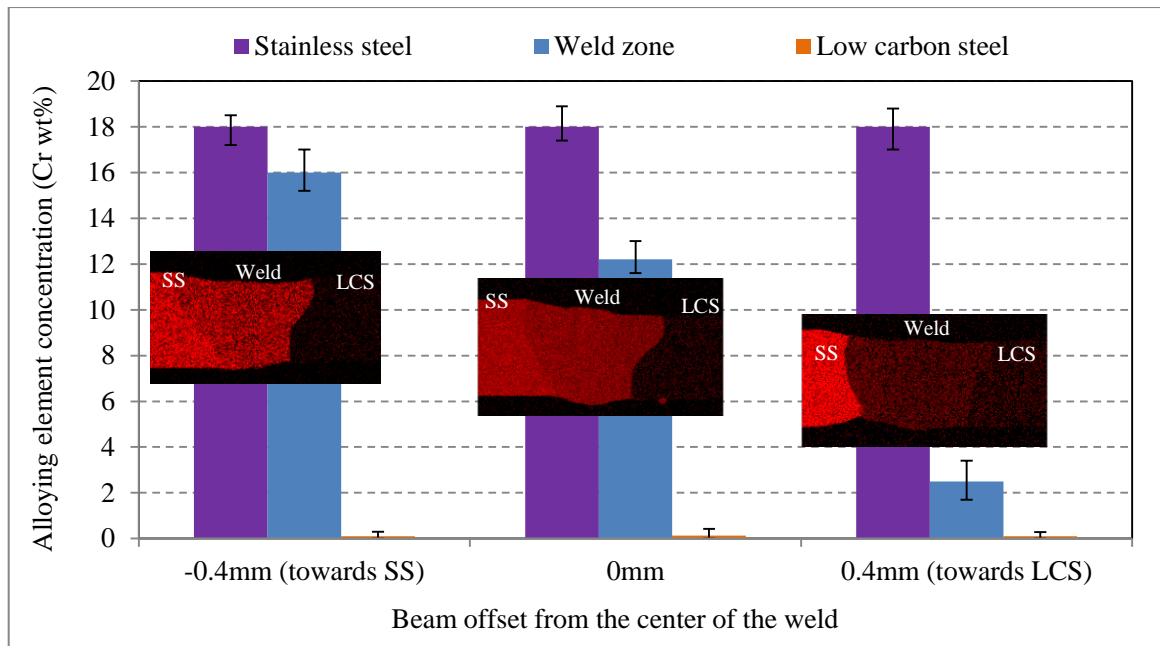
Figure 5-13 Effect of beam offset positions on chromium alloying concentration (inside image shows the EDS mapping of Cr element)

5.5   Summary

In this chapter an experimental investigation has conducted to understand the key parameters that control the microstructure and mechanical properties of a laser welded joint between low carbon and austenitic stainless steel. The results obtained in this work are summarized below.

1. Laser autogenous welding is a very promising technology for dissimilar welding of low carbon to austenitic stainless steel due to lower heat input, finer grain structure and more control over the process.

2. Specific point energy is one of the effective parameters to study the fluid flow and microstructure of the weld. A predominantly homogenous microstructure and well mixed fusion zone was produced with a specific point energy of greater than 17J for a 1mm thick joint.

3. It is essential to avoid brittle phases (martensite) as they significantly decrease the ductility of the weld, also it is always desirable to have a weld metal which contains more alloying element since they increase the toughness and corrosion resistance of the weld. As a result, the welding process parameters must be carefully chosen in order to avoid or supress the formation of unwanted microstructures and phases.

4. The hardness and the strength of the weld joint are related to the final microstructure which depends on specific point energy. As the specific point energy increase, the weld microstructure tends to form a martensitic structure. This is due to higher dilution of low carbon steel and lower concentration of alloying elements in fusion zone.

5. It is found that the beam alignment has substantial effect on concentration of alloying elements and the final microstructure. A predominantly austenitic fusion zone is obtained with a beam offset of 0.2-0.4mm towards the stainless steel. A beam offset towards low carbon steel resulted in a martensitic microstructure.

6. It is shown that the microstructure and consequent mechanical properties along the fusion zone of the dissimilar joint are highly dependent on the gradient of the redistribution of the alloying elements e.g. Cr, C, Ni. The redistribution of the alloying elements within the fusion zone depends on convection fluid flow during welding. The magnitude of convection fluid flow is expected to be closely related to specific point energy and cooling rate. Therefore it is essential to study the convection fluid flow and the influence of laser specific energy on it by developing a numerical simulation as discussed in the next chapter.

Chapter 6 Numerical Simulation of Transport Phenomena in Dissimilar Laser Welding

6.1 Introduction

In this chapter, a multiphase computational fluid dynamic model is developed with the objective of simulating the alloy composition in a dissimilar weld bead. A novel modelling approach to predict the alloying concentration and homogeneity of laser dissimilar welding of carbon to austenitic steel is presented. Prediction of the alloy composition will enable control of the microstructure and mechanical strength of a laser dissimilar weld. Using the model, independent predictions on weld properties are made for a range of laser parameters, and in all cases the results of the numerical model were found to be in close agreement with experimental observations. The present model provides a simple yet effective method to predicting the weld bead alloying concentration and homogeneity encompassing wide range of materials.

Dissimilar laser welding is more complicated than similar welding because of the different elemental composition and thermo-physical properties of metals [26, 119]. However, laser welded joints of low carbon and stainless steels are currently used in petrochemical and power plants industries and more generally are of interest for joining 3D structures, complex assemblies and high precision components [3, 101]. Despite the potential of laser dissimilar welding, uneven alloying concentration in the weld bead can often results in reduced weld strength [26, 46], unacceptable intermetallic phases and crack formation [83, 101]. Consequently, strategies to predict and control the alloy composition and alloy distribution of the weld bead are required to be identified.

This chapter investigates the effects of laser process parameters on, melt pool convection, change in weld bead surface topology, dilution of the weld zone and its subsequent structural performance. In the first part, a three dimensional CFD analysis is performed incorporating the buoyancy and surface tension effect to predict temperature history, weld bead surface profiles and dilution. In the second part a three dimensional FEM analysis is performed using the modified weld bead surface profile, thermal

history obtained from the CFD analysis and the change of material properties by dilution. Also, to find the effect of the applied energy on structural performance, a three dimensional FEA based residual stress analysis was performed incorporating the change thermal cycle inside the weld pool. The CFD and FEM analyses were performed using FLUENT and ANSYS codes respectively. The experimental results obtained with a CO_2 laser, was used to validate the simulation results, carried out under similar processing parameters.

6.2   Previous work

In most dissimilar welding process, the physical properties of the two metals to be joined can be different which can lead to complexities in heat flow, weld pool shape, solidification rate, microstructure, diffusion of alloys, and formation of intermetallic compounds. Hence, from a scientific standpoint, study of a dissimilar laser welding offers a number of challenges. Although there are fairly number of publications on the laser welding of joining of dissimilar metals, the review of literatures shows that a majority of them over simplified the dissimilar welding phenomena. A systematic study from a scientific angle in dissimilar laser welding is therefore desirable. Several numerical [88, 101-110] and experimental investigations [26, 46, 83, 101, 111] of laser dissimilar welding have been reported by various researcher's. Rosenthal [228] first proposed a mathematical model of a moving heat source under the assumption of quasi-steady state. After this work various studies have been performed on laser dissimilar welding simulation to investigate the nature of heat transfer, melt pool convection and residual stress distribution.

Zhao et al. [229] established a three-dimensional FEM model to investigate the temperature field under various laser powers and welding speed. The simulations were then applied to optimize the heat input at the interface of the two metals in order to decrease the formation of brittle intermetallic compounds during laser overlap welding of Ti6Al4V and 42CrMo. Their simulation however hasn't considered the influence of Marangoni convection and mass transport.

Cho et al. [230] developed a simulation model for the analysis of the molten pool and the alloying element distributions during CO_2 laser–GMA hybrid welding process. The distribution of chromium (Cr) and nickel (Ni) across the fusion zone was obtained. It is concluded that low molten region in weld contain lower content of alloying elements compare to higher molten region as a result of excessive flow at the rear part of the laser keyhole which pushes out the flow with higher alloy content toward higher molten region.

Recently, Esfahani et al. [5] investigated the microstructure and service performance of dissimilar joint between low carbon and austenitic stainless steel and discussed that the alloying element concentration has got a significant influence on the microstructure and service performance of the weld.

6.3   Formulation and grid structure

Figure 6-1 shows the initial mesh used for the CFD analysis. The computational domain with a dimension: length, L = 4mm, width, W = 8mm and thickness B = 1mm has been considered for computation. The model consists of 194,300 elements. A grid system of variable spacing has been utilized with a fine grid near the heat source and a course grid away from the heat source. The ambient temperature was set at 300K. The thermo-physical properties of austenitic stainless steel and low carbon steel used in the analysis are presented in chapter 3 and table 6-1.
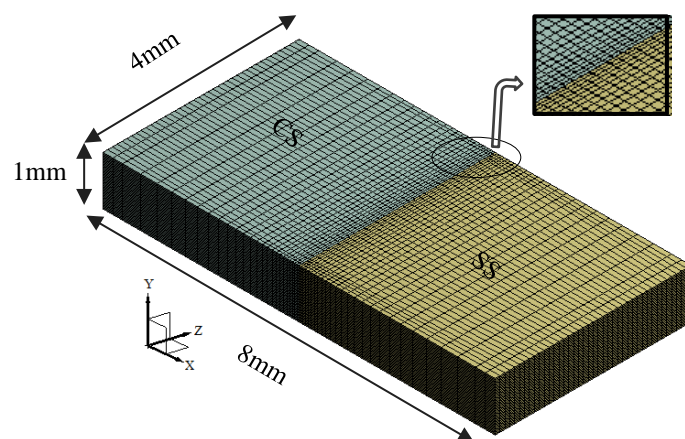
Figure 6-1 Mesh used for the analysis

Table 6-1 Thermal properties of the substrate [144]

Nomenclature	Stainless steel	Low carbon steel
Dynamic viscosity of liquid phase (kg/ms)	0.03	0.00578
Liquid temperature (K)	1770	1723
Solid temperature (K)	1670	1523
Latent heat of fusion (J/Kg)	400000	272000
Temperature coefficient of surface tension (N/mK)	-0.00043	-0.0005

6.3.1 Thermal analysis

The CFD analysis was performed to model the heat transfer, fluid flow and material diffusion, using the finite volume based code, Fluent. The mathematical model used in this work was based on the Reynolds-Averaged Navier–Stokes (RANS) time-dependent equations. The governing equations were composed of the conservation of mass, conservation of momentum, conservation of energy, transport equation for turbulence and volume fraction equation (modified continuity equation) [231]. The volume of fluid (VOF) model was used to account for two different materials (SS and CS) inside the met pool. The following simplifying assumptions made:

➢ The welding takes place in conduction mode (no keyhole formation) and the free surface of the melt pool changes according to the melt pool convection.

➢ The Elastic-plastic behaviour of the material during welding expansion and contraction is not taken into account in this model and only elastic mechanical properties are considered in the calculation of the residual stresses.

➢ Laser gas dynamic parameters such as, shielding gas jet, nozzle stand-off and nozzle exit diameter are assumed to have insignificant effects on the thermal history and weld bead shape characteristics.

➢ There is no chemical reaction or oxidation in the melt pool.

➢ The variation in mechanical behaviour during the welding process has insignificant effect on fluid flow dynamics.

Based on the volume fraction values, appropriate properties are assigned to each control volume within the domain. The tracking of the interface between the phases is accomplished by the solution of a continuity equation for the volume fraction of the

secondary phases. For the secondary phase (CS) and primary phase (SS), the volume fraction equation has the following form:

Secondary Phase $\qquad \frac{1}{\rho_2}\left[\frac{\partial}{\partial t}(\alpha_2\rho_2) + \nabla(\alpha_2\rho_2\vec{v}) = 0\right]$ $\qquad$ E. q (1)

Primary Phase $\qquad\qquad\qquad \alpha_1 = 1 - \alpha_2$ $\qquad$ E. q (2)

where α, ρ, t, $\vec{v}$ are volume fraction, density, time, and fluid velocity vector respectively. Subscripts 1 and 2 represent the primary and secondary phase respectively.

A single momentum equation is solved throughout the domain, and the resulting velocity field is shared among the phases such that:

$$\frac{\partial}{\partial t}(\rho\vec{v}) + \nabla(\rho\vec{v}\vec{v}) = -\nabla p + \nabla(\mu(\nabla\vec{v})) + \rho\vec{g} - S_w \qquad \text{E. q (3)}$$

where p, μ, and $\rho\vec{g}$ are static pressure, molecular viscosity, gravitational body force. The momentum sink (S_w) due to the reduced porosity in the mushy zone takes the following form:

$$S_w = \vec{v}\,\frac{(1-\beta)^2}{\beta^3+\varepsilon}\,A_{mush} \qquad \text{E. q (4)}$$

where ε is a small number (0.0001) to avoid division by zero in the solid region, a default value of 10^5 is used as mushy zone constant (A_{mush}), and employed in simulation since all the solutions converged with assumed value and the liquid fraction β is defined as:

$$\beta = \begin{cases} 1 & T > T_1 \\ (T - T_s)/(T_1 - T_s) & T_s \le T \le T_1 \\ 0 & T < T_s \end{cases} \qquad \text{E. q (5)}$$

with T_l, the temperature of the liquid and T_s the temperature of the solid. The value of β, ranges between 0 and 1, defining the extent of melting.

A single energy equation is solved throughout the domain. The energy equation is written in terms of the enthalpy (H) as following:

$$\frac{\partial(\rho H)}{\partial t} + \nabla(\rho\vec{v}H) = \nabla(k\nabla T) \qquad \text{E. q (6)}$$

where k is the thermal conductivity and T is the temperature.

Heat loss due to convection and radiation is considered over all the surfaces (Eq. 7) and a laser heat flux (Eq. 9) was used as the input laser heat source. Heat flux input with heat loss due to convection [232] is expressed as:

$$K\nabla T = q(x, y) - h_c(T - T_\infty)$$

E. q (7)

where h_c is the heat transfer coefficient, T_∞ is the ambient temperature and $q(x, y)$ is the laser heating source given by:

$$q(x, y) = P_{x,y}(1 - r_f)$$

E. q (8)

where r_f is the reflectivity of the material and $P_{x,y}$ is the laser heat flux, which is given by:

$$P_{x,y} = \frac{P}{r_b^2 \pi} \exp\left(-\frac{2r}{r_b^2}\right)$$

E. q (9)

where P is the total laser power, r is radial position within the beam and r_b is the laser beam diameter [232].

The fluid flow in the weld pool is driven by the combination of surface tension, viscous force and buoyancy force [88, 104, 106]. On the top and bottom surfaces, the shear stress (τ) caused by the variation of surface tension due to temperature difference is given by:

$$\tau = \frac{\partial \sigma}{\partial T} \nabla_s T$$

E. q (10)

where, $\dfrac{\partial \sigma}{\partial T}$ is the temperature coefficient of surface tension and $\nabla_s T$ is surface temperature gradient. During the computation, the surface tension gradient is expressed as a function of the surface temperature [94]. The shear stress given by equation (10) is applied to the momentum equations (Eq. 3).

The mixing of materials (CS and SS) is primarily due to melt pool convection, which is influenced by surface tension gradient, viscous and buoyancy forces. The weld bead surface topology is predominantly influenced by the direction of the melt pool movement [68]. In the CFD model, the nodes on the free surfaces (top and bottom of

the weld bead) were relocated according to the melt pool velocity and direction [233, 234]. Adaptive mesh refinement was employed in the CFD simulation in order to predict and track the new surface topology at every time step. A code written as user-defined functions (UDF) in the C programming language was used to apply a heat flux as a transient boundary condition on the top surface of the weld (Eq. 9) and to track the weld bead surface profile (coordinates of X,Y,Z points of each node in the fusion zone). The UDF was then dynamically linked with the Fluent CFD solver. The material was assumed to be homogeneous and isotropic.

6.3.2   Structural analysis

This nonlinear analysis calculates the residual stress resulting from the strains generated from expansion and contraction due to temperature change and phase transformations, and inelastic effects from plasticity and creep in the general case. The structural analysis was performed using the FEA solver, ANSYS Multiphysics 14.5.

During laser irradiation, heating is localized and large temperature variations occur over a small area of incidence. Because of the resulting temperature gradients, large thermal stresses are generated in the workpiece material. Thus, in accordance with normal practice in such cases, an elasto-plastic finite-element solution is sought to calculate the distribution of stresses within the material. The total strain vector $\{\varepsilon\}$ is given as:

$$\{\varepsilon\} = [D]^{-1}\{\sigma\} + \{\varepsilon^{th}\}$$ E. q (11)

where $\{\varepsilon^{th}\}$ is the thermal strain vector given by:

$$\varepsilon^{th} = \alpha_e \Delta T = \alpha_e (T - T_{ref})$$ E. q (12)

The coefficient of linear expansion α_e is a function of temperature and the equation (13) can be written as:

$$\varepsilon^{th} = \int_{T_{ref}}^{T} \alpha_e(T) dT$$ E. q (13)

The stress is related to strains by:

$$\{\sigma\} = [D]\{\varepsilon\}$$

<div align="right">E. q (14)</div>

The principal stresses (σ_1, σ_2, σ_3) are calculated from the cubic stress equation by:

$$\sigma^3 - I_1\sigma^2 - I_2\sigma - I_3 = 0$$

<div align="right">E. q (15)</div>

The three roots σ_1, σ_2, and σ_3 of equation (15) give the three principal stress at the origin through which equivalent stress can be estimated as:

$$\sigma' = \sqrt{\frac{1}{2}\left[(\sigma_1 - \sigma_2)^2 + (\sigma_2 - \sigma_3)^2 + (\sigma_3 - \sigma_1)^2\right]}$$

<div align="right">E. q (16)</div>

This is related to the strain by the relation $\sigma' = E\varepsilon'$. To develop a finite element procedure for the stress computation, the principle of virtual work is employed. Based on this approach, the equilibrium of any element under loading requires that for any compatible small virtual displacements imposed on the body in its state of equilibrium, the total virtual internal work or strain energy (δU) is equal to the total virtual external work due to the applied thermal loads (δV), i.e. $\delta U = \delta V$. The virtual displacements are zero at the boundary points and surfaces. For the static analysis of problems having linear geometry and thermo-elastic material behaviour, one can derive the following equation using the standard procedure as [235].

$$\int_V (\delta \varepsilon^T D\varepsilon - \delta\varepsilon^T D\varepsilon^t)dV = \int_V (\delta u^T f^B dV + \int_S (\delta u^T f^S dS + \delta u^T f^C$$

<div align="right">E. q (17)</div>

where V and S denote the volume and surface, f^B, f^S and f^C stand for the vectors of body, surface and concentrated forces, respectively.

The elemental displacement vector d_e is related to the nodal displacement d_i by:

$$d_e = Nd_i$$

<div align="right">E. q (18)</div>

where N are the matrix of shape or interpolation functions. The elemental strain vector ε_e is written as:

$$\varepsilon_e = Ld_e$$

<div align="right">E. q (19)</div>

where L is a differential operator matrix. Consequently, the strain vector ε_e is related to the nodal displacement vector d_i by:

$$\varepsilon_e = LNd_i = Bd_i$$

<div align="right">E. q (20)</div>

where B (=LN) is strain–displacement matrix that relates the displacements to the strain, hence Eq. (17) is reduced to the following matrix:

$$K_e d - F^t = F_e \qquad\qquad \text{E. q (21)}$$

where K_e is the elemental stiffness matrix, F^t is the element thermal load vector, and F_e is the total element force vector. They are expressed as:

$$K_e = \int_V (B^T D B dV \qquad\qquad \text{E. q (22)}$$

$$F^t = \int_V (B^T D \varepsilon^t dV \qquad\qquad \text{E. q (23)}$$

$$F_e = f^b + f^s + f^c \qquad\qquad \text{E. q (24)}$$

where D is stress–strain matrix, f^b is elemental body force vector, f^s is elemental surface force vector, and f^c is elemental concentrated force vector. Assembly of element matrices and vectors of equation (21) gives:

$$K_e d = F^t + F_e = F \qquad\qquad \text{E. q (25)}$$

where K_e, d and F are the global stiffness matrix, the global nodal displacement vector, and the global nodal load vector, respectively.

A solution of the above set of equations gives unknown nodal displacements and reaction forces in the model. Once the displacement fields due to the temperature gradients in the material is known, the corresponding strain and stress fields can be calculated [236].

Due to the thermal cycle and metallurgical changes, the structural material properties of the weld zone differs from the parent material. To account for these changes, the Young's modulus of the weld zone was estimated experimentally using the micro-hardness tested and used with the simulation (structural analysis). The parent material properties were the Young's modulus, Poisson's ratio, coefficient of thermal expansion, and yield stress, whose values as used in the analysis are adapted from Smithells Metals Reference Book [237] for the base material. The applied structural boundary conditions were such that, all the nodes on the sides of the base plate parallel to the direction of weld were constrained in all directions to simulate clamping effect on the substrate at that location. Each time step in the structural analysis corresponded to the same time

step in the thermal analysis, with the corresponding weld bead profile and the thermal history. The scheme employed in this study for sequentially coupling the CFD and FEM analysis along with the solution steps is given as a flow chart in Figure 6-2.
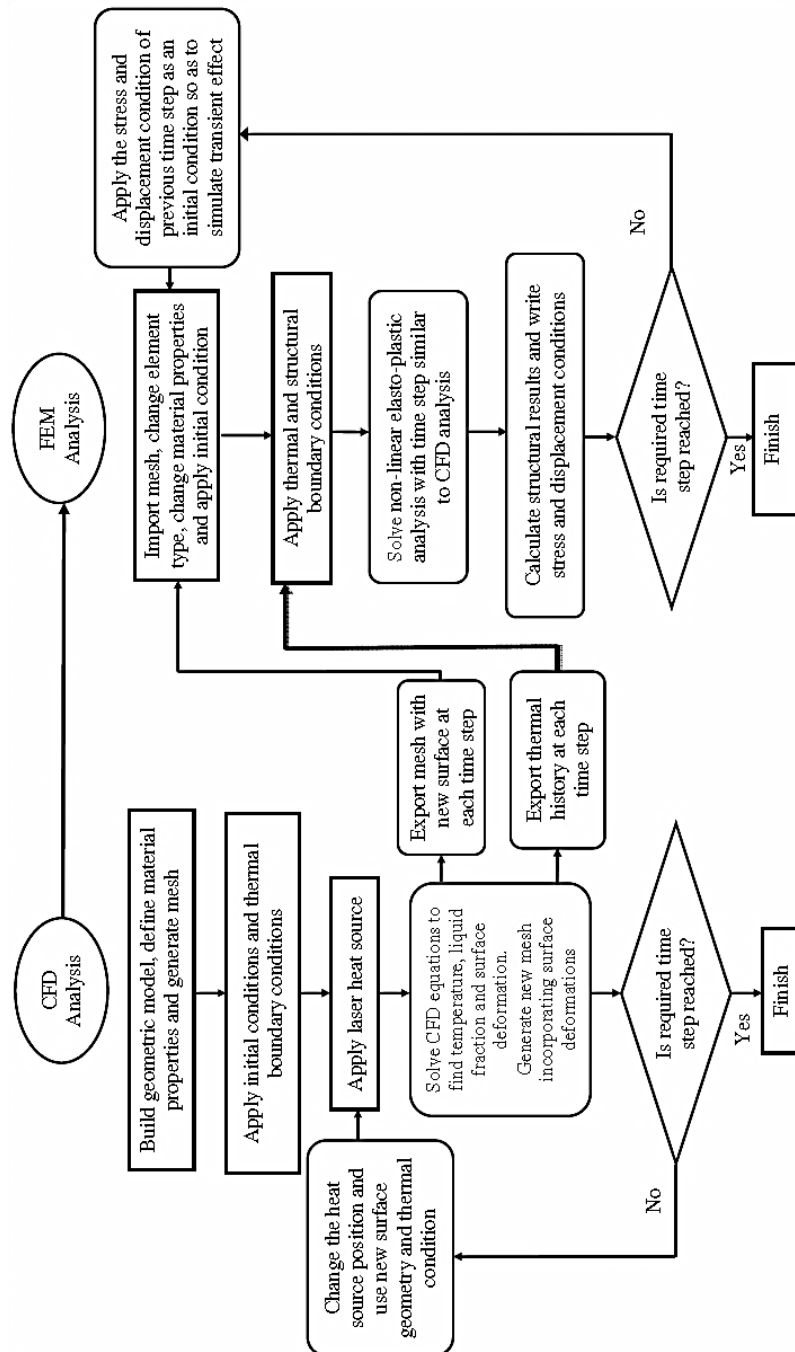
Figure 6-2 Flowchart explaining the sequential coupling and analysis steps [68]

137

6.4 Results and discussion

6.4.1 CFD results

The main objective of this research was to develop a CFD model that is not only capable of predicting the laser dissimilar welding thermal cycle and fluid flow but also to predict alloying concentration, weld bead homogeneity in the fusion zone, and weld bead structural characteristic. To get a better insight into the mechanisms of fluid flow and material mixing in the weld pool and to evaluate the robustness of the CFD model, three models were developed, with specific point energies of 50J, 17J, and 10J. In-line with the experimental configurations, the laser spot diameter of the beam was maintained at 0.5mm. The CFD analysis was performed for 100 time steps of which 80 steps were for the laser welding phase (corresponding to the welding length) and the remaining concerned the cooling phase. The time steps for the beam energies of 50J, 17J, and 10J were 10, 3.3 and 1.4 milliseconds respectively. This is in accordance to the element length along the laser beam traverse direction.

To highlight the non-linear heat transfer phenomena in dissimilar laser welding, the results are first presented in the form of temperature contours overlaid on the weld bead surface profile. Part of the absorbed energy is used to generate the weld pool and part of it is conducted into the solid base metal. Heat conduction is the major mode of heat transfer at the initial stage of welding, and in the intermediate stage, fluid convection becomes dominant, and significantly influences the heat transfer in vertical direction.

Iso-metric view

Midpoint cross-section transverse to weld direction (X-Y view)

| 3070 2740 2300 1860 1420 976 536 300 | 2800 2500 2100 1700 1300 900 500 300 | 2750 2460 2060 1670 1280 888 496 300 |

Temperature (K)

(a)   (b)   (c)

Figure 6-3 Comparison of temperature distribution for specific point energy of (a) 50J, (b) 17J, (c) 10J

Figure 6-3 (a), (b) and (c) show the temperature contours and the corresponding weld bead profiles for specific point energy of 50J, 17J and 10J respectively. The plots are generated after the temperature and weld bead profile reach a quasi-steady state. As can be seen from Fig. 6-3 (a), high specific point energy of 50J, results in a higher temperature which is attributed to longer laser interaction time. The X-Y views clearly show the asymmetric heat distribution observed with the dissimilar laser welding. This is due to the difference in thermal properties, and in all cases, the maximum temperature exceeds the melting temperature of the substrate.

Figure 6-4 Comparison of temperature inside and outside the melt pool for various specific point energies

The temperature dependence of the thermal conductivity of the materials significantly influences the position of maximum temperature in melt pool and away from melt pool (heat affected zone (HAZ)). Figure 6-4 shows the maximum temperature in the melt pool and 1 mm outside the melt pool. As seen from Figure 6-4, in all the cases, the maximum temperature was noticed within the low carbon steel, however in the region away from the molten pool (1mm away from melt pool), a higher temperature is noticed over the stainless steel. This is attributed to the temperature dependent thermal conductivity of the materials. At high temperature (above 1200K) low carbon steel has a relatively low thermal conductivity and heat accumulates over the low carbon steel, hence the maximum temperature occurs within the region of low carbon steel melt pool. At low temperature the thermal conductivity of stainless steel is less (table 6-2) and the temperature distribution is noticed accordingly.
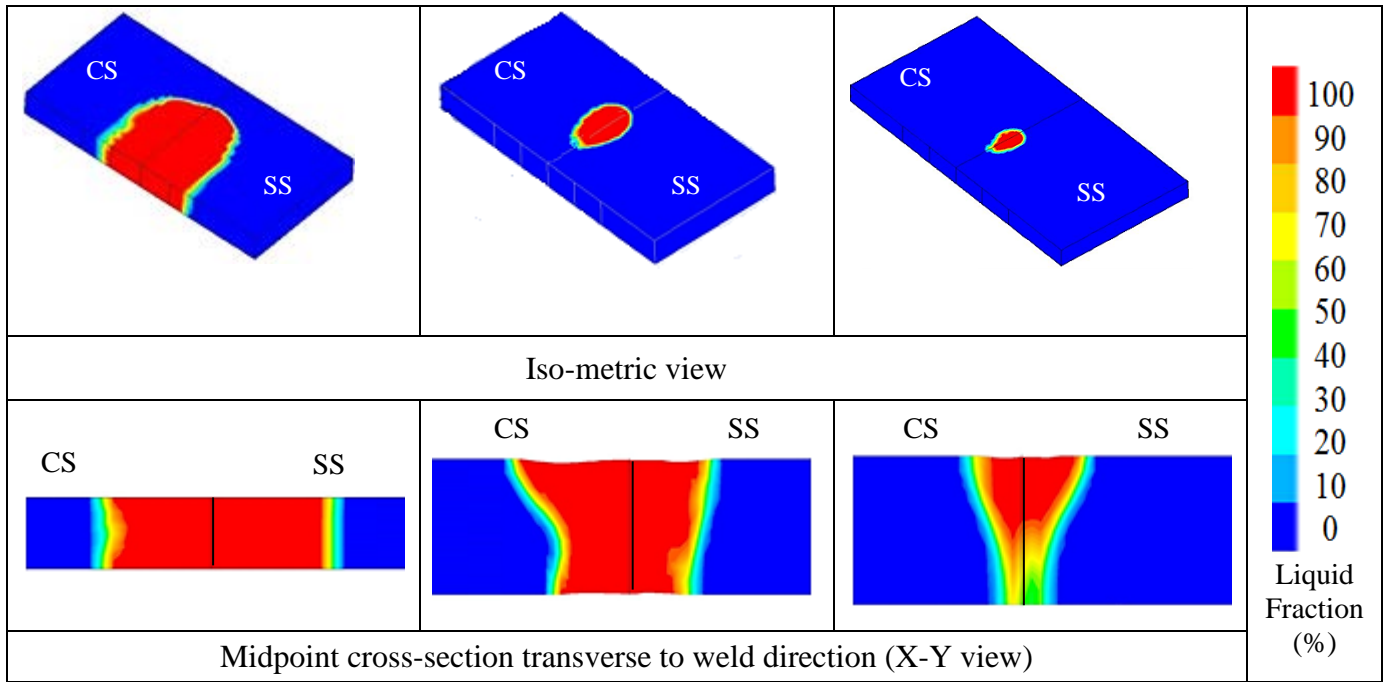
Figure 6-5 Comparison of melting and solidification distribution profiles for specific point energy of (a) 50J, (b) 17J, (c) 10J

Observation of similar asymmetric behaviour was noticed in the fusion zone liquid fraction and is presented in Figure 6-5 (for the energies of 50J, 17J and 10J). The X-Y views (Figure 6-5) represent the liquid fraction contour normal to the weld direction. As can be seen from the Figure 6-5, at low specific point energy, it is predominately the stainless steel which melts; however, with increased beam energy the melting rate of low carbon steel tends to be higher than stainless steel. This is attributed to the relatively low thermal conductivity of stainless steel at initial melting stage, which results in rapid heating and fast melting of stainless steel at the start of the melt pool formation (before low carbon steel reaches the melting temperature) [122]. However, higher thermal conductivity of the stainless steel at high temperature on the one hand, and lower thermal conductivity of carbon steel at the same high temperature on the other hand, results in a higher melting rate of CS at high specific point energy. The significant increase in thermal conductivity of stainless steel compare to carbon steel at high temperatures leads to an increase in temperature of low carbon steel (compared to stainless steel). It is also noted from the Figure 6-5, that the fusion zone surface profile changes with specific point energy. The surface was almost flat for high specific point energy of 50J whereas a hump in the middle of the fusion zone was noticed for specific point energy of 17J. This can be explained on basis of the melt pool size and flow

141

velocity distribution.

| Midpoint cross-section transverse to weld direction (X-Y view) | | |

| Top view (X-Z view) | | |

| 0.41 0.36 0.3 0.25 0.19 0.14 0.06 0 | 0.3 0.26 0.22 0.18 0.14 0.1 0.04 0 | 0.19 0.16 0.14 0.11 0.08 0.05 0.02 0 |

| Velocity (m/s) | | |
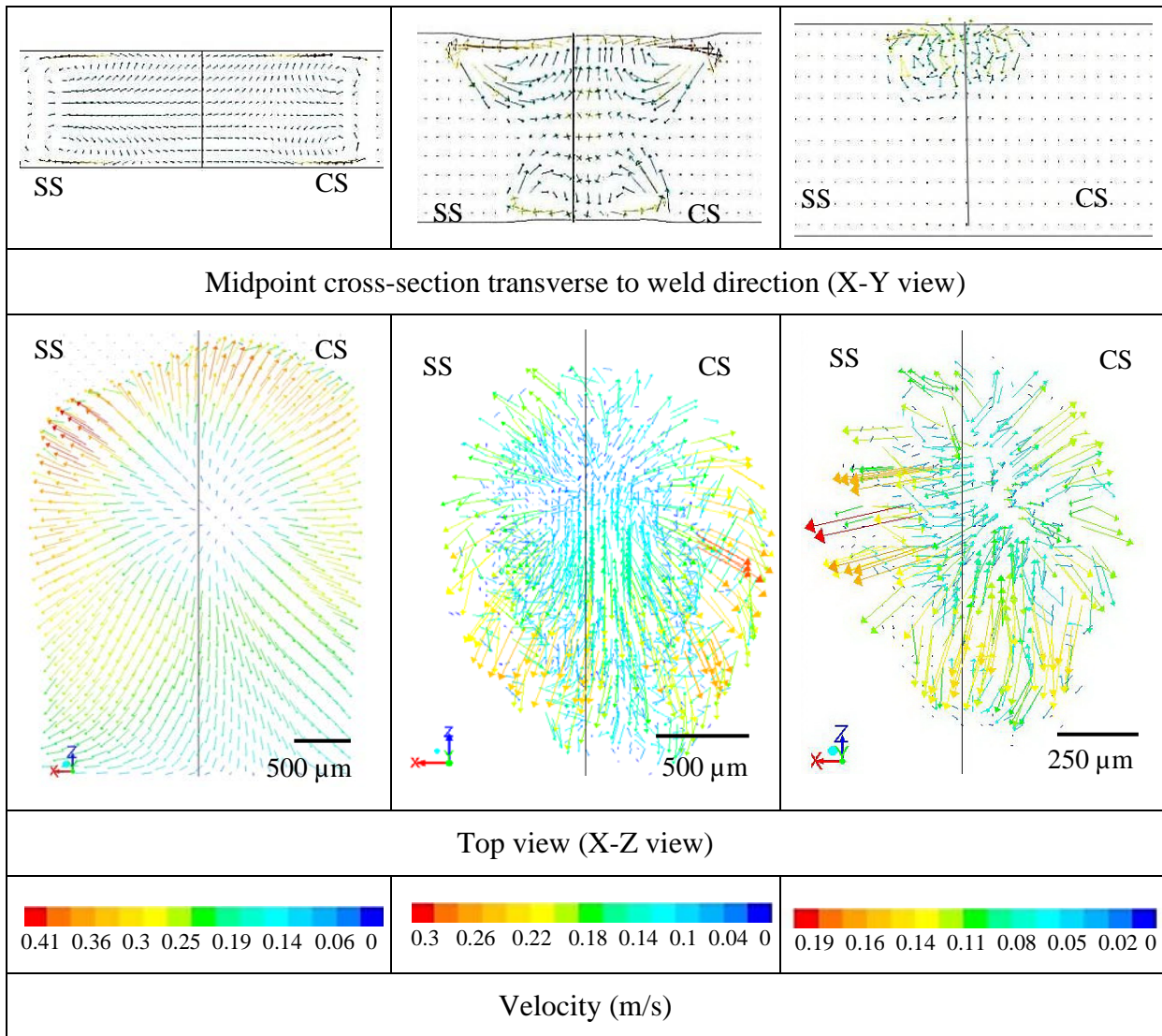
(a)   (b)   (c)

Figure 6-6 Comparison of top surface velocity vector for specific point energy of (a) 50J, (b) 17J, (c) 10J

Figure 6-6 shows the melt pool velocity in the midpoint cross-section (X-Y) and top surface (X-Z). The velocity inside the melt pool was driven by the surface tension gradient of the material, which again depends upon the surface temperature gradient and not on the maximum temperature. As the specific point energy increases, the thermal gradient and consequent surface tension force increases which result in higher fluid velocity in the melt pool. The negative thermal gradient of the surface tension in the melt pool causes an outward flow (Figure 6-6), which provides efficient transfer of heat from the centre to the weld periphery and from the surface to weld root. Relatively low fluid flow velocities (~0.18m/s) are found at low specific energy of 10J and

considerably higher magnitudes of velocities are noticed for a specific energies of 17J (0.3m/s) and 50J (0.41m/s). Also, the maximum velocity was found in the low carbon steel due to high temperature gradients within the low carbon steel. This increase in melt pool dynamics predominantly with the low carbon steel is the primary reason for an increase in the melting rate of low carbon steel (as can be seen from Figure 6-5). It is also worth mentioning that in the absence of magneto-hydrodynamics (MHD) forces in the laser welding of dissimilar alloys compare to other fusion welding processes, the fluids basically are driven by the Marangoni and buoyancy in the fusion zone [123]. As a result, the velocity at the top surface of the weld is significantly higher than that inside the fusion zone or the weld root.

The hump noticed for the specific point energy of 17J (Figure 6-5) is attributed to the difference in magnitude of the velocities in stainless steel and low carbon steel [140]. Although the negative surface tension gradient causes an outward flow, a difference in velocity magnitudes results in hump formation at the interface of the materials [103, 105] and [140]. With high specific point energy (50J) the width of the weld pool increases, which supresses hump and results in a predominantly uniform weld bead [140]. However, at low specific point energy (10J), the melt pool on the surface flow outwards (due to negative surface tension gradient) causing a slight depression in the weld pool centre [105]. The observed trend in surface topology is consistent with that reported by Mills [140] and Li [105].

It is clear that the fluid velocity can significantly influence the mixing and the homogeneity of the dissimilar weld bead. The extent of mixing and concentration of the alloying elements depends on the magnitude of surface tension driven fluid flow in molten pool. Figure 6-7 illustrates the midpoint cross-section (X-Y) phase field of the weld fusion zone for the specific point energy of 50J, 17J and 10J respectively. The phase field is a good indication of the mixing of weld metals inside the weld zone and can be used to estimate the alloying concentration and homogeneity of the weld bead [26, 233]. Increase in specific point energy results in higher temperature gradient at the melt pool surface. The high temperature gradient over the melt pool results in a negative temperature gradient of surface tension $\frac{d\gamma}{dT}$ which causes an intense outward flow by convection (from the centre to the weld periphery) that transports alloying elements from the parent metal into the molten pool, and consequently results in more

homogenous weld bead. As can be seen from the Figure 6-7, the two materials have undergone extensive mixing for the specific point energy of 50J and 17J, whereas there was minimal mixing at the low specific point energy of 10J. Similar trends are noticed in experimental observation of micro-hardness analysis along the fusion zone, which is shown in Figure 6-8. As can be seen from the Figure 6-8 the variation of the hardness within the weld bead decreases as the beam energy increases which suggests that the alloying element concentration in weld bead is inhomogeneous for specific point energies less than 17J. For specific point energies of 50J and 17J, the percentage variation of hardness within the fusion zone is close to 5%, whereas for 10J the percentage variation is in the range of 15-16%. Variation of hardness within the weld zone can undermine the efficacy of the joint and should be avoided [180], however high magnitude of specific point energies also can result in higher HAZ, martensitic weld microstructure (chapter 5), and/or residual stress in weld bead. The proposed model can be a useful tool, in estimating the homogeneity of the dissimilar weld zone, prior to the welding.

(a)   (b)   (c)
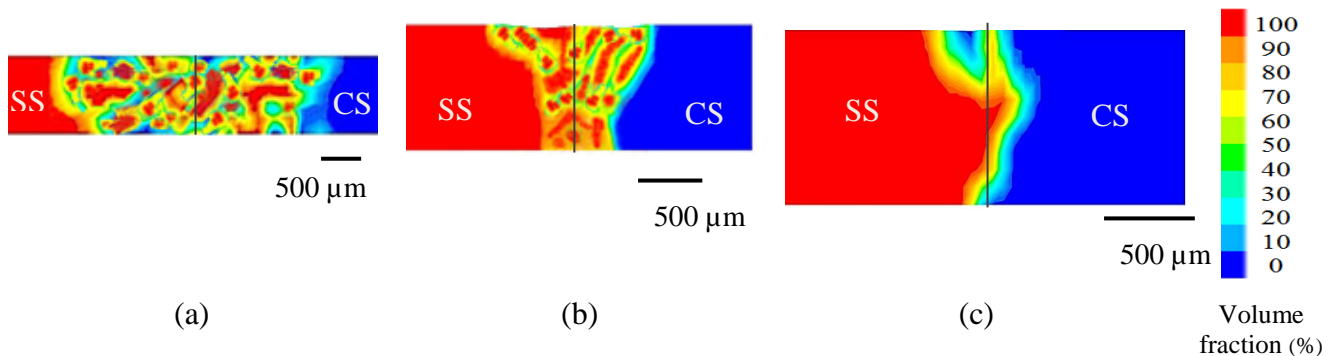
Figure 6-7 Comparison of volume fraction of stainless steel for specific point energy of (a) 50J, (b) 17J, (c) 10J

144
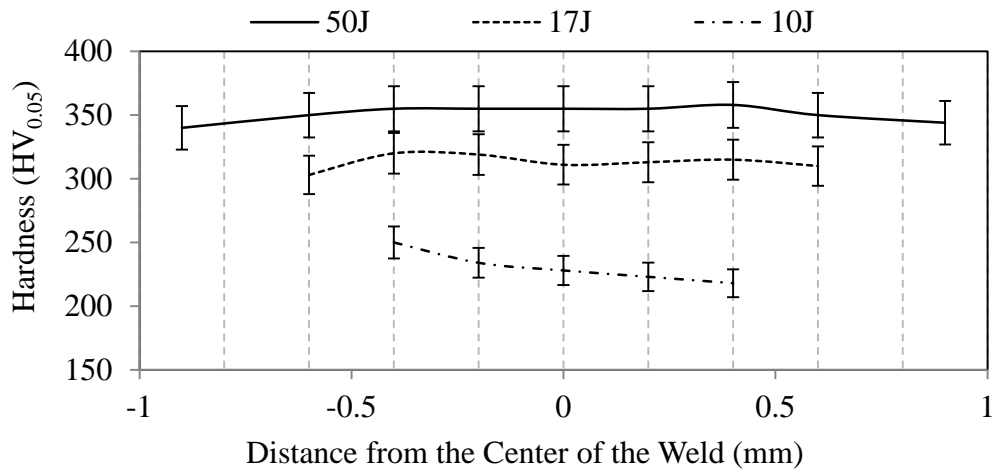
Figure 6-8 Experimental hardness profile of the weld fusion zone

Figure 6-9 shows the comparison of experimental (left side) and simulated (right side) fusion zone profile of dissimilar joint (cross-section along the centre of the sample) for various specific point energies. The contours of the simulated results show the normalised dilution of the low carbon steel. Dilution is defined as the percentage contribution of low carbon steel in the weld fusion zone and gives a good indication of the alloying concentration in the weld bead. In agreement with the experimental bead profile, the CFD model predicts the weld bead dilution (% melting of two materials) and surface condition of various specific point energies. Figure 6-10 shows the comparison of experimental (obtained from EDS analysis) and simulated dilution of low carbon steel. It is calculated from the ratio of the melt area of low carbon steel to the total weld bead area from the volume fraction value of each element (Figure 6-9).

It is worth mentioning that there is a marginal difference in weld geometry when compared to the CFD to experimental results. This may be attributable to assuming constant reflectivity and linear thermal conductivity of stainless steel above melting temperature in the CFD simulation which is not the case in actual experimentation. Such material property details were not available for the model.

145
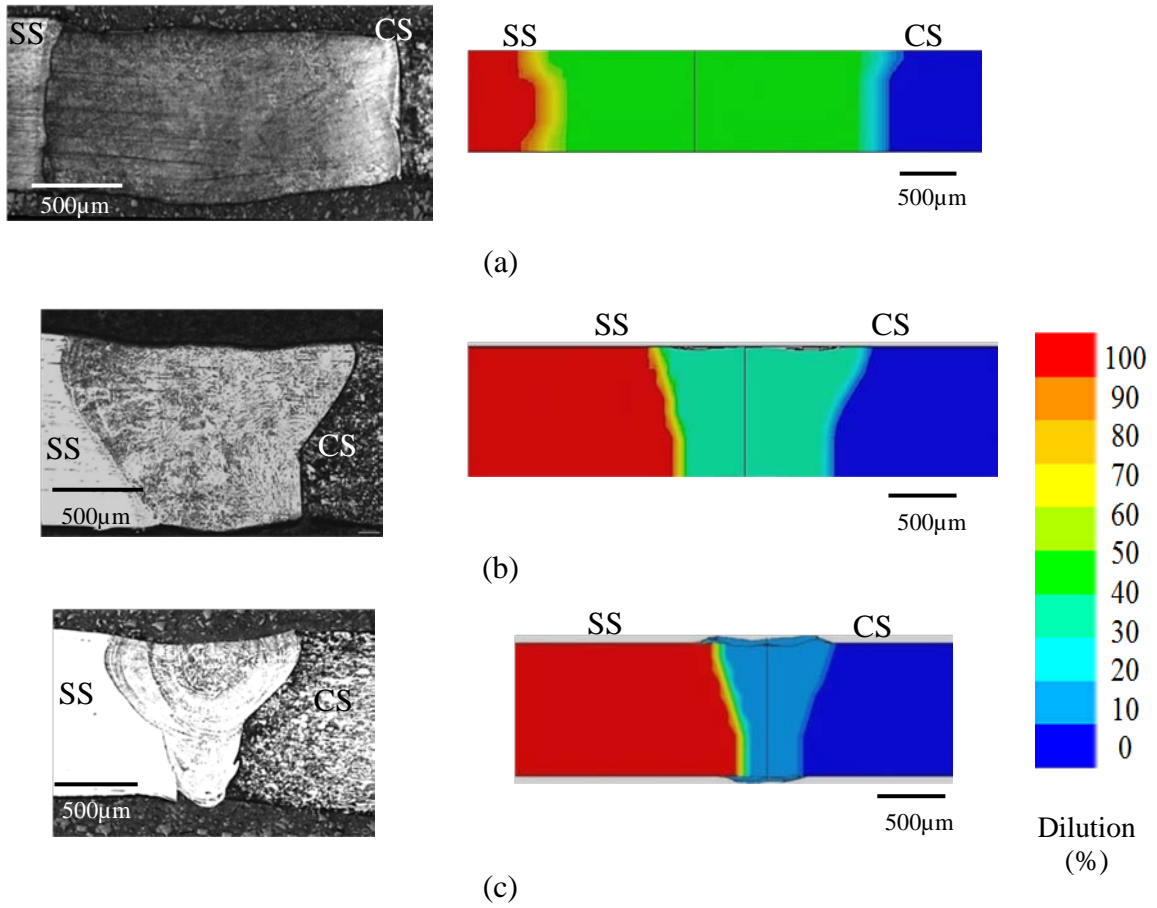
Figure 6-9 Comparison of experimental (left side) and simulated (right side) weld bead cross section profiles for specific point energy of (a) 50J, (b) 17J, (c) 10J
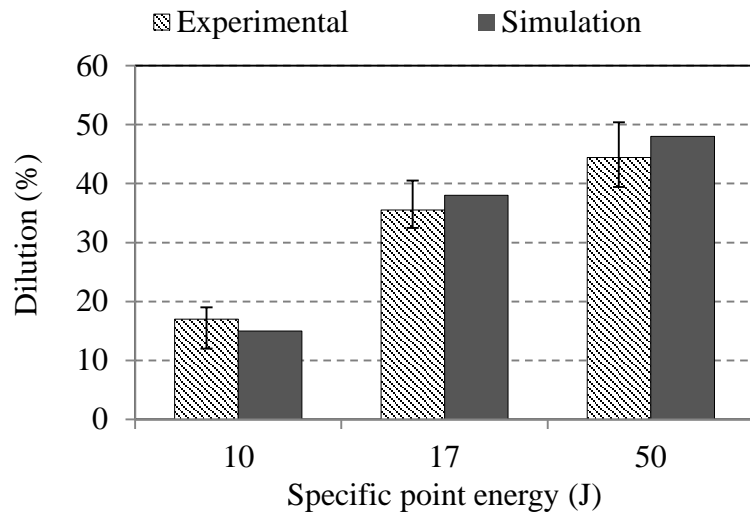
Figure 6-10 Comparison of percentage dilution of the weld bead

146

6.4.2 FEM results

The FEM investigation makes use of the modified geometry and the temperature history predicted by the CFD analysis. As revealed in the flowchart (Figure 6-2), each time step in the structural analysis makes use of a different mesh, generated by the CFD analysis at the corresponding time step. At the end of each time step, the CASE file, which contains information on the mesh geometry and node position, is exported from FLUENT (CFD analysis) and imported in to ANSYS (for thermo-structural analysis). In ANSYS, the imported hexahedral CFD mesh is converted in to solid186 element so as to perform the thermo-structural analysis.

SOLID186 was chosen due to its compatibility with the hexahedral mesh elements (mapped structured mesh) used with fluent. In this way, the surface topological effect of laser processing (CFD analysis) and the material properties are accounted for in the thermo-structural analysis (FEM analysis). Similarly, the thermal results are exported from FLUENT as an ASCII file (containing node number and the corresponding temperature) and imported, and mapped to the thermo-structural analysis geometry as input nodal boundary conditions. In the thermo-structural analysis, stress results are passed from one time step to the next time step (Figure 6-2) as an initial stress condition, thereby maintaining any transient effects.
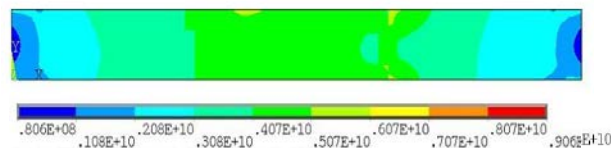
(a)
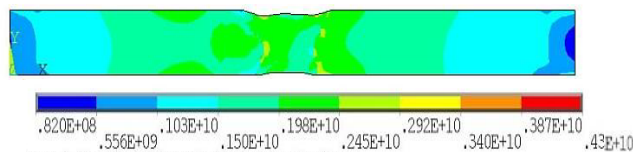
(b)
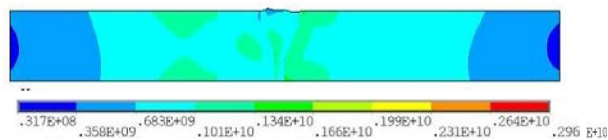
(c)

Figure 6-11 Von Mises stress (Pa) contour along the mid cross section profiles for specific point energy of (a) 50J, (b) 17J, (c) 10J

147

Figure 6-11 depicts the contour plots of Von Mises stress for various specific energies, as predicted by the structural analysis. The stress normal to the direction of weld on the centre of the Z axis along the X-Y plane is shown. The figure indicates that, there is a high stress magnitude for specific point energy of 50J and the magnitude of the stress reduces with a reduction in specific point energy. This is due to the fact that the stress in the structural analysis is primarily due to the thermal gradient and the same trend is noticed for thermal gradient in the thermal analysis. In Figure 6-11, the stress component is predicted to be almost zero at the side of the wall due to the applied constraints. In contrast, in the middle and towards the top surface there are large magnitudes of tensile stress. Most previous thermo-structural models [160, 238-240] use a fixed grid and assume the surface to be flat or in other words all welds to be perfectly net shaped. The variation of stress along the bead surface (Figure 6-12) and along the interface of weld-parent material found for various surface conditions cannot be predicted with the traditional model. Also, most models assume the mechanical properties of the weld to be the same as parent material, which is not the fact in reality. This model considered the actual material property of the weld bead for structural analysis. Plots of the Von Mises stress distribution along the middle the weld at mid-cross section on the X-Z plane is shown in Figure 6-12. As elucidated from the figure, increase in specific energy results in increased magnitude of the residual stress.
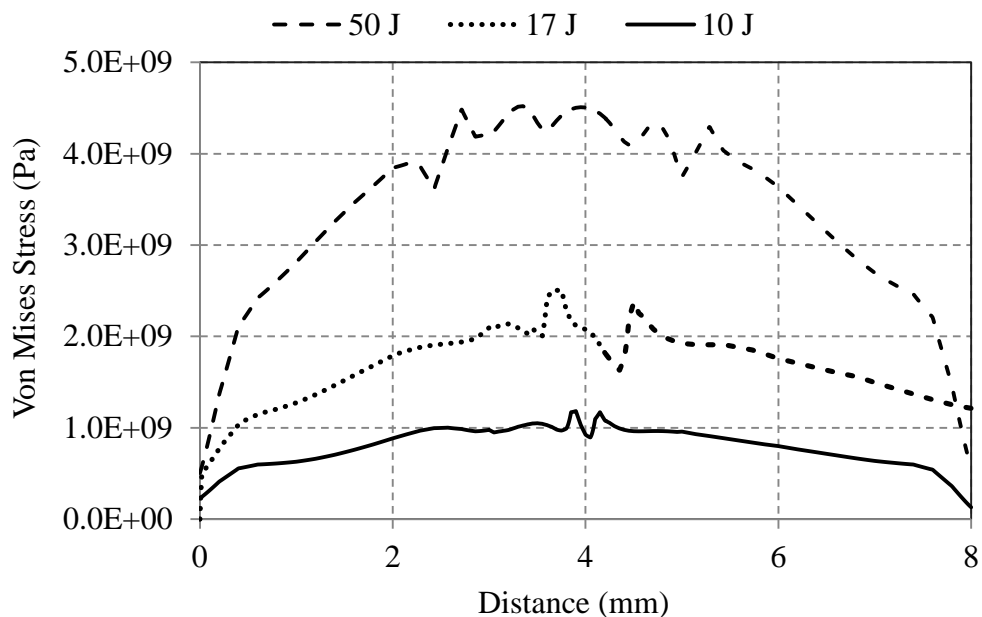
Figure 6-12 Von Mises stress along the middle of mid cross section of the weld sample after cool down to room temperature

6.5   Summary

The heat and mass transfer during laser welding of stainless steel-low carbon steel has been studied using a 3D transient numerical model. The study has demonstrated the prediction of dilution and homogeneity in the fusion zone of a dissimilar laser beam welding. Some of the important findings from the investigation are as follows:

1. The melt pool dynamics, surface topology and fusion zone dilution (alloy mixture) were significantly influenced by the thermal gradient and surface tension of the weld pool. Temperature dependant thermal properties lead to variations in dilution rate of materials in dissimilar laser welding.

2. With increase in laser energy, melt pool convection and mixing within the weld bead increase. Unlike similar materials, a minimum threshold of melt pool convection is essential to achieve a homogeneous weld bead.

3. A predominantly homogenous microstructure and well mixed fusion zone was produced with a specific point energy of greater than 17J for a 1 mm thick dissimilar joint.

4. Irrespective of the laser energy, a significantly low surface tension coefficient can undermine the weld bead homogeneity in dissimilar laser welding.

5. Temperature dependant thermal properties lead to variations in dilution rate of materials in dissimilar laser welding.

6. Using the model, independent predictions are made for a range of laser parameters, and in all cases the results of the numerical model were found to be in close agreement with experimental observations.

Chapter 7 Cooling Rate and its Effects on Dissimilar Laser Welding

7.1 Introduction

The last three chapters discussed the methodologies that can be used to address fundamental issues in laser welding of low carbon steel to stainless steel. This chapter extends the research to laser dissimilar welding of high carbon steel to stainless steel to highlight the importance of cooling rate and study the behaviour of heat affected zone region.

Laser dissimilar welding of high carbon steel is expected to be much more complex due to the inherent nature of high carbon steel to transforming in to hard brittle structure at high cooling rate. This chapter reports an investigation to control the brittle phase formation during laser dissimilar welding of high carbon steel to stainless steel. Whereas, more emphasis is given to the effect of cooling rate on weld microstructure, the significance of alloying composition on the microstructure and phase composition of the fusion zone were also experimentally investigated. Results show that the heat affected zone within the high carbon steel has significantly higher hardness than the weld area which severely undermines the weld quality. The high hardness cannot be addressed by controlling the laser parameters, and a new heat treatment strategy is proposed, to control the brittle phase formation in heat affected zone of high carbon steel.

The dissimilar welding of carbon steels to austenitic stainless steels (SS) has good potential in components such as pressure vessels, boilers, heat exchangers and connector in power plant, oil gas and transportation industry [168, 185]. Austenitic stainless steel is commonly used for components working at relatively high temperature and ferritic or carbon steel is used for components that operate at higher pressures. Nevertheless, fusion welding of dissimilar joints involves metallurgical and technical challenges including, formation of brittle phases, hydrogen cracking and solidification cracking in the fusion zone [3, 9, 69, 216, 241, 242]. Another major concern in

dissimilar welding of austenitic stainless steel-carbon steel is the existence of high hardness phases in the carbon steel HAZ [129, 180]. Such high hardness can lead to cracks formation and brittle phases, which eventually will lead to failure of the dissimilar joint during fabrication or service.

This chapter investigate the significance of cooling rate and alloying composition on controlling the microstructure and mechanical properties of the laser welded HCS and SS joint, and to study the homogeneity range of dissimilar joint and heat affected zone region.

7.2 Previous work

In 1991, an Austrian worker, Blumauer, developed a method of the joining of railway components, consisting of Mn steel and carbon steel, by applying an insert material made of stainless steel. His work was then followed by Zhang [185]. Zhang et al, [185] introduced dissimilar flash butt welding of the high manganese steel crossing and the high carbon steel rail using austenite–ferrite two-phase stainless steel as an insert (Figure 7-1). Their research considered both the flash welded joints of the carbon steel and the stainless steel, as well as the high manganese steel and the stainless steel. They performed annealing treatment (at 900°C for 10min) in order to eliminate the martensitic transformation in the HAZ of the high carbon steel rail and release the existed residual stress via the plastic deformation of the steel. A very promising weld was produced at the end, without martensite transformation at the HAZ and with acceptable tensile and impact strength.
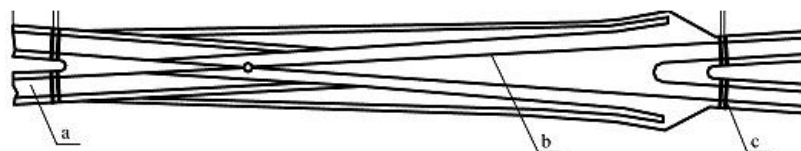
Figure 7-1 Schematic of crossing: (a) High carbon steel rail, (b) High manganese steel crossing and (c) Stainless steel insert.

151

Flash butt welding of high carbon steel to chrome–nickel stainless steel was investigated by Nikulina et al. [243]. A complex structure consisting of several phases was reported. Fatigue crack resistance of the weld joint was also tested and analysed via fractographic analysis. Finally, it was concluded that the creation of martensitic phases and its non-uniform distribution within the structure of the weld is a main reason for the reduction in the fatigue crack resistance of the welded joints.

The effect of various post-weld heat treatments (PWHTs) on the microstructure of gas tungsten arc welded dissimilar medium carbon steel and stainless steel was investigated by Pouraliakbar et al. [129]. They reported the formation of martensitic phases and grain boundary ferrite in the HAZ of medium carbon steel, which is attributed to the high cooling rate observed with the fusion welding process.

Laser welding of high carbon steel was performed by Ng [36] who studied the influence of laser heat treatment on service performance of the high carbon steel weldment. He concluded that the thermal cycle and cooling rate can have noticeable impact on the microstructure and service performance of the welded joint and that it can be significantly reduced via a dual beam technique. Accordingly, lower hardness and better service performance is obtained compare to the normal and pre-heated welds.

David Sa et al. [244] showed that the final microstructure of austenitic stainless steel weld metal is highly dependent on cooling rate and chemical composition. He concluded that rapid solidification of austenitic stainless steel weld metals result in significant alterations in the fusion zone microstructures, ranging from duplex austenitic-ferritic ($\gamma+\delta$) to fully austenitic and fully ferritic. Muthupandi et al. [245], investigated the effect of weld chemical composition, and heat input on the structure and properties of duplex stainless steel welds. They demonstrated that alloying elements concentration have more significant role than heat input and its consequent cooling rate on the ferrite to austenite ratio in the fusion zone.

As noted from literatures, most of the previous studies concentrate on dissimilar welding of low/medium carbon steel and stainless steel. Despite the potential applications [185, 246] of dissimilar welding of high carbon steel (HCS) and stainless steel, very few researches were attempted [185, 243, 246, 247] in this area and the issue of brittle phase formation during the welding of HCS and SS still exists. This is also attributed to the fact that laser welding of HCS and SS is more complex, due to the high cooling rate that prevails in laser processing, which accelerates the martensitic formation in HCS.

7.3 Experimental procedure

As stated earlier in chapter 3, the base materials used in this study was high carbon steel (hyper-eutectoid-BS 4659B01) and stainless steel (AISI 316L) sheets with a thickness of 1mm. The chemical compositions of the HCS and the SS are detailed in chapter 3. The thermo-physical properties of the substrate materials can be noted from the references [189-191]. The sample edges were cleaned and grind prior to welding and are positioned in full contact during the welding. Autogenous dissimilar laser welds were made on 50×50×1mm metal sheets using a continuous wave (CW) CO_2 laser in conduction mode. Figure 7-2 shows a schematic diagram of typical laser conduction welding process. A coaxial nozzle with argon as shielding gas, focus spot size of 0.5mm, and nozzle stand-off distance of 5mm is used for the experiments. Initial trial experiments were carried out to identify feasible processing parameters for the laser welding of HCS to SS.
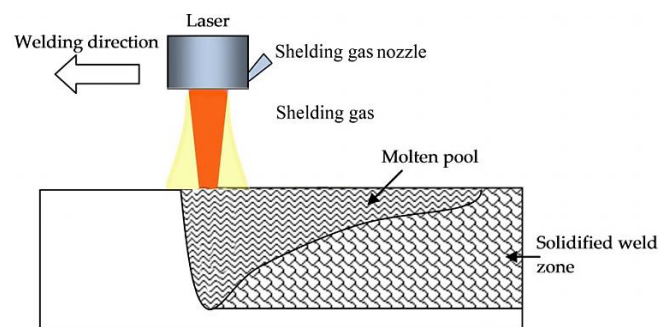
Figure 7-2 Schematic diagram of a laser dissimilar welding process

The laser power, interaction time, beam position, consequent specific point energy and power density were taken as key process variables, and their effects were investigated, with an aim to achieve good weld quality, including, predominantly austenitic microstructure (austenitic weld metal has the advantages of better resistance to hot cracking, higher work hardening rate, higher toughness), minimal variation in hardness across the HAZ and weld [82], and higher tensile strength in the weld (compare to the weaker part of the two parent metals).

To study the influence of cooling rate and alloying elements on the microstructure variation, five levels of input energies were chosen (within the weld-able range to achieve extremely low, average, extremely high cooling rate) and is shown in Table 7-1. A total of 80 experiments were performed with various parameters. Each experiment was repeated twice to confirm the repeatability. Various specific point energies (that will result in a wide range of cooling rate) were chosen, so as to investigate the influence of cooling rate on weld microstructure. The beam position with reference to the joint was shifted by up to ±0.4mm with an increments of 0.05mm, to study the influence the alloying concentration [5] on weld quality. The specific point energy was controlled based on the scanning speed with constant laser power [136]. Specific point energy (Equation 1) takes into account welding speed (V), laser beam diameter (D) and laser power (P) and is given by Eq.1 [136]:

$$Specific\ Point\ energy = \frac{P \times D}{V} \qquad\qquad E.q(1)$$

Table 7-1 Laser dissimilar welding parameters used in present investigation

	Speed (mm/s)	Power (W)	Specific point energy (J)	Beam offset (mm)
1	5	500	50	±0.4mm, increments of 0.05mm
2	7.5	500	33	±0.4mm, increments of 0.05mm
3	10	500	25	±0.4mm, increments of 0.05mm
4	12.5	500	20	±0.4mm, increments of 0.05mm
5	15	500	17	±0.4mm, increments of 0.05mm

The cooling rates values were calculated using analytical solution of one dimensional heat equation. The calculations were performed using the Adams and Rosenthal approach [228] and it provides a realistic estimate of the cooling rate [244]. The equation incorporates the influence of laser power, welding speed, and preheating temperature. Melting temperature of 1450°C and laser absorptivity of 20% was considered for all analytical calculations. The initial temperature was assumed as ambient temperature. The cooling rate is calculated based on the following equation [228]:

$$\frac{2\pi(T-T_0)kR}{Q} = exp\left[\frac{-V(R-x)}{2\alpha}\right] \qquad\qquad E.q\,(2)$$

Here T is liquidus temperature, T_0 is the workpiece temperature before welding (preheating temperature), k is workpiece thermal conductivity, Q is heat transferred from heat source to workpiece, V is the welding speed, α is the workpiece thermal diffusivity, namely, $k/\rho C$ (where ρ and C are density and specific heat of the workpiece respectively), and R is radial distance from the beam centre.

Considering $R=x$ (along the x axis of the workpiece), equation 2 can be written as follows:

$$T - T_0 = \frac{Q}{2\pi k x} \qquad\qquad E.q(3)$$

Hence, the temperature gradient along x direction is:

$$\left(\frac{\partial T}{\partial x}\right)_t = \frac{Q}{2\pi k}\frac{-1}{x^2} = -2\pi k\frac{(T-T_0)^2}{Q} \qquad\qquad E.q(4)$$

From above equation and by considering:

$$\left(\frac{\partial x}{\partial t}\right)_T = V \qquad\qquad E.q(5)$$

The cooling rate can be derived as follows:

$$\left(\frac{\partial T}{\partial t}\right)_x = \left(\frac{\partial T}{\partial x}\right)_t\left(\frac{\partial x}{\partial t}\right)_T = -2\pi kV\frac{(T-T_0)^2}{Q} \qquad\qquad E.q(6)$$

The thermal conductivity (in W/(m °K)) of the weld zone in the cooling rate equation was calculated based on the alloying concentration (dilution) of the weld zone [5] and the preheating temperature was taken as room temperature (in °C). The cooling rates (Equation 6) were calculated for a liquidus temperature of 1450°C [244].

As discussed in chapter 3, the laser welded samples were prepared for metallographic analysis as per ASTM E3-11 standards [196]. Metallographic samples were etched using the three etchants which are aforementioned in chapter 3. Microstructural characterizations of dissimilar joints were performed on their cross-sections by using both optical microscopy and SEM accompanied by EDS. A ferrite-scope was used to measure the ferrite number of the weld metals. To study and quantify the relationship between the microstructure and mechanical properties of the dissimilar joint, Vickers hardness of the weld metal was measured and tensile testing of cross-weld joints were performed according to ASTM E8M-04 (further detail of experimental procedure is discussed in chapter 3).

7.4 Results and discussion

7.4.1 Microstructural evaluation

Microstructure of the dissimilar joints depends mainly on the cooling rate and chemical composition [181, 248]. This is of significant importance for materials with high carbon content, that use technology such as laser welding, which operates at high cooling rate [9].

Figures 7.3(a-d) illustrate the optical microstructure of the laser welded SS-HCS. Figures 7.3(a) and (b) show the optical microstructure of as received HCS and SS respectively. As can be noticed from the figures, the microstructure of high carbon steel consists of ferrite with high amount of perlite (ferrite+globular cementite) (Figure 7-3(a)), and as shown in Figure 7-3(b), the microstructure of stainless steel was predominantly of equiaxed austenitic grains (γ).

Figures 7.3(c), 7.3(d) and 7.3(e) shows the optical microstructure of the HCS HAZ, the SS HAZ and fusion zone respectively. As noted from the figure, the microstructure of fusion zone was predominantly homogeneous and the microstructure of the HAZ

shows significant variations (from mainly pearlite to combination of martensite, and lower bainite microstructure). This is attributed to the high magnitude of melt pool convention in the fusion zone, which homogenizes the fusion zone microstructure [5]. The high thermal gradient of LBW process (excess of $10^5 °C/s$) along with high carbon content resulted in significant microstructural variation in the HCS HAZ [249]. It is worth mentioning that the microstructure variation is not noticeable in the HAZ of SS due to the non-transformable nature of austenitic stainless steel [5]. However, some austenite recrystallized grains can be seen in the SS HAZ (Figure. 7.3(d)) but they are not of significant concern [4].

(a) HCS base   (b) SS Base

(c) HCS HAZ   (d) SS HAZ

(e) Fusion zone
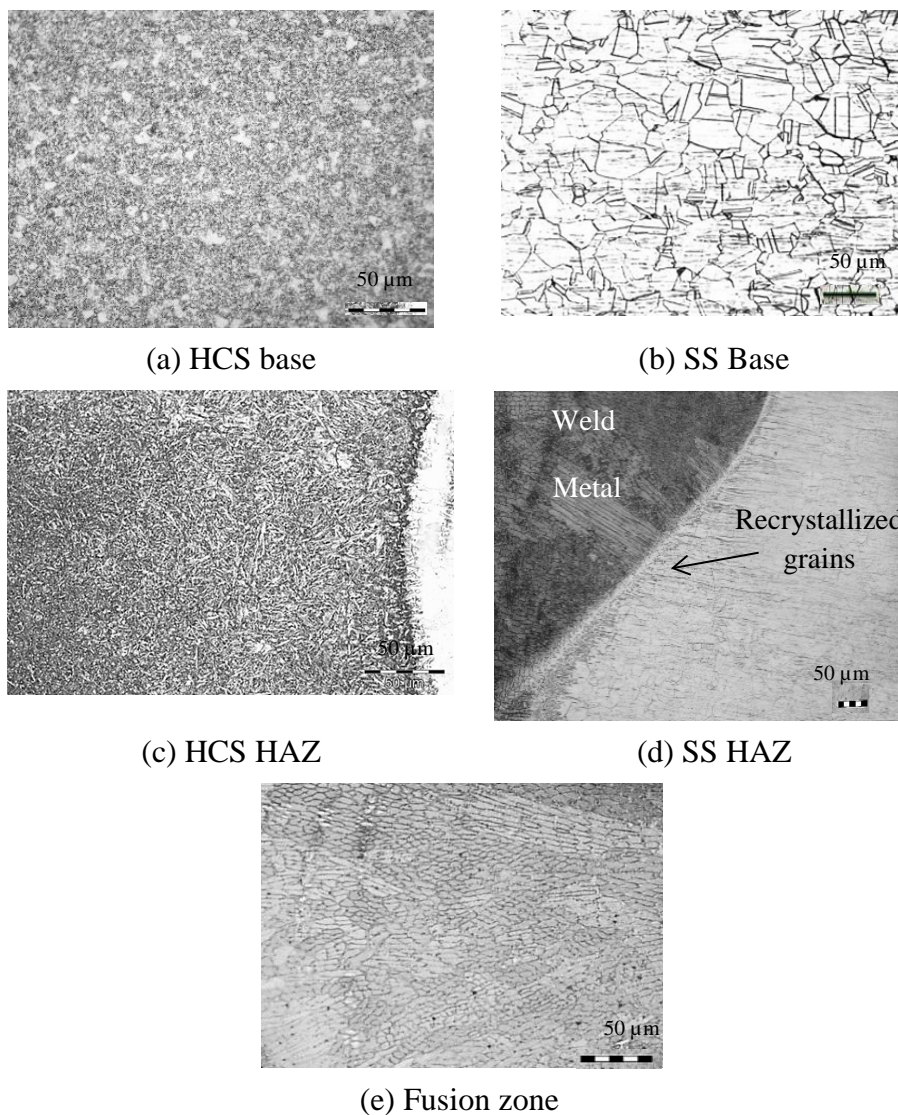
Figure 7-3 Optical micrograph of the parent metals and microstructures gradient in the HAZ of HCS (power = 500W, welding speed = 10mm/s, beam offset = -0.4mm)

A typical macrostructure of an austenitic/ferritic dissimilar laser welding can be seen in Figure 7-4. As can be seen in the figure, the solidification structure of the bulk fusion zone was predominantly fine columnar dendrites which had been nucleated at the fusion line and grown toward the centre of the molten pool. Dendritic structure is attributed to the very high cooling rate, which is around 10^4–10^6°C/s in the fusion zone of the laser welds [4, 249]. While the bulk of the dissimilar fusion zone solidified as above, the region near the stainless steel base metal fusion boundary displayed a cellular structure. This is due to the differences between the rates of undercooling at various areas of the weld.

It can also be seen from the figure that the weld microstructure is predominantly of austenitic-ferritic. Primary solidification of austenitic steels can occur as either austenite or ferrite. At higher Cr/Ni ratios, primary solidification occurs as δ-ferrite (FA solidification type) while at lower ratios, the solidification mode transforms to austenite (AF solidification type) [4, 250].
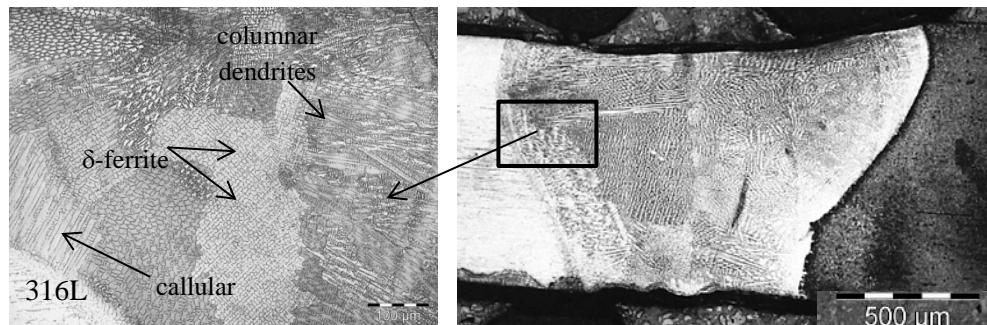
Figure 7-4 Optical micrograph of the laser welded HCS-SS fusion zone (power = 500W, welding speed = 10mm/s, beam offset = -0.4mm)

SEM-EDX analysis was performed on interdendritic zone of the weld illustrated in Figure 7-4, and the spectrum and alloying elements results is shown in Figure 7-5. Analysis result based on Ni and Cr contents proved the existence of delta ferrite in austenite grains. As a result of sufficient chromium content in the weld and due to segregation during solidification, some ferrite may form in the intercellular regions in the weld microstructure, resulting in an AF mode of solidification (primary austenite dendrites with some interdendritic δ ferrite).

It is also worth noting that the percentage of austenite, ferrite and martensitic microstructure within the fusion zone has been found to be very sensitive to alloying composition as well as kinetic factors (cooling rate) [5], and can change dramatically as the above factors vary during welding process.
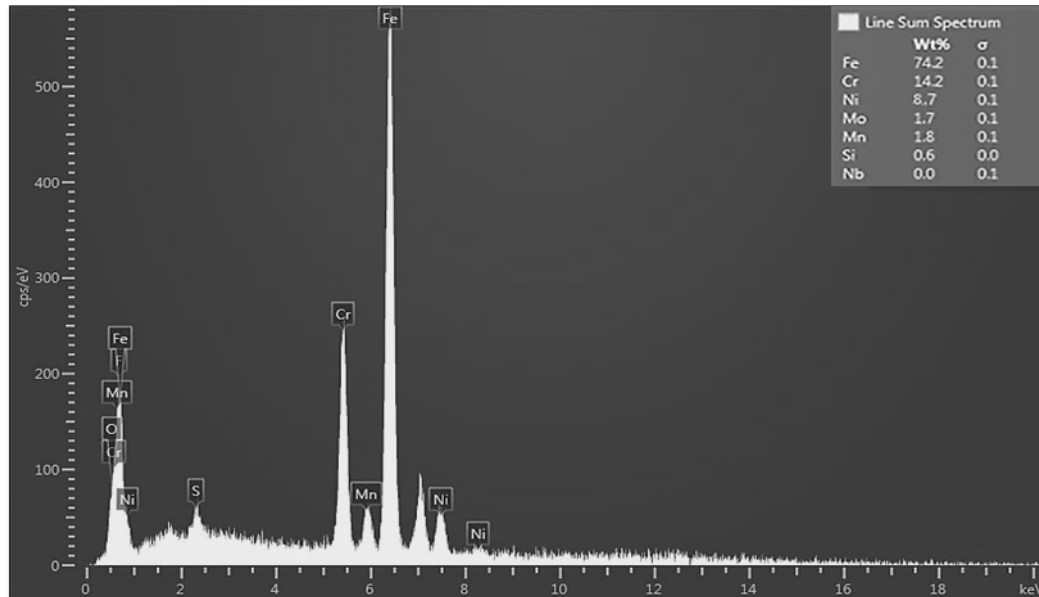
Figure 7-5 EDX spectra and chemical analysis of ferrite region (power = 500W, welding speed = 10mm/s, beam offset = -0.4mm)

7.4.2 Effect of cooling rate and alloying composition

The effect of the cooling rate and alloying element concentration on the consequent microstructure of the weld zone is shown in Table 7.2. As can be observed from the table, three distinct microstructures containing $(\gamma+\delta, \gamma+M, M)$ were noticed in the weld bead which their concentration are predominantly dependant on the alloying content and cooling rate. In addition, it can be seen, from the table, that decreasing the alloying content results in change of the microstructure from austenitic-ferritic $(\gamma+\delta)$ to completely martensitic (M). Figure 7-6(a), (b) and (c) illustrate the optical micrograph of various alloying elements levels at a constant cooling rate $(0.057 \times 10^{6} \,°C/sec)$.

(γ+δ)	(M)	(M)

(a) Cr 13%,Ni 7%	(b) Cr 9.6% Ni 5.2%	(c) Cr 4%, Ni 2.1%)
Cooling rate = 0.057×10^6 °C/sec		
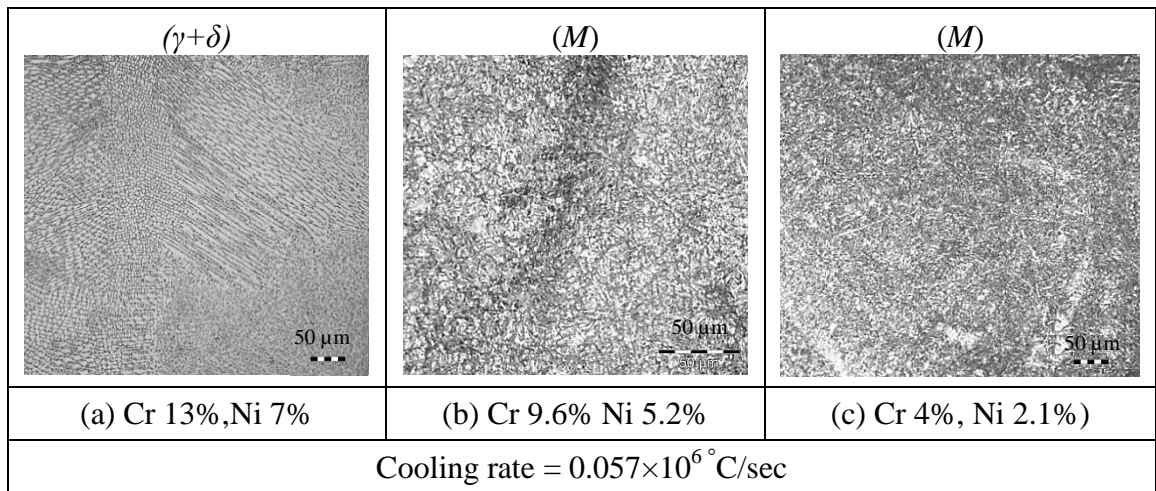
Figure 7-6 Effect of alloying concentration on the microstructure (a) Primary austenitic γ dendrites (light) with interdendritic δ ferrite, (b) Martensite, (c) Martensite

Table 7-2 Effect of cooling rate and alloying concentration on weld microstructure

Specific point energy (J)	Weld alloying element concentration [wt%]					Average cooling rate (10^6°C/sec)
	Cr 13% Ni 7%	Cr 11% Ni 6%	Cr 9.6% Ni 5.2%	Cr 7.37% Ni 3.8%	Cr 4% Ni 2.1%	
50	(γ+δ)	(γ+δ)	(γ+M)	(γ+M)	(M)	0.028
	-0.4	-0.3	-0.25	0	0.1	
33	(γ+δ)	(γ+δ)	(γ+M)	(γ+M)	(M)	0.043
	-0.35	-0.25	-0.1	0.1	0.15	
25	(γ+δ)	(γ+δ)	(M)	(M)	(M)	0.057
	-0.3	-0.2	0	0.15	0.2	
20	(γ+δ)	(γ+M)	(M)	(M)	(M)	0.071
	-0.1	0	0.1	0.25	0.3	
17	(γ+δ)	(γ+M)	(M)	(M)	(M)	0.085
	0	0.15	0.2	0.3	0.4	
	γ+δ = Austenitic-Ferritic; γ+M = Austenitic-Martensitic; M = Martensitic Beam offset toward stainless steel (-) Beam offset toward carbon steel (+)					

Table 7.2 summarises the key results of the experimentation (effect of the cooling rate and alloying element concentration on the consequent microstructure of the weld zone) performed using the parameters shown in table 7.2. The results were organised, so as to analyse the effect of alloying concentration with constant cooling rate, and the effect of cooling rate with constant alloying concentration. The alloying concentration (Cr%; Ni%) given in Table 7.2 was established through EDS analysis of the weld bead, and the microstructure was established by optical microscopy. The cooling rate given in Table 7.2 was calculated using equation 6. The variation of cooling rate with beam offset (alloying concentration) at each level of specific point energy was insignificant ($\pm 0.009 \times 10^{6}$ °C/sec) and an average was considered.

As seen from Table 7.2, increase in cooling rate at high level of alloying concentration (Cr 13%, Ni 7%) results in a transition of the weld microstructure from primary dendrite of (γ austenite with interdendritic δ ferrite) to primarily austenitic-dendrites. The microstructural modifications at high alloying concentration (Cr 13%, Ni 7%) are predominantly due to changes in the primary mode of solidification at high cooling rate. At low and intermediate cooling rates, the microstructure remains a mixture of austenite and ferrite as a result of segregation of the ferrite in the intercellular regions. However, as cooling rate increases, the microstructure will be predominantly austenitic (and hence lower Ferrite). This is consistent with the ferritometry test (Figure 7-7) of the weldment for the three levels of cooling rate at the constant alloying concentration.
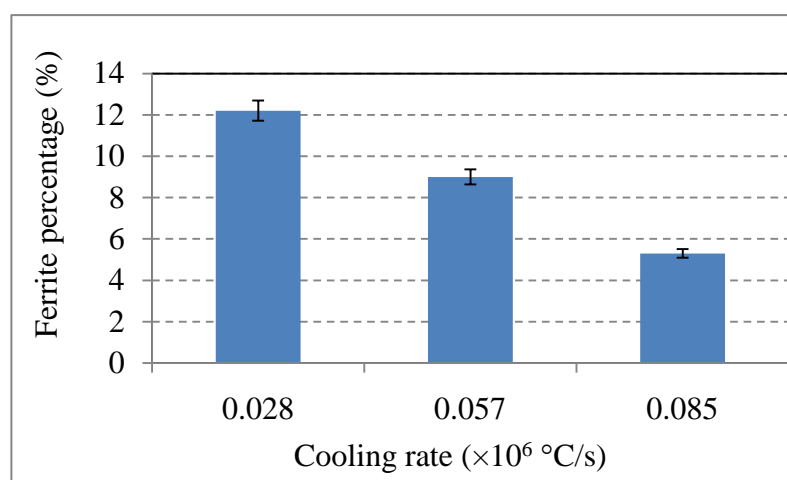
Figure 7-7 Effect of cooling rate on the percentage ferrite (0.028×10^{6} °C/sec, 0.057×10^{6} °C/sec, and 0.085×10^{6} °C/sec)

Figure 7-8 shows the effect of cooling rate at constant alloying composition of Cr 9.6%, and Ni 5.2%. Variation of cooling rate from 0.028 to 0.085 (10^6 °C/sec) at constant alloying concentration (Cr 9.6%, Ni 5.2%), result in microstructural transformation from austenitic-martensitic ($\gamma+M$) to predominantly martensitic (M). However, at lower alloying concentration (below Cr 9.6%, Ni 5.2%), the effect of cooling rate on the final microstructure becomes much more significantly, and experimental parameters at this range should be avoided.

($\gamma+M$)	(M)	(M)
(a) 0.028×10^6 °C/sec	(b) 0.057×10^6 °C/sec	(b) 0.085×10^6 °C/sec
Alloying Composition = Cr 9.6%, Ni 5.2%		
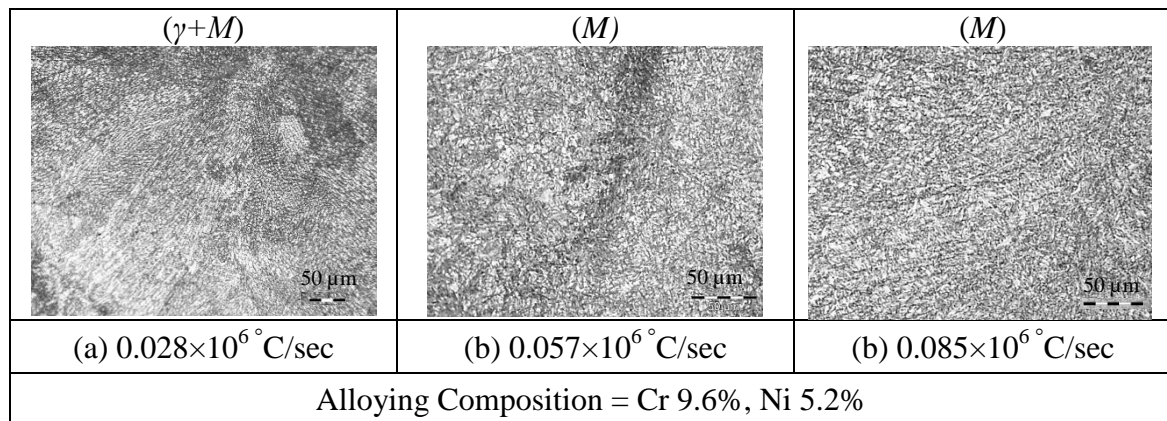
Figure 7-8 Effect of cooling rate on the microstructure (a) Austenitic-martensitic microstructure, (b) Martensite, (c) Martensite

Figure 7-9 shows the results of the micro hardness test, which confirms the phase transition behaviour (Figure 7-6 and 7-8) that occurs due to change in cooling rate and alloying concentration. As can be seen from Figure 7-9, increase in cooling rate results in increased hardness values. This is attributed to the formation of smaller size grains with increase in cooling rate and hence an increase in material resistance to plastic deformation. It can also be inferred that the effect of cooling rate on micro-hardness is low at high level of alloying content (e.g: 13% Cr; 7% Ni). This is due to the fact that higher alloying elements content restrict the phase transition (from austenite phase) [5, 125] and hence, the microstructure remain predominantly austenitic-ferritic ($\gamma+\delta$) irrespective of the cooling rate. However at low alloying content level (Figure 7-9; e.g: 4%Cr; 2.1%Ni) (due to higher dilution rate of HCS), the phase transition was significant. This is attributed to the higher carbon concentration in the fusion zone accompanied by high cooling rate, which results in martensitic formation.
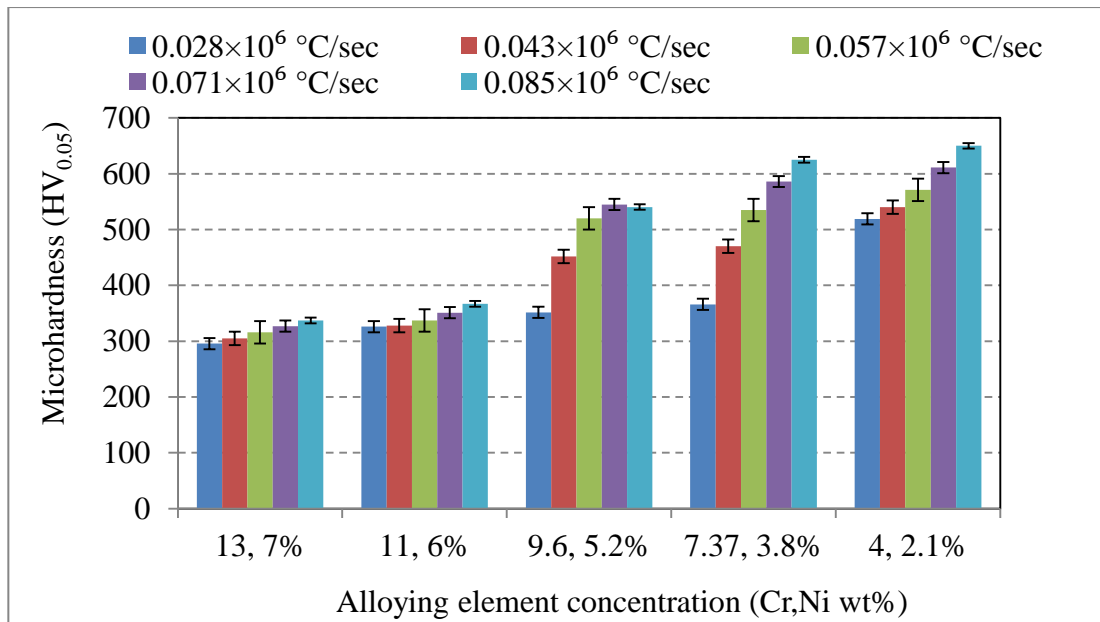
Figure 7-9 Effect of cooling rate and alloying concentration on weld microhardness

The formation of martensite is not favourable as it can lead to crack formation and weak in-service performance of the joint [4, 82, 111, 219, 242]. In order to have an austenitic weld metal, it is essential to maintain the higher alloying composition (greater than Cr 9.6%, Ni 5.2%) and cooling rate less than 0.085×10^{6}°C/sec. Accordingly, the weldment with cooling rate of 0.057×10^{6} °C/sec and alloying composition of (Cr 11%, Ni 6%) was chosen for further investigation (25J specific point energy and 0.2mm offset toward SS).

7.4.3   Mechanical performance of the dissimilar joint

Tensile tests were performed on the laser welded HCS-SS samples to assess its mechanical performance. Figure 7-10 shows the tensile stress-strain curve of the tested samples. The failure occurred at the heat affected zone of HCS and in a very brittle manner. SEM micrograph of the fractured HCS HAZ surface (tensile specimens in Figure 7-10) is illustrated in Figure 7-11. Presence of crystal planes (fine faceted cleavage) and the evident of cleavage fracture confirm that the failure occurred in a very brittle manner which is attributed to substantially low toughness in the HAZ region.
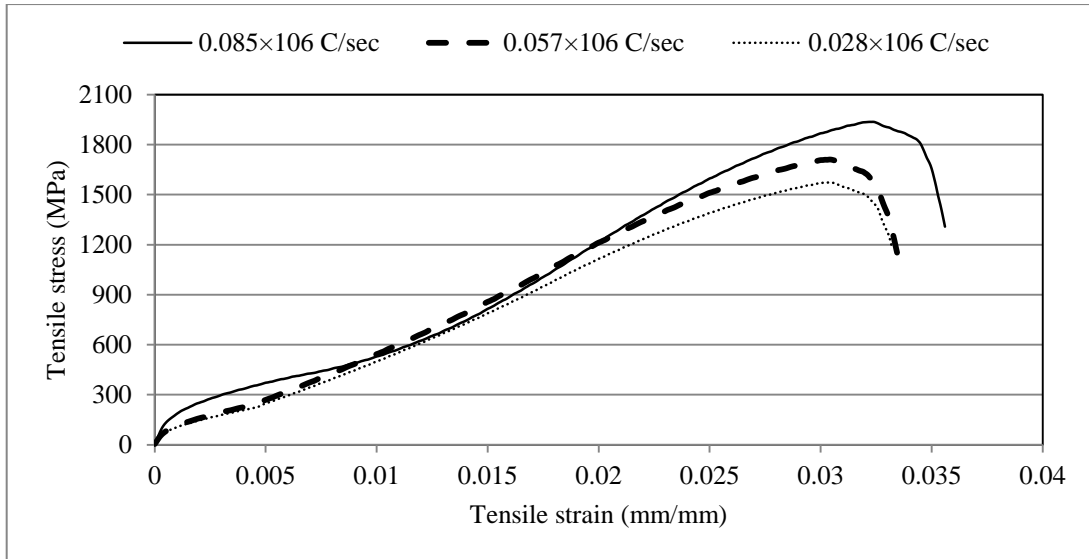
Figure 7-10 Tensile Stress-strain curve of LBW welded joint between SS and HCS
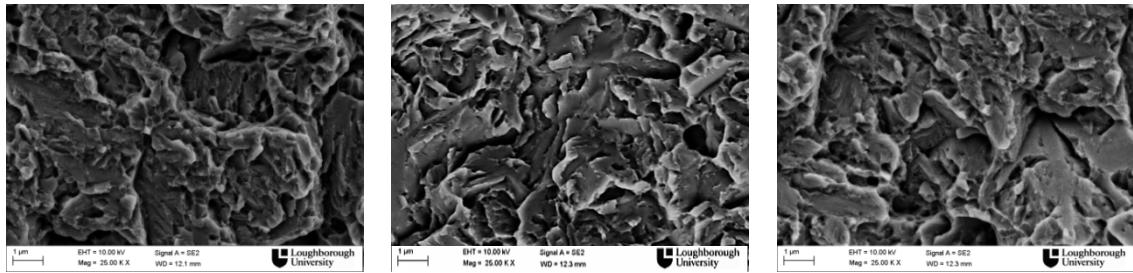
(a) 0.028×10^6 °C/sec   (b) 0.057×10^6 °C/sec   (c) 0.085×10^6 °C/sec

Figure 7-11 SEM micrograph of fracture surface of HCS HAZ after tensile testing

Further investigation on the hardness profiles of weld specimens with 0.028, 0.057, and 0.085×10^6 °C/sec (Figure 7-12) reveals a spike in hardness of the HCS HAZ. The high hardness value in the HAZ region is due to the change of microstructure from primarily pearlite to martensite structure with supersaturated carbon atoms in its crystal lattice. It seems the high cooling rate (despite of its positive role in weld microstructure at sufficient alloying level) resulted in a brittle and high hardness phase at the HCS HAZ. Irrespective of the weld microstructure and alloying composition, the high hardness and its uneven variation in the HAZ (Figure 7-3a) can significantly undermine the quality of the welded joint [5, 163]. The spike in the hardness is attributed to the cooling rate, which cannot be controlled by changing the alloying concentration. A new methodology is required to control the HCS HAZ, which is discussed in the next chapter.
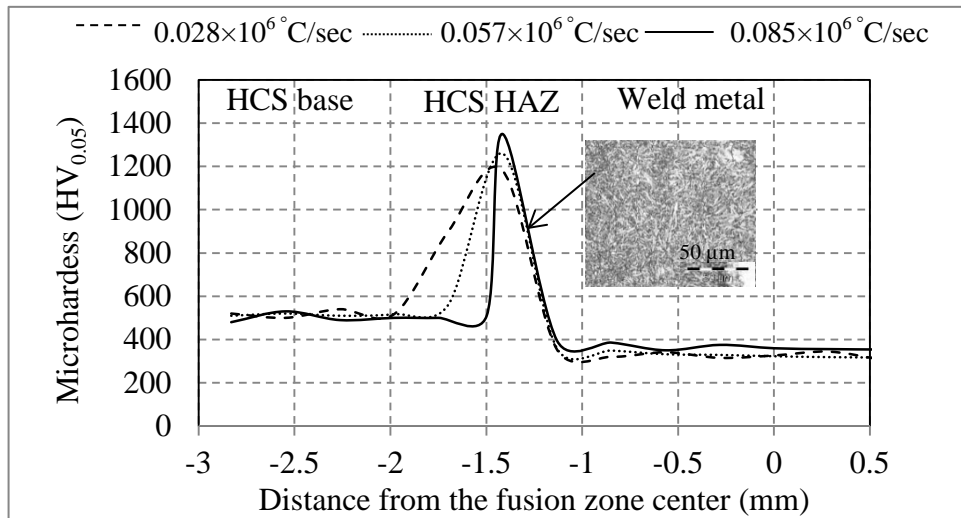
Figure 7-12 Micro-hardness profile of the dissimilar weld at various cooling rates (Cr 11%, Ni 6%)

7.5 Summary

In this chapter, the effect cooling rate and alloying element on the laser welding of high carbon to austenitic stainless steel was investigated. The microstructure, diffusion, hardness, and weld strength of the dissimilar weld zone were studied. The following conclusions are made from the experiments analysis:

1. Alloying composition and cooling rate significantly affects the microstructure of the laser welded HCS-SS fusion zone.
2. The laser parameters can be used to control the characteristic of the fusion zone, however its effect on HCS HAZ is minimal.
3. High cooling rate results in brittle phase at the HCS HAZ.
4. The effect of cooling rate on fusion zone microstructure is significant on material with higher carbon content.
5. During welding of high carbon steel to stainless steel, no noticeable microstructural variation was observed at the HAZ of stainless steel.
6. The martensitic microstructure in the HAZ of HCS affects the homogeneity of the weldment and can undermine the service performance of the welded joint.

Chapter 8 Numerical Simulation on Control of Cooling Rate in Laser Dissimilar Welding

8.1 Introduction

As discussed in the last chapter, laser parameters can be used to control the characteristic of the fusion zone, however its effect on the microstructure of HCS HAZ is minimal. The hard brittle phase (as a result of martensitic transformation) at the HAZ of HCS can significantly affects the homogeneity of the weldment and can leads to poor toughness and ductility that may result in crack formation and brittle fracture. The high hardness cannot be addressed by just controlling the laser parameters, but needs high control over the cooling rate of the respective material. A heat treatment strategy was proposed in this chapter to control the cooling rate of the heat affected zone of high carbon steel. Along with experimentation, a finite element analysis based numerical model was developed to achieve a heat treatment methodology that will produce a weld with optimum in-service performance.

8.2 Previous works

Numerical analysis was used as an effective tool to control the phase transformation in hard to weld materials like P92 or high carbon steel [163, 166, 174, 251-256]. Yaghi [108] developed a FE simulation of residual stresses during arc-welding of a P92 steel pipe. His model incorporated the different phase transformation into the structural analysis. In addition, the effects of post weld heat treatment (PWHT) (including both holding time and constants in the Norton creep law) on the residual stress distribution have been investigated. Figure 8-1 illustrates their result for martensite fraction of a solidified weld and HAZ in room temperature. Different phase transformations inside the steel's molten pool and HAZ are studied and their contradictory plastic and hardening behaviour over a wide range of temperature are investigated. The applied PWHT technique has shown to reduce very high tensile residual axial and hoop stresses, observed at the outside surface of the welded pipe, to approximately half the original value or even less.
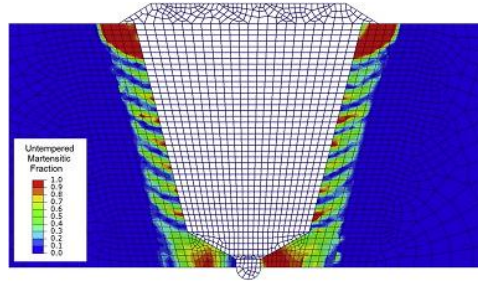
Figure 8-1 Martensite fraction of the P92 steel pipe joint [108]

A dual beam technique was employed by Ng [36] to investigate the effect of laser heat treatment on mechanical properties of the high carbon steel weldment. He concluded that the rapid cooling rate of the laser welding and the formation of brittle phases in the weld can be significantly controlled by using a post heating technique. Using such a technique, he achieved to produce a weld with low hardness and better mechanical properties compare to the normal and pre-heated welds.

Tawfik et al. [257] studied the effect of localised, rapid post-weld heat treatment on residual stresses of high carbon steel during flash-butt welding. Tawfik used a high pressure gas burner to perform localised post-weld heat treatment in the rail foot as shown in Figure 8-2. He used a sequentially coupled thermo-mechanical finite element (FE) model incorporating the phase transformation characteristics to analyse the mechanical properties of the joint and high carbon steel's HAZ. He showed that varying the post-weld cooling condition by reheating (reducing the cooling rate of the rail foot), can significantly reduce the magnitude of the residual stresses without affecting the microstructural characteristics of the rail material.
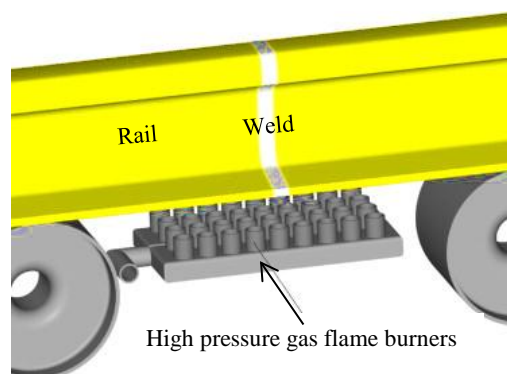
Figure 8-2 Post-weld heat treatment setup used for flash-butt welding

Deng and Murakawa [224] investigated the temperature field, microstructure and service performance in a multipass butt welded joint of 2.25Cr-1Mo steel pipes, considering the influence of solid state phase transformation. It was discussed that in order to obtain an accurate prediction of the joint stress filed in the joint, it is essential to consider phase dependent material properties.

In an investigation carried out by Lee et al. [166], the effect of cooling rate on the mechanical properties of carbon and stainless steel butt weld was investigated using a FE simulation. They found that the residual stress is higher inside the stainless steel weld metal due to its lower thermal conductivity and larger coefficient of thermal expansion compare to carbon steel.

Becker et al. [258] investigated phase transformation, phase dependent material properties and residual stresses using experimentally obtained continuously cooling transformation (CCT) diagrams.

Deng [163] reported that the solid state phase transformation in medium carbon steel has significantly higher influence on residual stresses and distortion magnitude than low carbon steel. This is due to larger dilatation and lower transformation temperature.
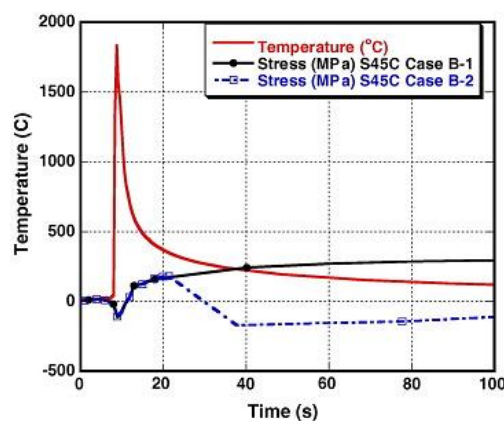
Figure 8-3 Temperature and stress history of a point in fusion zone with (Case B-2) and without (Case B-1) the consideration of martensitic phase transformation [163]

Figure 8-3 shows his results for the sensitivity of medium carbon steel's residual stress to martensitic phase transformation at fusion zone. Within the martensitic transformation range (Case B-2), a compressive stress is generated during undercooling because of a large volume change of austenite to martensite. On the other hand, under the condition of ignoring the phase transformation effect (Case B-1), a very high tensile stress existed in the weld zone. Comparing the results of medium carbon steel to low carbon steel, he concluded that martensitic transformation has a significant effect on the residual stress for medium carbon steel but has less influence for low carbon steel.

As noted from the literature, heat treatment can be used to control the solid state phase transformation in the weld and HAZ microstructure. The present study aims to use heat treatment as an efficient tool to control the cooling rate of the HCS HAZ during the laser welding of HCS-SS. Along with experimentation, a finite element analysis based numerical model was developed to achieve a heat treatment methodology that will produce a weld with optimum in-service performance.

8.3 Finite element modelling

8.3.1 Thermal analysis

A numerical model was developed based on finite element (FEA) formulation, to establish the optimum cooling rate of the HCS HAZ to reduce martensitic formation. The FEA model was based on sequentially coupled thermal-metallurgical formulation and was solved using ANSYS [231] codes. In laser welding of HCS, the martensitic transformation of the solid material (HAZ) occurs during the cooling cycle, between 800°C and 500°C ($\nabla t_{8/5}$) [166]. A secondary heat source was used in the FEA model to simulate heat treatment so as to achieve the controlled cooling rate. The secondary heat source maintains the welded joint (fusion zone and HAZ) at 800°C till the end of welding cycle, and cools the joint with a controlled cooling rate.

The laser welding parameters were kept constant as optimum parameters which are derived from previous chapter (specific energy of 25J). Three set of scenarios where chosen to investigate the influence of three heat treatment times (referred to as short, intermediate and long) on the martensitic phase formation in HCS HAZ:

169

Case-I: Uncontrolled cooling rate of $\nabla t_{8/5}$=0.1sec (without any heat treatment);

Case-II: Controlled cooling rate of $\nabla t_{8/5}$=40sec;

Case-III: Controlled cooling rate of $\nabla t_{8/5}$=140sec.

All the analyses are performed incorporating temperature dependent thermal properties of the base metal. The following assumptions are made in the formulation of the FE model:

- As the main focus is on HAZ, the meltpool phenomena such as Marangoni effects, buoyancy force and viscous force were not considered in the model;
- There is no chemical reaction or oxidation in the melt pool;
- The two plates of dissimilar materials were in perfect contact;
- Thermal properties of the material like density, specific heat and conductivity are temperature-dependent.

The prediction of transformation to martensitic microstructure for each element within the FEA model was performed based on its peak temperature (during welding process), and the cooling time from 800$^{\text{o}}$C to 500$^{\text{o}}$C ($\nabla t_{8/5}$) (during cooling process) [166]. Accordingly, the heat conduction problem is solved firstly in the weldment, and its results employed later in developed subroutines to describe A-M transformation. The following equation can be used to describe temperature variations inside the parts being welded:

$$\frac{\partial}{\partial x}\left(k\frac{\partial T}{\partial x}\right) + \frac{\partial}{\partial y}\left(k\frac{\partial T}{\partial y}\right) + \frac{\partial}{\partial z}\left(k\frac{\partial T}{\partial z}\right) + Q(x,y) = \rho C\frac{\partial T}{\partial t} \qquad \text{E. q(1)}$$

Here T denotes the temperature, k the thermal conductivity, C the specific heat, Q the heat flux, t welding time, and x, y and z show welding directions, transverse direction and thickness direction, respectively. At the beginning of the process, i.e., $t = 0$, the entire model was at the 800°C temperature while during welding (Case-II and Case-III), the boundary conditions were taken into account. Convection heat loss boundary conditions were assumed on surface boundaries except for the region affected by the laser beam, as presented in Eq. 2:

$$k\frac{\partial T}{\partial n} = h(T - T_a)$$
E.q(2)

Where n denotes the normal direction to the surface boundary, T_a is the ambient temperature and h is convection heat transfer coefficient. The convection coefficient was taken as $20\text{W/m}^2\text{K}$ for the surfaces in contact with ambient air. For the surfaces that are in contact with the backing plate, the convection coefficient was taken as $80\text{W/m}^2\text{K}$.

A code written as Ansys APDL programming language was used in order to apply a heat flux as a transient boundary condition on the top surface of the weld and the heat flux is given by:

$$Q(x, y) = \frac{P(1 - r_f)}{r_b^2 \pi} \exp\left(-\frac{2r}{r_b^2}\right)$$
E.q(3)

where P is the total laser power, r_f is the reflectivity of the material, r is radial position within the beam and r_b is the laser beam diameter.

In this study, a mesh model as shown in Figure 8-4 was used. The computational domain with a dimension: length, L = 50mm, width, W = 50mm and thickness B = 1mm has been considered for computation.
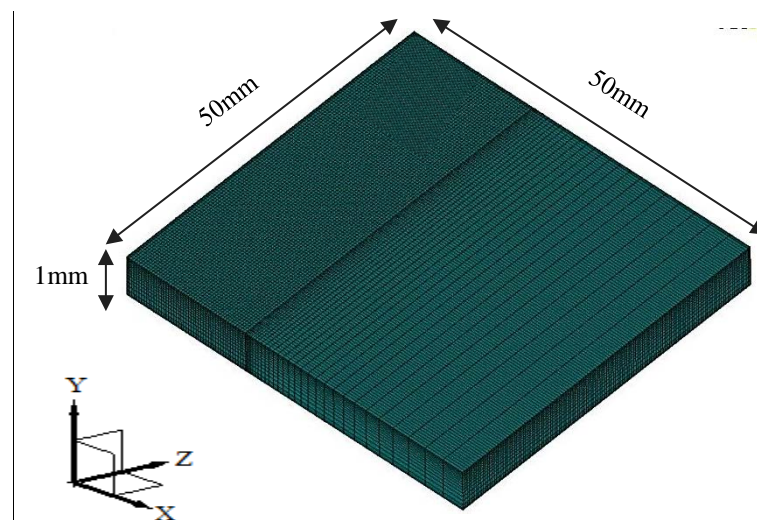
Figure 8-4 Mesh model used for the analysis

Since the thermal conductivity of SS is considerably lower than HCS at solid state and no noticeable microstructural transformation occurs in SS HAZ [4, 5], modelling of heat treatment is conducted only for HCS. This can guarantee more precise prediction of phases. Hence, only one half of the model was selected as the analysis model. Since it was expected to have severe temperature gradient close to the beam interaction with workpieces, very fine elements are chosen in weld pool region to achieve accurate results. Thus, the mesh is generated in such a way that the size of the elements increase exponentially in the transverse direction, i.e., the x-axis. For all the three scenarios, the calculation was carried out with a uniform structured mesh composed of 100,000 hexahedral cells. Temperature-dependent material properties were employed for high carbon steel, and the thermo-physical properties are detailed in chapter 3.

8.3.2   Phase transformation

As stated earlier, in order to determine the phase (Martensitic) transformation in HAZ a subroutine was developed and incorporated with the thermal model. The subroutine in particular makes a relationships between the peak temperature and cooling time $\nabla t_{8/5}$ of each node in HAZ and the fraction of martensite which has obtained from HCS CCT diagrams [163, 255, 259, 260]. In this code, the solidus temperature of the material is defined as 1493°C. In addition, the heat affected zone (HAZ) is defined as the region where the material has been heated to temperatures in the range of 810°C (AC_3) to 1440°C. Therefore, all points with peak temperature higher than the temperature AC_3 were considered to undergo martensitic transformation during cooling to the onset temperature M_s. When the temperature during cooling reached to the end temperature M_f, martensitic transformation was considered to be full and complete. The phase transformation temperatures (A_1, A_3, M_s and M_f) of HCS are summarized in Table 8.1 [36].

Table 8-1 Phase transformation temperatures of HCS [36]

$A_1(^oC)$	$A_3(^oC)$	$M_s(^oC)$	$M_f(^oC)$
720	810	230	140

The CCT diagram with austenization temperature of 810°C was considered for the HCS HAZ [261]. The temperature also considers grain growth of the austenite phase. It is worth noting that each curve in the CCT diagram represents a continuous cooling

profile. Hence, the decomposition of the austenite into different phases at different cooling rates can be obtained from the cooling curve of the CCT curve corresponding to a particular cooling rate under continuous cooling conditions. In this research, only the martensite fraction is predicted using this method. The relationships between cooling time $\nabla t_{8/5}$ and the fraction of martensite (obtained from CCT diagrams) for HCS steel is shown in Figure 8-5.
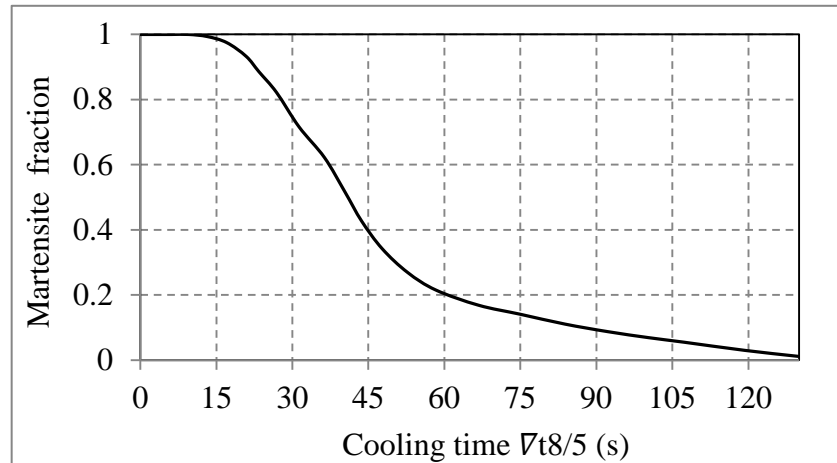
Figure 8-5 Martensite fraction as a function of cooling time ($\nabla t_{8/5}$) for HCS

Direct validation of the numerical simulation results, with same heat treatment method was beyond the scope of this study. However, experiments where performed using a stationary laser beam which gives similar cooling rate at the HCS HAZ ($\nabla t_{8/5}$). A two-colour pyrometer was utilized to probe the cooling trend of the HAZ. The experimental samples were analysed using XRD and EBSD to identify the phases and to determine their relative amount using the integral breadth method.

8.4 Results and discussion

Figure 8.6 shows the temperature contours and welding direction in the finite element simulation model of the optimum weld joint with specific point energy of 25J, without any additional heat treatment. As can be seen, the maximum temperature was much above the melting temperature, and most region of the plate is at room temperature. Figure 8.7 shows the temperature distributions during welding at various locations from the fusion zone. The maximum temperature at the point with 1.2mm distance from the fusion boundary (in HCS HAZ) is about 1200°C and it decreases between 800°C to

500°C in less than a 0.2 (sec) time period. Interpretation of this cooling rate with the martensitic fraction diagram [36], reveals that the microstructure will completely transform to martensite in HAZ. It is, therefore, no surprise that the HAZ hardness of the HCS is noticeably higher during laser dissimilar welding (Chapter 7). The decrease of temperature with distance has a nonlinear trend, which is mainly attributed to the local heating of the laser and the nonlinear variation of the material's thermo-physical properties with temperature [190].
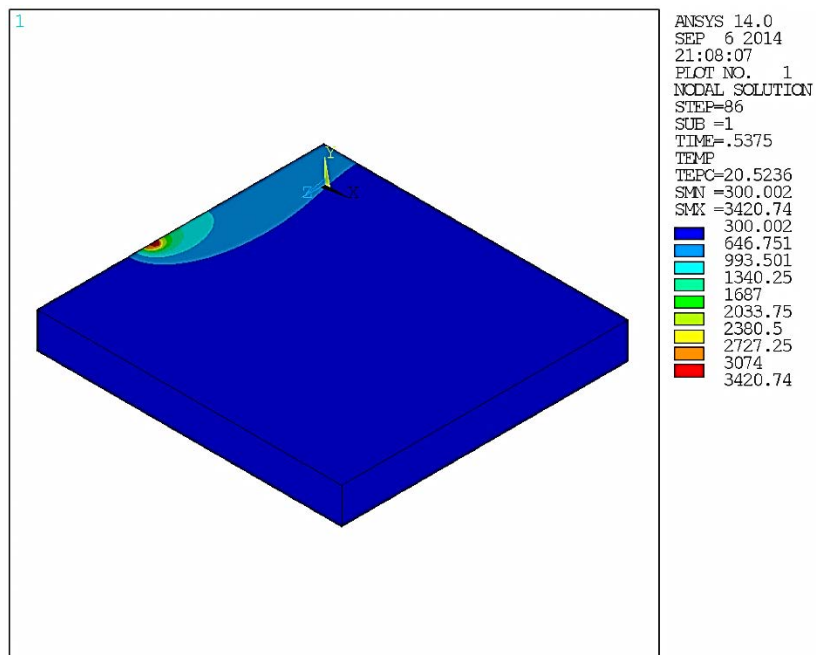
Figure 8-6 Temperature contours (K) of the HCS during the welding process
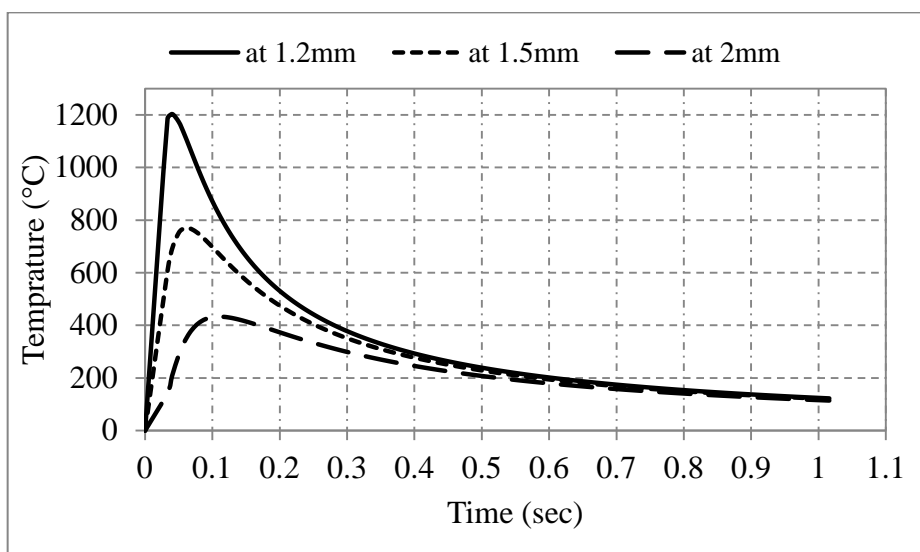
Figure 8-7 Temperature histories during laser welding for the optimum weld specimen with 25J with different distances from the fusion zone

174

Figure 8-8 shows the thermal history at the top-middle of the HAZ for various controlled cooling time ($\nabla t_{8/5}$) and Figure 8-9 shows cooling cure between 800 and 500°C. All the three models follow same heating rate and cooling rate till it reaches 800°C, however, the cooling rate between 800-500°C were controlled in the numerical model (through external heat source/input) to achieve the required phase transformation criteria's. Similar observation with different temperature magnitude happens all over the fusion zone and HAZ.
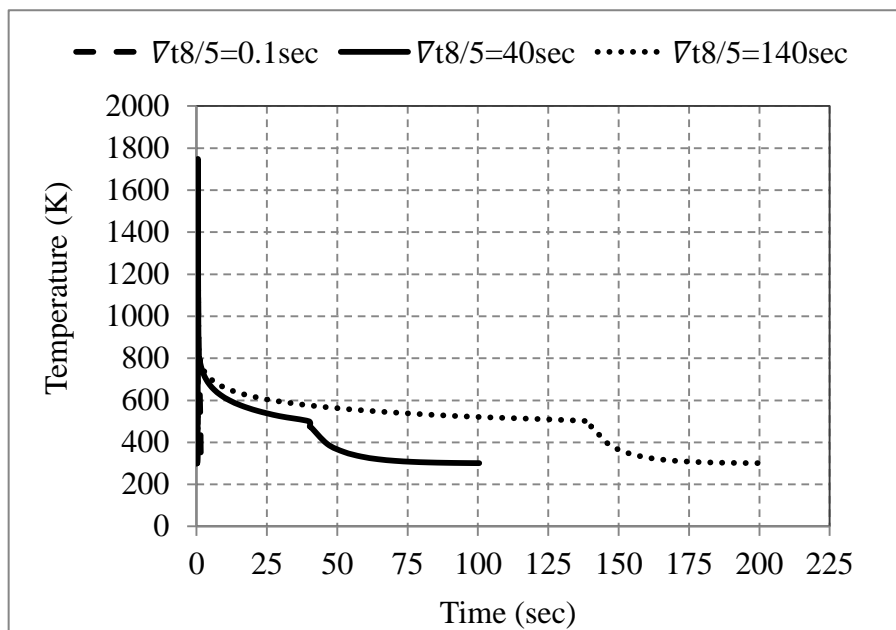
Figure 8-8 Temperature cycle over the HCS HAZ weld for various controlled cooling time ($\nabla t_{8/5}$=0.1sec, 40sec, and 140sec)
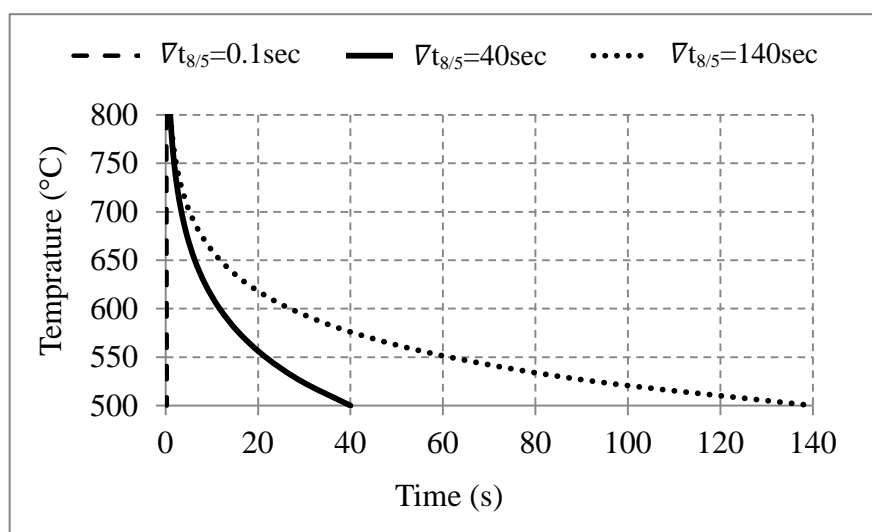
Figure 8-9 Cooling cycle between 800 to 500°C over the HCS HAZ weld for various controlled cooling time ($\nabla t_{8/5}$=0.1sec, 40sec, and 140sec)
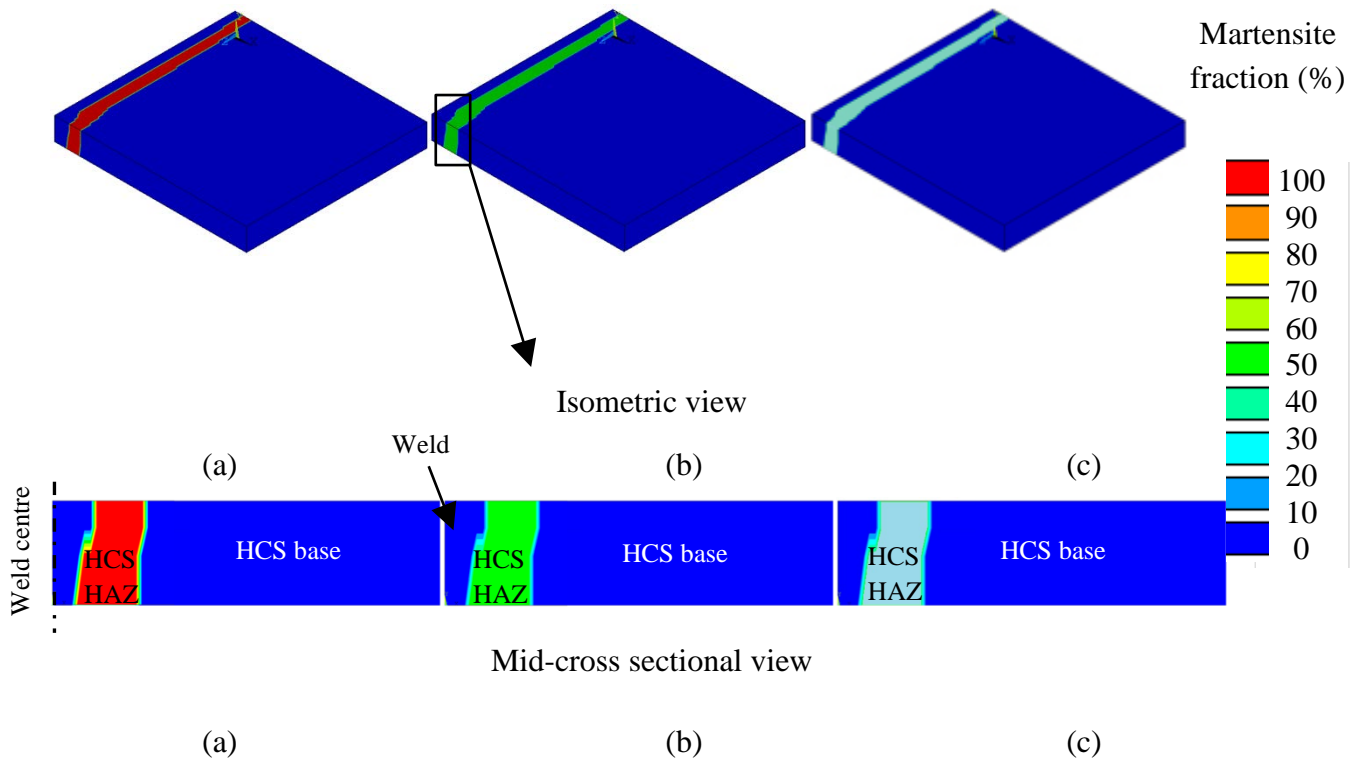
Figure 8-10 Martensite fraction (%) in HCS HAZ for various controlled cooling times
(a) $\nabla t_{8/5}$=0.1sec, (b) $\nabla t_{8/5}$=40sec and (c) $\nabla t_{8/5}$=100sec

Figure 8-10 shows the contour image of the martensitic fraction obtained after the substrate reaches room temperature. As can be seen from the Figure 8-10, controlling of the cooling time results in a significant decrease in martensite fraction (from 100% to 20%). The increase in controlled cooling time, promotes the diffusion of carbon atoms out of the crystal structure, resulting in less martensite formation [125].

Experimental validation of the model was performed using a stationary laser beam similar to spot welding, but with varying power levels to follow the trend of the cooling rate in Figure 8-8 which gives similar cooling rate at the HCS HAZ ($\nabla t_{8/5}$).
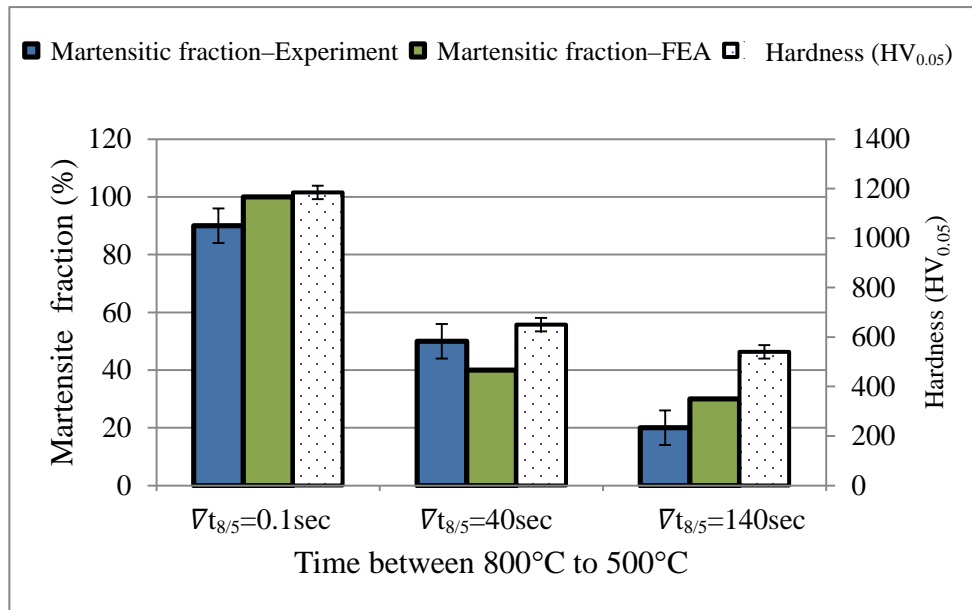
Figure 8-11 Calculated and measured martensite fraction (%) in HCS HAZ

Figure 8-11 shows the comparison of martensite fraction obtained from simulation and experimentation (X-ray diffractometer). In agreement with the experimental results, the FEA model predicts the decrease in martensitic fraction with increase in controlled cooling time ($\nabla t_{8/5}$). The decrease in the martensite volume fraction is attributed to the slower cooling rate, which provides sufficient time for the carbon to diffuse out of the crystal structure [69].
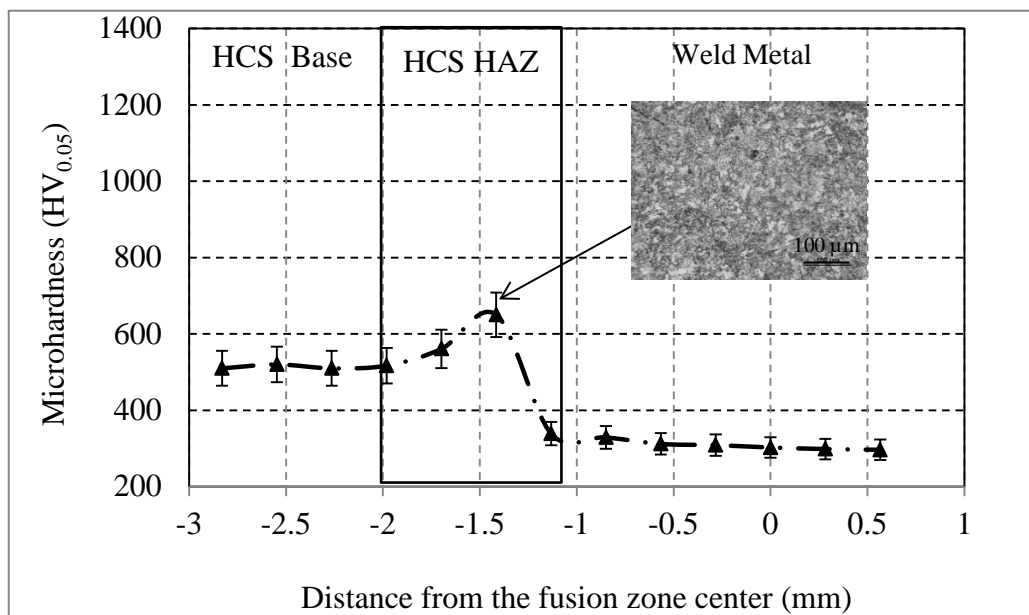
Figure 8-12 Microhardness profile and optical micrograph of the HCS zone obtained with controlled cooling rate ($\nabla t_{8/5}$=40sec)

Figure 8-12 depicts the hardness profiles and optical microscopic image of the weld sample with controlled cooling time ($\nabla t_{8/5}$) of 40sec. As can be seen from the Figure 8-12, the optimum HCS HAZ hardness ($650HV_{0.05}$ [36, 125]) was obtained at the heat treatment time of $\nabla t_{8/5}$=40sec. The results of the hardness and optical metallography of heat treated HAZ agrees qualitatively with the FEA prediction.

8.5 Conclusion

This study presents the FE model for numerical simulation of heat treatment methodology in high carbon steel heat affected zone (HCS HAZ) during laser welding. The proposed method is used to predict the solid-state phase transformation (martensitic transformation) in HCS HAZ, and the following conclusions have been drawn.

1. The martensitic formation in HCS HAZ can be controlled by using suitable heat treatment methods and the optimal $\nabla t_{8/5}$ cooling time to achieve desirable HCS-SS welded joint was found to be around 40sec.

2. FEA analysis can be used to estimate and control the martensitic fraction in laser welding of HCS, and in all cases the results of the numerical model were found to be in close agreement with experimental observations.

3. Superior service performance with optimal hardness is obtained by controlling the martensitic phase formation of HCS HAZ.

4. The present model can be developed to predict the formation other phases (i.e. pearlite, bainite) in HAZ and study the effect of phase transformation on the residual stress of the dissimilar joint.

Chapter 9 Conclusions and Future Work

9.1 Conclusions

By investigating the dissimilar laser welding process using laser material interaction parameters a deep understanding have been obtained and some of the important phenomena mentioned in the literature have been explained. From the work presented in this thesis the following can be concluded:

- Welding speed, laser power and beam offset significantly influences the laser dissimilar welding process. The laser dissimilar weld width is significantly influenced by welding speed, whilst HAZ width is controlled by both by beam offset and welding speed.

- Specific point energy, which is a function of laser power and interaction time, is one of the effective parameter to control the dissimilar laser welding process. As specific point energy was independent of the beam diameter, the outcomes of this research can be exploited for various CO_2 laser systems with different beam diameters.

- Specific point energy has significant effect on surface morphology of the weld bead. Welding with high specific point energy result in a predominantly flat weld bead surface, while insufficient specific point energy leads to weld bead with concave shape and solidification boundary ripples.

- A predominantly homogenous microstructure and well mixed fusion zone was obtained with a specific point energy greater than 17J for dissimilar welding of 1mm thick carbon steel and stainless steel.

- Specific point energy significantly influences the dissimilar weld microstructure between carbon steel and stainless steel and subsequently the hardness and the strength of the dissimilar weld joint. As the specific point energy increases, the weld microstructure tends to form a martensitic structure, which is not favourable for industrial applications.

179

- The beam alignment has significant effect on dilution and subsequent alloying concentration. A predominantly austenitic fusion zone was obtained with a beam offset of 0.2-0.4mm towards the stainless steel. A beam offset towards low carbon steel result in martensitic microstructure and should be avoided.

- CFD based numerical modelling is an effective tool to investigate dissimilar laser welding, and in specific to get a good insight of melt pool dynamics, dilution and the weld bead homogeneity.

- A CFD model results shows that the melt pool dynamics, surface topology and fusion zone dilution were significantly influenced by the thermal gradient and surface tension of the weld pool. Significant variations in thermal conductivity of the stainless steel at its melting point result in a non-linear variation of the alloy concentration and melt ratio in the dissimilar weld bead.

- With increase in specific point energy, melt pool convection and mixing within the weld bead increase. Unlike similar materials, a minimum threshold of melt pool convection is essential to achieve a homogeneous weld bead. Irrespective of the laser energy, a small magnitude (close to zero) of surface tension temperature coefficient can undermine the weld bead homogeneity in dissimilar laser welding.

- Fundamental investigations of dissimilar welding show that the alloying composition and subsequent microstructure is directly related to melt pool flow dynamics and dilution of carbon steel.

- Welding of high carbon steel to stainless steel is much more challenging and the cooling rate has significant influence in laser welding of material with high carbon content compared to low carbon content materials.

- Laser parameters including specific point energy and offset can be used to control the characteristic of the fusion zone, however their effect on controlling the microstructure in high carbon steel HAZ is minimal. High cooling rate results in brittle martensitic phases in the high carbon steel HAZ which significantly undermine the service performance of the dissimilar welded joint.

- The martensitic formation in high carbon steel HAZ can be controlled by using suitable heat treatment methodology and the optimal cooling time ($\nabla t_{8/5}$) to achieve desirable metallurgy was found to be around 40sec.

9.2   Future work recommendations

➢ Although the potential of major processing parameters and their interactions on the dissimilar microstructure has been presented, more numerical and experimental investigations are required to understand the importance of other processing parameters such as shielding gas flow rate, different gas types (e.g. Nitrogen, combination of Argon and Nitrogen) and the stand-off distance on the final microstructure and phase fraction of the weldment.

➢ Impact and fatigue strength measurements of laser welded dissimilar joints of carbon steel and austenitic stainless are required to be studied, and the benefits of laser welding on suppressing the formation of intermetallics (e.g. $Cr_{23}C_6$ and Cr_7C_3) at the weld interface and along grain boundaries need to be explored further.

➢ Microstructural analyses and characterisation of laser dissimilar welding (Chapters 5 and 7) opens up further opportunities for investigating the formation of delta-ferrite and kinetics of sigma phase precipitation and consequent embrittlement in weld.

➢ The numerical approach (chapter 8) can be further exploited to predict detailed formation of other phases (i.e. pearlite, bainite) in the HAZ of carbon steel during laser dissimilar welding. Due to its capability to balance conservation of mass, momentum, and energy and solve transport equation for turbulence and volume fraction equation (modified continuity equation) at the melt pool level, it could give more accurate prediction of alloy composition in the fusion zone along with transformed phases in the carbon steel's HAZ. As a result a comprehensive analysis of dissimilar joint can be obtained and optimisation of the dissimilar joint can be carried out with minimum trade-off between weld microstructure and HAZ mechanical properties. In addition the CFD model can be employed for

studying laser welding of different dissimilar metal combinations in particular welding of aluminium to stainless steel in automotive industry.

➢ The second possible extension of the numerical approach is to investigate the effects of solid-state phase transformation on dissimilar welding residual stress and distortion in the HAZ of carbon steels. The important considerations may be the effect of volume change due to austenite–martensite transformation on the final residual stress and the welding distortion. In addition, the current model ignores plastic behaviour of the material for calculation of the residual stress in weldment, hence this limitation can be considered in further investigations.

➢ The heat treatment methodology proposed in this thesis can be extended to butt welding of high carbon steel to stainless steel, by using a secondary laser beam or beam shaping or gas torch.

References

1.   Mukherjee, S., et al., *Transport phenomena in conduction mode laser beam welding of Fe–Al dissimilar couple with Ta diffusion barrier.* International Journal of Heat and Mass Transfer, 2010. 53(23): p. 5274-5282.

2.   Kreimeyer, M. and G. Sepold. *Processing of laser joined aluminum-steel tailored blanks in overlap and butt joint configuration.* in *ICALEO 2002-21st International Congress on Applications of Laser and Electro-Optics.* 2002.

3.   Anawa, E. and A.-G. Olabi, *Optimization of tensile strength of ferritic/austenitic laser-welded components.* Optics and Lasers in Engineering, 2008. 46(8): p. 571-577.

4.   Torkamany, M., J. Sabbaghzadeh, and M. Hamedi, *Effect of laser welding mode on the microstructure and mechanical performance of dissimilar laser spot welds between low carbon and austenitic stainless steels.* Materials & Design, 2012. *34*: p. 666-672.

5.   Esfahani, R., J. Coupland, and S. Marimuthu, *Microstructure and mechanical properties of a laser welded low carbon-stainless steel joint.* Journal of Materials Processing Technology, 2014.

6.   Khalifeh, A., A. Dehghan, and E. Hajjari, *Dissimilar joining of AISI 304L/St37 steels by TIG welding process.* Acta Metallurgica Sinica (English Letters), 2013. 26(6): p. 721-727.

7.   Hsieh, C.-C. and W. Wu, *Precipitation of Phase Using General Diffusion Equation with Comparison to Vitek Diffusion Model in Dissimilar Stainless Steels.* Journal of Metallurgy, 2012. 2012.

8.   Anawa EM, O.A., Hashmi MSJ, *Optimization of ferritic/austenitic laser welded component*, in *AMPT2006 international conference*2006: Las Vegas [NV], USA, .

9.   Jafarzadegan, M., et al., *Microstructure and Mechanical Properties of a Dissimilar Friction Stir Weld between Austenitic Stainless Steel and Low Carbon Steel.* Journal of Materials Science & Technology, 2013. 29(4): p. 367–372.

10.   Sedek, P., et al., *Residual stress relief in MAG welded joints of dissimilar steels.* International journal of pressure vessels and piping, 2003. 80(10): p. 705-713.

11.   Khan, M., et al., *Laser beam welding of dissimilar stainless steels in a fillet joint configuration.* Journal of Materials Processing Technology, 2012. 212(4): p. 856-867.

12.   Wang, S., Q. Ma, and Y. Li, *Characterization of microstructure, mechanical properties and corrosion resistance of dissimilar welded joint between 2205 duplex stainless steel and 16MnR.* Materials & Design, 2011. 32(2): p. 831-837.

13.   Handbook, W., *Welding Process.* American Welding Society (AWS), Eight Edition, 1991. 2.

14.   Ranjbarnodeh, E., et al., *Finite element modeling of the effect of heat input on residual stresses in dissimilar joints.* The International Journal of Advanced Manufacturing Technology, 2011. 55(5-8): p. 649-656.

15.   Ribolla, A., G.L. Damoulis, and G.F. Batalha, *The use of Nd: YAG laser weld for large scale volume assembly of automotive body in white.* Journal of Materials Processing Technology, 2005. 164: p. 1120-1127.

16.   Eghlio, R.M., *Laser net shape welding of steels*, 2012, University of Manchester.

17.   Barik, A., *Joining of Dissimilar Materials using: Yag Laser Welding*, 2010.

18.   Steen, W.M., J. Mazumder, and K.G. Watkins, *Laser material processing*2003:

Springer.

19. Brickstad, B. and B. Josefson, *A parametric study of residual stresses in multi-pass butt-welded stainless steel pipes.* International journal of pressure vessels and piping, 1998. 75(1): p. 11-25.

20. Sánchez-Amaya, J., et al., *Laser welding of AA 5083 samples by high power diode laser.* Science and Technology of Welding & Joining, 2009. 14(1): p. 78-86.

21. Sibillano, T., et al., *Optical detection of conduction/keyhole mode transition in laser welding.* Journal of Materials Processing Technology, 2007. 191(1): p. 364-367.

22. Okon, P., et al. *Laser welding of aluminium alloy 5083.* in *21st International Congress on Applications of Lasers and Electro-Optics.* 2002.

23. Jandaghi, M., et al., *Alloying element losses in pulsed Nd: YAG laser welding of stainless steel 316.* Journal of Physics D: Applied Physics, 2008. 41(23): p. 235503.

24. Duley, W.W., *Laser welding* 1999: Wiley.

25. Dawes, C., *Laser welding: A practical guide* 1992: Woodhead Publishing.

26. Sun, Z. and J. Ion, *Laser welding of dissimilar metal combinations.* Journal of Materials Science, 1995. 30(17): p. 4205-4214.

27. Locke, E., E.D. Hoag, and R. Hella, *Deep penetration welding with high-power CO 2 lasers.* Quantum Electronics, IEEE Journal of, 1972. 8(2): p. 132-135.

28. Zhu, J., L. Li, and Z. Liu, *CO 2 and diode laser welding of AZ31 magnesium alloy.* Applied Surface Science, 2005. 247(1): p. 300-306.

29. Suder, W., *Study of fundamental parameters in hybrid laser welding*, in *School of Applied Sciences* 2011, Cranfield University.

30. Salminen, A., H. Piili, and T. Purtonen, *The characteristics of high power fibre laser welding.* Proceedings of the Institution of Mechanical Engineers, Part C: Journal of Mechanical Engineering Science, 2010. 224(5): p. 1019-1029.

31. Kawahito, Y., M. Mizutani, and S. Katayama, *Elucidation of high-power fibre laser welding phenomena of stainless steel and effect of factors on weld geometry.* Journal of Physics D: Applied Physics, 2007. 40(19): p. 5854.

32. Fabbro, R., et al., *Study of CW Nd-Yag laser welding of Zn-coated steel sheets.* Journal of Physics D: Applied Physics, 2006. 39(2): p. 401.

33. Cao, X. and M. Jahazi, *Effect of welding speed on butt joint quality of Ti–6Al–4V alloy welded using a high-power Nd: YAG laser.* Optics and Lasers in Engineering, 2009. 47(11): p. 1231-1241.

34. Chen, W., P. Ackerson, and P. Molian, *CO 2 laser welding of galvanized steel sheets using vent holes.* Materials & Design, 2009. 30(2): p. 245-251.

35. Baardsen, E., D. Schmatz, and R. Bisaro, *High speed welding of sheet steel with a CO 2 laser.* Welding journal, 1973. 52: p. 227-229.

36. Ng, E.E.S., *Laser welding of high carbon steels*, 1999, University of Glasgow.

37. Hiraga, H., et al., *Effects of the shielding gas and laser wavelength in laser welding magnesium alloy sheets.* Welding international, 2002. 16(6): p. 442-450.

38. Sanders, P., et al., *High power Nd: YAG and CO2 laser welding of magnesium.* Journal of Laser Applications, 1999. 11(2): p. 96-103.

39. Leong, K., et al., *ICALEO 98: Laser Materials Processing Conference.* Orlando, FL, 1998: p. 16-19.

40. Li, L., *The advances and characteristics of high-power diode laser materials processing.* Optics and Lasers in Engineering, 2000. 34(4): p. 231-253.

41. Chen, Y., et al., *Experimental study on welding characteristics of CO2 laser TIG hybrid welding process.* Science and Technology of Welding & Joining, 2006.

11(4): p. 403-411.

42. Balasubramanian, K., et al., *Numerical and experimental investigation of laser beam welding of AISI 304 stainless steel sheet.* Adv. Produc. Engineer. Manag, 2008. 3(2): p. 93-105.

43. Khan, M., et al., *Experimental investigation on laser beam welding of martensitic stainless steels in a constrained overlap joint configuration.* Journal of Materials Processing Technology, 2010. 210(10): p. 1340-1353.

44. Li, Y., et al., *Microstructures and mechanical properties of H62 brass-316L stainless steel in overlap welded joints by continuous-wave laser.* The International Journal of Advanced Manufacturing Technology, 2015: p. 1-8.

45. Kim, J. *Parametric Evaluation of C02 Laser Beam Welding.* in *ASME Symposium on Welding and Joining Processes.* 1991. ASME PED.

46. Mai, T.A. and A.C. Spowage, *Characterisation of dissimilar joints in laser welding of steel–kovar, copper–steel and copper–aluminium.* Materials Science and Engineering: A, 2004. 374(1–2): p. 224-233.

47. Kristensen, J., *Thick Plate CO2-Laser based hybrid welding of structural steels.* Welding in the World, 2009. 53(1-2): p. 48-57.

48. El-Batahgy, A.-M., *Effect of laser welding parameters on fusion zone shape and solidification structure of austenitic stainless steels.* Materials Letters, 1997. 32(2): p. 155-163.

49. Walsh, C., *Laser welding–literature review.* Materials Science and Metallurgy Department, University of Cambridge, England, 2012.

50. Liao, Y.-C. and M.-H. Yu, *Effects of laser beam energy and incident angle on the pulse laser welding of stainless steel thin sheet.* Journal of Materials Processing Technology, 2007. 190(1): p. 102-108.

51. Nekouie Esfahani, M.R., J. Coupland, and S. Marimuthu, *Microstructural and mechanical characterisation of laser-welded high-carbon and stainless steel.* The International Journal of Advanced Manufacturing Technology, 2015: p. 1-8.

52. Kannatey-Asibu Jr, E., *Principles of laser materials processing.* Vol. 4. 2009: John Wiley & Sons.

53. Tzeng, Y.-f., *Parametric analysis of the pulsed Nd: YAG laser seam-welding process.* Journal of Materials Processing Technology, 2000. 102(1): p. 40-47.

54. Cheng, W.-H., W.-H. Wang, and J.-C. Chen, *Defect formation mechanisms in laser welding techniques for semiconductor laser packaging.* Components, Packaging, and Manufacturing Technology, Part B: Advanced Packaging, IEEE Transactions on, 1996. 19(4): p. 764-769.

55. Jouvard, J., K. Girard, and O. Perret, *Keyhole formation and power deposition in Nd: YAG laser spot welding.* Journal of Physics D: Applied Physics, 2001. 34(18): p. 2894.

56. Sathiya, P., M.K. Mishra, and B. Shanmugarajan, *Effect of shielding gases on microstructure and mechanical properties of super austenitic stainless steel by hybrid welding.* Materials & Design, 2012. 33: p. 203-212.

57. Keskitalo, M., et al., *Laser welding of duplex stainless steel with nitrogen as shielding gas.* Journal of Materials Processing Technology, 2015. 216: p. 381-384.

58. Westin, E.M. and M.D. Serrander, *Experience in welding stainless steels for water heater applications.* Welding in the World, 2012. 56(5-6): p. 14-28.

59. Safdar, S., L. Li, and M. Sheikh, *Numerical analysis of the effects of non-conventional laser beam geometries during laser melting of metallic materials.* Journal of Physics D: Applied Physics, 2007. 40(2): p. 593.

60. Torkamany, M., F.M. Ghaini, and R. Poursalehi, *Dissimilar pulsed Nd: YAG laser*

welding of pure niobium to Ti–6Al–4V. Materials & Design, 2014. 53: p. 915-920.

61. Kaplan, A., *Absorptivity modulation on wavy molten steel surfaces: The influence of laser wavelength and angle of incidence.* Applied Physics Letters, 2012. 101(15): p. 151605.

62. Sattari-Far, I. and Y. Javadi, *Influence of welding sequence on welding distortions in pipes.* International journal of pressure vessels and piping, 2008. 85(4): p. 265-274.

63. Sanderson, A., C. Punshon, and J. Russell, *Advanced welding processes for fusion reactor fabrication.* Fusion engineering and design, 2000. 49: p. 77-87.

64. Bach, F.-W., et al., *Non vacuum electron beam welding of light sheet metals and steel sheets.* Welding in the World, 2003. 47(3-4): p. 4-10.

65. Pellkofer, D., G. Engelhard, and S. Foerner, *Advantages of the tungsten-arc welding.* 1985.

66. Marya, M., et al. *Fundamentals in the fusion welding of magnesium and its alloys.* in *Proceedings of Seventh International Symposium of the Japan Welding Society on Today and Tomorrow in the Science and Technology of Welding and Joining.* 2001.

67. Mult, E., et al., *Laser and electron beam welding of magnesium materials.* Schweissen und Schneiden/Welding & Cutting, 2000. 52(8).

68. Marimuthu, S., et al., *Coupled Computational Fluid Dynamic and Finite Element Multiphase Modeling of Laser Weld Bead Geometry Formation and Joint Strengths.* Journal of Manufacturing Science and Engineering, 2013. 135(1): p. 011004.

69. Arivazhagan, N., et al., *Investigation on AISI 304 austenitic stainless steel to AISI 4140 low alloy steel dissimilar joints by gas tungsten arc, electron beam and friction welding.* Materials & Design, 2011. 32(5): p. 3036-3050.

70. Yan, J., M. Gao, and X. Zeng, *Study on microstructure and mechanical properties of 304 stainless steel joints by TIG, laser and laser-TIG hybrid welding.* Optics and Lasers in Engineering, 2010. 48(4): p. 512-517.

71. Sun, Z., *Feasibility of producing ferritic/austenitic dissimilar metal joints by high energy density laser beam process.* International journal of pressure vessels and piping, 1996. 68(2): p. 153-160.

72. Kohyama, A., et al., *Electron beam welding of titanium and Ti-6AL-4V thick plates.* Journal of Nuclear Materials, 1984. 122(1): p. 772-776.

73. Schultz, H., *Electron beam welding*1994: Elsevier.

74. Yunlian, Q., et al., *Electron beam welding, laser beam welding and gas tungsten arc welding of titanium sheet.* Materials Science and Engineering: A, 2000. 280(1): p. 177-181.

75. Miles, M., et al., *Comparison of formability of friction stir welded and laser welded dual phase 590 steel sheets.* Science and Technology of Welding & Joining, 2006. 11(4): p. 384-388.

76. Sun, Z. and R. Karppi, *The application of electron beam welding for the joining of dissimilar metals: an overview.* Journal of Materials Processing Technology, 1996. 59(3): p. 257-267.

77. Bagger, C. and F.O. Olsen, *Review of laser hybrid welding.* Journal of laser applications, 2005. 17(1): p. 2-14.

78. Yang, Y. and S. Lee, *A study on the joining strength of laser spot welding for automotive applications.* Journal of Materials Processing Technology, 1999. 94(2): p. 151-156.

79. Zhao, H. and T. DebRoy, *Weld metal composition change during conduction mode*

laser welding of aluminum alloy 5182. Metallurgical and materials transactions B, 2001. 32(1): p. 163-172.

80. Nordberg, H., *Fatigue properties of stainless steel lap joints.* SAE Transactions: Journal of Materials & Manufacturing, 2006. 114: p. 675s-690s.

81. Phanikumar, G., P. Dutta, and K. Chattopadhyay. *Laser Processing of Dissimilar Metals.* in *ISOMALM 2000: International Symposium on Materials Ageing and Life Management.* 2000.

82. Sun, Z. and T. Moisio, *Laser beam welding of austenitic/ferritic dissimilar steel joints using nickel based filler wire.* Materials Science and Technology, 1993. 9(7): p. 603-608.

83. Torkamany, M., S. Tahamtan, and J. Sabbaghzadeh, *Dissimilar welding of carbon steel to 5754 aluminum alloy by Nd: YAG pulsed laser.* Materials & Design, 2010. 31(1): p. 458-465.

84. Phanikumar, G., *Experimental and Computational studies on laser processing of dissimilar metals*, 2002, Indian Institute of Science, Bangalore, India.

85. Oreper, G. and J. Szekely, *Heat-and fluid-flow phenomena in weld pools.* Journal of Fluid Mechanics, 1984. 147(1): p. 53-79.

86. Heiple, C. and J. Roper, *Mechanism for minor element effect on GTA fusion zone geometry.* Welding journal, 1982. 61(4): p. 97.

87. SALDI, Z.S., *Marangoni driven free surface flows in liquid weld pools.*

88. He, X., P. Fuerschbach, and T. DebRoy, *Heat transfer and fluid flow during laser spot welding of 304 stainless steel.* Journal of Physics D: Applied Physics, 2003. 36(12): p. 1388.

89. Kou, S. and D. Sun, *Fluid flow and weld penetration in stationary arc welds.* Metallurgical Transactions A, 1985. 16(2): p. 203-213.

90. Srinivasan, J. and B. Basu, *A numerical study of thermocapillary flow in a rectangular cavity during laser melting.* International Journal of Heat and Mass Transfer, 1986. 29(4): p. 563-572.

91. Pang, S., et al., *A three-dimensional sharp interface model for self-consistent keyhole and weld pool dynamics in deep penetration laser welding.* Journal of Physics D: Applied Physics, 2011. 44(2): p. 025301.

92. Yang, L., X. Peng, and B. Wang, *Numerical modeling and experimental investigation on the characteristics of molten pool during laser processing.* International Journal of Heat and Mass Transfer, 2001. 44(23): p. 4465-4473.

93. Ahsan, M.N., *Modelling and analysis of laser direct metal deposition of Ti-6Al-4V alloy*, 2011, University of Manchester.

94. Zhao, C., et al., *The effect of oxygen on transitional Marangoni flow in laser spot welding.* Acta Materialia, 2010. 58(19): p. 6345-6357.

95. Zacharia, T., et al., *Weld pool development during GTA and laser beam welding of type 304 stainless steel, Part II—experimental correlation.* Welding journal, 1989. 68(12): p. 510s-519s.

96. Waheed, S., *Effects of wire feeding direction and location in multiple layer diode laser direct metal deposition,2006.* University of Manchester

97. Voelkel, D.D. and J. Mazumder, *Visualization of a laser melt pool.* Applied optics, 1990. 29(12): p. 1718-1720.

98. Lei, Y., et al., *Numerical analysis of the competitive influence of Marangoni flow and evaporation on heat surface temperature and molten pool shape in laser surface remelting.* Computational materials science, 2001. 21(3): p. 276-290.

99.   Rai, R. and T. DebRoy, *Tailoring weld geometry during keyhole mode laser welding using a genetic algorithm and a heat transfer model.* Journal of Physics D: Applied Physics, 2006. 39(6): p. 1257.

100.   Kim, H.-J., et al., *Effects of Cu/Al intermetallic compound (IMC) on copper wire and aluminum pad bondability.* Components and Packaging Technologies, IEEE Transactions on, 2003. 26(2): p. 367-374.

101.   Anawa, E.M. and A.G. Olabi, *Control of welding residual stress for dissimilar laser welded materials.* Journal of Materials Processing Technology, 2008. 204(1–3): p. 22-33.

102.   Chakraborty, N., *The effects of turbulence on molten pool transport during melting and solidification processes in continuous conduction mode laser welding of copper–nickel dissimilar couple.* Applied Thermal Engineering, 2009. 29(17): p. 3618-3631.

103.   Chung, F. and P. Wei, *Mass, momentum, and energy transport in a molten pool when welding dissimilar metals.* Journal of heat transfer, 1999. 121(2): p. 451-461.

104.   Hu, Y., et al., *Heat and mass transfer in laser dissimilar welding of stainless steel and nickel.* Applied Surface Science, 2012. 258(15): p. 5914-5922.

105.   Li, L., R. Eghlio, and S. Marimuthu, *Laser net shape welding.* CIRP Annals-Manufacturing Technology, 2011. 60(1): p. 223-226.

106.   Phanikumar, G., K. Chattopadhyay, and P. Dutta, *Modelling of transport phenomena in laser welding of dissimilar metals.* International Journal of Numerical Methods for Heat & Fluid Flow, 2001. 11(2): p. 156-174.

107.   Wei, P. and F. Chung, *Unsteady Marangoni flow in a molten pool when welding dissimilar metals.* Metallurgical and Materials Transactions B, 2000. 31(6): p. 1387-1403.

108.   Yaghi, A., et al., *Finite element simulation of residual stresses induced by the dissimilar welding of a P92 steel pipe with weld metal IN625.* International journal of pressure vessels and piping, 2013. 111: p. 173-186.

109.   Youtsos, A. and D.E. Katsareas. *Residual stress prediction in dissimilar metal weld pipe joints using the finite element method.* in *Materials Science Forum.* 2005. Trans Tech Publ.

110.   Ranjbarnodeh, E., et al., *Prediction of temperature distribution in dissimilar arc welding of stainless steel to carbon steel.* Proceedings of the Institution of Mechanical Engineers, Part B: Journal of Engineering Manufacture, 2012. 226(1): p. 117-125.

111.   Missori, S. and C. Koerber, *Laser beam welding of austenitic-ferritic transition joints.* Welding journal, 1997. 76(3): p. 125-134.

112.   Theron, M., C. Van Rooyen, and L. Ivanchev. *CW Nd: YAG laser welding of dissimilar sheet metals.* 2007. ICALEO-International Congress on Applications of Lasers & Electro-Optics.

113.   Borrisutthekul, R., Y. Miyashita, and Y. Mutoh, *Dissimilar material laser welding between magnesium alloy AZ31B and aluminum alloy A5052-O.* Science and Technology of Advanced Materials, 2005. 6(2): p. 199-204.

114.   Ozaki, H. and M. Kutsuna, *Laser-roll welding of a dissimilar metal joint of low carbon steel to aluminium alloy using 2 kW fibre laser.* Welding international, 2009. 23(5): p. 345-352.

115.   Naffakh, H., M. Shamanian, and F. Ashrafizadeh, *Weldability in dissimilar welds between Type 310 austenitic stainless steel and Alloy 657.* Journal of Materials Science, 2008. 43(15): p. 5300-5304.

116.   Li, Z. and G. Fontana, *Autogenous laser welding of stainless steel to free-cutting*

steel for the manufacture of hydraulic valves. Journal of Materials Processing Technology, 1998. 74(1): p. 174-182.

117. Chen, H.-C., et al., *Gap-free fibre laser welding of Zn-coated steel on Al alloy for light-weight automotive applications.* Materials & Design, 2011. 32(2): p. 495-504.

118. Paventhan, R., P. Lakshminarayanan, and V. Balasubramanian, *Fatigue behaviour of friction welded medium carbon steel and austenitic stainless steel dissimilar joints.* Materials & Design, 2011. 32(4): p. 1888-1894.

119. Anawa, E. and A.-G. Olabi, *Using Taguchi method to optimize welding pool of dissimilar laser-welded components.* Optics & Laser Technology, 2008. 40(2): p. 379-388.

120. Sadeghian, M., M. Shamanian, and A. Shafyei, *Effect of heat input on microstructure and mechanical properties of dissimilar joints between super duplex stainless steel and high strength low alloy steel.* Materials & Design, 2014. 60: p. 678-684.

121. Pascu, A., et al., *Chemical and Mechanical Characterisation of AISI 304 and AISI 1010 Laser Welding.* Materials and Manufacturing Processes, 2015(just-accepted).

122. Marashi, P., et al., *Microstructure and failure behavior of dissimilar resistance spot welds between low carbon galvanized and austenitic stainless steels.* Materials Science and Engineering: A, 2008. 480(1): p. 175-180.

123. Bahrami, A. *Modeling of Transport Phenomena in Dissimilar GTA Weld Metals.* in *9th International Conference on Trends in Welding Research.* 2012. Asm.

124. Radaj, D., *Heat effects of welding temperature field, residual stress, distortion, 1992*, Springer-Verlag, Berlin.

125. Kou, S., *Welding metallurgy*1987: Cambridge Univ Press.

126. David, S., S. Babu, and J. Vitek, *Welding: Solidification and microstructure.* JOM, 2003. 55(6): p. 14-20.

127. Olabi, A., K. Benyounis, and M. Hashmi, *Application of response surface methodology in describing the residual stress distribution in CO2 laser welding of AISI304.* Strain, 2007. 43(1): p. 37-46.

128. Benyounis, K. and A. Olabi, *Optimization of different welding processes using statistical and numerical approaches–A reference guide.* Advances in Engineering Software, 2008. 39(6): p. 483-496.

129. Pouraliakbar, H., et al., *Designing of CK45 carbon steel and AISI 304 stainless steel dissimilar welds.* Materials Research, 2014. 17(1): p. 106-114.

130. Satyanarayana, V., G. Madhusudhan Reddy, and T. Mohandas, *Dissimilar metal friction welding of austenitic–ferritic stainless steels.* Journal of Materials Processing Technology, 2005. 160(2): p. 128-137.

131. Benyounis, K., A. Olabi, and M. Hashmi, *Effect of laser welding parameters on the heat input and weld-bead profile.* Journal of Materials Processing Technology, 2005. 164: p. 978-985.

132. Tam, S., L.E. Lim, and K. Quek, *Application of Taguchi methods in the optimization of the laser-cutting process.* Journal of Materials Processing Technology, 1992. 29(1): p. 63-74.

133. Olabi, A., et al., *An ANN and Taguchi algorithms integrated approach to the optimization of CO< sub> 2</sub> laser welding.* Advances in Engineering Software, 2006. 37(10): p. 643-648.

134. Negarestani, R., *Laser Cutting of Carbon Fibre-Reinforced Polymer Composite Materials*, in *Mechanical Engineering*2010, The University of Manchester.

135. Moradi, M. and M. Ghoreishi, *Influences of laser welding parameters on the geometric profile of NI-base superalloy Rene 80 weld-bead.* The International

Journal of Advanced Manufacturing Technology, 2011. 55(1-4): p. 205-215.

136. Suder, W. and S. Williams, *Investigation of the effects of basic laser material interaction parameters in laser welding.* Journal of Laser Applications, 2012. 24: p. 032009.

137. Khan, M., L. Romoli, and G. Dini, *Laser beam welding of dissimilar ferritic/martensitic stainless steels in a butt joint configuration.* Optics & Laser Technology, 2013. 49: p. 125-136.

138. Heiple, C. and P. Burgardt, *Effects of SO2 shielding gas additions on GTA weld shape.* Welding journal, 1985. 64(6): p. 159-162.

139. Zacharia, T., A. Eraslan, and D. Aidun, *Modeling of autogenous welding.* Welding journal, 1988. 67(3): p. 53s-62s.

140. Mills, K., et al., *Marangoni effects in welding.* Philosophical Transactions-Royal Society of London Series A Mathematical Physical and Engineering Sciences, 1998: p. 911-926.

141. Lu, S., H. Fujii, and K. Nogi, *Marangoni convection and weld shape variations in Ar–O$_2$ and Ar–CO$_2$ shielded GTA welding.* Materials Science and Engineering: A, 2004. 380(1): p. 290-297.

142. Xue, Z., et al., *Molten pool characterization of laser lap welded copper and aluminum.* Journal of Physics D: Applied Physics, 2013. 46(49): p. 495501.

143. Wu, C., T. Zhang, and Y. Feng, *Numerical analysis of the heat and fluid flow in a weld pool with a dynamic keyhole.* International Journal of Heat and Fluid Flow, 2013. 40: p. 186-197.

144. Zhang, W., et al., *Modeling of heat transfer and fluid flow during gas tungsten arc spot welding of low carbon steel.* Journal of Applied Physics, 2003. 93(5): p. 3022-3033.

145. Bäuerle, D., *Laser processing and chemistry.* Vol. 3. 2000: Springer Berlin.

146. Anthony, T. and H. Cline, *Surface rippling induced by surface-tension gradients during laser surface melting and alloying.* Journal of Applied Physics, 1977. 48(9): p. 3888-3894.

147. Wang, Y. and H. Tsai, *Effects of surface active elements on weld pool fluid flow and weld penetration in gas metal arc welding.* Metallurgical and Materials Transactions B, 2001. 32(3): p. 501-515.

148. Kotecki, D., D. Cheever, and D. Howden, *Mechanism of ripple formation during weld solidification.* Welding journal, 1972. 51(8): p. 368.

149. Ma, C., et al., *Melt Pool Flow and Surface Evolution During Pulsed Laser Micro Polishing of Ti6Al4V.* Journal of Manufacturing Science and Engineering, 2013. 135(6): p. 061023.

150. Baumgart, P., et al., *A new laser texturing technique for high performance magnetic disk drives.* Magnetics, IEEE Transactions on, 1995. 31(6): p. 2946-2951.

151. Chen, S., D. Cahill, and C. Grigoropoulos, *Melting and surface deformation in pulsed laser surface micromodification of Ni-P disks.* Journal of heat transfer, 2000. 122(1): p. 107-112.

152. Willis, D. and X. Xu, *Transport phenomena and droplet formation during pulsed laser interaction with thin films.* Journal of heat transfer, 2000. 122(4): p. 763-770.

153. Tzeng, Y.-F., *Effects of operating parameters on surface quality for the pulsed laser welding of zinc-coated steel.* Journal of Materials Processing Technology, 2000. 100(1): p. 163-170.

154. Youtsos, A., *Residual Stress and Its Effect on Fatigue and Fracture*, 2006, Springer, Amsterdam.

155. Daneshpour, S., et al., *Mechanical and fatigue behaviour of laser and resistance*

spot welds in advanced high strength steels. Science and Technology of Welding & Joining, 2009. 14(1): p. 20-25.

156. Daneshpour, S., et al., *Failure behaviour of laser spot welds of TRIP800 steel sheets under coach–peel loading.* Science and Technology of Welding & Joining, 2007. 12(6): p. 508-515.

157. Alenius, M., et al., *Exploring the mechanical properties of spot welded dissimilar joints for stainless and galvanized steels.* WELDING JOURNAL-NEW YORK-, 2006. 85(12): p. 305.

158. Pouranvari, M., et al., *Influence of fusion zone size and failure mode on mechanical performance of dissimilar resistance spot welds of AISI 1008 low carbon steel and DP600 advanced high strength steel.* Materials & Design, 2011. 32(3): p. 1390-1398.

159. Nadimi, S., et al., *Investigation and analysis of weld induced residual stresses in two dissimilar pipes by finite element modeling.* Journal of Applied Sciences, 2008. 8(6): p. 1014-1020.

160. Ranjbarnodeh, E., et al., *Effect of welding parameters on residual stresses in dissimilar joint of stainless steel to carbon steel.* Journal of Materials Science, 2011. 46(9): p. 3225-3232.

161. Akbari, D. and I. Sattari-Far, *Effect of the welding heat input on residual stresses in butt-welds of dissimilar pipe joints.* International journal of pressure vessels and piping, 2009. 86(11): p. 769-776.

162. Lee, C.-H. and K.-H. Chang, *Temperature fields and residual stress distributions in dissimilar steel butt welds between carbon and stainless steels.* Applied Thermal Engineering, 2012. 45: p. 33-41.

163. Deng, D., *FEM prediction of welding residual stress and distortion in carbon steel considering phase transformation effects.* Materials & Design, 2009. 30(2): p. 359-366.

164. Mochizuki, M., M. Hayashi, and T. Hattori, *Numerical analysis of welding residual stress and its verification using neutron diffraction measurement.* Journal of engineering materials and technology, 2000. 122(1): p. 98-103.

165. Deng, D., et al., *Prediction of residual stresses in a dissimilar metal welded pipe with considering cladding, buttering and post weld heat treatment.* Computational materials science, 2009. 47(2): p. 398-408.

166. Lee, C.-H. and K.-H. Chang, *Numerical analysis of residual stresses in welds of similar or dissimilar steel weldments under superimposed tensile loads.* Computational materials science, 2007. 40(4): p. 548-556.

167. Katsareas, D.E. and A. Youtsos. *Residual stress prediction in dissimilar metal weld pipe joints using the finite element method.* in *Materials Science Forum.* 2005. Trans Tech Publ.

168. Hajiannia, I., M. Shamanian, and M. Kasiri, *Microstructure and mechanical properties of AISI 347 stainless steel/A335 low alloy steel dissimilar joint produced by gas tungsten arc welding.* Materials & Design, 2013. 50: p. 566-573.

169. Chen, G., et al., *High-temperature short-term tensile test and creep rupture strength prediction of the T92/TP347H dissimilar steel weld joints.* Engineering Failure Analysis, 2012. 26: p. 220-229.

170. Zeng, C., W. Tian, and L. Hua, *A comprehensive study of thermal damage consequent to laser surface treatment.* Materials Science and Engineering: A, 2013. 564: p. 381-388.

171. Kong, F., et al., *Modeling of temperature field and grain growth of a dual phase steel DP980 in direct diode laser heat treatment.* Journal of Materials Processing

Technology, 2009. 209(18): p. 5996-6003.

172. Nady, A., et al. *Numerical Modeling of Residual Stress and Prediction of Heat Affected Zone Induced by PTA Process*. in *Materials Science Forum*. 2010. Trans Tech Publ.

173. Elmer, J., et al., *Kinetic modeling of phase transformations occurring in the HAZ of C-Mn steel welds based on direct observations*. Acta Materialia, 2003. 51(12): p. 3333-3349.

174. Lee, C.-H. and K.-H. Chang, *Finite element simulation of the residual stresses in high strength carbon steel butt weld incorporating solid-state phase transformation*. Computational materials science, 2009. 46(4): p. 1014-1022.

175. Sterjovski, Z., D. Dunne, and S. Ambrose, *Evaluation of cross-weld properties of quenched and tempered pressure vessel steel before and after PWHT*. International journal of pressure vessels and piping, 2004. 81(6): p. 465-470.

176. Ha, Y.S., et al., *Analysis of post-weld deformation at the heat-affected zone using external forces based on the inherent strain*. International Journal of Precision Engineering and Manufacturing, 2007. 8(4): p. 56-62.

177. Kim, J.-W. and C.-G. Kim, *Design of a laser welded thin metal tube structure incorporating welding distortion and residual stress*. International Journal of Precision Engineering and Manufacturing, 2010. 11(6): p. 925-930.

178. Dewan, M.W., et al., *Effect of post-weld heat treatment and electrolytic plasma processing on tungsten inert gas welded AISI 4140 alloy steel*. Materials & Design, 2014. 54: p. 6-13.

179. Chen, X., et al., *Effects of an ultrasonically excited TIG arc on CLAM steel weld joints*. The International Journal of Advanced Manufacturing Technology, 2012. 60(5-8): p. 537-544.

180. Baghjari, S.H. and S.A.A. Akbari Mousavi, *Effects of pulsed Nd:YAG laser welding parameters and subsequent post-weld heat treatment on microstructure and hardness of AISI 420 stainless steel*. Materials & Design, 2013. 43(0): p. 1-9.

181. Sireesha, M., et al., *Microstructural features of dissimilar welds between 316LN austenitic stainless steel and alloy 800*. Materials Science and Engineering: A, 2000. 292(1): p. 74-82.

182. Ming, H., et al., *Microstructural characterization of an SA508–309L/308L–316L domestic dissimilar metal welded safe-end joint*. Materials Characterization, 2014. 97: p. 101-115.

183. Kell, J., *Melt pool and microstructure manipulation using diffractive holographic elements in high power conduction laser welding*, 2007, © James Kell.

184. Davis, J.R., *Stainless steels*1994: ASM international.

185. Zhang, F., et al., *Flash butt welding of high manganese steel crossing and carbon steel rail*. Materials Science and Engineering: A, 2007. 454: p. 288-292.

186. Marshall, P., *Austenitic stainless steels: microstructure and mechanical properties*1984: Springer Science & Business Media.

187. National Physical Laboratory and the University of Cambridge. *Materials Algorithms Project*. 2014 [cited 2014 13 August].

188. Verhoeven, J.D., *Steel metallurgy for the non-metallurgist*2007: ASM International.

189. Toparli, M., et al., *Thermal stress analysis of HVOF sprayed WC–Co/NiAl multilayer coatings on stainless steel substrate using finite element methods*. Journal of Materials Processing Technology, 2007. 190(1): p. 26-32.

190. Attarha, M. and I. Sattari-Far, *Study on welding temperature distribution in thin welded plates through experimental measurements and finite element simulation.*

Journal of Materials Processing Technology, 2011. 211(4): p. 688-694.

191. Ranjbarnodeh, E., et al., *Effect of welding parameters on the heat-affected zone of AISI409 ferritic stainless steel.* International Journal of Minerals, Metallurgy, and Materials, 2012. 19(10): p. 923-929.

192. Ng, E.S. and I.A. Watson, *Characteristics of CO2 laser welded high carbon steel gauge plate.* Journal of Laser Applications, 1997. 9(1): p. 15-21.

193. Lippold, J.C., *Welding Metallurgy and Weldability*2014: John Wiley & Sons.

194. Hicks, J., *Welded joint design*1999: Elsevier.

195. Handbook, W., *Vol. 2, Welding Processes, 1991.* Ed. RL O'Brien, Miami, Fla.: American Welding Society: p. 550-552.

196. Peasura, P. and L. Sumarn, *Effect of Post Weld Heat Treatment on Carbon Steel AISI 1050 in Heat Effected Zone.* Advanced Materials Research, 2013. 650: p. 612-615.

197. Testing, A.S.f. and M. Philadelphia, *Standard guide for preparation of metallographic specimens.* 2011.

198. Sathiya, P., et al., *Effect of shielding gases on mechanical and metallurgical properties of duplex stainless-steel welds.* Journal of Materials Science, 2009. 44(1): p. 114-121.

199. Elmesalamy, A., *Narrow gap laser welding of 316L stainless steel for potential application in the manufacture of thick section nuclear components.* 2013.

200. Rajakumar, S., C. Muralidharan, and V. Balasubramanian, *Influence of friction stir welding process and tool parameters on strength properties of AA7075-T< sub> 6</sub> aluminium alloy joints.* Materials & Design, 2011. 32(2): p. 535-549.

201. Derringer, G., *Simultaneous optimization of several response variables.* Journal of quality technology, 1980. 12: p. 214-219.

202. Negarestani, R., et al., *Numerical simulation of laser machining of carbon-fibre-reinforced composites.* Proceedings of the Institution of Mechanical Engineers, Part B: Journal of Engineering Manufacture, 2010. *224*(7): p. 1017-1027.

203. Manonmani, K., N. Murugan, and G. Buvanasekaran, *Effects of process parameters on the bead geometry of laser beam butt welded stainless steel sheets.* The International Journal of Advanced Manufacturing Technology, 2007. 32(11-12): p. 1125-1133.

204. K. Y. Benyounis, A.G.O.a.M.S.J.H., *Estimation of mechanical properties of laser welded joints using RSM*, in *22nd International Manufacturing Conference*31 Aug.- 2 Sep. 2005: Institute of Technology Tallaght, Dublin- Ireland. p. 565-571.

205. Eghlio, R., A. Pinkerton, and L. Li, *Characterization of weld bead geometry in fibre laser butt welding of mild steel sheets by means of statistical modelling.* Lasers in engineering, 2012. 22(5-6): p. 281-298.

206. Mackwood, A. and R. Crafer, *Thermal modelling of laser welding and related processes: a literature review.* Optics & Laser Technology, 2005. 37(2): p. 99-115.

207. Henrikson, P., *Visualisation of weld pool surface flow during TIG welding of stainless steel 316l plates.* Mathematical Modelling of Weld Phenomena, 2005. 7: p. 125-147.

208. Zhou, J. and H. Tsai, *Investigation of mixing and diffusion processes in hybrid spot laser–MIG keyhole welding.* Journal of Physics D: Applied Physics, 2009. 42(9): p. 095502.

209. Hosseinpour, V., M. Kazemeini, and A. Mohammadrezaee, *Optimisation of Ru-promoted Ir-catalysed methanol carbonylation utilising response surface methodology.* Applied Catalysis A: General, 2011. 394(1): p. 166-175.

210. Mason, R.L., R.F. Gunst, and J.L. Hess, *Statistical design and analysis of*

experiments: with applications to engineering and science. Vol. 474. 2003: John Wiley & Sons.

211. Tadamalle, A., Y. Reddy, and E. Ramjee, *Influence of laser welding process parameters on weld pool geometry and duty cycle.* Advances in Production Engineering & Management, 2013. 8(1).

212. Yue, C., et al., *Kinetic analysis of the austenite grain growth in GCr15 steel.* Journal of materials engineering and performance, 2010. 19(1): p. 112-115.

213. Leondes, C.T., *Computer-Aided Design, Engineering, and Manufacturing: Systems Techniques and Applications, Volume II, Computer-Integrated Manufacturing.* Vol. 2. 2002: CRC Press.

214. Mendez, P.F. and T.W. Eagar, *Penetration and defect formation in high-current arc welding.* Welding journal, 2003. 82(10): p. 296.

215. Wei, P., H. Liu, and C. Lin, *Scaling weld or melt pool shape induced by thermocapillary convection.* International Journal of Heat and Mass Transfer, 2012. 55(9): p. 2328-2337.

216. Lippold, J.C. and D.J. Kotecki, *Welding metallurgy and weldability of stainless steels.* Welding Metallurgy and Weldability of Stainless Steels, by John C. Lippold, Damian J. Kotecki, pp. 376. ISBN 0-471-47379-0. Wiley-VCH, March 2005., 2005. 1.

217. Sundar, M., et al., *Effect of process parameters on the cutting quality in lasox cutting of mild steel.* The International Journal of Advanced Manufacturing Technology, 2009. 40(9-10): p. 865-874.

218. Berretta, J.R., et al., *Pulsed Nd: YAG laser welding of AISI 304 to AISI 420 stainless steels.* Optics and Lasers in Engineering, 2007. 45(9): p. 960-966.

219. Omar, A., *Effects of welding parameters on hard zone formation at dissimilar metal welds.* Welding journal, 1998. 77(2): p. 86-93.

220. Sun, Z. and T. Moisio, *Weld metal/ferritic steel interface in laser welded austenitic/ferritic dissimilar steel joints.* Journal of materials science letters, 1994. 13(11): p. 802-805.

221. Hassan, E.M., *Feasibility and optimization of dissimilar laser welding components.* 2008.

222. Bachmann, M., et al., *Numerical simulation of full-penetration laser beam welding of thick aluminium plates with inductive support.* Journal of Physics D: Applied Physics, 2012. *45*(3): p. 035201.

223. Boyer, H.E. and T.L. Gall, *Metals handbook; desk edition.* 1985.

224. Deng, D. and H. Murakawa, *Finite element analysis of temperature field, microstructure and residual stress in multi-pass butt-welded 2.25 Cr–1Mo steel pipes.* Computational materials science, 2008. 43(4): p. 681-695.

225. Banovic, S., I. DuPont, and A. Marder, *Dilution control in gas-tungsten-arc welds involving superaustenitic stainless steels and nickel-based alloys.* Metallurgical and Materials Transactions B, 2001. 32(6): p. 1171-1176.

226. Olson, D.L., *ASM handbook: welding, brazing, and soldering.* Vol. 6. 1993: Asm Intl.

227. Savit͡skiĭ, E.M., *The influence of temperature on the mechanical properties of metals and alloys* 1961: Stanford University Press.

228. Rosenthal, D., *Mathematical theory of heat distribution during welding and cutting.* Welding journal, 1941. 20(5): p. 220–234.

229. Zhao, S., et al., *Numerical simulation and experimental investigation of laser overlap welding of Ti6Al4V and 42CrMo.* Journal of Materials Processing Technology, 2011. 211(3): p. 530-537.

230. Cho, W.-I., et al., *Numerical study of alloying element distribution in CO< sub> 2</sub> laser–GMA hybrid welding.* Computational materials science, 2010. 49(4): p. 792-800.
231. Fluent, *13.0 User's Guide.* ANSYS Inc, 2009.
232. Mazumder, J. and W. Steen, *Heat transfer model for CW laser material processing.* Journal of Applied Physics, 1980. 51(2): p. 941-947.
233. Amara, E.H. and R. Fabbro, *Modeling of humps formation during deep-penetration laser welding.* Applied Physics A: Materials Science and Processing, 2010. 101(1): p. 111-116.
234. Semak, V. and A. Matsunawa, *The role of recoil pressure in energy balance during laser materials processing.* Journal of Physics D: Applied Physics, 1997. 30(18): p. 2541-2552.
235. Bathe, K.-J., *Finite element procedures* 2006: Klaus-Jurgen Bathe.
236. Sunar, M., B. Yilbas, and K. Boran, *Thermal and stress analysis of a sheet metal in welding.* Journal of Materials Processing Technology, 2006. 172(1): p. 123-129.
237. William F. Gale, T.C.T., *Smithells Metals Reference Book* 2004: Elsevier.
238. Sahin, S., et al., *Modelled and measured residual stresses in a bimaterial joint.* Journal of Materials Processing Technology, 2003. 132(1-3): p. 235-241.
239. Josefson, B.L., *Prediction of residual stresses and distortions in welded structures.* Journal of Offshore Mechanics and Arctic Engineering, 1993. 115(1): p. 52.
240. Sundar, M., et al., *Finite element analysis of residual stress and distortion in laser welded stainless plate.* International Journal for Manufacturing Science & Production, 2007. 8(24): p. 123-136.
241. Joseph, A., et al., *Evaluation of residual stresses in dissimilar weld joints.* International journal of pressure vessels and piping, 2005. 82(9): p. 700-705.
242. Jafarzadegan, M., et al., *Microstructural characterization in dissimilar friction stir welding between 304 stainless steel and st37 steel.* Materials Characterization, 2012. 74: p. 28-41.
243. Nikulina, A., et al., *Microstructure and fracture behaviour of flash butt welds between dissimilar steels.* Science and Technology of Welding and Joining, 2014.
244. David, S., et al., *Effect of rapid solidification on stainless steel weld metal microstructures and its implications on the Schaeffler diagram*, 1987, Oak Ridge National Lab., TN (USA).
245. Muthupandi, V., et al., *Effect of weld metal chemistry and heat input on the structure and properties of duplex stainless steel welds.* Materials Science and Engineering: A, 2003. 358(1): p. 9-16.
246. Ananthapadmanaban, D., et al., *A study of mechanical properties of friction welded mild steel to stainless steel joints.* Materials & Design, 2009. 30(7): p. 2642-2646.
247. Di, X., S. Deng, and B. Wang, *Effect of pulse current on mechanical properties and dendritic morphology of modified medium manganese steel welds metal.* Materials & Design, 2014.
248. Zambon, A. and F. Bonollo, *Rapid solidification in laser welding of stainless steels.* Materials Science and Engineering: A, 1994. 178(1): p. 203-207.
249. Chande, T. and J. Mazumder, *Estimating effects of processing conditions and variable properties upon pool shape, cooling rates, and absorption coefficient in laser welding.* Journal of Applied Physics, 1984. 56(7): p. 1981-1986.
250. David, S.A., G. Goodwin, and D. Braski, *Solidification behavior of austenitic stainless steel filler metals* 1980: Department of Energy, Oak Ridge National Laboratory.
251. Leblond, J., J. Devaux, and J. Devaux, *Mathematical modelling of transformation*

plasticity in steels I: case of ideal-plastic phases. International journal of plasticity, 1989. 5(6): p. 551-572.

252. Lee, C.-H., *Computational modelling of the residual stress evolution due to solid-state phase transformation during welding.* Modelling and Simulation in Materials Science and Engineering, 2008. 16(7): p. 075003.

253. Ferro, P., et al., *The influence of phase transformations on residual stresses induced by the welding process—3D and 2D numerical models.* Modelling and Simulation in Materials Science and Engineering, 2006. 14(2): p. 117.

254. Oddy, A., J. Goldak, and J. McDill, *Numerical analysis of transformation plasticity in 3D finite element analysis of welds.* European journal of mechanics. A. Solids, 1990. 9(3): p. 253-263.

255. Yaghi, A., et al., *Finite element simulation of welding and residual stresses in a P91 steel pipe incorporating solid-state phase transformation and post-weld heat treatment.* The Journal of Strain Analysis for Engineering Design, 2008. 43(5): p. 275-293.

256. Pasquale, P., W. Burget, and W. Pfeiffer, *Residual stresses and deformation in dissimilar girth welds: Numerical simulations and experimental verifications.* Zeitschrift für Metallkunde, 2001. 92(3): p. 270-274.

257. Tawfik, D., P.J. Mutton, and W.K. Chiu, *Experimental and numerical investigations: Alleviating tensile residual stresses in flash-butt welds by localised rapid post-weld heat treatment.* Journal of Materials Processing Technology, 2008. 196(1): p. 279-291.

258. Becker, M., et al., *Prediction and measurement of phase transformations, phase dependent properties and residual stresses in steels.* OSTI report, 2005(8550544).

259. Adil, G. and S. Bhole, *HAZ Hardness and Microstructure Predictions of Arc Welded Steels—I. Review of Predictive Models.* Canadian metallurgical quarterly, 1992. 31(2): p. 151-157.

260. Piekarska, W., M. Kubiak, and Z. Saternus, *Numerical Simulation of Deformations in T-Joint Welded by the Laser Beam.* Archives of Metallurgy and Materials, 2013. 58(4): p. 1391-1396.

261. Vander Voort, G.F., *Atlas of time-temperature diagrams for irons and steels*1991: ASM international.

Appendix- A: Published Papers

These papers have been removed from the Open Access version for third party copyright reasons